

# POLYMORPHS, COCRYSTALS AND SOLID SOLUTIONS

NEW APPROACHES FOR THE DESIGN AND GROWTH OF  
ORGANIC AND PHARMACEUTICAL MATERIALS

By  
**MARTA DABROS**

A Dissertation Submitted to the Faculty of the  
WORCESTER POLYTECHNIC INSTITUTE



In partial fulfillment of the requirements for the  
Degree of Doctor of Philosophy  
in Chemistry  
by

---

January 2009

APPROVED:

---

Dr. Venkat R. Thalladi  
Advisor

---

Dr. Dhandapani Venkataraman  
External Reviewer, UMass Amherst

---

Dr. James P. Dittami  
Committee Member

---

Dr. John C. MacDonald  
Committee Member

---

Dr. Kristin N. Wobbe  
Head of Department

THIS PAGE LEFT INTENTIONALLY BLANK

## **ACKNOWLEDGEMENTS**

It is my pleasure to thank my supervisor Professor Venkat Thalladi for his scientific guidance and encouragement throughout my Ph.D. career.

I would like to acknowledge the support of the members of the Department of Chemistry and Biochemistry at WPI. I thank my thesis committee members Professors John MacDonald, James Dittami, and Dhandapani Venkataraman for their time and evaluation. In particular, I thank Professor MacDonald for many valuable suggestions over the last few years.

I would like to express many thanks to Dr. Richard Staples and Dr. Jingwei Huang at Harvard University for collecting numerous single crystal X-ray datasets. Special thanks to Richard for his discussions and passing his contagious enthusiasm.

I wish to thank my colleagues and friends who directly and indirectly helped me to accomplish this project. I thank my labmates Salimgerey Adilov, Jason Cox and Paul Emery for their support and discussions. I thank Salim for being a friend and for making us laugh in difficult times. I wish to thank all the undergraduate students who passed through our group for bringing new energy into the lab every year.

I wish to thank my parents and my husband for their continuous support especially when it was most required.

THIS PAGE LEFT INTENTIONALLY BLANK

## TABLE OF CONTENTS

### 1. SINGLE AND MULTICOMPONENT PHARMACEUTICAL SOLIDS

1.1	Introduction	3
1.2	Molecules and Molecular Aggregates	3
1.3	The Four Phases of Matter	3
1.4	Pharmaceutically Relevant Condensed Phases	4
1.5	Amorphous Solids	5
1.6	Crystalline Solids	6
1.7	Polymorphs	6
1.8	Solvates	7
1.9	Salts	8
1.10	Cocrystals	8
1.11	Ionic Cocrystals	9
1.12	Solid Solutions	10
1.13	Summary and Conclusion	10
1.14	References	11

### 2. PARITY DEPENDENT FACE-SELECTIVE CRYSTAL GROWTH OF CARBAMAZEPINE ON SELF-ASSEMBLED MONOLAYERS

2.1	Introduction	17
2.2	Nucleation	17
2.3	Crystal Growth by Heterogeneous Nucleation	18
2.4	Self-Assembled Monolayers	19
2.5	SAMs as Templates for Crystal Growth	21
2.6	Parity of Alkyl Chains and Orientation of Terminal Groups	21
2.7	Amide Dimers in Carbamazepine Polymorphs	22
2.8	Parity of Alkyl Chains and Orientation of Terminal Groups	23
2.9	Crystallization of Carbamazepine on SAMs	24
2.10	Oriented Crystal Growth	24
2.11	Calibration of Powder X-Ray Diffraction Patterns	26
2.12	Geometric Epitaxy Between SAMs and Growth Faces	28
2.13	Carboxy Terminated SAMs versus Plasma Treated Glass Slides	30
2.14	Parity Dependent Face-Selective Crystal Growth	30
2.15	Conclusion	31
2.16	References	32

### 3. SUPPRESSION OF NUCLEATION AT FLUOROUS INTERFACES – A NEW PARADIGM FOR THE SELECTIVE GROWTH OF STABLE POLYMORPHS

3.1	Polymorphism	37
3.2	High-Throughput Screening	37
3.3	Isomorphic Additives	37
3.4	Monolayers as Substrates	38
3.5	Single Crystals as Substrates	38
3.6	Polymers as Substrates	39
3.7	Crystallization inside Capillaries	39
3.8	Crystallization inside Nanoscale Chambers	39
3.9	Laser Induced Nucleation	39
3.10	Sonocrystallization	40

3.11	Contact Line crystallization	40
3.12	High Pressure Crystallization	40
3.13	Disappearing Polymorphs	40
3.14	Fluorous Surfaces	41
3.15	Promotion versus Inhibition	42
3.16	Nitrofurantoin	42
3.17	Plasma Treatment of Glass Substrates	44
3.18	Fabrication of Fluorous Monolayers	44
3.19	Crystal Growth in Hydroxylated and Fluorous Vials	45
3.20	Visual Observations	46
3.21	IR and Raman Characterization of Polymorphs	48
3.22	Single Crystal X-Ray Diffraction Analysis	50
3.23	Powder X-Ray Diffraction Analysis	54
3.24	Thermal Analysis	55
3.25	Effect of Rate of evaporation	56
3.26	Effect of Initial concentration	57
3.27	Remnant Concentration	58
3.28	Polymorph Selection by Ostwald Ripening	59
3.29	Summary and Conclusion	60
3.30	References	61
<b>4.</b>	<b>FLUOROUS PHARMACEUTICALS – INHIBITION OF NUCLEATION AT HYDROPHILIC SURFACES</b>	
4.1	Pharmaceuticals with Fluorous Fragments	69
4.2	Enantiotropic and Monotropic Phase Transitions	70
4.3	Flufenamic Acid	71
4.4	Crystal Growth in Hydroxylated and Fluorous Vials	72
4.5	Visual Observations	73
4.6	IR Spectroscopic Characterization of Solid Forms	74
4.7	Crystal Structures of Forms I and III	76
4.8	Powder X-Ray Diffraction Analysis	79
4.9	Thermal Analysis of Phase Transitions	79
4.10	Crystal Growth above the Phase Transition Temperature	81
4.11	Summary and Conclusion	82
4.12	References	83
<b>5.</b>	<b>SUPRAMOLECULAR SOLID SOLUTIONS – A NEW APPROACH TO MULTICOMPONENT ORGANIC ALLOYS</b>	
5.1	Background	87
5.2	Molecular Crystals	87
5.3	Cocrystals	88
5.4	Molecular Solid Solutions	88
5.5	Supramolecular Solid Solutions	88
5.6	Supramolecular Synthons	89
5.7	DABCO and 4-X-Phenols	90
5.8	Crystal Structures of Binary Cocrystals	91
5.9	Continuous Series of Ternary Solid Solutions	94
5.10	Spectroscopic Characterization of Ternary Solid Solutions	97
5.11	Trends in the Melting Points of Solid Solutions	97

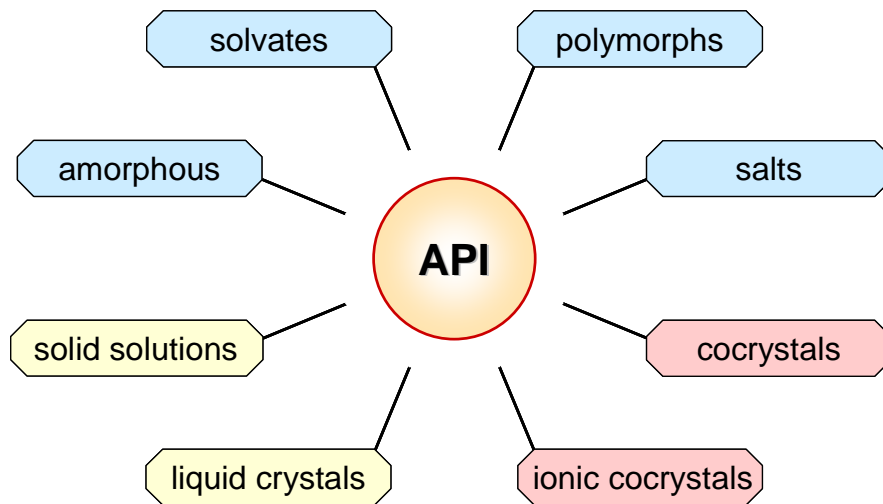
5.12	Quaternary and Quinary Solid Solutions	98
5.13	Preparation of Cocrystals and Solid Solutions by Grinding	102
5.14	Multicomponent Solids with DABCO and 3-X-Phenols	103
5.15	Multicomponent Solids with 4,4'-Bipyridyl and 4- and 3-X-Phenols	110
5.16	Multicomponent Solids with Hydroxy...Amino Recognition	111
5.17	Summary and Conclusion	118
5.18	References	119

## 6. SYNTHESIS AND STRUCTURES OF TRIGONAL MANGANESE CARBOXYLATES – TOWARD OCTUPOLAR NONLINEAR OPTICAL MATERIALS

6.1	Introduction	125
6.1.1	Background	125
6.1.2	Dipolar Organic Materials	125
6.1.3	Octupolar Symmetries	125
6.1.4	Octupolar <i>Molecular</i> Materials	126
6.1.5	Octupolar 2D <i>Supramolecular</i> Materials	127
6.1.6	Critical Need for 3D Octupolar Supramolecular Materials	128
6.1.7	Functionalized Materials based on Metal Carboxylate Clusters	129
6.2	Design, Synthesis, and IR Analysis of TMCs	130
6.2.1	Design strategy for 3D Octupolar Materials	130
6.2.2	Synthetic Approach	131
6.2.3	Known Structural Chemistry of TMCs – CSD Analysis	132
6.2.4	Synthesis of Discrete TMCs	133
6.2.5	Selection of Ligands (Acids and Pyridines)	134
6.2.6	Spectroscopic Characterization of TMCs	136
6.3	Crystal Structural Analysis of TMCs	138
6.3.1	General Considerations in Structural Analysis	138
6.3.2	Structures Adopting Idealized Acentric $6^3$ Networks	140
6.3.3	Crystal Structure of $[\text{Mn}_3\text{O}(\text{BA})_6\text{Py}_3]^+[\text{ClO}_4]^- \cdot \text{C}_6\text{H}_6$	140
6.3.4	Crystal Structure of $[\text{Mn}_3\text{O}(\text{BA})_6(4\text{-Picoline})_3]^+[\text{ClO}_4]^- \cdot \text{C}_6\text{H}_6$	144
6.3.5	Crystal Structure of $[\text{Mn}_3\text{O}(\text{BA})_6(4\text{-Picoline})_3]^+[\text{ClO}_4]^- \cdot \text{CH}_2\text{Cl}_2$	145
6.3.6	Crystal Structure of $[\text{Mn}_3\text{O}(\text{BA})_6(3\text{-Picoline})_3]^+[\text{ClO}_4]^- \cdot \text{C}_6\text{H}_6$	145
6.3.7	Crystal Structure of $[\text{Mn}_3\text{O}(p\text{TA})_6(\text{Py})_3]^+[\text{ClO}_4]^-$ : Acentric $4^4$ and $\bar{C}$ entric $3^6$ Networks	146
6.3.8	Structures Adopting Acentric $4^4$ and $\bar{A}$ centric $3^6$ Networks	149
6.3.9	Crystal Structure of $[\text{Mn}_3\text{O}(m\text{TA})_6(\text{Py})_3]^+[\text{ClO}_4]^-$	150
6.3.10	Crystal Structure of $[\text{Mn}_3\text{O}(p\text{TA})_6(4\text{-Picoline})_3]^+[\text{ClO}_4]^- \cdot \text{CH}_2\text{Cl}_2$	150
6.3.11	Crystal Structure of $[\text{Mn}_3\text{O}(p\text{TA})_6(3\text{-Picoline})_3]^+[\text{ClO}_4]^- \cdot \text{C}_6\text{H}_6$	151
6.3.12	Crystal Structure of $[\text{Mn}_3\text{O}(m\text{TA})_6(4\text{-Picoline})_3]^+[\text{ClO}_4]^-$	152
6.3.13	Crystal Structure of $[\text{Mn}_3\text{O}(3\text{CIBA})_6(4\text{-Picoline})_3]^+[\text{ClO}_4]^-$	153
6.3.14	Crystal Structure of $[\text{Mn}_3\text{O}(m\text{TA})_6(3,4\text{-Lutidine})_3]^+[\text{ClO}_4]^-$	154
6.4	Clusters of Higher Nuclearity	155
6.4.1	Synthesis and Structure of $\text{Mn}_6(\text{OOCR})_{10}(\text{CH}_3\text{CN})_4$	155
6.4.2	Synthesis, Structure, and Magnetic Properties of $\text{Mn}_{13}\text{-}\mu^3\text{O}_2\text{-}\mu^2\text{O}_6(\text{OOCR})_{12}(\text{C}_2\text{H}_5\text{O})_6$	156
6.5	Summary and Conclusion	157
6.5	References	158

THIS PAGE LEFT INTENTIONALLY BLANK

# 1 SINGLE AND MULTICOMPONENT PHARMACEUTICAL SOLIDS



THIS PAGE LEFT INTENTIONALLY BLANK

## 1.1 INTRODUCTION

Solid state chemistry, in its many facets, is the guiding principle for different projects carried out in this thesis. Most of the projects discussed here involve organic and pharmaceutical materials and some projects are based on metal-organic clusters and frameworks. All projects focus on the design, synthesis and characterization of these compounds in the solid state and emphasize the pharmaceutical applications of the methods developed and materials prepared. The objective of this introductory chapter is to discuss various condensed phases of matter used in pharmaceutical processing,<sup>1</sup> and point to areas where the contents of this thesis make some contributions. Our work involves oriented crystal growth on surfaces that offer complementary functional groups, control of polymorphism using fluorinated substrates that inhibit heterogeneous nucleation, preparation of binary cocrystals that use single- and multi-point hydrogen bonds, and synthesis of multicomponent solid solutions that contain a target molecule and several isosteric components. Crystals, polymorphs, solvates, neutral cocrystals, ionic cocrystals, and solid solutions are the various phases that we specifically prepared or fortuitously encountered in this work.<sup>2-6</sup> In the following sections we highlight the properties of these phases and discuss their relevance in pharmaceutical development.

## 1.2 MOLECULES AND MOLECULAR AGGREGATES

Molecules are a collection of atoms bound together by covalent bonds. The assembly of molecules depends on their size, chemical composition, and three-dimensional structure. Molecules, when aggregate into macroscopic state, can adopt different structures and have different energies. The macroscopic forms that are homogeneous in chemical composition and physical state and that exhibit defined boundaries are called *phases*. Molecules exist as phases and the bulk properties of a given compound are defined by its phase structure and composition.

In different phases, molecules are at different separations and orientations and participate in intermolecular interactions of different strength and geometry. These interactions, though weak, influence the material properties of a given compound; in the pharmaceutical realm, they determine the important traits such as solubility, bioavailability and long-term stability. Controlling the phase structure and composition is therefore an essential part in drug development.

## 1.3 THE FOUR PHASES OF MATTER

We generally consider matter to adopt one of the four possible phases: gases, liquids, mesophases and solids. In gases, molecules are far apart and their relative orientation and separation do not significantly affect macroscopic properties. In liquids, though the molecules are closer to each other than they are in gases, the relative orientation and separation of the components hardly affects the bulk properties of the liquids. In crystalline solids, molecules are locked into specific orientations and separations and changes in orientations and separations between components lead to *different* solid phases (polymorphs) with different macroscopic properties.

Mesophases possess some characteristics of liquids and some of solids. In liquids molecules have positional, orientational, conformational and vibrational freedom. In crystalline solids all freedoms but the vibrational one are absent. Mesophases are formed when certain freedoms are introduced into the solid state. For example, solids in which the components have (a) positional freedom result in liquid crystals, (b) orientational freedom result in plastic crystals, and (c) conformational freedom result in condic crystals. Together, liquid crystals, plastic crystals and condic crystals are called mesophases.<sup>7</sup>

#### 1.4 PHARMACEUTICALLY RELEVANT CONDENSED PHASES

It is essential to understand the structures and energetics of phases to master their synthesis and control their properties. In previous section, we discussed the structural aspects of the phases. As the molecular motion and intermolecular separation decrease when one goes from gases, to liquids, to mesophases, and to solids, the packing order and intermolecular attraction increase in the same order. Thus, the more condensed the phases get the lower is their free energy. Crystalline solids are energetically the most stable of the phases and are most often used in drug development.<sup>8</sup> Figure 1.1 shows some of the macroscopic forms used in pharmaceutical formulations. In addition to the phases discussed above, it contains the amorphous solid phase and multicomponent phases such as salts, solvates and cocrystals. Below we will discuss the properties of these distinct forms and their relevance in dosage design and our work.

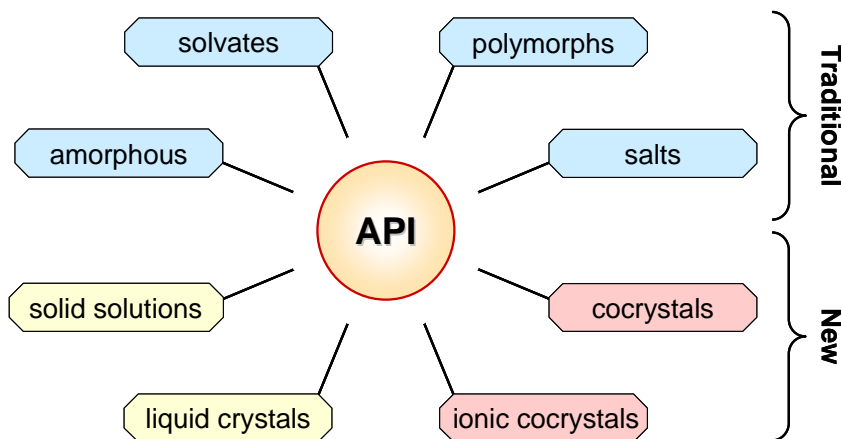


**Figure 1.1** Schematic representations of different forms that can be generated from an active pharmaceutical ingredient (API). Solid forms indicated in blue are traditionally used in pharmaceutical industry. Forms in yellow and pink have been proposed as new types of phases for drug formulations.

## 1.5 AMORPHOUS SOLIDS

Amorphous solids, also called glasses, are condensed phases of matter that lack long range molecular order, but possess some short range order.<sup>9</sup> Though amorphous solids are widely studied, little is known about their structure. Most of this structural information is obtained on inorganic glasses and that information is extended to organic amorphous materials. Amorphous solids are formed by kinetic pathways; they are metastable with respect to their crystalline counterparts. Glasses are generally prepared by cooling a material below its melting point and arresting the positions of molecules within this super cooled liquid. Pharmaceutical amorphous solids are prepared by methods such as spray drying, rapid solvent evaporation, temperature quenching, lyophilization, and mechanical compaction.<sup>9</sup>

Amorphous solids have lower packing efficiency, higher molecular disorder and higher potential energy than crystals. Higher energy of amorphous solids leads to their lower stability but also to higher solubility, bioavailability and reactivity.<sup>10</sup> The differences in energy between the two solid states often results in the transformation of the amorphous solid to the crystalline solid. This transformation is dictated by the kinetic barrier; higher the barrier the greater the stability of amorphous solids. The path to crystallization is often induced by humidity, temperature, pressure or some other external factor. The processes in the early development, lyophilization for example, often produce solids that are more amorphous than crystalline, and exhibit superior solubilities and bioavailabilities. In late stage development, however, purer and larger quantities of the drugs readily yield crystalline solids that exhibit inferior dissolution properties. Recognition and control of the solid phases are thus crucial in drug development. Figure 1.2 shows different forms an API can adopt for use in formulations.

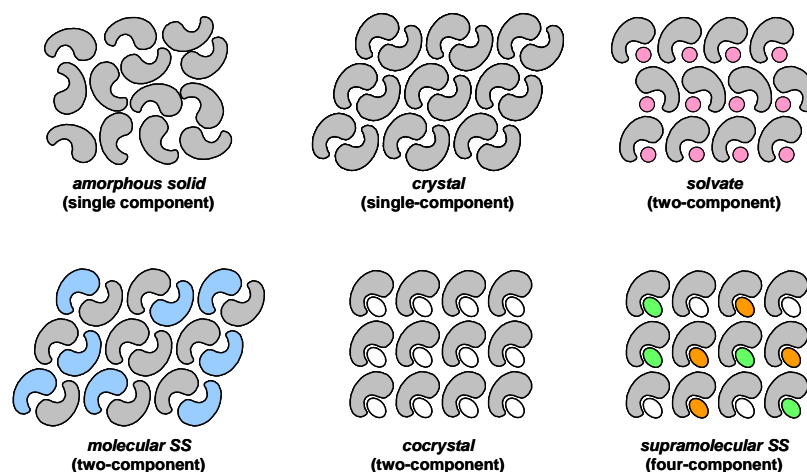


**Figure 1.2** Schematic representations of various solid state forms API (grey object). Pink circles represent solvent molecules and blue objects represent molecule that are isosteric with API. White, green and orange ovals represent molecules that can form hydrogen bonds with API to yield cocrystals or solid solutions. The term SS stands for solid solution.

## 1.6 CRYSTALLINE SOLIDS

Crystalline solids, the most widely used condensed phases in pharmaceutical practice,<sup>8</sup> exhibit short range *and* long range molecular order. Short range order in crystals arises from specific, directional, and attractive interactions between complementary portions of molecules. Long range order results in a macroscopic phase with lowest potential energy. Crystals, with their periodic structures, lend themselves well to diffraction analysis and allow the determination of three-dimensional structures of molecules and intermolecular packing. From this data, one can glean information about molecular composition, conformation, and stereochemistry, and intermolecular interactions, packing patterns, and packing efficiency.<sup>11-13</sup> Crystals are the most stable condensed phases and are most sought after targets in drug development. Extensive research has been done in areas of crystal growth, structure determination, and the design of crystal structures. In Chapter 2 we discuss the importance of heterogeneous nucleation in crystal growth and how it may impact the oriented growth of carbamazepine. The fields of crystal engineering<sup>5</sup> and supramolecular chemistry<sup>13</sup> enhanced our understanding that properties of a compound are dependent on molecular *and* supramolecular structure. In the following sections, we discuss various forms in which the single or multicomponent crystals can be obtained and how these forms affect the properties of the target compound.

## 1.7 POLYMORPHS

The ability of a chemical entity to crystallize in more than one solid state structures is known as polymorphism.<sup>2</sup> An oft quoted statement asserts that *every compound has different polymorphic forms, and the number of forms known for a given compound is proportional to the time and money spent in research on that compound.*<sup>14</sup> A well known example is ROY, a pharmaceutical intermediate that at the moment has seven reported polymorphs.<sup>15</sup> It is estimated that about 30% of the pharmaceuticals exhibit polymorphism.<sup>3</sup>

Polymorphs can exhibit different lattice structures or different molecular conformations or both. *Conformational polymorphism* refers to structures in which molecules exist in different conformations but retain the same packing arrangement. *Packing polymorphism*, exhibited by many rigid molecules, refers to crystals in which the components retain the same conformation but show different packing arrangements. Different polymorphs of the same molecule often exhibit very different properties and behave as different materials. They may show different thermodynamic, kinetic, spectroscopic, mechanical and physicochemical properties. This awareness is very important in fields where products are commercialized as crystalline solids (such as drugs, food additives, pigments, explosives).

In pharmaceutical industry, thermodynamically most stable polymorphs are often chosen as final drug products because they are less likely to convert to other macroscopic phases. The disadvantage of this approach is that usually the most stable polymorph is the least soluble therefore shows the lowest bioavailability. When the most stable form is not identified during the initial polymorph screening it may have devastating consequences

on the marketed drug. A well known example is the case of ritanovir (Norvir).<sup>16</sup> During the formulation process only form I was discovered. After about two years on the market capsules containing ritanovir drug failed to dissolve due to the precipitation of new, thermodynamically more stable form of the drug (form II). The difference in solubility of form I and form II is about five fold. The original I drug formulation had to be taken back from the market and the new formulation had to be developed. This extreme example shows the importance of extensive work in the early development to identify all possible forms and their stabilities. We show in Chapters 3 and 4 a unique method that promotes the crystallization of more stable polymorphs under conditions that are favorable for the growth of less stable polymorphs.

### 1.8 SOLVATES

Besides single component polymorphs, organic compounds can also exist as solvates, salts and other multicomponent materials such cocrystals or solid solutions. Of practical interest are solid forms containing solvents, where solvent molecule is incorporated in the crystal lattice in a stoichiometric or a non-stoichiometric ratio. They are generally known as solvates but sometimes also called as pseudopolymorphs. Solvates are capable of bringing significant changes in properties compared to polymorphs of the API molecule.<sup>17-19</sup>

During the drug development process pharmaceutical solids are exposed to solvents or solvent vapors. The most common solvent-based processes that lead to the formation of solvates in pharmaceutical industry are precipitation, crystallization, wet granulation or dissolution. The tendency of an API molecule to form solvates is highly related with its molecular structure, ability to form hydrogen bonds, and overall size and shape. A molecule that possesses greater number of hydrogen bond donors than acceptors (or vice versa) will show higher tendency to form solvates. In addition, the tendency of solvation increases with the size of the molecule and ionization.

Nucleation of unsolvated crystals from solvent requires solute-solvent interactions to be replaced by solute-solute interactions. Relatively stable solute-solvent interactions may lead to formation of solvated crystals. An analysis of the Cambridge Structural Database (CSD) showed that water is most frequently met as solvate former due its abundance in atmosphere, its small size and its ability to behave as both hydrogen bond donor and acceptor.<sup>20</sup> In general, more than 57% of drug molecules form polymorphs or solvates.<sup>6</sup> The antibacterial drug sulfathiazole forms an incredibly high number of solvates, over one hundred of them.<sup>21</sup>

Solvates can be attractive candidates for drug development especially when they exhibit higher solubility compared to other solid state forms. In contrast, unintended hydrate formation can lead to decreased solubility in blood and failure of an otherwise potent drug. Solvates are common among drug substances and a better knowledge of solvent-API interactions will help to understand and control complex behavior of molecules. Solvents, most often than not, included into crystal lattice by chance, not by choice. The

intended incorporation of a foreign chemical entity into a drug substance can lead to a neutral cocrystal, an ionic cocrystal or a salt.

### 1.9 SALTS

Drug discovery has gone through significant changes in the last decade. The increased use of combinatorial chemistry, computational modeling in drug discovery as well as the recent change in the *in vitro* biology screening method from manual screening of aqueous soluble drugs to high-throughput screening of compounds soluble in DMSO led to compounds with very low solubility. Newly proposed drugs typically tend to have larger molecular size and a greater number of hydrogen bonding groups, leading to a significant decrease in solubility. Consequently, targeted compounds have low aqueous solubility limiting their use for oral absorption.

Polymorphs and solvates offer limited variation of solid forms of a given API. In case of insoluble drugs, crystal engineering approaches allow us to design new solid forms without altering the chemical activity of the compound. The most common method involves salt formation.<sup>22</sup> To create a salt, a drug candidate must possess ionizable (acidic or basic) functional group. Typically, a stable salt is formed when the difference in *pK<sub>a</sub>* values between the acid and base is at least two units. Usually, preparation of drug salts significantly improves its aqueous solubility and bioavailability compared to the corresponding uncharged molecule making salts suitable choice for drug formulation.

### 1.10 COCRYSTALS

When a drug molecule is weakly basic or acidic, cocrystals (Figure 1.2) can be used as new alternatives to salts.<sup>23</sup> There are many views on what constitutes a cocrystal.<sup>24</sup> According to one definition, at least two components of the crystal should interact through hydrogen bonding or other noncovalent interactions. An additional constraint proposed is that all components should be solids at room temperature.<sup>25</sup> Cocrystals are described in literature under different names such as organic molecular compounds or complexes.<sup>26</sup> Widely known examples of molecular complexes were reported a century ago, where derivatives of hydroquinone complexed with quinine were used to produce photographic films. The term cocrystal itself was used for the first time in a 1963 patent,<sup>27</sup> where adducts of different phenols and amines were examined as photosensitive compositions to create colored images.

Cocrystals can be designed by crystal engineering approaches.<sup>12</sup> Typically molecules containing complementary functional groups that can form specific heteromeric synthons can crystallize together to give a cocrystal. Cocrystals significantly change the intermolecular interactions and modify crystal packing. Thus, cocrystals can be used to alter the physical and pharmaceutical properties of the drugs. Most of the small molecule drugs possess functional groups capable of forming hydrogen bonds, making them suitable candidates for cocrystallization. Formation of drug cocrystal provides new opportunity to design different solid forms with enhanced pharmaceutical properties

while the activity of the API is unchanged.<sup>28</sup> In Chapter 5 we discuss the preparation of cocrystals and their utility in preparing supramolecular solid solutions.

There are several recent examples that illustrate the utility of cocrystals in pharmaceutical phases.<sup>29-37</sup> For example, nicotinamide (form of vitamin B-3) in the pure form of drug shows high hygroscopicity and deliquescent behavior under humidity. Crystalline adducts of nicotinamide and fatty acids in 1:1 ratio significantly improve the hygroscopic behavior of the drug.<sup>38</sup> In the solid state nicotinamide molecules interact with each other through hydrogen bonding associated with amide groups, while fatty acids form heterosynthons with the pyridyl N-atoms of the drug. The acid-pyridyl synthon reduces the affinity of the drug towards water and hence improves its hygroscopicity.

### 1.11 IONIC COCRYSTALS

The distinction between salts and ionic cocrystals is related more to the way they are made than the charges on the components within them.<sup>32</sup> Salts, traditionally, are formed by mineral acids or alkaline or other metal hydroxide bases.<sup>22</sup> The counter ions in these traditional salts are spherical and often their location within a crystal is determined by close packing than specific directional interactions. Ionic cocrystals on the other hand are made with the specific objective of bringing together the participating molecules into particular local geometries. The components within these ionic cocrystals are typically connected by charge-assisted hydrogen bonds.

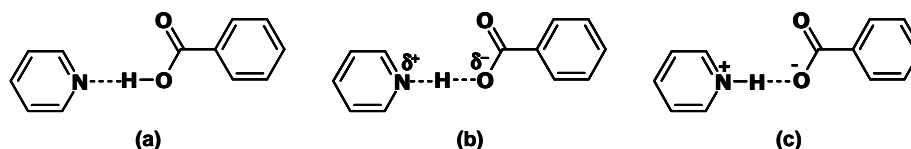


**Figure 1.3** Representation of the molecular complexes where (a) proton transfer is absent, (b) proton is partially transferred, and (c) where proton is fully transferred.

Ionic cocrystals can be distinguished by the location of proton between cocrystallized acid and base, where complete proton transfer occurs. Such proton transfer is absent in neutral cocrystals. It is generally proven that ionic cocrystals are formed if  $\Delta pK_a$  ( $pK_{a_{base}} - pK_{a_{acid}}$ ) is greater than 3, neutral cocrystals will mostly result if  $\Delta pK_a$  is less than 0, and if  $\Delta pK_a$  is between 0 and 3 both can be obtained or cocrystals with partial proton transfer are formed. The extent of proton transfer is strongly influenced by  $\Delta pK_a$  values as well as crystalline environment (crystal structure). For the practical use in drug development both cocrystals and ionic cocrystals can be valuable. Ionic cocrystals are desirable in case where API solubility is an issue; solubility of ionized complex in water is generally higher. In cases where the dissolution rate is more important than solubility, cocrystals of API can be more beneficial. However, in some cases both cocrystals and ionic cocrystals may show almost identical physical properties.

### 1.12 SOLID SOLUTIONS

Crystalline materials where the lattice sites are occupied with the random population of two or more components are called solid solutions (Figure 1.2).<sup>39</sup> Most molecular complexes are prepared as cocrystals; to date only a small number of molecular solid solutions are reported. Traditionally, organic alloys are formed by molecules with similar shapes and sizes. Creation of an alloy of an arbitrary organic compound is extremely difficult because most organic molecules possess intricate shapes and participate in directional intermolecular interactions.

Solid solutions can be interstitial or substitutional. The former are obtained when a second component is incorporated into the voids present in the crystals of the first component. In this work, we are interested in substitutional solid solutions, where the second component replaces the first component at random sites within its crystal. Extensive work carried out by Kitaigorodskii showed that organic substitutional solid solutions can be made when the participating components have the same shape, same size and adopt similar crystal structures.<sup>39</sup> Owing to these restrictions, not every compound can form solid solutions; the restrictions are particularly stringent for pharmaceutical molecules. In Chapter 5 we present a new approach to prepare *supramolecular* solid solutions of any compound that is capable of forming cocrystals.<sup>40</sup>

### 1.13 SUMMARY AND CONCLUSION

Condensed phases of matter can exist as crystals, amorphous solids or mesophases. The differences in the molecular separations and orientations within these phases result in their different macroscopic properties. Controlling the phase obtained is therefore an important step in drug development. Polymorphs are crystalline materials of the same chemical entity with different structures. Our work in Chapters 3 and 4 describes suppression of nucleation as a new technique to control the crystal growth and enhance the yield of stable polymorphs. Crystalline solids can be single or multicomponent, and among the latter, salts and solvates have been studied for a long time and used extensively in marketed drugs. New forms of multicomponent phases include cocrystals and solid solutions; the utility of these phases in pharmaceutical formulations is slowly emerging in current research. Our work in Chapter 5 discusses a new method for the preparation of supramolecular solid solutions in which the properties of the resultant materials are finely tuned based on the nature and relative content of the components.

**1.14 REFERENCES**

1. Cui, Y., A material science perspective of pharmaceutical solids. *Int. J. Pharm.* **2007**, *339*, 3-18.
2. Bernstein, J., *Polymorphism in Molecular Crystals*. Clarendon Press: Oxford, **2002**.
3. Brittain, H. G., *Polymorphism in Pharmaceutical Solids*. Marcel Dekker: New York, **1999**.
4. Byrn, S. R.; Pfeiffer, R. R.; Stowell, J. G., *Solid-State Chemistry of Drugs*. 2nd ed.; SSCI: West Lafayette, **1999**.
5. Desiraju, G. R., *Crystal Engineering: The Design of Organic Solids*. Elsevier: Amsterdam, **1989**.
6. Hilfiker, R., *Polymorphism in the Pharmaceutical Industry*. Wiley-VCH: Weinheim, **2006**.
7. Wunderlich, B., A classification of molecules, phases, and transitions as recognized by thermal analysis. *Thermochim. Acta* **1999**, *340-341*, 37-52.
8. Vippagunta, S. R.; Brittain, H. G.; Grant, D. J., Crystalline solids. *Adv. Drug. Deliv. Rev.* **2001**, *48*, 3-26.
9. Yu, L., Amorphous pharmaceutical solids: preparation, characterization and stabilization. *Adv. Drug. Deliv. Rev.* **2001**, *48*, 27-42.
10. Hancock, B. C.; Zografi, G., Characteristics and Significance of the Amorphous State in Pharmaceutical Systems. *J. Pharm. Sci.* **1997**, *86*, 1-12.
11. Desiraju, G. R., Supramolecular synthons in crystal engineering - a new organic synthesis. *Angew. Chem. Int. Ed.* **1995**, *34*, 2311-2327.
12. Etter, M. C., Hydrogen bonds as design elements in organic chemistry. *J. Phys. Chem.* **1991**, *95*, 4601-4610.
13. Lehn, J. M., *Supramolecular Chemistry: Concepts and Perspectives*. John-Wiley: New York, **1995**.
14. McCrone, W. C., Polymorphism. In *Physics and Chemistry of the Organic Solid State*, Fox, D.; Labes, M. M.; Weissberger, A., Eds. Wiley Interscience: New York, **1965**; Vol. 2, pp 725-767.
15. Chen, S.; Guzei, I. A.; Yu, L., New Polymorphs of ROY and New Record for Coexisting Polymorphs of Solved Structures. *J. Am. Chem. Soc.* **2005**, *127*, 9881-9885.
16. Chemburkar, S. R.; Bauer, J.; Deming, K.; Spiwek, H.; Patel, K.; Morris, J.; Henry, R.; Spanton, S.; Dziki, W.; Porter, W.; Quick, J.; Bauer, P.; Donaubaue, J.; Narayanan, B. A.; Soldani, M.; Riley, D.; McFarland, K., Dealing with the Impact of Ritonavir Polymorphs on the Late Stages of Bulk Drug Process Development. *Org. Proc. Res. Dev.* **2000**, *4*, 413-417.
17. Griesser, U. J., The importance of solvates. In *Polymorphism in the Pharmaceutical Industry*, Hilfiker, R., Ed. Wiley-VCH: Weinheim, **2006**; pp 211-233.
18. Khankari, R. K.; Grant, D. J. W., Pharmaceutical hydrates. *Thermochim. Acta* **1995**, *248*, 61-79.
19. Guillory, J. K., Generation of polymorphs, hydrates, solvates, and amorphous solids. In *Polymorphism in Pharmaceutical Solids*, Brittain, H. G., Ed. Marcel Dekker: New York, **1999**; Vol. 95, pp 183-226.

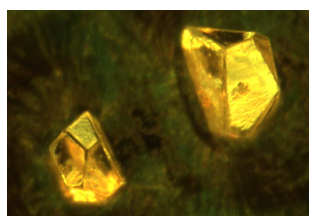
20. Gorbitz, C. H.; Hersleth, H.-P., On the inclusion of solvent molecules in the crystal structures of organic compounds. *Acta Crystallogr.* **2000**, *B56*, 526-534.
21. Bingham, A. L.; Hughes, D. S.; Hursthouse, M. B.; Lancaster, R. W.; Tavener, S.; Threlfall, T. L., Over one hundred solvates of sulfathiazole. *Chem. Commun.* **2001**, 603-604.
22. Heinrich Stahl, P.; Wermuth, C. G.; Editors, *Handbook of Pharmaceutical Salts: Properties, Selection, and Use*. Wiley-VCH: Weinheim, **2008**.
23. Almarsson, O.; Zaworotko, M. J., Crystal engineering of the composition of pharmaceutical phases. Do pharmaceutical co-crystals represent a new path to improved medicines? *Chem. Commun.* **2004**, 1889-1896.
24. Stahly, G. P., Diversity in Single- and Multiple-Component Crystals. The Search for and Prevalence of Polymorphs and Cocrystals. *Cryst. Growth. Des.* **2007**, *7*, 1007-1026.
25. Ling, A. R.; Baker, J. L., Halogen derivatives of quinone. Part III. Derivatives of quinhydrone. *J. Chem. Soc.* **1893**, *63*, 1314-1327.
26. Herbstein, F. H., *Crystalline Molecular Complexes and Compounds: Structure and Principles*. Oxford University Press: New York, **2006**.
27. Lawton, W. R.; Lopez, E. F. Heat developable diazo copy sheet. US 3076707, **1963**.
28. Vishweshwar, P.; McMahon, J. A.; Bis, J. A.; Zaworotko, M. J., Pharmaceutical co-crystals. *J. Pharm. Sci.* **2006**, *95*, 499-516.
29. Bak, A.; Gore, A.; Yanez, E.; Stanton, M.; Tufekcic, S.; Syed, R.; Akrami, A.; Rose, M.; Surapaneni, S.; Bostick, T.; King, A.; Neervannan, S.; Ostovic, D.; Koparkar, A., The co-crystal approach to improve the exposure of a water-insoluble compound: AMG 517 sorbic acid co-crystal characterization and pharmacokinetics. *J. Pharm. Sci.* **2008**, *97*, 3942-3956.
30. Chen, A. M.; Ellison, M. E.; Peresyphkin, A.; Wenslow, R. M.; Variankaval, N.; Savarin, C. G.; Natishan, T. K.; Mathre, D. J.; Dormer, P. G.; Euler, D. H.; Ball, R. G.; Ye, Z.; Wang, Y.; Santos, I., Development of a pharmaceutical cocrystal of a monophosphate salt with phosphoric acid. *Chem. Commun.* **2007**, 419-421.
31. Childs, S. L.; Chyall, L. J.; Dunlap, J. T.; Smolenskaya, V. N.; Stahly, B. C.; Stahly, G. P., Crystal Engineering Approach To Forming Cocrystals of Amine Hydrochlorides with Organic Acids. Molecular Complexes of Fluoxetine Hydrochloride with Benzoic, Succinic, and Fumaric Acids. *J. Am. Chem. Soc.* **2004**, *126*, 13335-13342.
32. Childs, S. L.; Stahly, G. P.; Park, A., The salt-cocrystal continuum: the influence of crystal structure on ionization state. *Mol. Pharm.* **2007**, *4*, 323-338.
33. Hickey, M. B.; Peterson, M. L.; Scoppettuolo, L. A.; Morrisette, S. L.; Vetter, A.; Guzman, H.; Remenar, J. F.; Zhang, Z.; Tawa, M. D.; Haley, S.; Zaworotko, M. J.; Almarsson, O., Performance comparison of a co-crystal of carbamazepine with marketed product. *Eur. J. Pharm. Biopharm.* **2007**, *67*, 112-119.
34. McNamara, D. P.; Childs, S. L.; Giordano, J.; Iarriccio, A.; Cassidy, J.; Shet, M. S.; Mannion, R.; O'Donnell, E.; Park, A., Use of a glutaric acid cocrystal to improve oral bioavailability of a low solubility API. *Pharm. Res.* **2006**, *23*, 1888-1897.
35. Remenar, J. F.; Morrisette, S. L.; Peterson, M. L.; Moulton, B.; MacPhee, J. M.; Guzman, H. R.; Almarsson, O., Crystal engineering of novel cocrystals of a triazole drug with 1,4-dicarboxylic acids. *J. Am. Chem. Soc.* **2003**, *125*, 8456-8457.

36. Trask, A. V.; Motherwell, W. D. S.; Jones, W., Physical stability enhancement of theophylline via cocrystallization. *Int. J. Pharm.* **2006**, *320*, 114-123.
37. Walsh, R. D. B.; Bradner, M. W.; Fleischman, S.; Morales, L. A.; Moulton, B.; Rodriguez-Hornedo, N.; Zaworotko, M. J., Crystal engineering of the composition of pharmaceutical phases. *Chem. Commun.* **2003**, 186-187.
38. Yokoyama, S.; Sunohara, M.; Fujie, T., Hygroscopicities of 3-aminopyridine (3AP) and fatty acid complexes (FA-3AP), and the release of 3AP from FA-3AP. *Chem. Pharm. Bull.* **1993**, *41*, 1876-1878.
39. Kitaigorodsky, A. I., *Mixed Crystals*. Springer-Verlag: New York, **1984**.
40. Dabros, M.; Emery, P. R.; Thalladi, V. R., A supramolecular approach to organic alloys: cocrystals and three- and four-component solid solutions of 1,4-diazabicyclo[2.2.2]octane and 4-X-phenols (X = Cl, CH<sub>3</sub>, Br). *Angew. Chem. Int. Ed.* **2007**, *46*, 4132-4135.

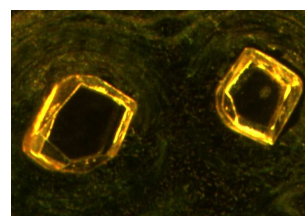
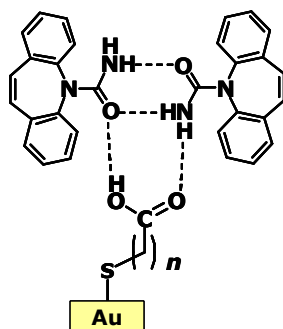
THIS PAGE LEFT INTENTIONALLY BLANK

# 2

## PARITY DEPENDENT FACE-SELECTIVE CRYSTAL GROWTH OF CARBAMAZEPINE ON SELF-ASSEMBLED MONOLAYERS



*n* = even  
{012}



*n* = odd  
{101}

THIS PAGE LEFT INTENTIONALLY BLANK

## 2.1 INTRODUCTION

Most pharmaceuticals are developed and marketed as solids. Crystalline solids, owing to their long term stability, are used in pharmaceutical formulations in preference to amorphous solids.<sup>1</sup> Consequently, fundamental understanding of crystallization and the control of crystal growth are critical in the early development of pharmaceuticals and their manufacturing. Much effort in pharmaceutical crystallization is centered on the manipulation of crystal size and shape, to control the chemical properties such as dissolution and mechanical properties such as flowability. Many pharmaceutical molecules, however, crystallize as polymorphs; that is, they adopt more than one solid state structure.<sup>2-3</sup> Polymorphs exhibit different physicochemical properties and harnessing polymorphism is a prerequisite in establishing the control over crystal size, shape and other properties.<sup>4</sup> In the next chapter, we will describe the methods that are currently used in the selective growth of polymorphs. In this chapter, we wish to explore heterogeneous nucleation as a means to control the crystal growth of polymorphic drugs.<sup>5</sup> Crystals often grow on foreign substrates such as dust particles and the driving force for this heterogeneous attachment is best appreciated by an understanding of nucleation.<sup>6</sup>

## 2.2 NUCLEATION

We begin with an intuitive picture of nucleation occurring in solution. In a crystallization solution, solute molecules either as monomers or as small discrete assemblies act as crystal growth units. For simplicity, we assume that the molecules are spherical and that they assemble into progressively larger cubic clusters and ultimately into a crystal with simple cubic topology (Figure 2.1a). In these clusters, each spherical molecule assumes octahedral geometry and forms six noncovalent bonds with neighboring solute or solvent

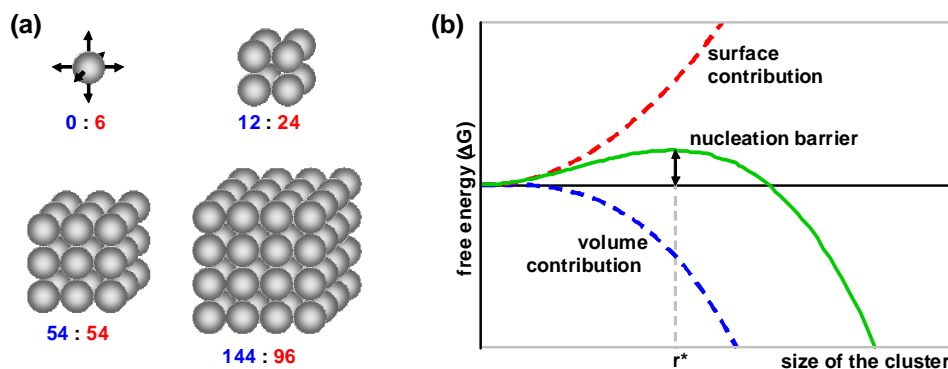


**Figure 2.1** (a) Schematic representation of nucleation. Molecules are represented as spheres. The numbers below the clusters show the number of bonds formed by the spheres; the numbers on the left indicate bonds within a cluster (volume contribution) and the numbers on the right indicate the interfacial bonds (surface contribution). The  $3 \times 3 \times 3$  cluster represents a critical nucleus with radius  $r^*$ . (b) Free energy of clusters as a function of the size of the cluster showing the volume and surface contributions, critical radius ( $r^*$ ), and nucleation barrier. This figure is adapted from reference 6.

molecules. An isolated solute molecule forms six bonds with solvent molecules and a  $2 \times 2 \times 2$  cluster with eight molecules exhibits 12 solute-solute bonds and 24 solute-solvent bonds. The bonds between solute molecules hold the cluster together and the bonds between solute and solvent molecules tend to break the cluster apart. The former bonds represent the volume contribution in Figure 2.1b and the latter represent the surface contribution. As the cluster grows, the number of bonds within a cluster increase and after some critical size, these intra-cluster bonds dominate the bonds between cluster and the solvent molecules. In the hypothetical model depicted in Figure 2.1a, the  $3 \times 3 \times 3$  cluster with 27 molecules represents the critical size in which the surface and volume contributions are equal (assuming that solute-solute and solute-solvent bonds are of equal strength). The cluster with this critical size is called the critical nucleus; clusters smaller than this nucleus are likely to dissolve back into solution and clusters larger than the nucleus are likely to grow into a crystal.

Nucleation is the process of overcoming the critical nucleus and the energy required to overcome this critical size is represented as the nucleation barrier in Figure 2.1b. *Homogeneous nucleation*, therefore, does not ensue until the solution reaches a certain supersaturation that is enough to surpass the nucleation barrier. Another path to nucleation is to lower the nucleation barrier; this lowering can be achieved by decreasing the surface free energy of the nucleus at the cluster-solvent interface. Thus, clusters, when attached to foreign surfaces, can readily reach the critical size and grow beyond the critical nucleus. This phenomenon is termed as *heterogeneous nucleation*.

### 2.3 CRYSTAL GROWTH BY HETEROGENEOUS NUCLEATION

Biom mineralization, the growth of minerals such as calcite and hydroxyapatite in living organisms, is mediated by specific interfacial interactions between proteins and growing crystal nuclei.<sup>7</sup> The understanding that barrier to nucleation is lowered by foreign surfaces and that biom mineralization involves specific interfacial chemical complementarity, inspired the idea of designer interfaces for crystal growth.<sup>8</sup> A well-known illustration of the engineered interfaces as templates for crystal growth is given by nucleation of ice at the Langmuir monolayers formed by long chain alcohols.<sup>9</sup> Related work showed that oriented crystal growth of glycine on Langmuir monolayers formed by  $\alpha$ -amino acid amphiphiles is mediated by chemical and geometric epitaxy at the interface.<sup>10</sup> Several other substrates, Langmuir-Blodgett monolayers,<sup>8</sup> silane monolayers,<sup>11-12</sup> self-assembled monolayers (SAMs),<sup>13-25</sup> and polymer and single crystal surfaces,<sup>26-29</sup> have been extensively used for the crystal growth of organic and inorganic compounds. These studies showed that it is possible to control the orientation, size, and polymorphism of the growing compounds using interfacial molecular recognition. In this chapter, we are interested in using the thiol SAMs formed on gold as templates for the crystal growth of pharmaceutical compounds. Specifically, we will discuss the crystallization of carbamazepine on SAMs with  $-\text{COOH}$  groups at the interface and the dependence of growth orientation on even or odd number of methylene groups in the alkyl spacers within the SAMs.<sup>30</sup>

## 2.4 SELF-ASSEMBLED MONOLAYERS

Long chain alkanethiol derivatives form structured two-dimensional monolayers (SAMs) when brought into contact with metal substrates such as gold and silver.<sup>31-32</sup> Figure 2.2 shows the two step process of the fabrication of thiol SAMs on gold. Thiol groups and gold atoms have high affinity for each other; they form strong Au-S bonds at the exposed gold surfaces. Formation of these bonds is the first step in the fabrication of SAMs; the Au-S bonds lower the surface free energy of the gold. In the second step, the long alkyl chains reorganize on the surface such that they establish an energy-minimized inter-grooved packing. It is the self-organization of these alkyl chains that imparts the adjective *self-assembled* to the monolayers formed by alkanethiol derivatives. For the most part, {111} faces are exposed at the exterior surfaces of gold substrates because of their lower surface free energy compared to the other possible growth faces. Figure 2.3 shows a schematic illustration of the two-dimensional order of thiol SAMs formed on {111} faces of gold substrates. We can consider SAMs as two-dimensional crystals with their lattice parameters being determined by the lattice of underlying metal substrate. We will use these lattice parameters in our epitaxy calculations discussed in Section 2.12.

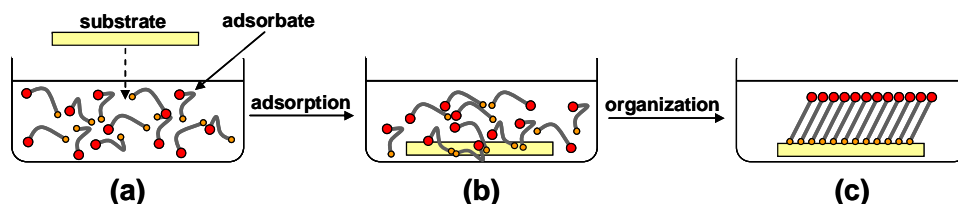


**Figure 2.2** Preparation of thiol SAMs on gold substrates (yellow rectangles). The adsorbates contain thiol groups (orange circles) for binding to gold substrates, alkyl or aryl spacers (grey strings) for self-assembly, and terminal groups (red circles) for desired surface chemistry. The process involves (a) immersion: submerging the substrate in a solution of adsorbates, (b) adsorption: formation of Au-S bonds at the surface of gold, and (c) self-assembly: organization of adsorbates to expose terminal groups at the interface.

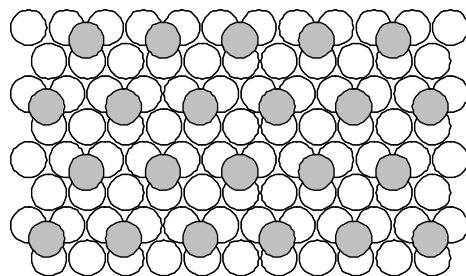


**Figure 2.3** Cross-sectional diagram of a thiol SAM on the {111} face of gold. White circles represent the top layer of Au atoms in the substrate and the grey circles represent the S atoms of the SAM. Notice the periodic arrangement of grey circles (thiol molecules).

The fabrication of thiol SAMs is simple and fast (Figure 2.2) and they offer a convenient way to tailor the surface properties. It is possible to manipulate the property of the surface by modifying the terminal functional groups while leaving the rest of the molecule unchanged. For example, hydrophobic or hydrophilic surfaces can be achieved by changing the terminal group of the monolayer from  $-\text{CH}_3$  to  $-\text{COOH}$ .

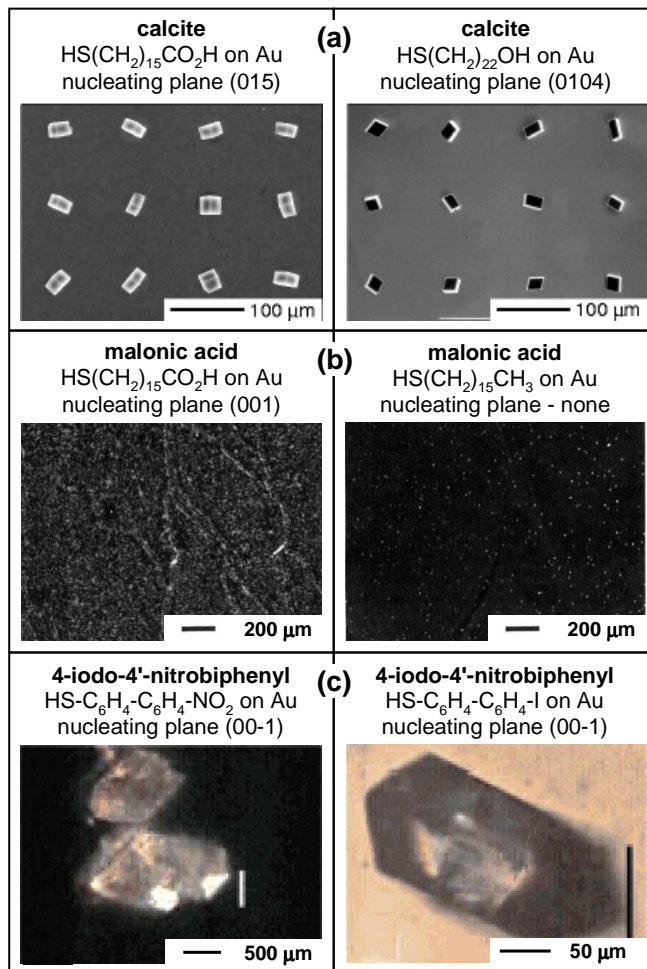


**Figure 2.4** Crystal growth on SAMs. **(a)** Oriented growth of calcite on micropatterned substrates that contain islands of protic SAMs surrounded by SAMs terminated with methyl groups.<sup>15</sup> Note that different  $-\text{COOH}$  and  $-\text{OH}$  terminal groups promote the nucleation on different crystal planes. **(b)** Malonic acid crystallization on hydrogen bonding and hydrophobic SAMs. Note the higher nucleation density on SAMs exposing  $-\text{COOH}$  groups.<sup>25</sup> **(c)** Oriented growth of a polar crystal based on  $-\text{NO}_2 \cdots \text{I} -$  interactions on aryl SAMs exposing  $-\text{NO}_2$  or  $-\text{I}$  groups.<sup>21</sup>

## 2.5 SAMs AS TEMPLATES FOR CRYSTAL GROWTH

The periodic structure, a high degree of order, and tailorable surface chemistry of SAMs made them attractive templates for crystal growth in many studies.<sup>13-25</sup> Figure 2.4 shows some representative examples. Thiol SAMs containing alkyl spacers and exposing protic functional groups such as  $-OH$ ,  $-COOH$ ,  $-SO_3H$  promoted the growth of calcite crystals on specific planes (Figure 2.4a).<sup>15</sup> This growth is mediated by deprotonation at the interface, binding of  $Ca^{2+}$  ions to carboxylate or other anionic terminal groups, and growth of crystals by sequential attachment of  $Ca^{2+}$  and  $CO_3^{2-}$  ions. The planes on which the nucleation took place are determined by the underlying geometry (Au, Ag or Pd) and the exposed functionalities ( $-COO^-$ ,  $-O^-$  or  $-SO_3^-$ ). Crystallization of malonic acid on thiol SAMs with alkyl spacers and  $-COOH$ ,  $-CH_3$ , or ester terminal groups showed that the nucleation density and growth orientation depend on the interfacial functional groups (Figure 2.4b).<sup>25</sup> The  $-COOH$  groups, owing to their polar character and hydrogen bonding ability, showed higher rates of nucleation and promoted the growth of malonic acid crystals on  $\{001\}$  faces. 4-Iodo-4'-nitrobiphenyl crystallizes in an acentric space group and is an example of a polar crystal.<sup>33</sup> Crystallization of this compound on thiol SAMs with aryl spacers revealed that oriented growth occurs on SAMs exposing  $-I$  or  $-NO_2$  groups (Figure 2.4c).<sup>21</sup> Goniometry and Beilstein tests for halogens revealed that crystal faces exposing  $-NO_2$  groups attach to the SAMs with terminal  $-I$  groups and vice versa. These examples illustrate that SAMs provide simple and versatile means for the templated growth of crystals and that heterogeneous nucleation of crystals can be mediated by ionic bonds, hydrogen bonds or other noncovalent bonds such as  $-NO_2 \cdots I-$  interactions.

## 2.6 PARITY OF ALKYL CHAINS AND ORIENTATION OF TERMINAL GROUPS

The emergence of thiol SAMs formed on metal substrates as templates for heterogeneous crystal growth can be related to, among other things, their structural modularity. Figure 2.5a shows the modular structure of a SAM. We and others have explored the variations in the nature of the terminal groups (e.g.  $NH_2$ ,  $SO_3H$ ), spacers (e.g. alkyl, aryl), and the metal substrates (e.g. Au, Ag) towards applications such as control of nucleation, formation of micropatterned crystals, interfacial enantioselectivity, and selective growth of polymorphs and semiconducting materials.<sup>25, 13-24</sup> In this chapter we report the effect of another variable, the *parity* of alkyl chain, on the face-selective crystal growth of a drug polymorph.<sup>30</sup> In general, the parity of an alkyl chain denotes whether the number of C-atoms in that chain is odd or even. In Au-SAMs based on alkyl spacers, the terminal groups adopt two different orientations with respect to the SAM surface depending on whether the alkyl chain contains an even or odd number of methylene groups (Figures 2.5b and 2.5c).<sup>34-35</sup> While exploring the effect of synthetic surfaces on the polymorphism of pharmaceutical drugs (Chapter 3),<sup>24</sup> we discovered that SAMs made of mercaptoundecanoic acid (**1**) and mercaptohexadecanoic acid (**2**) nucleate different faces of the *P*-monoclinic polymorph (*PMP*) of carbamazepine (Section 2.7). These two SAMs have the same terminal groups; they differ in the parity of the alkyl chain. The SAMs with an even number of methylene groups between the thiol and terminal X groups, project the

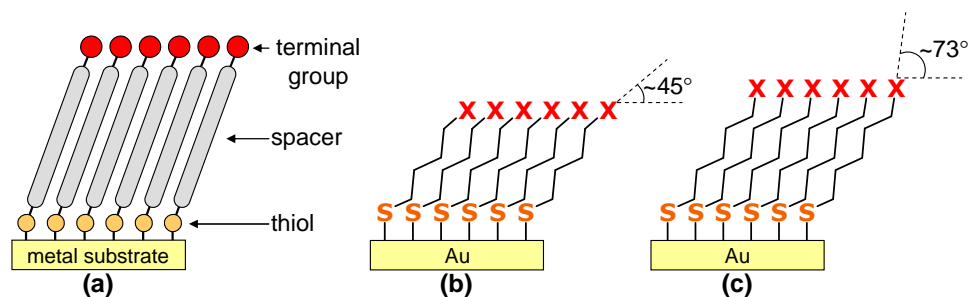


**Figure 2.5** (a) Schematic representation of a thiol SAM showing its structural modularity: different parts of the SAM (terminal group, spacer and the metal substrate) can be varied independent of each other. Idealized structures of thiol SAMs containing (b) even and (c) odd number of methylene groups. Notice the difference in the angles between C–X bonds and the SAM surface.

terminal C–X bonds at  $\sim 45^\circ$  with respect to the surface horizontal (Figure 2.5b).<sup>34</sup> When the SAMs are made of alkyl chains with an odd number methylene groups (Figure 2.5c) the C–X bonds are projected at a steeper angle ( $\sim 73^\circ$ ) with respect to the surface horizontal. We show here that the difference in the orientation of terminal groups is instrumental in determining the faces on which the *PMP* crystals grow on the SAMs.

## 2.7 AMIDE DIMERS IN CARBAMAZEPINE POLYMORPHS

Carbamazepine, a drug used in the treatment of epilepsy, trigeminal neuralgia, and other diseases, has been used as a model pharmaceutical in the preparation of cocrystals, prediction of crystal structures, and investigation of polymorphism and phase transitions.<sup>36-39</sup> Of the four known polymorphs of this drug, the *PMP* and trigonal polymorphs can be crystallized from solutions, the former being more stable than the latter. In addition, carbamazepine readily forms a dihydrate (in the presence of water) and several solvates. One of the distinct features of the four polymorphs of carbamazepine is that they all contain amide hydrogen bonded dimers.<sup>38</sup> Our hypothesis in this work is that the growth units (Figure 2.1a) for nucleation and growth of these polymorphs are dimeric assemblies of carbamazepine. The structures of *PMP* and the trigonal polymorph shown in Figure 2.6 reveal that these polymorphs are built from the packing of amide dimers. These two polymorphs have distinct morphologies; *PMP* crystallizes as blocks (see Figure 2.8 below) and the trigonal polymorph as needles.

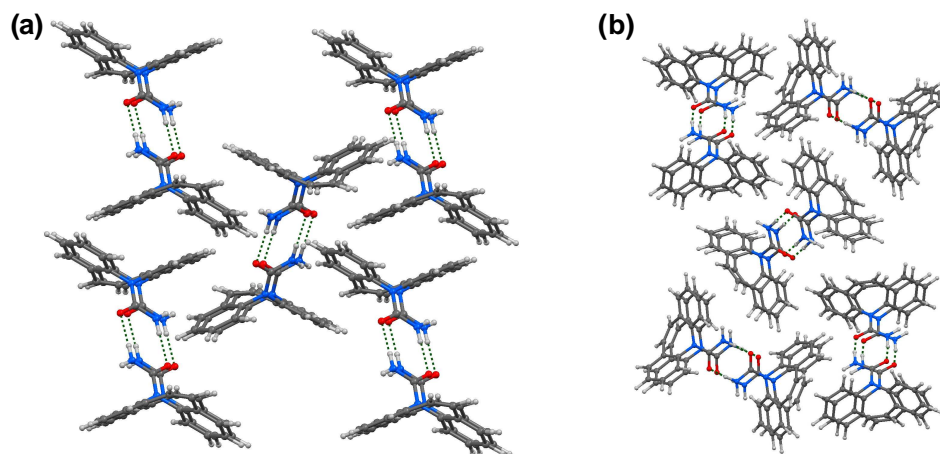


**Figure 2.6** Crystal structures (a) *P*-monoclinic and (b) trigonal polymorphs of carbamazepine. Notice amide dimers formed by hydrogen bonds and the differences in the mutual packing of these dimers.

## 2.8 PREPARATION AND CHARACTERIZATION OF SAMs

We fabricated thiol SAMs on gold coated glass slides by immersing the slides in 1-3 mM ethanolic solutions of thiols **1** and **2**, and 1-undecanethiol (**3**) and 1-hexadecanethiol (**4**) (Figure 2.7). Gold coated glass slides purchased from Evaporated Metal Films had two layers of metal coating: a  $\sim 50$  Å thick chromium adhesive layer and a  $\sim 1000$  Å thick gold layer. The slides had a thickness of 1 mm; we cut them into  $\sim 15$  mm  $\times$  25 mm pieces and treated them with oxygen plasma for 30 sec in a plasma etcher. This plasma treatment helped in the removal of any organic contaminants adsorbed on the surface. After soaking the substrates for 8-16 hours in ethanolic solutions of SAMs, we removed the substrates, rinsed them with copious amounts of ethanol and dried them with a stream of nitrogen. We used freshly prepared SAM substrates for characterization and crystal growth experiments. We characterized the SAMs by contact angle goniometry, ellipsometry and grazing incidence IR spectroscopy; the results we obtained are in agreement with those reported in the literature. The measured contact angles had a maximum error of  $2.5^\circ$ : SAM-1 ( $28.2^\circ$ ); SAM-2 ( $26.4^\circ$ ); SAM-3 ( $94.3^\circ$ ); SAM-4 ( $98.6^\circ$ ); and bare gold ( $76.2^\circ$ ). The heights of SAMs measured with ellipsometry had a maximum error of 1.2 Å: SAM-1 (13.1 Å); SAM-2 (22.2 Å); SAM-3 (18.5 Å); and SAM-4 (21.7 Å).

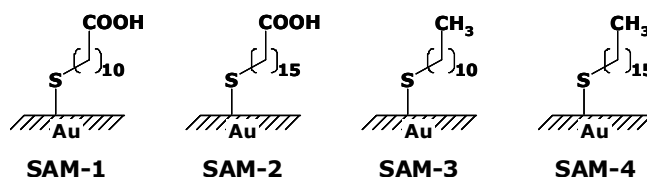


**Figure 2.7** Schematic structures of the SAMs **1-4** showing two different terminal groups.

## 2.9 CRYSTALLIZATION OF CARBAMAZEPINE ON SAMs

We used SAMs **1-4** as templates, and untreated gold slides (**5**), bare glass slides (**6**) and plasma treated glass slides (**7**) as controls. Substrates **6** and **7** are hydrophilic (contact angles  $19.3 \pm 5.2$  and  $13.9 \pm 2.6^\circ$  respectively) and they are expected to mimic the hydrogen bonding nature of the SAMs **1** and **2**, but without the structural and orientational specificity of the SAMs. We dissolved carbamazepine in benzene and kept the solution at  $60^\circ\text{C}$  for about 20 minutes until its volume is reduced to reach a concentration of 25 mM. We cooled the solution to room temperature and filtered it into 50 mL beakers (that contained the SAM substrates) such that each beaker is filled with  $\sim 15$  mL of the solution. We covered the beakers with perforated aluminum foils and kept them in a desiccator. Inside the desiccator, freshly baked drierite (97%  $\text{CaSO}_4$  and 3%  $\text{CoCl}_2$ ) maintained the relative humidity at  $\sim 0\%$ . Higher humidity levels (30-100%) can cause the crystallization of dihydrate in preference to the anhydrous forms.

The solvent evaporated slowly under equilibrium conditions in the desiccator and crystals appeared on SAMs **1** and **2** in three to four days. We allowed the solvent to evaporate for three to four more days and carefully extracted the substrates from the solution. A small fraction of crystals ( $\sim 5\%$  on SAMs **1** and **2**) fell off the surface during this withdrawal; these crystals did not bond strongly to the substrate and we assumed that they grew in solution and not on the substrate. We noticed a small number of crystals on hydrophobic SAMs **3** and **4**; these crystals fell off during the withdrawal of the substrate. At the time of the withdrawal, the remaining solution in the beakers is fairly concentrated (supersaturated); removal of substrates from this solution led to the precipitation of a thin layer of carbamazepine on the slides and also on the crystals.

We washed the substrates with small volumes of benzene to partially remove this precipitate and also to detach any weakly bound crystals. In the case of hydrophobic SAMs **3-4** and bare gold substrate, this washing removed one or two crystals that still remained on the substrates. On SAMs **1** and **2**, however, this washing dissolved small portions ( $\sim 2-5\%$ ) of the crystals and left trace amounts of precipitate around the crystals. We characterized this precipitate to be the trigonal polymorph (needle shaped crystals) by powder X-ray diffraction (PXRD) analysis. A small peak (at  $2\theta \approx 9^\circ$ ) corresponding to this precipitated polymorph can be seen in the PXRD patterns of samples grown on SAMs **1-2** (see Figure 2.13 below). We confirmed from independent experiments that crystals of trigonal polymorph grow exclusively when supersaturated benzene solutions are subjected to rapid evaporation.

## 2.10 ORIENTED CRYSTAL GROWTH

We repeated the crystal growth experiments at least five times and in all the trials, crystals of *PMP* grew on SAMs **1-2** and little or no crystal growth occurred on substrates **3-5**. We will discuss the crystallization on glass substrates in Section 2.13. Examination of the SAM substrates under an optical microscope (Figure 2.8) revealed that crystals grow on different faces on SAMs **1** and **2**. In order to test the facial selectivity across the whole surface, we analyzed the crystals with PXRD while they were still intact on the

substrate. We modified the sample holder for the PXRD such that the SAM substrate can be subjected to X-ray diffraction directly (Figure 2.9a). We collected the X-ray data in  $\theta$ - $2\theta$  mode; in this mode the diffraction is observed only from those planes that are parallel to the SAM substrate.

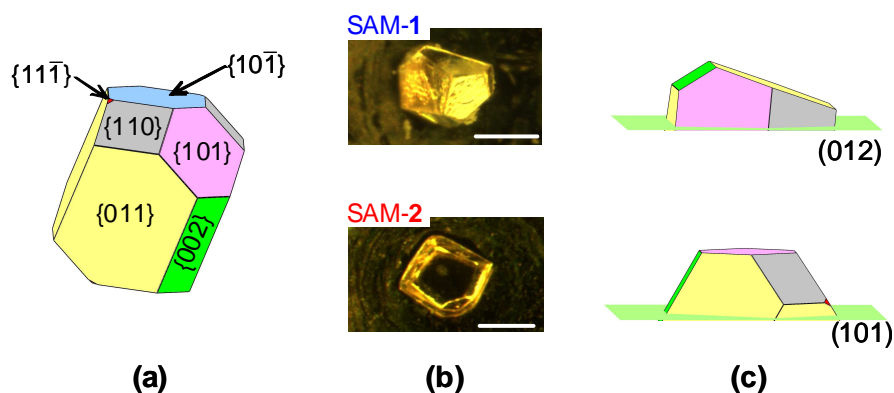


**Figure 2.8** (a) Morphology of the *PMP* calculated using the Bravais-Friedel-Donnay-Harker theory. Symmetry independent faces are shaded with different colors. (b) Microscopic images of the crystals grown on SAMs **1** and **2**. Scale bars = 1 mm. (c) View down (101) and (012) showing the relative orientation of crystal faces with respect to the growth planes. Color scheme is the same as in (a).

The PXRD patterns of crystals grown on SAMs **1** and **2** show one strong diffraction peak in each case (Figures 2.9b and 2.9c). In the case of SAM-**2**, this peak corresponds to (101) indicating that crystals grow on their {101} faces on this SAM (Figure 2.9c). The only other peak at  $2\theta = 27.4^\circ$  corresponds to the related higher index plane (202). In the case of SAM-**1** the most intense peak corresponds to (012) suggesting that crystals grow on {012} faces on this SAM. Closer inspection of Figures 2.9b shows peaks corresponding to the related higher index plane and planes that are nearly parallel to (012) (see Figure 2.11 below). The rationale for the observed facial selectivity in crystal growth is discussed in Section 2.14. In the next section, we describe the PXRD method used in the analysis given above.

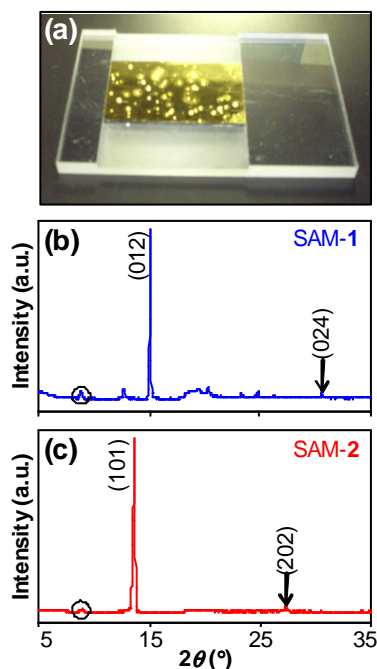


**Figure 2.9** (a) Sample holder for the onboard diffraction analysis of crystals grown on SAMs. Experimental powder X-ray diffraction patterns of *PMP* crystals grown on (b) SAM-1 and (c) SAM-2. In (b) and (c), the hump at  $2\theta \approx 17^\circ$  is due to the diffraction from background; the circled peaks at  $2\theta \approx 9^\circ$  arise from the diffraction of trigonal polymorph precipitated during the handling of substrates.

### 2.11 CALIBRATION OF POWDER X-RAY DIFFRACTION PATTERNS

As shown in Figure 2.9a we developed a modified sample holder that can hold the SAM substrate such that the diffraction is observed only from those planes that are parallel to the SAM surface. We calibrated the diffraction from the new sample holder by comparing the X-ray diffraction patterns *PMP* powders spread on regular sample holder as well as on the gold slide of the new sample holder (Figure 2.10).

The X-ray data collected on *PMP* powders spread on gold slides (with the modified sample holder) showed strong diffraction peaks from Au(111) at  $2\theta \approx 38^\circ$ . We used this Au(111) peak to calibrate the diffraction patterns obtained from the crystals grown on SAMs **1** and **2**. This internal calibration allowed us to identify the peak positions with certainty. The sole peak from the trigonal polymorph (at  $2\theta \approx 9^\circ$ ; Figure 2.11) also acted as a second, independent peak with which we could calibrate the diffraction patterns of crystals grown on SAMs **1** and **2**. The images on the left in Figure 2.11 show the full-scale diffraction patterns of crystals grown on SAMs **1-2**. The images on the right in Figure 2.11 show the same patterns with the y-scale (intensity scale) expanded.

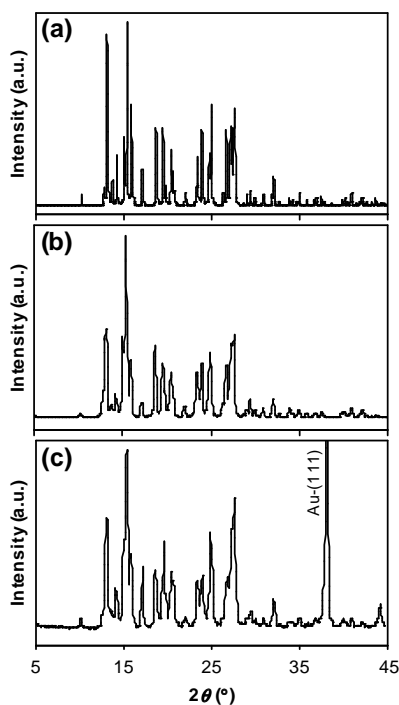


**Figure 2.10** (a) Calculated and (b-c) experimental PXRD patterns of *PMP* crystals. The pattern in (b) is taken by placing the powdered *PMP* samples on a regular sample holder and the one in (c) by placing the sample on a gold slide in the modified holder. The peaks belonging to the Au substrate can be seen at  $2\theta \approx 36.5, 38$  and  $44^\circ$ .

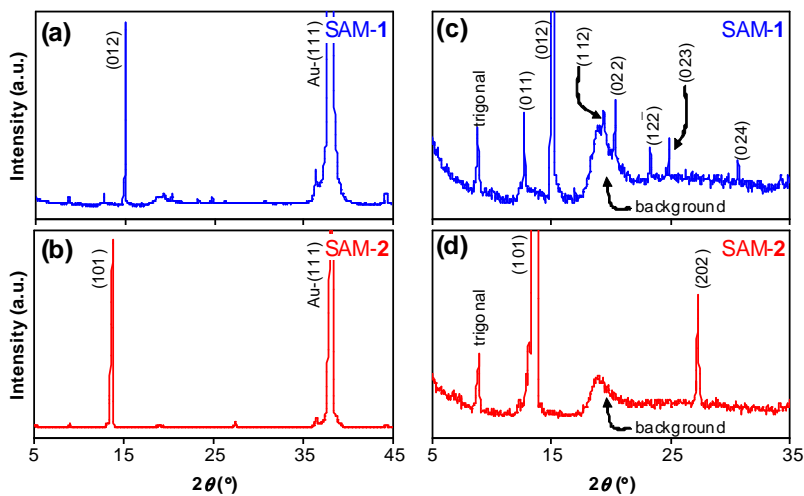


**Figure 2.11** Full-scale (a-b) and expanded (c-d) powder diffraction patterns of crystals grown on SAM-1 (top) and SAM-2 (bottom). The peaks labeled 'trigonal' correspond to the trigonal polymorph.

Crystals grown on SAM-2 show diffraction peaks from (101) and the corresponding higher index plane (202). No other peaks are seen even at this level of expansion indicating a very high degree of face-selective crystal growth on this SAM. Crystals grown on SAM-1 show diffraction peaks from (012) and the corresponding higher index plane (024); it also shows peaks related to several other planes that are nearly parallel to (012). This may indicate lesser degree of order in SAM-1, partial misalignment of the crystals during the growth, or during the benzene wash, imperfections in the substrate, or growth of crystals on these other planes. In any event, the intensity of the (012) peaks is much higher (100%) than the other peaks (4-8%) and SAM-1 indeed shows a high degree of selectivity for the growth of crystals on their {012} faces. It should be noted that occasionally (in two of the nine experiments) a small fraction of *PMP* crystals grew on their {101} faces on SAM-1 substrates. We will discuss the nature of chemical epitaxy at the growth interface in Section 2.14. In the following section, we explore the geometric epitaxy based on the lattice parameters of the growth planes and the underlying SAMs.

## 2.12 GEOMETRIC EPITAXY BETWEEN SAMs AND GROWTH FACES

We used the lattice matching program EpiCalc to determine geometric epitaxy.<sup>40</sup> EpiCalc determines the lattice registry by rotating an overlayer lattice ( $b_1$ ,  $b_2$ ,  $\beta$ ) on a substrate lattice ( $a_1$ ,  $a_2$ ,  $\alpha$ ) through a series of azimuthal angles ( $\theta$ ) (Figure 2.12).<sup>41</sup> For each azimuthal angle, the program calculates a dimensionless potential  $V/V_0$ , whose value depends on the type of epitaxy between the two lattices (Table 2.1).

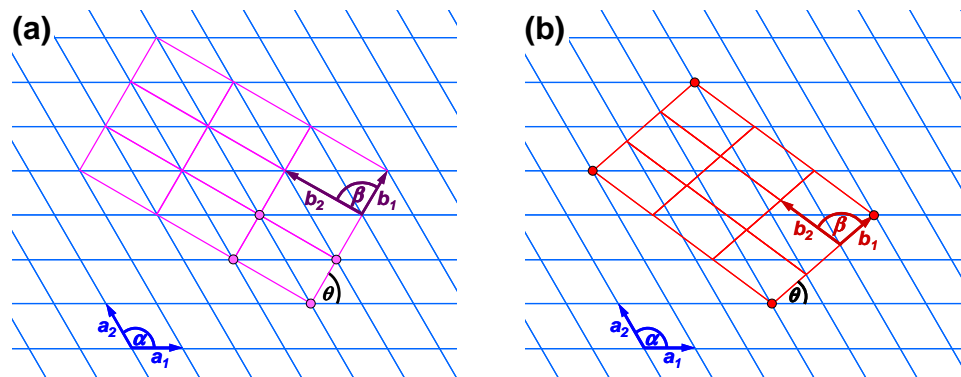


**Figure 2.12** Schematic representation of (a) commensurate and (b) coincident epitaxy. Substrate lattice ( $a_1$ ,  $a_2$ ,  $\alpha$ ) is drawn in blue; overlayer lattices ( $b_1$ ,  $b_2$ ,  $\beta$ ) are drawn in magenta or red. In (a) all the lattice points of overlayer reside on the lattice points of substrate. In (b) the vertices of a  $3 \times 3$  supercell, not the basic cell, of the overlayer lattice reside on vertices of the substrate lattice.

**Table 2.1** Relationship between the values of  $V/V_o$  and the type of epitaxy.<sup>41</sup>

$V/V_o$	Epitaxy	Symmetry of Substrate Lattice
1	incommensurate	any
0.5	coincident	any
0	commensurate	non-hexagonal
-0.5	commensurate	hexagonal

Commensurate epitaxy, an ideal form of epitaxy, involves the matching of every lattice point of the overlayer with the substrate lattice points (Figure 2.12a). Coincident epitaxy, less ideal but more common form of epitaxy, involves the matching of some lattice points of the overlayer with substrate lattice points. One way to look at coincident epitaxy is that a supercell (an integral multiple of basic unit cell; e.g.,  $3 \times 3$  supercell in Figure 2.12b) of the overlayer exhibits commensurate epitaxy with the substrate. It follows then that the smaller the size of the supercell greater is the epitaxial match between two lattices. If the two lattices do not exhibit commensurate or coincident epitaxy, they are said to be incommensurate. Table 2.1 shows the relationship between the values of  $V/V_o$  and the type of epitaxy.

**Table 2.2** Parameters for geometric epitaxy. Basic cell represents the unit cell of the crystal planes corresponding the macroscopic face under consideration. Supercell represents a nonprimitive cell obtained by extending the basic cell along  $b_1$  and  $b_2$  axes. The numbers in the *multipliers* column refer to the number of times  $b_1$  and  $b_2$  are multiplied to generate the supercell.

face	basic cell			super cell		$\alpha^\circ$	$V/V_o$
	$b_1$	$b_2$	$\beta$	multipliers	area ( $\text{\AA}^2$ )		
{002}	7.54	11.16	90.00	$1 \times 3$	252.44	51.46	0.50
{011}	7.54	17.83	92.23	$2 \times 1$	268.67	58.90	0.50
{101}	11.16	16.15	90.00	$2 \times 1$	360.47	14.55	0.51
{110}	13.46	13.91	91.60	$3 \times 1$	561.47	46.41	0.50
{012}	7.54	26.29	91.51	$1 \times 3$	594.47	51.25	0.50
{10-1}	11.16	15.49	90.00	$4 \times 1$	691.47	41.22	0.68
{11-1}	13.46	15.49	104.32	$4 \times 1$	808.07	45.71	0.56

All the SAMs have the same 2D lattice ( $a_1 = a_2 = 4.97 \text{ \AA}$  and  $\alpha = 120^\circ$ ; Figure 2.3). We determined the 2D lattice parameters for all possible growth faces of *PMP* and listed them as basic cell parameters in Table 2.2. We performed epitaxy calculations for each of these faces against the substrate SAM lattice with a  $0.01^\circ$  increment in  $\theta$ , and allowed each overlayer lattice vector ( $b_1$  and  $b_2$ ) to be multiplied four times at the most. We analyzed the results to obtain the values of  $\theta$  corresponding to the best lattice match along with other related parameters (Table 2.2). These results indicate that five of the seven possible faces of *PMP* exhibit coincident epitaxy. The {101} and {012} faces on which the *PMP* crystals grew on SAMs **1** and **2** are part of the five faces, suggesting that crystal growth on these faces is not hampered by geometric incommensurate epitaxy.

### 2.13 CARBOXY TERMINATED SAMs VERSUS PLASMA TREATED GLASS SLIDES

Figure 2.13a shows a microscopic image of the crystals grown on SAM **2**. As mentioned above, washing of the substrates with benzene led to the partial dissolution of the crystals; this is the reason some of the crystal faces are not as well defined as expected. This image is selected to show the precipitation of trigonal polymorph around the *PMP* crystals grown on the SAMs. We also carried out crystallizations of carbamazepine on glass slides and plasma treated glass slides placed in 50 mL beakers. The plasma treated slides are highly hydrophilic and expose silanol groups at the interface. We wished to test if surface hydrophilicity or hydrogen bonding groups without the orientational specificity and geometric structure can lead to face selective crystal growth. As can be seen from Figure 2.13b face-selective crystal growth is not observed on glass slides, at least to the exclusive extent seen on SAMs **1** and **2**. Powder X-ray diffraction also revealed that the crystals grown on glass slides or plasma treated glass slides gave multiple diffraction peaks with no consistency between different trials.

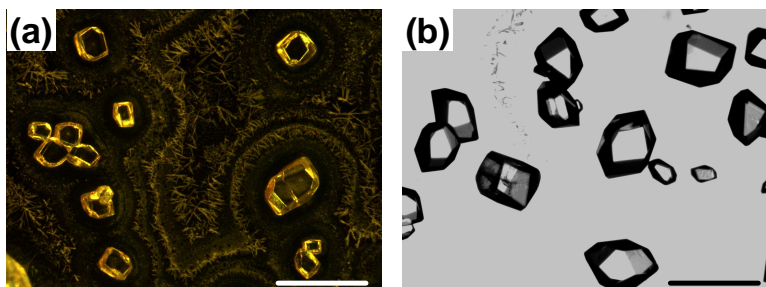


**Figure 2.13** Optical microscopic images of crystals grown on (a) SAM-2 and (b) plasma treated glass slide. Notice in (a) smaller, needle like crystals that belong to the trigonal polymorph. This image was taken from the experiment where the number of trigonal polymorph crystals precipitated was high. Notice in (b) various growth orientations of *PMP* crystals. Scale bars = 2 mm.

### 2.14 PARITY DEPENDENT FACE-SELECTIVE CRYSTAL GROWTH

The major difference between SAMs **1** and **2** is the parity of alkyl chains. As shown in Figure 2.5 the terminal groups in these two SAMs adopt different orientations with respect to the growth surface. The carboxy groups on SAM-2 are nearly perpendicular to the surface; in SAM-1 they are at a shallower inclination with respect to the surface. Why do *PMP* crystals nucleate from different faces on SAMs **1** and **2**? The relative orientation of the amide group of *PMP* with respect to the (012) and (101) planes suggests a possible answer to this question.

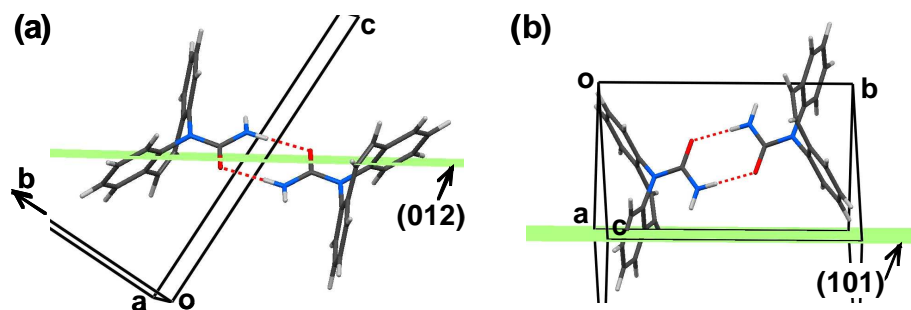


**Figure 2.14** Relative orientation of carbamazepine dimers with respect to (012) and (101) planes. Notice the shallow inclination of amide dimer in (a) and near perpendicular arrangement in (b).

In the crystal structure of *PMP*, molecules assemble into dimers through hydrogen bonding between the amide groups. It is reasonable to assume that molecules form hydrogen bonded dimers in solution and that these dimers assemble further into nuclei and crystals. The amide H-atom *not* involved in the formation of dimer and the second lone pair of amide O-atom are capable of participating in hydrogen bonds with the carboxy groups at the SAM interface. The angle between the amide dimers and (012) plane is  $43^\circ$ ; the corresponding angle for (101) plane is  $73^\circ$  (Figure 2.14).<sup>42</sup> It is instructive to compare these angles ( $43^\circ$  and  $73^\circ$ ) with the angles at which the carboxy groups are projected at the surface of SAMs **1** and **2** ( $\sim 45^\circ$  and  $\sim 73^\circ$ ; Figure 2.5). The carboxy groups on SAM-**1** are coplanar with the amide groups at (012) planes, whereas the carboxy groups on SAM-**2** are coplanar with the amide groups at (101) planes. Given that hydrogen bonding between carboxy and amide groups is greatly facilitated when the two groups are coplanar, it is likely that *PMP* crystal nuclei interact with SAM-**1** through their {012} faces and with SAM-**2** through their {010} faces.

## 2.15 CONCLUSION

The parity of alkyl chains is rarely used as a tool to control interfacial phenomena.<sup>43-44</sup> In this work, we showed that the parity of alkyl chains does play a determining role in the face-selective nucleation of *organic* compounds. Further work showed that this oriented growth can be extended to other carboxy terminated SAMs with even or odd number of methylene groups. Thiol SAMs containing hydroxy terminal groups did not show this level of specificity; often these SAMs showed peaks corresponding to (101), (012) and some other planes irrespective of the parity of the alkyl chains. These results suggest that the two-point hydrogen bond recognition between the carboxy groups and the amide dimers exert greater influence over interfacial molecular recognition compared to the hydrogen bonds formed by hydroxy groups.

**2.15 REFERENCES**

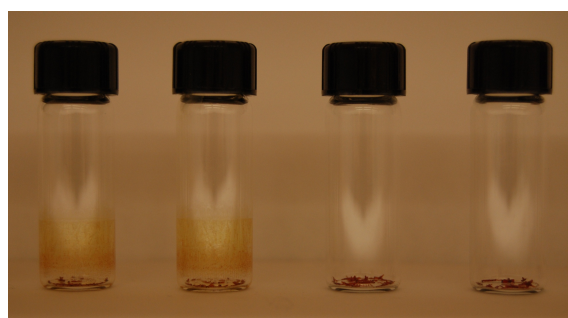
1. Byrn, S. R.; Pfeiffer, R. R.; Stowell, J. G., *Solid-State Chemistry of Drugs*. 2nd ed.; SSCI: West Lafayette, **1999**.
2. Brittain, H. G., *Polymorphism in Pharmaceutical Solids*. Marcel Dekker: New York, 1999; p 427 pp.
3. Hilfiker, R., *Polymorphism in the Pharmaceutical Industry*. Wiley-VCH: Weinheim, 2006; p 414 pp.
4. Bernstein, J., *Polymorphism in Molecular Crystals*. Clarendon Press: Oxford, **2002**.
5. Mullin, J. W., *Crystallization*. 4th ed.; Butterworth-Heinemann: New York, **2001**.
6. Garcia-Ruiz, J. M., Nucleation of protein crystals. *J. Struct. Biol.* **2003**, *142*, 22-31.
7. Mann, S., *Biomineralization*. Oxford University Press: New York, **2002**.
8. Kuzmenko, I.; Rapaport, H.; Kjaer, K.; Als-Nielsen, J.; Weissbuch, I.; Lahav, M.; Leiserowitz, L., Design and Characterization of Crystalline Thin Film Architectures at the Air-Liquid Interface: Simplicity to Complexity. *Chem. Rev.* **2001**, *101*, 1659-1696.
9. Gavish, M.; Popovitz-Biro, R.; Lahav, M.; Leiserowitz, L., Ice nucleation by alcohols arranged in monolayers at the surface of water drops. *Science* **1990**, *250*, 973-975.
10. Landau, E. M.; Levanon, M.; Leiserowitz, L.; Lahav, M.; Sagiv, J., Transfer of structural information from Langmuir monolayers to three-dimensional growing crystals. *Nature* **1985**, *318*, 353-356.
11. Carter, P. W.; Ward, M. D., Directing Polymorph Selectivity During Nucleation of Anthranilic Acid on Molecular Substrates. *J. Am. Chem. Soc.* **1994**, *116*, 769-770.
12. Briseno, A. L.; Mannsfeld, S. C. B.; Ling, M. M.; Liu, S.; Tseng, R. J.; Reese, C.; Roberts, M. E.; Yang, Y.; Wudl, F.; Bao, Z., Patterning organic single-crystal transistor arrays. *Nature* **2006**, *444*, 913-917.
13. Meldrum, F. C.; Flath, J.; Knoll, W., Chemical Deposition of PbS on Self-Assembled Monolayers of 16-Mercaptohexadecanoic Acid. *Langmuir* **1997**, *13*, 2033-2049.
14. Kuther, J.; Seshadri, R.; Knoll, W.; Tremel, W., Templated growth of calcite, vaterite and aragonite crystals on self-assembled monolayers of substituted alkylthiols on gold. *J. Mater. Chem.* **1998**, *8*, 641-650.
15. Aizenberg, J.; Black, A. J.; Whitesides, G. M., Control of crystal nucleation by patterned self-assembled monolayers. *Nature* **1999**, *398*, 495-498.
16. Aizenberg, J.; Black, A. J.; Whitesides, G. M., Oriented Growth of Calcite Controlled by Self-Assembled Monolayers of Functionalized Alkanethiols Supported on Gold and Silver. *J. Am. Chem. Soc.* **1999**, *121*, 4500-4509.
17. Kang, J. F.; Zaccaro, J.; Ulman, A.; Myerson, A., Nucleation and Growth of Glycine Crystals on Self-Assembled Monolayers on Gold. *Langmuir* **2000**, *16*, 3791-3796.
18. Lee, A. Y.; Ulman, A.; Myerson, A. S., Crystallization of Amino Acids on Self-Assembled Monolayers of Rigid Thiols on Gold. *Langmuir* **2002**, *18*, 5886-5898.
19. Banno, N.; Nakanishi, T.; Matsunaga, M.; Asahi, T.; Osaka, T., Enantioselective crystal growth of leucine on a self-assembled monolayer with covalently attached leucine molecules. *J. Am. Chem. Soc.* **2004**, *126*, 428-429.
20. Hiremath, R.; Varney, S. W.; Swift, J. A., Selective growth of a less stable polymorph of 2-iodo-4-nitroaniline on a self-assembled monolayer template. *Chem. Commun.* **2004**, 2676-2677.

21. Hiremath, R.; Varney, S. W.; Swift, J. A., Oriented Crystal Growth of 4-Iodo-4'-nitrobiphenyl on Polar Self-Assembled Monolayer Templates: A Case for Chemical Epitaxy. *Chem. Mater.* **2004**, *16*, 4948-4954.
22. Briseno, A. L.; Aizenberg, J.; Han, Y.-J.; Penkala, R. A.; Moon, H.; Lovinger, A. J.; Kloc, C.; Bao, Z., Patterned Growth of Large Oriented Organic Semiconductor Single Crystals on Self-Assembled Monolayer Templates. *J. Am. Chem. Soc.* **2005**, *127*, 12164-12165.
23. Hiremath, R.; Basile, J. A.; Varney, S. W.; Swift, J. A., Controlling Molecular Crystal Polymorphism with Self-Assembled Monolayer Templates. *J. Am. Chem. Soc.* **2005**, *127*, 18321-18327.
24. Cox, J. R.; Dabros, M.; Shaffer, J. A.; Thalladi, V. R., Selective crystal growth of the anhydrous and monohydrate forms of theophylline on self-assembled monolayers. *Angew. Chem. Int. Ed.* **2007**, *46*, 1988-1991.
25. Frostman, L. M.; Bader, M. M.; Ward, M. D., Nucleation and Growth of Molecular Crystals on Self-Assembled Monolayers. *Langmuir* **1994**, *10*, 576-582.
26. Mitchell, C. A.; Yu, L.; Ward, M. D., Selective Nucleation and Discovery of Organic Polymorphs through Epitaxy with Single Crystal Substrates. *J. Am. Chem. Soc.* **2001**, *123*, 10830-10839.
27. Cashell, C.; Corcoran, D.; Hodnett, B. K., Secondary nucleation of the b-polymorph of L-glutamic acid on the surface of a-form crystals. *Chem. Commun.* **2003**, 374-375.
28. Yu, L., Nucleation of One Polymorph by Another. *J. Am. Chem. Soc.* **2003**, *125*, 6380-6381.
29. Price, C. P.; Grzesiak, A. L.; Matzger, A. J., Crystalline polymorph selection and discovery with polymer heteronuclei. *J. Am. Chem. Soc.* **2005**, *127*, 5512-5517.
30. To our knowledge, there is only one other study that explored the effect of alkyl chain parity in a SAM on the nucleation of crystals. This study reported the crystal growth of the mineral calcium carbonate. See: Han, Y.-J.; Aizenberg, J., *Angew. Chem. Int. Ed.* **2003**, *42*, 3668-3670.
31. Ulman, A., Formation and Structure of Self-Assembled Monolayers. *Chem. Rev.* **1996**, *96*, 1533-1554.
32. Love, J. C.; Estroff, L. A.; Kriebel, J. K.; Nuzzo, R. G.; Whitesides, G. M., Self-Assembled Monolayers of Thiolates on Metals as a Form of Nanotechnology. *Chem. Rev.* **2005**, *105*, 1103-1169.
33. Sarma, J. A. R. P.; Allen, F. H.; Hoy, V. J.; Howard, J. A. K.; Thaimattam, R.; Biradha, K.; Desiraju, G. R., Design of an SHG-active crystal, 4-iodo-4'-nitrobiphenyl: the role of supramolecular synthons. *Chem. Commun.* **1997**, 101-102.
34. Laibinis, P. E.; Whitesides, G. M.; Allara, D. L.; Tao, Y. T.; Parikh, A. N.; Nuzzo, R. G., Comparison of the structures and wetting properties of self-assembled monolayers of n-alkanethiols on the coinage metal surfaces, copper, silver, and gold. *J. Am. Chem. Soc.* **1991**, *113*, 7152-7167.
35. Tao, F.; Bernasek, S. L., Understanding Odd-Even Effects in Organic Self-Assembled Monolayers. *Chem. Rev.* **2007**, *107*, 1408-1453.
36. Cruz Cabeza, A. J.; Day, G. M.; Motherwell, W. D. S.; Jones, W., Amide Pyramidalization in Carbamazepine: A Flexibility Problem in Crystal Structure Prediction? *Cryst. Growth Des.* **2006**, *6*, 1858-1866.

37. Fleischman, S. G.; Kuduva, S. S.; McMahon, J. A.; Moulton, B.; Bailey Walsh, R. D.; Rodriguez-Hornedo, N.; Zaworotko, M. J., Crystal Engineering of the Composition of Pharmaceutical Phases: Multiple-Component Crystalline Solids Involving Carbamazepine. *Cryst. Growth Des.* **2003**, *3*, 909-919.
38. Grzesiak, A. L.; Lang, M.; Kim, K.; Matzger, A. J., Comparison of the four anhydrous polymorphs of carbamazepine and the crystal structure of form I. *J. Pharm. Sci.* **2003**, *92*, 2260-2271.
39. Harris, R. K.; Ghi, P. Y.; Puschmann, H.; Apperley, D. C.; Griesser, U. J.; Hammond, R. B.; Ma, C.; Roberts, K. J.; Pearce, G. J.; Yates, J. R.; Pickard, C. J., Structural Studies of the Polymorphs of Carbamazepine, Its Dihydrate, and Two Solvates. *Org. Proc. Res. Dev.* **2005**, *9*, 902-910.
40. Hillier, A. C.; Ward, M. D., Epitaxial interactions between molecular overlayers and ordered substrates. *Phys. Rev. B* **1996**, *54*, 14037-14051.
41. Last, J. A.; Hooks, D. E.; Hillier, A. C.; Ward, M. D., The Physicochemical Origins of Coincident Epitaxy in Molecular Overlayers: Lattice Modeling vs Potential Energy Calculations. *J. Phys. Chem. B* **1999**, *103*, 6723-6733.
42. The crystal structure of *PMP* is determined by multiple authors. In this work we used the  $P2_1/n$  structure reported in "Himes, V. L.; Mighell, A. D.; De Camp, W. H. *Acta Crystallogr.*, **1981**, *B37*, 2242". It should be noted that the amide dimers adopt two distinct inclinations ( $43^\circ$  and  $79^\circ$ ) with respect to (101) planes. Whereas the dimer with shallower ( $43^\circ$ ) inclination is located within the plane, the dimer with steeper ( $79^\circ$ ) inclination is projected away from the plane.
43. Popovitz-Biro, R.; Wang, J. L.; Majewski, J.; Shavit, E.; Leiserowitz, L.; Lahav, M., Induced freezing of supercooled water into ice by self-assembled crystalline monolayers of amphiphilic alcohols at the air-water interface. *J. Am. Chem. Soc.* **1994**, *116*, 1179-1191.
44. Gupta, V. K.; Abbott, N. L., Design of surfaces for patterned alignment of liquid crystals on planar and curved substrates. *Science* **1997**, *276*, 1533-1536.

# 3

## SUPPRESSION OF NUCLEATION AT FLUOROUS INTERFACES – A NEW PARADIGM FOR THE SELECTIVE GROWTH OF STABLE POLYMORPHS



THIS PAGE LEFT INTENTIONALLY BLANK

### 3.1 POLYMORPHISM

Polymorphs are crystalline materials that have the same chemical composition but different solid state structures. The differences in structures of polymorphs lead to differences in their properties.<sup>1</sup> Though polymorphism affects a range of compounds, control of polymorphism is acutely important in pharmaceuticals because changing the polymorph can alter the dissolution rate, bioavailability, shelf-life and other properties of a drug.<sup>2-4</sup> Consequently, early discovery of polymorphs is vital to drug development, both to avoid late-stage manufacturing problems<sup>5</sup> and to protect intellectual property.<sup>1</sup> In this chapter, we describe a generic method that directs the growth of thermodynamically stable polymorphs under conditions that favor the formation of kinetic polymorphs. Our method uses an iconoclastic concept – suppression of nucleation at xenophobic interfaces – to hamper the nucleation of kinetic polymorphs and promote the growth of thermodynamic polymorphs.

Extensive research on polymorphism has resulted in (a) classification of different types of polymorphs, (b) development of analytical methods for characterization of polymorphs, (c) understanding of the physics and chemistry underlying phase transitions, (d) computational approaches for the prediction of polymorphism, and (d) control of bulk properties of crystals. Very little work, however, has been done in the area of selective growth of polymorphs.<sup>6</sup> Below, we will give various methods that are being developed and practiced in the crystallization of polymorphs. Some of these methods are advanced to the extent that they are commercialized and some are still in the conceptual stage. These methods illustrate the current interest in studying the polymorphism. More broadly, these methods recognize polymorphism as an opportunity and a challenge to develop new concepts that are relevant to crystal growth and solid state chemistry.<sup>7</sup>

### 3.2 HIGH-THROUGHPUT SCREENING

Changing solvents, solvent mixtures, temperature, rate of evaporation and rate of cooling are the traditional approaches towards the discovery of polymorphs.<sup>8</sup> These classical methods have recently been automated into a high-throughput screening (HTS) system.<sup>9</sup> Most pharmaceutical industries now use the HTS routinely and several recent examples illustrate the success of this approach. For example, a study involving a number of different solvent combinations and local temperature conditions resulted in the discovery of an elusive third polymorph of acetaminophen.<sup>10</sup> The principal advantage of HTS method is that it is generic. It can be applied to any compound with limited or no knowledge of its molecular or crystal structures and properties. Further, it uses small quantities of compounds to carry out a large number of experiments in a short time period. Yet, the HTS is a trial and error method and relies mostly on the probability of finding a target polymorph rather than following a designed approach.

### 3.3 ISOMORPHIC ADDITIVES

Remarkable examples of polymorphic control are offered by marine organisms that can, for example, selectively grow a specific polymorph of CaCO<sub>3</sub> (calcite or aragonite).<sup>11-12</sup>

These examples demonstrate the specific recognition between growing crystal planes and macromolecules in biological matrices. Extending these ideas to synthetic systems, tailor-made auxiliaries have been prepared to intervene in the kinetics of crystallization so as to control crystal morphology and polymorphism.<sup>13</sup> A small percentage of additives that are structurally similar to the target material can incorporate preferentially into specific growth planes and impede the growth in particular directions. Similarly, isomorphic additives can be designed such that they block the growth of the stable polymorph and promote the growth of a metastable polymorph.<sup>14-15</sup> Though harnessing crystallization through additives is an attractive area of research, only a few examples have been studied so far.<sup>16-17</sup> One limitation in the design of additives is that it requires prior knowledge of the crystal structures of the polymorphs.

### 3.4 MONOLAYERS AS SUBSTRATES

Crystallization is often mediated by heterogeneous nucleation, which can occur on the surfaces of dust particles, glass vials, or foreign templates.<sup>18</sup> Biomineralization inspired a number of studies to explore the nucleation and crystal growth at interfaces. Monolayers of amphiphilic molecules at air-water interface,<sup>19-20</sup> monolayers of organosilane derivatives,<sup>21-23</sup> and thiol self-assembled monolayers (SAMs)<sup>24-25</sup> on metal substrates have all been used in the past twenty years to examine and control the early stages of crystal growth.<sup>26-28</sup> These studies showed that face selective crystal growth is predominant in many systems, indicating that molecular level interactions between substrate and growing nucleus are responsible for such selectivity. The results of these studies suggested the possibility of controlling the growth of polymorphs using tailor-made surfaces. Polymorphs have different crystal structures and it may be possible to glean crystal planes specific to one polymorph and provide surface templates that promote the nucleation of these planes. Some recent reports, published by our group and others, showed that SAMs can indeed nucleate polymorphs based on specific interfacial interactions.<sup>29-33</sup>

### 3.5 SINGLE CRYSTALS AS SUBSTRATES

Freshly cut single crystal surfaces are best examples of two-dimensional templates. Recent research using faces of freshly grown single crystal substrates showed that a multimorphic pharmaceutical intermediate grows as a metastable polymorph on certain faces of pimelic acid crystals.<sup>34</sup> Crystalline substrates lend themselves well to the geometry matching programs that can be used to find close matches between crystallographic planes of the substrate and polymorphic crystals.<sup>35</sup> Nucleation of one crystal on another<sup>36-40</sup> has important implications in the growth kinetics of polymorphs.<sup>38</sup> For example, it is possible that a fast growing polymorph can nucleate on a slow growing (but fast nucleating) polymorph.<sup>39</sup> Such outcomes point to the importance of control of nucleation *and* growth of desired polymorphs. The practical limitation of these substrates is that it is difficult to identify and prepare crystals that can act as templates and that do not tend to dissolve in solutions.

### 3.6 POLYMERS AS SUBSTRATES

Polymer chemistry, one of the most matured fields in chemical sciences, affords the ready availability of different types of polymers with a variety of functionalities incorporated into the backbone. Recently, polymer chunks are used in a high throughput setting to screen for polymorphism in pharmaceuticals and other compounds.<sup>41-43</sup> For example, when acetaminophen is crystallized from solutions containing 84 different polymers, about one third nucleated the metastable orthorhombic form, one third the stable monoclinic polymorph, and the rest a mixture of both forms.<sup>41</sup> These studies indicate that a one-to-one matching of complementary molecular units at the interface may not be necessary for templated growth, but more likely profusion of a set of functional groups and certain charge density can nucleate specific polymorphs. These results provide us with the impetus to explore the use of silane monolayers crafted on glass slides and vials as substrates for polymorph discovery and selection.

### 3.7 CRYSTALLIZATION INSIDE CAPILLARIES

Crystallization in confined spaces can also lead to the selective growth of polymorphs. In bulk solutions (of volume mL to L) density fluctuations and impurities such as dust particles lower the nucleation barrier for crystallization, and thermodynamically stable polymorph can grow at the expense of other metastable polymorphs. When solutions are confined to volumes as small as nanoliters the fluctuation and contamination effects are minimized and the solution can continue to evaporate under quiescent conditions to reach high supersaturations. Under these conditions the nuclei of kinetic polymorphs have greater chances of survival, that is, they do not dissipate and convert to the thermodynamically stable polymorph. Recent work using glass capillaries for crystal growth showed that it is indeed possible to grow the kinetically stable polymorphs of pharmaceutical compounds in reproducible manner.<sup>44-45</sup>

### 3.8 CRYSTALLIZATION INSIDE NANOSCALE CHAMBERS

Often, but not always, different polymorphs have different morphologies. One can assume that crystal nuclei of such polymorphs have morphologies similar to the fully grown crystals. Crystallization of the corresponding compounds in confined nanospaces can lead to the growth of one polymorph over the other based on its fit with respect to the nanochamber. Initial proof for this concept came from a recent work, which showed that crystallization of anthranilic acid in nanoporous glass results in polymorph selection based on the shape of the nanocavities.<sup>46</sup> Further work showed that this approach can be extended to other systems as well.<sup>47</sup>

### 3.9 LASER INDUCED NUCLEATION

Supersaturated solutions of certain organic compounds yield different polymorphs when they are illuminated with intense pulses of lasers.<sup>48</sup> The type of polymorph obtained is determined by the nature of the polarization of the laser. This laser induced nucleation depends on the level of supersaturation but not on the wavelength used. It is argued that

the interaction of the laser with pre-nucleation clusters is different for linearly and circularly polarized lights.<sup>49</sup> Linear alignment of molecules occurs in the presence of linearly polarized light and circularly polarized light results in the planar alignment of molecules in the clusters. Though laser induced nucleation is still in its infancy, it is an attractive alternative to other methods discussed here because it offers a generic, contaminant-free nonchemical approach to influence the crystallization of polymorphs.

### 3.10 SONOCRSTALLIZATION

Sonocrystallization refers to the crystallization under the influence of ultrasonic sound in a pulsed or continuous format, typically in the range of 20 kHz to 5 MHz. Ultrasound assisted crystallization has been practiced for several decades. Ultrasound imparts nonchemical disturbances to the sample; it is found to increase the rate of nucleation and decrease the metastable zone width.<sup>50</sup> In the past, ultrasound is often used to induce nucleation, reduce the crystal size and narrow the particle size distribution. Recent results suggest that it is possible to influence the crystallization of polymorphs using ultrasound.<sup>51-53</sup> In addition, the homogenizing effect of ultrasound can be used to promote the formation of cocrystals and solid solutions where multiple components are required to be brought together at a molecular level.

### 3.11 CONTACT LINE CRYSTALLIZATION

It is common observation that precipitation occurs at the solvent front when a saturated solution is evaporated in a vessel. Recent work showed that, kinetic polymorphs that have lower nucleation barrier can crystallize at this solvent front.<sup>54-55</sup> Once formed, crystals of the metastable polymorph can stay stable and not transform to the stable polymorph because they are not in touch with the solution. This process of crystal growth at the evaporating solvent front is termed as contact line crystallization.

### 3.12 HIGH PRESSURE CRYSTALLIZATION

Different polymorphs have different densities and it should, in principle, be possible to influence the polymorphism by changing the applied pressure on crystallization solution. Indeed, recently it has been shown that new polymorphs and solvates of acetaminophen, piracetam and other compounds can be grown in high pressure (up to 100 GPa) chambers.<sup>56-59</sup> While some high pressure polymorphs are not stable at standard conditions, the ability to grow crystals at high pressures and determine their structures is relevant to the understanding of phase transitions that can occur during pharmaceutical processes such as comminution and compression.<sup>60</sup>

### 3.13 DISAPPEARING POLYMORPHS

In previous sections, we discussed different methods that are being explored for polymorph selection. To underscore the importance of the method discussed in this chapter, it is important to recall one of the well-known but strange phenomena of crystallization, the *disappearing* of polymorphs.<sup>61</sup> In most cases, the reason for the

vanishing of an existing crystal form is attributed to the formation of a new, thermodynamically more stable polymorph. The most devastating effect of this phenomenon is seen in ritanovir, an anti-retroviral drug used in the treatment of AIDS. This drug had to be recalled after being on the market for two years because a more stable form with markedly lower dissolution rate started to crystallize at the manufacturing sites. The initial formulations contained the now metastable, but then only known, modification that readily transformed to the more stable polymorph. Fortunately, a new formulation of the drug that contains the stable polymorph could be developed and marketed, but only after much work and time.<sup>5</sup> The phenomenon of disappearing polymorphs and the case of ritanovir illustrate the importance of the discovery of all possible, and especially the stable, polymorphs of a given drug at an early stage in the discovery. We show in this chapter that fluoruous surfaces can act as nucleation inhibitors of kinetic polymorphs and thereby allow the growth of stable polymorphs through the process of Ostwald ripening.

### 3.14 FLUOROUS SURFACES

The term *fluorous* is coined, as an analogue of *aqueous*, to represent fluorinated media with hydrophobic and oleophobic properties.<sup>62</sup> Today, the adjective *fluorous* refers to species that are highly or completely fluorinated saturated organic molecules or molecular fragments. Fluorous species are immiscible with their organic and aqueous counterparts and as such they offer new avenues for chemical synthesis. There is immense interest in fluoruous species towards applications in separations, scavenging, catalysis, passivation, and biomaterials.<sup>63</sup> We are interested in *fluorous surfaces* in this work and we prepare them in the form of silane monolayers bearing polyfluoroalkyl chains,  $-(\text{CH}_2)_2-(\text{CF}_2)_n-\text{CF}_3$ . Exposure of substrates with hydroxy groups (such as hydrolyzed glass slides with Si–OH groups) to silanizing reagents (such as  $\text{X}_3\text{SiR}$ ;  $\text{X} = \text{Cl}$  or alkoxy) results in nucleophilic displacement reactions at the surface. These reactions lead to Si–O–Si bonds at the interface and to a monolayer of molecules connected to each other as well as to the surface (Figure 3.1).<sup>24</sup>

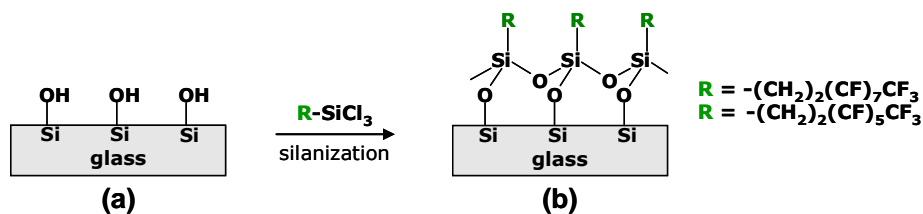


**Figure 3.1** Schematic structures of (a) a hydroxylated surface showing silanol groups and (b) fluoruous surface showing silane monolayers.

Silanizing reagents are brought into contact with the substrates either in the vapor phase or in solution.<sup>64</sup> The amount of water in the solution affects the reaction on the surface and excess amounts of water leads to bulk polymerization in the solution. Generally, only small amount of water is required for reactions at the interface. We assume in this work that the trace amounts of water adsorbed on the hydrophilic glass surface is enough to

promote the reaction. Compared to thiol SAMs formed on gold, silane monolayers are not well-packed and less ordered but display greater chemical and thermal stability (up to 125 °C). They are stable in organic solvents and in acidic media but slowly degrade in basic media. In this work, we used trichlorosilanes because of their high reactivity compared to the trialkoxysilanes. As the -R groups, we used the fluoros chains  $-(\text{CH}_2)_2-(\text{CF}_2)_5-\text{CF}_3$  and  $-(\text{CH}_2)_2-(\text{CF}_2)_7-\text{CF}_3$ ; these polyfluoroalkyl (or perfluoroalkyl if we consider the fluoros part) groups are more reactive than their alkyl counterparts and they can form silane monolayers even in the absence of water.<sup>65</sup> The perfluoroalkyl chains afford fluoros surfaces that are *xenophobic*, making them good candidates for testing the inhibition of nucleation at the interfaces.

### 3.15 PROMOTION VERSUS INHIBITION

It is important to distinguish our work with fluoros surfaces from the previous work carried out with other types of surfaces. Both methods attempt to influence the polymorphism by controlling the heterogeneous nucleation. Previous work with different kinds of surfaces (Langmuir and silane monolayers, thiol SAMs, and single crystal and polymer surfaces) attempted the growth of polymorphs by *promoting* the nucleation through *complementary* functional groups and *attractive* interfacial interactions. In most of these cases, the selective growth of polymorphs is based on serendipity or prior knowledge of the crystal structures or a high-throughput approach. Save for the high throughput method, these approaches are highly specific to a given compound.

Our work with fluoros surfaces attempts to grow the stable polymorphs by *inhibiting* the nucleation (of kinetic polymorphs) through *xenophobic* functional groups and *unattractive* interfacial interactions. Our approach does not require prior knowledge of the crystal structures of polymorphs and it is generic and applicable to any compound that itself is not fluoros or does not contain fluoros fragments. Interfacial repulsion is a well-practiced phenomena in nature (e.g., Lotus leaf) and domestic and commercial products (e.g., Teflon). The fluoros surfaces we use have the same amorphous structure and the xenophobic characteristics as Teflon. Our fluoros surfaces are optically transparent, thermally stable, and inexpensive; they can be made on any glass substrate.

### 3.16 NITROFURANTOIN

We chose nitrofurantoin, an antibiotic active against many urinary tract pathogens, as a model pharmaceutical to demonstrate the unique ability of the fluoros surfaces in the selective growth of stable polymorphs. Earlier work from our group showed that among eight different silane monolayers (with different head groups and spacers) perfluoroalkyl monolayers showed a high degree of selectivity in the crystal growth of indomethacin polymorphs.<sup>66</sup> The two polymorphs of indomethacin have completely different structures, morphologies, and densities; the difference between their lattice energies is large so differentiating the stable polymorph from the metastable form using fluoros surfaces is relatively easy. In this work, we wished to select a system that is dimorphic in which the two polymorphs have practically similar lattice energies. We surmised that such a system will test the true efficacy of the method discussed here.

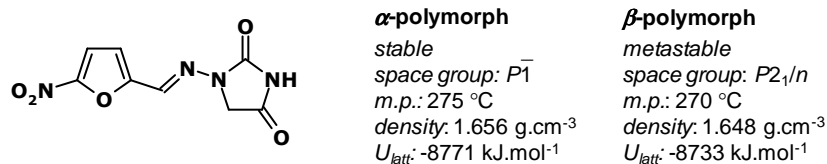


**Figure 3.2** Molecular structure of nitrofurantoin and the important solid state properties of its two polymorphs. Density, melting point and crystal structure data for the polymorphs are taken from reference 67. We calculated the lattice energies using the Universal Force Field incorporated in the GULP module of the program Materials Studio.

Nitrofurantoin is a planar molecule (Figure 3.2) and derives its name from the two five-membered rings it contains, furan and hydantoin. It crystallizes in two solid state structures;<sup>67</sup>  $\alpha$ -polymorph is slightly more stable than the  $\beta$ -polymorph. Both polymorphs are reported to have near similar densities and melting points; both adopt layered crystal structures (Section 3.22) and have near similar lattice energies (Figure 3.2).<sup>68</sup> Most crystallization conditions produce the  $\beta$ -polymorph readily and it is this less stable form that is used in the marketed products. Yet, the  $\alpha$ -polymorph is reported to have better dissolution characteristics (Figure 3.3) which can decrease the side effect emesis seen in some patients.<sup>69</sup> These findings amplified our interest in developing a method that yields the stable  $\alpha$ -polymorph exclusively under conditions favorable for the growth of metastable  $\beta$ -polymorph. Nitrofurantoin absorbs light in the visible region ( $\lambda_{max}$ : 366 nm) and gives pale-yellow to orange-red solutions depending on concentration. The intensity of the solution color is proportional to its concentration and we follow the changes in concentration visually, gravimetrically, and spectroscopically to assess the rate of crystallization in vials exposing highly hydrophilic or xenophobic surfaces.

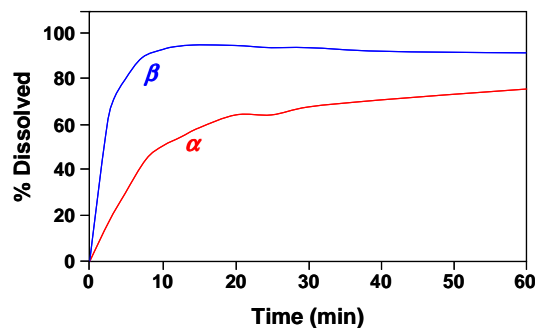


**Figure 3.3** Mean powder dissolution rates for  $\alpha$ - and  $\beta$ -polymorphs of nitrofurantoin. Adopted from reference 69.

### 3.17 PLASMA TREATMENT OF GLASS SUBSTRATES

We used 1 dram glass vials for crystallization and glass microscope slides as controls to test the surface properties. We cleaned these substrates (slides and vials) with water and dried them prior to plasma oxidation. Glass is made of amorphous silica and contains surface siloxy and silanol groups. Treating the glass substrates with oxygen plasma removed surface contaminants and increased the content of hydroxyl groups. We oxidized the substrates with oxygen plasma for 30-40 seconds using the SPI Plasma Prep II etcher that operated at 13.56 MHz under a 200 micron vacuum. The substrates are highly reactive when they are taken out of the plasma etcher and atmospheric humidity helped the formation of surface silanol groups (Figure 3.1a). To avoid any other surface reactions, we used these vials for crystallization experiments immediately after plasma treatment.

### 3.18 FABRICATION OF FLUOROUS MONOLAYERS

We fabricated silane monolayers with fluorine head groups by treating the plasma-oxidized glass substrates with silanizing reagents  $\text{Cl}_3\text{Si}-(\text{CH}_2)_2-(\text{CF}_2)_5-\text{CF}_3$  or  $\text{Cl}_3\text{Si}-(\text{CH}_2)_2-(\text{CF}_2)_7-\text{CF}_3$ . Initial experiments in this work used the surfaces with  $-\text{C}_6\text{F}_{13}$  and  $-\text{C}_8\text{F}_{17}$  groups. The results obtained from both monolayers are qualitatively similar. From here on, we only report the results obtained with fluorine monolayers that exposed  $-\text{C}_6\text{F}_{13}$  groups at the interface.

We prepared ~1 mM solutions of the silanizing reagents in dichloromethane and quickly transferred these solutions into plasma treated vials until they are filled. To keep the solutions away from atmospheric moisture, we capped the vials and allowed the silanization to take place for about ninety minutes. We monitored the vials throughout this time and discarded any vials that showed excessive cloudiness, which is an indication of disproportionate bulk polymerization. Shorter times may lead to incomplete surface polymerization and longer reaction times typically lead to multilayers on the surface. In our work, the length of silanization (that is, formation of surface monolayers or possible multilayers) did not affect the outcome of our crystal growth experiments. Once the solution treatment is complete, we rinsed the vials thoroughly with dichloromethane followed by ethyl acetate to remove any unreacted silane monomers. We baked the vials in an oven at 100-110 °C for three hours to complete the reaction between any dangling silanol groups at the interface of glass and silanizing reagent.

We assumed that the fabrication of silane monolayers on the glass substrates is complete (Figure 3.1b) after the heat treatment. These monolayers showed distinct wetting behavior characteristic of perfluorinated surfaces. Contact angle measurements (Figure 3.4) showed that the water droplets bead on the fluorine monolayers ( $\theta = 105^\circ$ ) and fully spread on the plasma treated glass ( $\theta = 0^\circ$ ). We use these highly hydrophilic vials as the *sticky* substrates and the fluorine vials as *nonstick* substrates. We expect the vials with surface silanol groups to promote the nucleation of kinetic polymorph and the vials with fluorine surfaces to inhibit any nucleation at the interface. We refer to the former substrates as hydroxylated vials and the latter as fluorine vials.

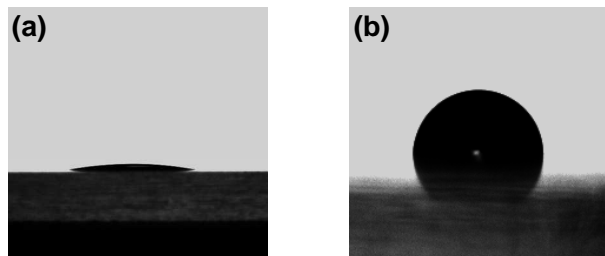


**Figure 3.4** Spreading and beading of one microliter droplet of water on (a) hydroxylated and (b) fluorinated surfaces. The image in (a) is taken a fraction of a second after the drop is placed; within a second the droplet spreads completely on the surface and becomes invisible to the camera.

### 3.19 CRYSTAL GROWTH IN HYDROXYLATED AND FLUOROUS VIALS

At the beginning of each series of crystal growth experiments, we prepared a large quantity of 21 mM nitrofurantoin solution in acetonitrile. We started with 17-19 mM solution and heated it at 60 °C for 15-20 minutes until its volume is reduced to give the required 21 mM concentration. We transferred this freshly prepared solution to ten hydroxylated and ten fluorinated 1 dram vials until each one of the vessels is filled to a third of its height (~ 1.8 mL). To control the rate of evaporation, we covered the vials with perforated aluminum foils or closed them with screw-caps containing a set number of holes.

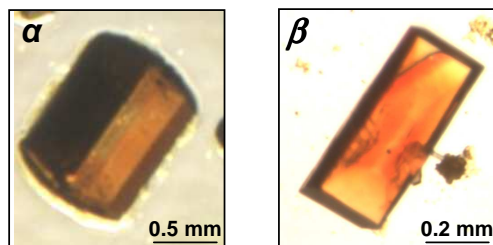


**Figure 3.5** Experimental crystal morphologies of  $\alpha$ - and  $\beta$ -polymorphs of nitrofurantoin grown from 21 mM acetonitrile solutions.

In fluorinated vials, one or two initial crystals of the  $\alpha$ -polymorph appeared at the bottom of the vessels after 70-75 hours when 35-50% of the solution had evaporated. The solution is fully evaporated in both vials in 120-140 hours. Crystals in the fluorinated vials had thick tabular morphology, orange color, and sizes in the range 0.5-1.2 mm (Figure 3.5). In hydroxylated vials, multiple crystals of the  $\beta$ -polymorph appeared on the walls, at the solvent front, within 4-6 hours. As the evaporation continued, more crystals of the  $\beta$ -polymorph grew along the moving solvent front (Figure 3.6). In stark contrast, no crystals are seen on the walls of fluorinated vials (Figure 3.6) in hundreds of crystallization

experiments carried out in this work. Crystals on the walls of hydroxylated vials had thin plate-like morphology, pale-yellow color, and smaller sizes in the range 0.01-0.5 mm (Figure 3.5). These experiments are repeated at least eight times using 21 mM solutions of nitrofurantoin and the results obtained are similar. We characterized the materials formed at various locations in the vials using optical microscopy, infrared (IR) and Raman spectroscopy, single crystal and powder X-ray diffraction (PXRD) analysis, differential scanning calorimetry (DSC) and thermal gravimetric analysis (TGA).

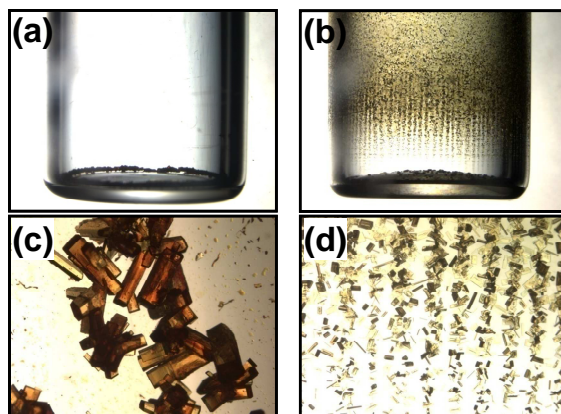


**Figure 3.6** Crystallization of nitrofurantoin in fluorinated (left) and hydroxylated (right) vials. (a-b) Side views of the vials showing clean walls of fluorinated vials and crystal-laden walls of hydroxylated vials. (c) View perpendicular to the bottom of the fluorinated vial showing crystals of  $\alpha$ -polymorph. (d) Magnified view of the wall of hydroxylated vial showing crystals of  $\beta$ -polymorph.

### 3.20 VISUAL OBSERVATIONS

The color of nitrofurantoin solution and optical transparency of glass vials allowed us to visually monitor the progress of crystallization. Figure 3.7 shows three distinct stages during the evaporation of solutions in hydroxylated and fluorinated vials. At the onset of crystallization (Figure 3.7a), freshly transferred solutions in both types of vials are pale-yellow in color and show opposing wetting behavior in vials with different surfaces. The concave menisci in hydroxylated vials indicate that the solution wets the walls of these vials. In contrast, the menisci are flat in fluorinated vials; the solution does not wet the walls of fluorinated vials confirming the xenophobic nature of these surfaces.

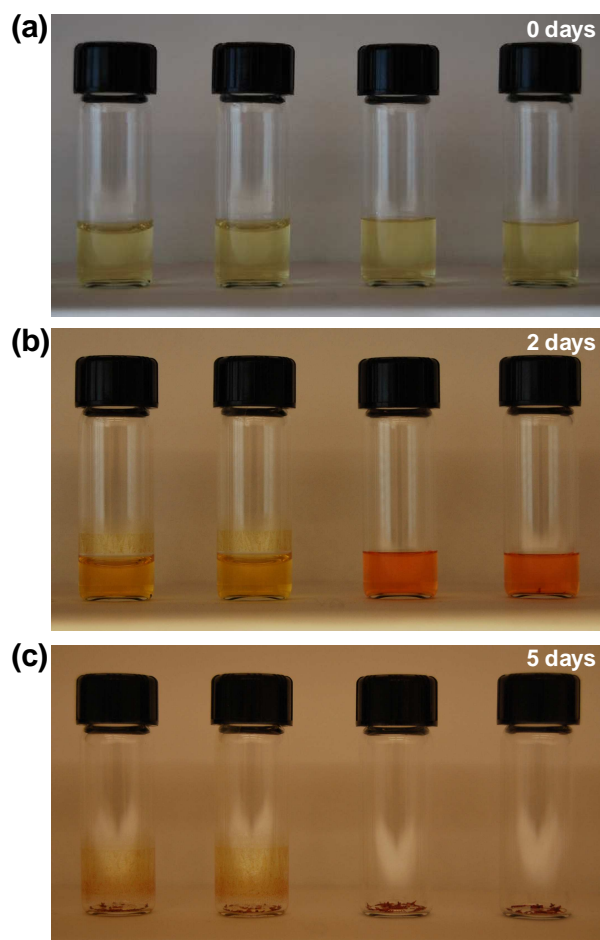


**Figure 3.7** Monitoring of crystal growth in hydroxylated (left two) and fluorinated (right two) vials. Notice the differences in the menisci in two types of vials in top two images and darkening of solution color in fluorinated vials in the middle image. Notice the crystal growth on the walls of hydroxylated vials.

An image taken after 48 hours of evaporation (Figure 3.7b) shows two important characteristics of crystallization. First, crystal growth occurs on the walls of hydroxylated vials as solvent evaporates and nothing crystallizes on the walls of fluorinated vials. Second, the solutions in different vials show markedly different colors indicating different concentrations of the remaining solutions. In hydroxylated vials the solution turns slightly orange (or dark-yellow) compared to the beginning. In fluorinated vials, however, the solution displays an intense orange-red color with a much higher concentration of nitrofurantoin. These observations can be explained by the suppressed nucleation and crystal growth on the walls of the fluorinated vials, which lead to a higher remnant concentration.

Following the evaporation further, we observed that some crystals are formed in the bulk solution in fluoruous vials (as well as in hydroxylated vials) that sank to the bottom and continued to grow. At the completion of the evaporation (Figure 3.7c), crystals are found only at the bottom of fluoruous vials; on the hydroxylated vials crystals are found on the walls and at the bottom. Characterization of the crystals using various techniques described below confirmed that while the stable  $\alpha$ -polymorph crystallized selectively in fluoruous vials the metastable  $\beta$ -polymorph crystallized in hydroxylated vials.

### 3.21 IR AND RAMAN CHARACTERIZATION OF POLYMORPHS

We collected the IR spectra of polymorphs on a Spectrum One FT-IR Spectrometer (Perkin Elmer) equipped with an ATR (attenuated total reflectance) accessory. Acquisition of ATR-IR spectra is fast and uses a small amount (1-2 mg) of sample. The two polymorphs of the nitrofurantoin showed distinguishable IR absorptions (Figure 3.8); thus we used IR spectroscopy as the first technique to characterize the products of crystallization.

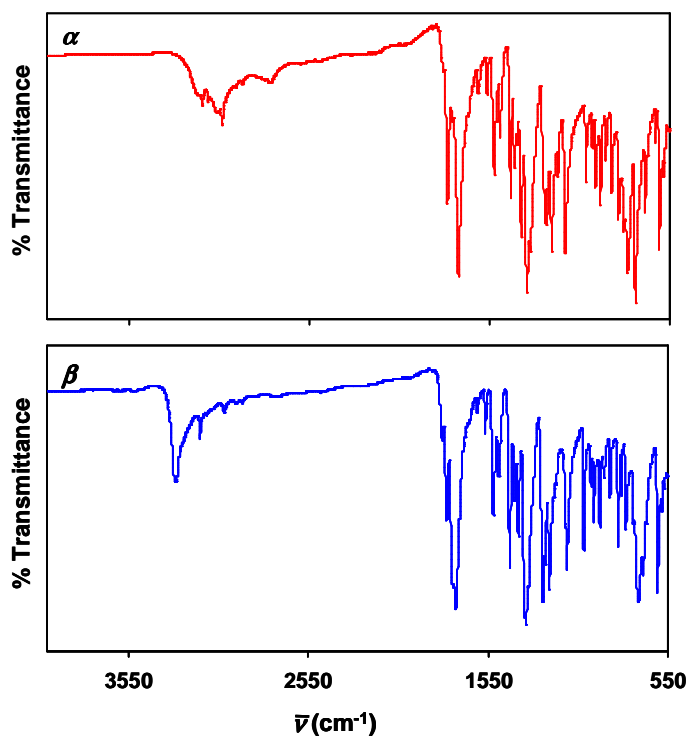


**Figure 3.8** IR Spectra of  $\alpha$ - (top) and  $\beta$ -polymorphs (bottom) of nitrofurantoin grown in fluoruous and hydroxylated vials.

We used the overall pattern as well as several characteristic bands to distinguish between the polymorphs and assess the hydrogen bond strengths in the solid state. The N-H stretching vibrations of the imide group result in a relatively broad band with a peak at  $3140\text{ cm}^{-1}$  in  $\alpha$ -polymorph and a narrower band at  $3279\text{ cm}^{-1}$  in  $\beta$ -polymorph. The N-H out-of-plane bending absorptions are observed at  $740\text{ cm}^{-1}$  in  $\alpha$ -polymorph and at  $713\text{ cm}^{-1}$  in  $\beta$ -polymorph. The differences in the stretching and bending frequencies infer different hydrogen bond interactions of the N-H groups in the two polymorphs. The N-H group in  $\alpha$ -polymorph participates in stronger N-H $\cdots$ O interactions ( $d_{\text{N}\cdots\text{O}}$ :  $2.85\text{ \AA}$ ,  $\theta_{\text{N-H}\cdots\text{O}}$ :  $171^\circ$ ) than in  $\beta$ -polymorph ( $d_{\text{N}\cdots\text{O}}$ :  $2.82\text{ \AA}$ ,  $\theta_{\text{N-H}\cdots\text{O}}$ :  $155^\circ$ ; see Section 3.22 for more details).<sup>70</sup> Stronger hydrogen bonding interactions shift the stretching frequencies to the lower value (due to the lengthening of N-H covalent bond) and bending frequencies to the higher value (due to strengthening of H $\cdots$ O noncovalent bond).

The differences in hydrogen bonding can also be observed in the C=O stretching frequencies. Both  $\alpha$ - and  $\beta$ -polymorphs show strong bands for C=O groups at  $1719\text{ cm}^{-1}$  and  $1728\text{ cm}^{-1}$  respectively. Lower stretching frequency indicates longer C=O bond in the  $\alpha$ -polymorph, again attributed to stronger hydrogen bonding. The broadness of the C=O band in the  $\beta$ -polymorph is due to the significantly different C=O distances,  $1.22$  and  $1.19\text{ \AA}$ . The corresponding C=O distances in the  $\alpha$ -polymorph are  $1.21$  and  $1.20\text{ \AA}$ . The longer C=O bond in each corresponds the carbonyl group that participates in hydrogen bonding. The differences in IR absorption intensities and positions allowed the quick identification of the two polymorphs of nitrofurantoin.

We collected the Raman spectra of two polymorphs on a DXR Raman Microscope (Thermo Scientific). Raman spectroscopy does not require sample preparation; it is complementary to IR spectroscopy and provides information on molecular vibrations. The high sensitivity of this technique allows the detection of small changes in vibrational frequencies that may occur due to changes in conformations or crystalline environment. Figure 3.9 shows the Raman spectra of  $\alpha$ - and  $\beta$ -polymorphs of nitrofurantoin.

The main differences between the two polymorphs are seen in the positions and relative intensities of -NO<sub>2</sub> group and C=N bonds. The -NO<sub>2</sub> stretch occurs at  $1342\text{ cm}^{-1}$  in  $\alpha$ -polymorph and  $1347\text{ cm}^{-1}$  in  $\beta$ -polymorph. This small shift may be attributed to the different N-O distances arising from C-H $\cdots$ O-N interactions in the crystals. There are also noticeable differences in the relative peak intensities in the fingerprint region. For example, an intense band associated with C=N appears at  $1609\text{ cm}^{-1}$  for  $\alpha$ -polymorph; the same band is relatively weak in the  $\beta$ -polymorph and appears at  $1608\text{ cm}^{-1}$ .

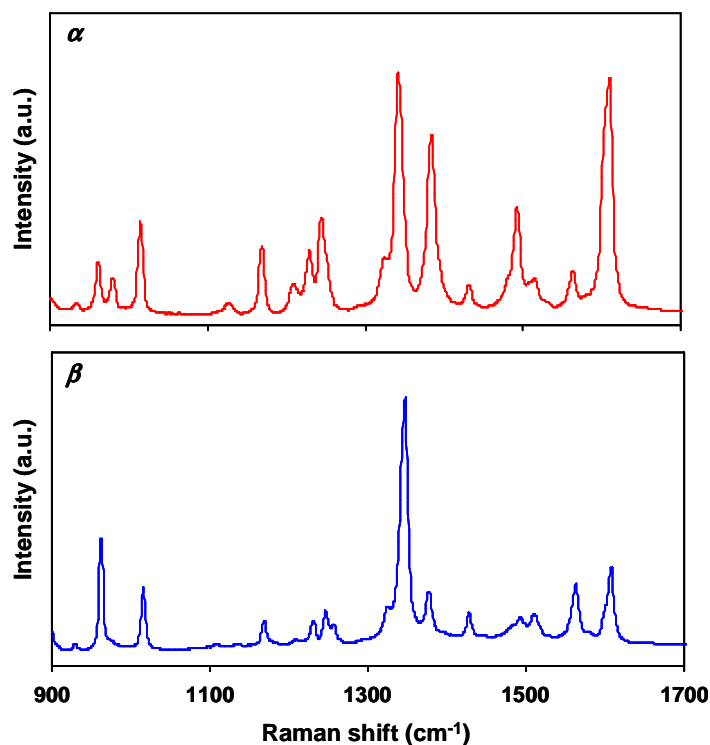


**Figure 3.9** Raman Spectra of  $\alpha$ - (top) and  $\beta$ -polymorphs (bottom) of nitrofurantoin grown in fluoruous and hydroxylated vials.

### 3.22 SINGLE CRYSTAL X-RAY DIFFRACTION ANALYSIS

The two polymorphs of nitrofurantoin had similar morphologies, PXRD patterns (Section 3.23), and thermograms (Section 3.24). In order to unequivocally assess the identity of the polymorphs, we characterized their structures by single crystal X-ray analysis. We selected the crystals suitable for diffraction under a microscope and mounted them on a kapton loop and mesh using a small amount of paratone or mineral oil. We collected the X-ray data using Mo- $K\alpha$  radiation ( $\lambda = 0.71073 \text{ \AA}$ ) on a Bruker APEX II diffractometer equipped with CCD detector and Oxford Cryostream Plus low-temperature device. Table 3.1 lists the parameters for data collection and structure refinement.<sup>71</sup>

Nitrofurantoin molecules adopt planar conformations in both  $\alpha$ - and  $\beta$ -polymorphs. Molecules pack into layers in both cases (Figure 3.10); hydrogen bonds are seen within the layers and van der Waals and  $\pi$ -stacking interactions are seen between the layers. Though layers are separated by shorter distances in the  $\beta$ -form, stronger stacking interactions between furan and hydantoin rings are seen in the  $\alpha$ -polymorph. Despite the differences in the intralayer and interlayer arrangements, the overall packing efficiencies of both polymorphs are almost identical (Table 3.1).

**Table 3.1** Crystallographic data for  $\alpha$ - and  $\beta$ -polymorphs of nitrofurantoin. The temperature of data collection is given as  $T$ . Packing coefficient,  $C_k^*$ , is calculated using the program PLATON.<sup>72</sup>

	$\alpha$	$\beta$
Emp. formula	C <sub>8</sub> H <sub>6</sub> N <sub>4</sub> O <sub>5</sub>	C <sub>8</sub> H <sub>6</sub> N <sub>4</sub> O <sub>5</sub>
Formula wt.	238.17	238.17
Crystal system	triclinic	monoclinic
Space group	$P-1$	$P2_1/n$
$a$ (Å)	6.7903(3)	7.6783(6)
$b$ (Å)	7.6026(4)	6.4505(5)
$c$ (Å)	9.7657(5)	18.7849(16)
$\alpha$ (°)	106.993(2)	90
$\beta$ (°)	103.841(2)	91.910(5)
$\gamma$ (°)	92.355(2)	90
$V$ (Å <sup>3</sup> )	464.78(4)	929.88(13)
$Z$	2	4
$D_{\text{calc}}$ (Mg/m <sup>3</sup> )	1.702	1.701
$F$ (000)	244	488
$\mu$	0.145	0.145
$R_1$	0.0350	0.0367
$wR_2$	0.1006	0.1031
GoF	1.050	1.036
$N$ -total	5926	15027
$N$ -independent	2902	2956
$N$ -observed	2590	2422
$N$ -parameters	158	178
$T$ (K)	100	100
$\theta$ range	2.26-30.93	2.83-31.03
Index ranges	-9 $\leq h \leq$ 9	-11 $\leq h \leq$ 11
	-5 $\leq k \leq$ 10	-8 $\leq k \leq$ 9
	-14 $\leq l \leq$ 14	-27 $\leq l \leq$ 27
Crystal size (mm <sup>3</sup> )	0.40×0.37×0.20	0.25×0.16×0.16
Crystal shape	prism	plate
Crystal color	orange	yellow-orange
Solvent	CH <sub>3</sub> CN	CH <sub>3</sub> CN
$C_k^*$	0.751	0.749

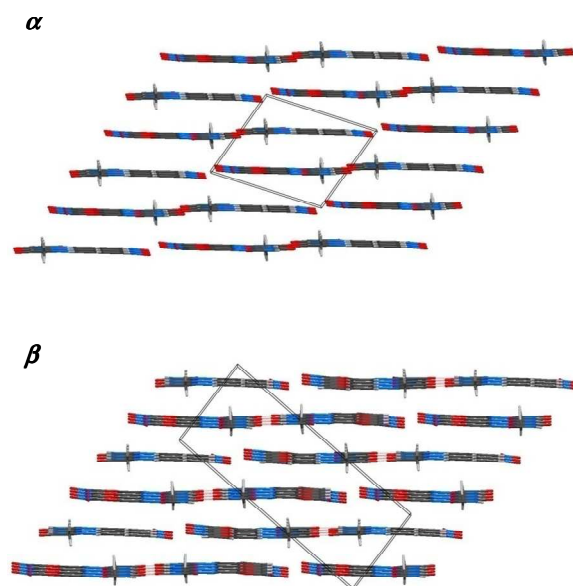


**Figure 3.10** Interlayer packing in  $\alpha$ - (top) and  $\beta$ -polymorphs (bottom) of nitrofurantoin.

Within the layers, molecules form head-to-head hydrogen bonded dimers in the  $\alpha$ -form and head-to-tail catemers in the  $\beta$ -form (Figure 3.11). The dimers and catemers are further linked by C–H $\cdots$ O interactions to form two-dimensional networks. We mentioned in the previous section that IR spectra suggest that  $\alpha$ -polymorph exhibits stronger N–H $\cdots$ O hydrogen bonds than the  $\beta$ -polymorph. In this context, it is interesting to look at the geometrical parameters of the N–H $\cdots$ O hydrogen bonds. One of the quick indicators of the hydrogen bond strengths is the distance between the donor and acceptor atoms (in this case, N and O atoms). Consideration of the N $\cdots$ O distances alone ( $\alpha$ : 2.84 Å;  $\beta$ : 2.80 Å)<sup>73</sup> would lead us to the erroneous conclusion that hydrogen bonds are stronger in the  $\beta$ -form.

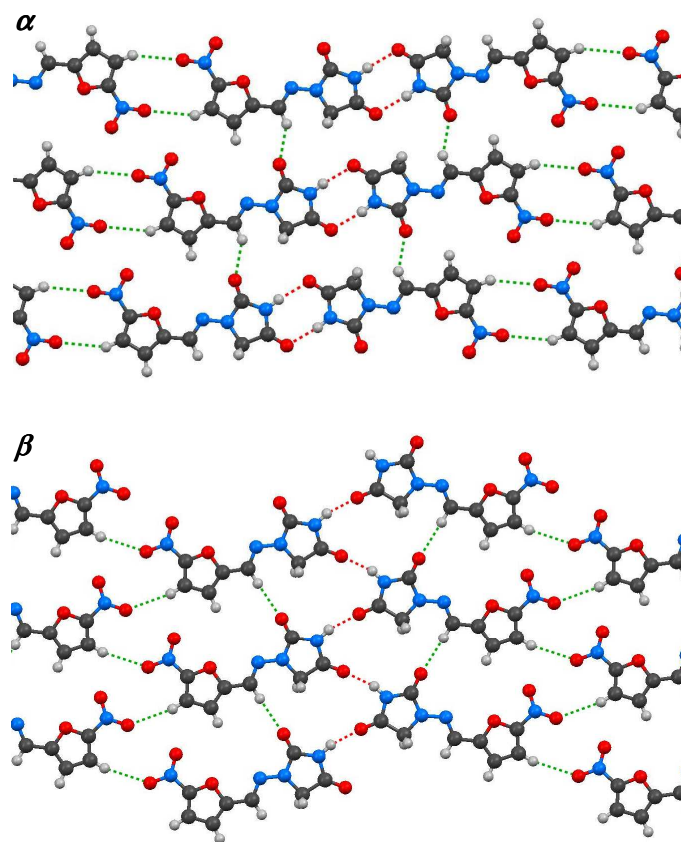


**Figure 3.11** Dimeric and catemeric arrangement of N–H...O hydrogen bonds within the layers in the crystal structures of  $\alpha$ - (top) and  $\beta$ -polymorphs (bottom) of nitrofurantoin.

In our X-ray studies, we have located the H-atoms of the imide groups from the difference Fourier maps and refined them without constraints. In the  $\beta$ -form, the imide N–H bond is bent towards the O-atom to try to form a linear hydrogen bond ( $\theta_{\text{N–H...O}}$ :  $162^\circ$ ). This bending of N–H bond leads to a strained geometry at the imide N-atom. Formation of fully linear hydrogen bond ( $\theta_{\text{N–H...O}}$ :  $180^\circ$ ) will require a much greater strain at the N-atom. For this reason, the N–H...O hydrogen bond is weaker in the  $\beta$ -form. In the  $\alpha$ -polymorph no such strain is required to form a linear hydrogen bond. One other factor, the angle at the acceptor,<sup>74</sup> also contributes to the weakening of hydrogen bond in the  $\beta$ -polymorph. Only in the  $\alpha$ -polymorph are the hydrogen bonds formed along the direction of acceptor lone pairs (the C=O...H angles in the  $\alpha$ - and  $\beta$ -polymorphs are  $118^\circ$  and  $176^\circ$ ). In summary, the stable  $\alpha$ -polymorph of nitrofurantoin forms stronger hydrogen bonds with geometries closer to the ideal values. The  $\beta$ -polymorph, in attempting to attain these ideal supramolecular geometries, imparts molecular strain in itself and becomes less stable.<sup>75</sup>

### 3.23 POWDER X-RAY DIFFRACTION ANALYSIS

We collected the X-ray diffraction data on powder (polycrystalline) samples on a Bruker D8 FOCUS diffractometer using Cu-K $\alpha$ -radiation ( $\lambda = 1.54056 \text{ \AA}$ ) equipped with a vertical goniometer and a one-dimensional scintillation counter as the detector. The X-rays are generated at power settings of 40 kV and 40 mA. For X-ray data collection Bragg-Brentano geometry is applied. Before PXRD analysis, the crystals obtained from the experiments are gently pulverized with mortar and pestle, transferred into the glass sample holders ( $1.6 \text{ cm} \times 2.0 \text{ cm}$ ) and exposed to X-rays over the  $2\theta$  range  $5\text{--}45^\circ$  in the increments of  $0.04^\circ$  and at a scan rate of  $3^\circ$  per minute. Figure 3.12 shows experimental powder patterns of both nitrofurantoin polymorphs along with the patterns calculated from their single crystal X-ray structures. The experimental PXRD patterns confirm that crystals grown in the fluoruous vials belong to the  $\alpha$ -polymorph while crystals grown in the hydroxylated vials represent the  $\beta$ -polymorph. Generally, PXRD method is the most common and unequivocal tool to identify the solid state phases. In the case of anhydrous polymorphs of nitrofurantoin, the powder diffraction patterns are very similar. The most intense peaks for both polymorphs occur at almost the same  $2\theta$  value,  $28.6^\circ$  and  $28.8^\circ$  for  $\alpha$ - and  $\beta$ -polymorphs respectively. As expected, these most intense peaks correspond to the planes (021) and (20-4) containing closely packed layers of nitrofurantoin molecules.

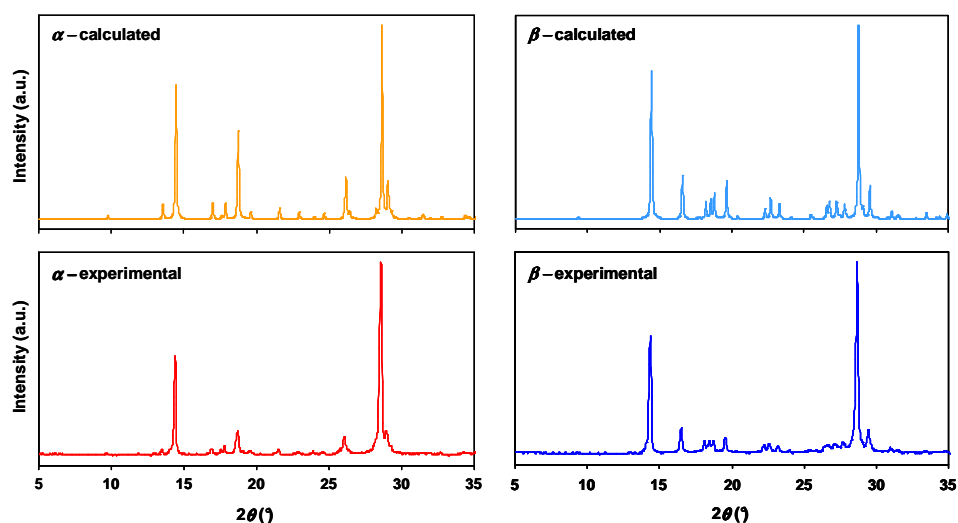


**Figure 3.12** Calculated (top) and experimental (bottom) PXRD patterns of  $\alpha$ - (left) and  $\beta$ -polymorphs (right) of nitrofurantoin.

### 3.24 THERMAL ANALYSIS

We collected the DSC data with a DSC-2920 (TA Instruments) calorimeter in hermetically sealed and crimped aluminum pans. Samples are heated in the range of 25-350°C at different heating rates of 5, 10, 15, 20, 25 and 30 °C per minute. The DSC traces of  $\alpha$ - and  $\beta$ -polymorphs are shown in Figure 3.13. Both polymorphs show similar behavior, a small endotherm corresponding to their melting followed by a large exotherm associated with their decomposition. The decomposition of the drug upon heating is also confirmed by independent TGA experiments. It is known that, upon heating nitrofurantoin decomposes into gases such carbon monoxide, carbon dioxide and nitrogen oxides. In addition, this drug decomposes if contacted with metals such as aluminum. In our experiments, we noted that the  $\alpha$ -polymorph undergoes decomposition faster than the  $\beta$ -polymorph when heated in aluminum pans. Under slow heating conditions, the decomposition exotherm overshadows the melting endotherms (Figure 3.13). The melting and decomposition traces get separated and shift to higher temperatures at higher rate of heating. With the lowest rate of heating, 5 °C per minute, the melting endotherms are not easily detected, especially in case of  $\alpha$ -polymorph.

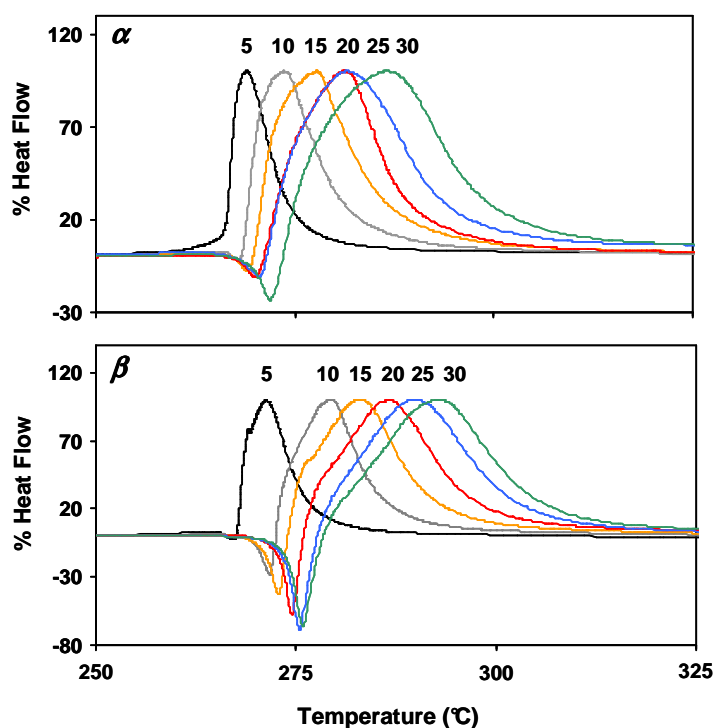


**Figure 3.13** DSC Thermograms of  $\alpha$ - (top) and  $\beta$ -polymorphs (bottom) of nitrofurantoin showing melting endotherms followed by exotherms corresponding to decomposition. The thermograms are collected at different rates of heating (5-30 °C per minute).



### 3.26 EFFECT OF INITIAL CONCENTRATION

All the work presented until Section 3.24 is based on 21 mM acetonitrile solutions that are evaporated at a rate of 0.45 mL per day. The choices of solvent, initial concentration and rate of evaporation came from several initial experiments that led us to find ideal conditions for exploiting the xenophobic nature of fluoruous surfaces. In this section, we present the effect of initial concentration on the outcome of crystallization. We kept the size of the vial (1 dram), initial volume (1.8 mL), solvent (acetonitrile), and rate of evaporation (0.45 mL/day) constant in these experiments. We began with 2 mM solutions and gradually increased the concentrations up to 40 mM and documented the results (Figure 3.15). As above, we repeated the experiments five times and within each experiment we tested five fluoruous and five hydroxylated vials. The data presented in Figure 3.15 is based on all these experiments.

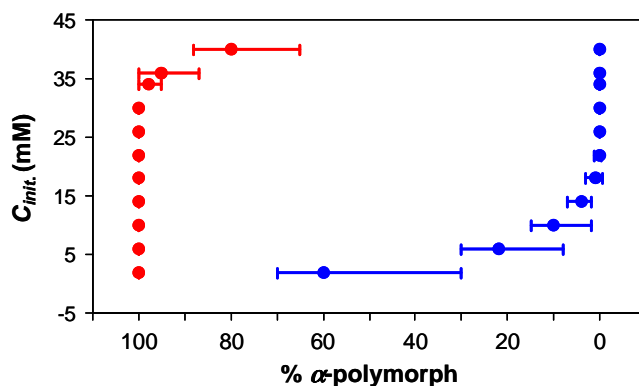


**Figure 3.15** Relative amount of  $\alpha$ -polymorph in fluoruous (red) and hydroxylated (blue) vials as a function of initial concentration. Note the exclusive growth of  $\alpha$ -polymorph in fluoruous vials when the initial concentration is less than 30 mM. Note also the exclusive growth of  $\beta$ -polymorph in hydroxylated vials when the initial concentration is greater than 20 mM.

At concentrations below 30 mM,  $\alpha$ -polymorph consistently and selectively crystallized in fluoruous vials. At higher concentrations, partial crystallization of  $\beta$ -polymorph is seen in these vials; higher the concentration, greater is the mole fraction of the  $\beta$ -polymorph. In hydroxylated vials, solutions with initial concentrations greater than 20 mM gave the crystals of  $\beta$ -polymorph exclusively. Solutions with lower concentrations (2 to 16 mM) gave a mixture of  $\alpha$ - and  $\beta$ -polymorphs; typically crystals of  $\alpha$ -polymorph are always seen at the bottom of the vials. Higher the dilution, greater is the mole fraction of the  $\alpha$ -polymorph. It is important to distinguish the results in the two types of vials. Fluoruous vials can yield the crystals of stable polymorph under conditions that normally favor the growth of metastable polymorph, but the reverse is not true for hydroxylated vials. The exclusive growth of metastable polymorph in hydroxylated vials occurs only when other conditions (higher initial concentrations or faster rates of evaporation) allow it. For the

results reported in this and the previous section, we separated the crystals of two polymorphs into lots by visual inspection, quantified the lots by gravimetry, and characterized them by IR spectroscopy.

### 3.27 REMNANT CONCENTRATION

One of the best clues about the processes that happen inside the fluorous vials is given by the darkening of solution color as a function of evaporation. From the inspection of several experiments, we noted that solutions in fluorous vials turned increasingly more intense in color than the ones in hydroxylated vials (Figure 3.7). To assess these changes in a more quantitative manner, we set up a triplicate of experiments with 21 mM acetonitrile solutions that evaporated at a rate of 0.45 mL per day. In each experiment, we used 20 fluorous and 20 hydroxylated vials, each with 1.8 mL of the solution. As the evaporation continued we tested the remnant concentration of the solution, every four hours, in both types of vials. We measured the remnant concentration in every experiment by gravimetry (by taking 0.1 mL of solution, evaporating it on a cover slip, and weighing) and one experiment by UV-Vis spectroscopy (by taking 0.1 mL of solution and subjecting it to serial dilutions and plotting the  $\lambda_{\max}$  against a calibration trace).

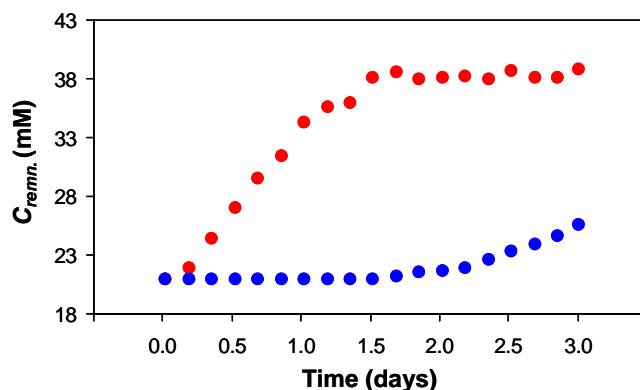


**Figure 3.16** Remnant concentrations of the solutions in fluorous (red) and hydroxylated (blue) vials as a function of evaporation time. Notice the steep increase in the remnant concentration in fluorous vials for one and half days. Each point in the plot represents a mean value from three experiments. The data had a minimum error of 4% and a maximum error of 21%.

The results from these triplicate experiments (Figure 3.16) show that concentration of the remaining solutions increase steeply in fluorous vials until about 36 hours and stay constant for 36 more hours. We found it difficult to measure the remnant concentration after this point because the solution is highly supersaturated and leads to immediate precipitation when touched with a micropipette or a needle. In contrast, the concentrations of the solutions in hydroxylated vials remained constant and increased

only slightly after about 40 hours of evaporation. These results suggest, as can be visually observed, that crystallization of metastable polymorph on the walls of hydroxylated vials keeps the remnant concentration of the solution constant. In the fluorous vials, decreased volumes and lack of crystallization increase the remnant concentration. The flattening of concentration in fluorous vials after certain time indicates the homogeneous nucleation in solution and crystallization of the stable polymorphs.

### 3.28 POLYMORPH SELECTION BY OSTWALD RIPENING

We tested two contrasting surfaces, one highly hydrophilic and the other xenophobic, for the crystal growth of nitrofurantoin. Some salient facts of our experiments are: (a) crystals of  $\beta$ -polymorph appear on the walls of hydroxylated vials within few hours, (b) these crystals are formed at the evaporating solvent front and continue to grow on the vial walls until the completion of evaporation, (c) no crystals are formed on the walls of fluorous vials even at faster rates of evaporation and higher initial concentrations, (d) fluorous vials yield only the  $\alpha$ -polymorph (under most conditions) and hydroxylated vials give the  $\beta$ -polymorph, (e) only in fluorous vials the remnant concentration continues to increase for a significant time after the beginning of crystallization, (f) the number of crystals formed in hydroxylated vials far exceeds the number of crystals in fluorous vials, and (g) crystals of the stable polymorph formed in fluorous vials are significantly larger than the crystals of metastable polymorph grown in hydroxylated vials.

These results can be best understood by two interrelated processes well-known in physical organic chemistry, Ostwald rule of stages and Ostwald ripening. Ostwald rule of stages states that “in all processes, it is not the most stable state with the lowest amount of free energy that is initially formed but the least stable state lying nearest in the free energy to the original state”. According to this rule, the nuclei of the kinetic form, the  $\beta$ -polymorph, nucleate first because their free energy is lying closer to the free energy of solute molecules in the saturated solution. Another way expressing this idea is that the  $\beta$ -polymorph has a smaller nucleation barrier than the  $\alpha$ -polymorph (Figure 3.17) and hence it can nucleate first.

Nucleation, described in Chapter 2, is a critical step in the crystallization of different polymorphs. Each polymorph has its own characteristic nucleation barrier,  $\Delta G^*$  and critical size of the cluster,  $r^*$  that is stable enough to grow into a crystal. Molecules in supersaturated solutions aggregate to form nuclei of different polymorphs. Various nuclei compete for molecules dissolved in solution and kinetic nuclei tend to adsorb most molecules at the beginning. Kinetic nuclei are usually higher in number at the onset of crystallization because of their lower nucleation barrier. Kinetic nuclei are formed faster in the solution but they also have greater solubility (than nuclei of thermodynamic polymorphs) and tend to dissolve more readily. If these kinetic nuclei can stick to some surface to lower their surface energy, they can survive in the solution and grow further into crystals. This is the process that is observed when crystallization is performed in the hydroxylated vials. In other words, crystal growth of kinetic polymorph is promoted by heterogeneous nucleation on the hydroxylated surfaces.

In case of fluorous vials, the xenophobic nature of the vial surfaces does not allow the adsorption of kinetic nuclei on to the vial walls and forces these nuclei to dissolve back into solution. We call this process the suppression of nucleation at fluorous interfaces. With time, increased supersaturation lowers the nucleation barrier of the thermodynamic form, the  $\alpha$ -polymorph, and promotes the formation of nuclei of this stable polymorph. Given that thermodynamic nuclei have lower solubility than the kinetic nuclei, crystals of  $\alpha$ -polymorph tend to grow while those of  $\beta$ -polymorph dissolve back into solution. This process, the growth of a thermodynamic polymorph at the expense of a kinetic polymorph, is called Ostwald ripening.

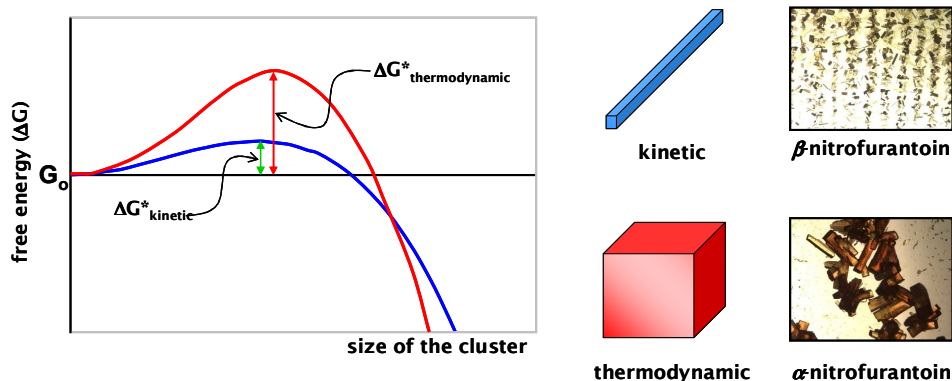


**Figure 3.17** Free energy diagram for a dimorphic system showing the nucleation barriers for kinetic (blue) and thermodynamic (red) polymorphs. Note that  $\Delta G^*$  and  $r^*$  of kinetic polymorph are smaller than  $\Delta G^*$  and  $r^*$  of thermodynamic polymorph.

### 3.29 SUMMARY AND CONCLUSION

We developed a new and generic method to promote the growth of the stable polymorphs by suppressing the nucleation of metastable polymorph at xenophobic interfaces. While previous methods use *promotion* of heterogeneous nucleation as a means to drive crystal growth on the surfaces, our method uses *inhibition* of heterogeneous nucleation to selectively grow crystals away from the surfaces. Unlike the previous approaches, our method does not require prior knowledge of the crystal structures of polymorphs and as such it should be applicable to many pharmaceutical and other types of compounds that exhibit polymorphism. We have shown that crystallization in fluorous vessels can be an effective tool to distinguish between polymorphs that have similar densities, packing fractions and lattice energies. Further work, not presented here, has shown that same results can be obtained with the trigonal and *P*-monoclinic polymorphs of carbamazepine. Fluorous surfaces are *not omniphobic*; they are *xenophobic*. In this context, it will be interesting to test the crystallization of compounds that contain fluorous moieties. Indeed, up to 20% of pharmaceuticals now contain fluorine atoms and a good portion of them contain fluorous fragments. In the next chapter we will discuss the reverse inhibition in the growth of a polymorphic drug that exhibits fluorous crystal faces.

**3.30 REFERENCES**

1. Bernstein, J., *Polymorphism in Molecular Crystals*. Clarendon Press: Oxford, **2002**.
2. Brittain, H. G., *Polymorphism in Pharmaceutical Solids*. Marcel Dekker: New York, **1999**.
3. Byrn, S. R.; Pfeiffer, R. R.; Stowell, J. G., *Solid-State Chemistry of Drugs*. 2nd ed.; SSCI: West Lafayette, **1999**.
4. Hilfiker, R., *Polymorphism in the Pharmaceutical Industry*. Wiley-VCH: Weinheim, **2006**.
5. Chemburkar, S. R.; Bauer, J.; Deming, K.; Spiwek, H.; Patel, K.; Morris, J.; Henry, R.; Spanton, S.; Dziki, W.; Porter, W.; Quick, J.; Bauer, P.; Donaubauber, J.; Narayanan, B. A.; Soldani, M.; Riley, D.; McFarland, K., Dealing with the Impact of Ritonavir Polymorphs on the Late Stages of Bulk Drug Process Development. *Org. Proc. Res. Dev.* **2000**, *4*, 413-417.
6. Rodriguez-Spong, B.; Price, C. P.; Jayasankar, A.; Matzger, A. J.; Rodriguez-Hornedo, N., General principles of pharmaceutical solid polymorphism. A supramolecular perspective. *Adv. Drug Delivery Rev.* **2004**, *56*, 241-274.
7. Desiraju, G. R., *Crystal Engineering: The Design of Organic Solids*. Elsevier: Amsterdam, **1989**.
8. Allesoe, M.; Van Den Berg, F.; Cornett, C.; Joergensen, F. S.; Halling-Soerensen, B.; De Diego, H. L.; Hovgaard, L.; Aaltonen, J.; Rantanen, J., Solvent diversity in polymorph screening. *J. Pharm. Sci.* **2008**, *97*, 2145-2159.
9. Morissette, S. L.; Almarsson, O.; Peterson, M. L.; Remenar, J. F.; Read, M. J.; Lemmo, A. V.; Ellis, S.; Cima, M. J.; Gardner, C. R., High-throughput crystallization: polymorphs, salts, co-crystals and solvates of pharmaceutical solids. *Adv. Drug Delivery Rev.* **2004**, *56*, 275-300.
10. Peterson, M. L.; Morissette, S. L.; McNulty, C.; Goldsweig, A.; Shaw, P.; LeQuesne, M.; Monagle, J.; Encina, N.; Marchionna, J.; Johnson, A.; Gonzalez-Zugasti, J.; Lemmo, A. V.; Ellis, S. J.; Cima, M. J.; Almarsson, O., Iterative High-Throughput Polymorphism Studies on Acetaminophen and an Experimentally Derived Structure for Form III. *J. Am. Chem. Soc.* **2002**, *124*, 10958-10959.
11. Lowenstam, H. A.; Weiner, S., *On Biomineralization*. Oxford University Press: New York, **1989**.
12. Mann, S., *Biomineralization*. Oxford University Press: New York, **2002**.
13. Lahav, M.; Leiserowitz, L., Tailor-made auxiliaries for the control of nucleation, growth and dissolution of two- and three-dimensional crystals. *J. Phys. D* **1993**, *26*, B22-B31.
14. Davey, R. J.; Blagden, N.; Potts, G. D.; Docherty, R., Polymorphism in Molecular Crystals: Stabilization of a Metastable Form by Conformational Mimicry. *J. Am. Chem. Soc.* **1997**, *119*, 1767-1772.
15. He, X.; Stowell, J. G.; Morris, K. R.; Pfeiffer, R. R.; Li, H.; Stahly, G. P.; Byrn, S. R., Stabilization of a Metastable Polymorph of 4-Methyl-2-nitroacetanilide by Isomorphic Additives. *Cryst. Growth Des.* **2001**, *1*, 305-312.
16. Kwon, O. P.; Kwon, S.-J.; Jazbinsek, M.; Choubey, A.; Losio, P. A.; Gramlich, V.; Guenter, P., Morphology and Polymorphism Control of Organic Polyene Crystals by Tailor-made Auxiliaries. *Cryst. Growth Des.* **2006**, *6*, 2327-2332.

17. Lancaster, R. W.; Karamertzanis, P. G.; Hulme, A. T.; Tocher, D. A.; Lewis, T. C.; Price, S. L., The polymorphism of progesterone: stabilization of a 'disappearing' polymorph by co-crystallization. *J. Pharm. Sci.* **2007**, *96*, 3419-3431.
18. Mullin, J. W., *Crystallization*. 4th ed.; Butterworth-Heinemann: New York, **2001**.
19. Kuzmenko, I.; Rapaport, H.; Kjaer, K.; Als-Nielsen, J.; Weissbuch, I.; Lahav, M.; Leiserowitz, L., Design and Characterization of Crystalline Thin Film Architectures at the Air-Liquid Interface: Simplicity to Complexity. *Chem. Rev.* **2001**, *101*, 1659-1696.
20. Frostman, L. M.; Ward, M. D., Nucleation of Molecular Crystals beneath Guanidinium Alkanesulfonate Monolayers. *Langmuir* **1997**, *13*, 330-337.
21. Briseno, A. L.; Mannsfeld, S. C. B.; Ling, M. M.; Liu, S.; Tseng, R. J.; Reese, C.; Roberts, M. E.; Yang, Y.; Wudl, F.; Bao, Z., Patterning organic single-crystal transistor arrays. *Nature* **2006**, *444*, 913-917.
22. Carter, P. W.; Ward, M. D., Directing Polymorph Selectivity During Nucleation of Anthranilic Acid on Molecular Substrates. *J. Am. Chem. Soc.* **1994**, *116*, 769-770.
23. Toworfe, G. K.; Composto, R. J.; Shapiro, I. M.; Ducheyne, P., Nucleation and growth of calcium phosphate on amine-, carboxyl- and hydroxyl-silane self-assembled monolayers. *Biomater.* **2005**, *27*, 631-642.
24. Ulman, A., Formation and Structure of Self-Assembled Monolayers. *Chem. Rev.* **1996**, *96*, 1533-1554.
25. Love, J. C.; Estroff, L. A.; Kriebel, J. K.; Nuzzo, R. G.; Whitesides, G. M., Self-Assembled Monolayers of Thiolates on Metals as a Form of Nanotechnology. *Chem. Rev.* **2005**, *105*, 1103-1169.
26. Aizenberg, J.; Black, A. J.; Whitesides, G. M., Control of crystal nucleation by patterned self-assembled monolayers. *Nature* **1999**, *398*, 495-498.
27. Banno, N.; Nakanishi, T.; Matsunaga, M.; Asahi, T.; Osaka, T., Enantioselective crystal growth of leucine on a self-assembled monolayer with covalently attached leucine molecules. *Journal of the American Chemical Society* **2004**, *126*, 428-429.
28. Meldrum, F. C.; Flath, J.; Knoll, W., Chemical Deposition of PbS on Self-Assembled Monolayers of 16-Mercaptohexadecanoic Acid. *Langmuir* **1997**, *13*, 2033-2049.
29. Cox, J. R.; Dabros, M.; Shaffer, J. A.; Thalladi, V. R., Selective crystal growth of the anhydrous and monohydrate forms of theophylline on self-assembled monolayers. *Angewandte Chemie, International Edition* **2007**, *46*, 1988-1991.
30. Frostman, L. M.; Bader, M. M.; Ward, M. D., Nucleation and Growth of Molecular Crystals on Self-Assembled Monolayers. *Langmuir* **1994**, *10*, 576-582.
31. Hiremath, R.; Basile, J. A.; Varney, S. W.; Swift, J. A., Controlling Molecular Crystal Polymorphism with Self-Assembled Monolayer Templates. *Journal of the American Chemical Society* **2005**, *127*, 18321-18327.
32. Hiremath, R.; Varney, S. W.; Swift, J. A., Selective growth of a less stable polymorph of 2-iodo-4-nitroaniline on a self-assembled monolayer template. *Chem. Commun.* **2004**, 2676-2677.
33. Lee, A. Y.; Ulman, A.; Myerson, A. S., Crystallization of Amino Acids on Self-Assembled Monolayers of Rigid Thiols on Gold. *Langmuir* **2002**, *18*, 5886-5898.
34. Mitchell, C. A.; Yu, L.; Ward, M. D., Selective Nucleation and Discovery of Organic Polymorphs through Epitaxy with Single Crystal Substrates. *J. Am. Chem. Soc.* **2001**, *123*, 10830-10839.

35. Hillier, A. C.; Ward, M. D., Epitaxial interactions between molecular overlayers and ordered substrates. *Phys. Rev. B* **1996**, *54*, 14037-14051.
36. Bonafede, S. J.; Ward, M. D., Selective Nucleation and Growth of an Organic Polymorph by Ledge-Directed Epitaxy on a Molecular Crystal Substrate. *J. Am. Chem. Soc.* **1995**, *117*, 7853-7861.
37. Cashell, C.; Corcoran, D.; Hodnett, B. K., Secondary nucleation of the  $\beta$ -polymorph of L-glutamic acid on the surface of  $\alpha$ -form crystals. *Chem. Commun.* **2003**, 374-375.
38. Yu, L., Nucleation of One Polymorph by Another. *J. Am. Chem. Soc.* **2003**, *125*, 6380-6381.
39. Yu, L., Survival of the fittest polymorph: how fast nucleator can lose to fast grower. *CrystEngComm* **2007**, *9*, 847-851.
40. Carter, P. W.; Ward, M. D., Topographically directed nucleation of organic crystals on molecular single-crystal substrates. *J. Am. Chem. Soc.* **1993**, *115*, 11521-11535.
41. Lang, M.; Grzesiak, A. L.; Matzger, A. J., The Use of Polymer Heteronuclei for Crystalline Polymorph Selection. *J. Am. Chem. Soc.* **2002**, *124*, 14834-14835.
42. Liberski, A. R.; Tizzard, G. J.; Diaz-Mochon, J. J.; Hursthouse, M. B.; Milnes, P.; Bradley, M., Screening for Polymorphs on Polymer Microarrays. *J. Comb. Chem.* **2008**, *10*, 24-27.
43. Price, C. P.; Grzesiak, A. L.; Matzger, A. J., Crystalline polymorph selection and discovery with polymer heteronuclei. *J. Am. Chem. Soc.* **2005**, *127*, 5512-5517.
44. Chyall, L. J.; Tower, J. M.; Coates, D. A.; Houston, T. L.; Childs, S. L., Polymorph Generation in Capillary Spaces: The Preparation and Structural Analysis of a Metastable Polymorph of Nabumetone. *Cryst. Growth Des.* **2002**, *2*, 505-510.
45. Childs, S. L.; Chyall, L. J.; Dunlap, J. T.; Coates, D. A.; Stahly, B. C.; Stahly, G. P., A Metastable Polymorph of Metformin Hydrochloride: Isolation and Characterization Using Capillary Crystallization and Thermal Microscopy Techniques. *Cryst. Growth Des.* **2004**, *4*, 441-449.
46. Ha, J.-M.; Wolf, J. H.; Hillmyer, M. A.; Ward, M. D., Polymorph Selectivity under Nanoscopic Confinement. *J. Am. Chem. Soc.* **2004**, *126*, 3382-3383.
47. Hamilton, B. D.; Hillmyer, M. A.; Ward, M. D., Glycine Polymorphism in Nanoscale Crystallization Chambers. *Cryst. Growth Des.* **2008**, *8*, 3368-3375.
48. Zaccaro, J.; Matic, J.; Myerson, A. S.; Garetz, B. A., Nonphotochemical, laser-induced nucleation of supersaturated aqueous glycine produces unexpected g-polymorph. *Cryst. Growth Des.* **2001**, *1*, 5-8.
49. Erdemir, D.; Chattopadhyay, S.; Guo, L.; Ilavsky, J.; Amenitsch, H.; Segre, C. U.; Myerson, A. S., Relationship between Self-Association of Glycine Molecules in Supersaturated Solutions and Solid State Outcome. *Phys. Rev. Lett.* **2007**, *99*, 115702.
50. Lyczko, N.; Espitalier, F.; Louisnard, O.; Schwartzentruber, J., Effect of ultrasound on the induction time and the metastable zone widths of potassium sulphate. *Chem. Engg. J.* **2002**, *86*, 233-241.
51. Childs, S. L.; Mougín, P.; Stahly, B. C. Screening for solid pharmaceutical forms by ultrasound crystallization and cocrystallization using ultrasound. 2005089375, **2005**.
52. Kurotani, M.; Hirasawa, I., Polymorph control of sulfamerazine by ultrasonic irradiation. *J. Cryst. Growth* **2008**, *310*, 4576-4580.
53. Louhi-Kultanen, M.; Karjalainen, M.; Rantanen, J.; Huhtanen, M.; Kallas, J., Crystallization of glycine with ultrasound. *Int. J. Pharm.* **2006**, *320*, 23-29.

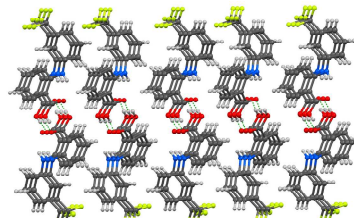
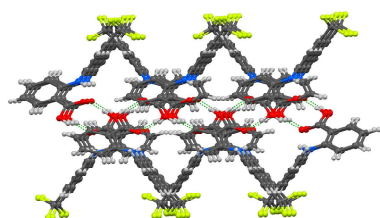
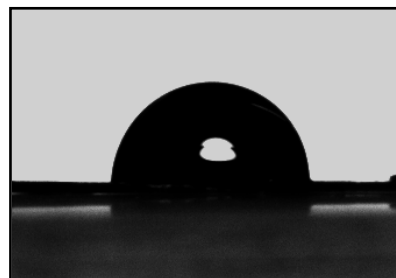
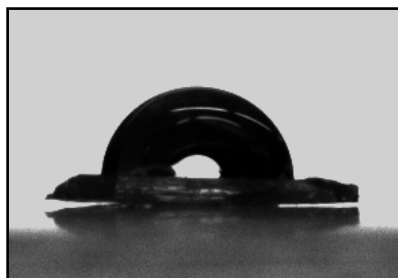
54. Capes, J. S.; Cameron, R. E., Contact line crystallization to obtain metastable polymorphs. *Cryst. Growth Des.* **2007**, *7*, 108-112.
55. Capes, J. S.; Cameron, R. E., Effect of polymer addition on the contact line crystallization of paracetamol. *CrystEngComm* **2007**, *9*, 84-90.
56. Dawson, A.; Allan, D. R.; Belmonte, S. A.; Clark, S. J.; David, W. I. F.; McGregor, P. A.; Parsons, S.; Pulham, C. R.; Sawyer, L., Effect of High Pressure on the Crystal Structures of Polymorphs of Glycine. *Cryst. Growth Des.* **2005**, *5*, 1415-1427.
57. Fabbiani, F. P. A.; Allan, D. R.; David, W. I. F.; Davidson, A. J.; Lennie, A. R.; Parsons, S.; Pulham, C. R.; Warren, J. E., High-Pressure Studies of Pharmaceuticals: An Exploration of the Behavior of Piracetam. *Cryst. Growth Des.* **2007**, *7*, 1115-1124.
58. Fabbiani, F. P. A.; Allan, D. R.; David, W. I. F.; Moggach, S. A.; Parsons, S.; Pulham, C. R., High-pressure recrystallisation - a route to new polymorphs and solvates. *CrystEngComm* **2004**, *6*, 504-511.
59. Fabbiani, F. P. A.; Allan, D. R.; Parsons, S.; Pulham, C. R., An exploration of the polymorphism of piracetam using high pressure. *CrystEngComm* **2005**, *7*, 179-186.
60. Fabbiani, F. P. A.; Pulham, C. R., High-pressure studies of pharmaceutical compounds and energetic materials. *Chem. Soc. Rev.* **2006**, *35*, 932-942.
61. Dunitz, J. D.; Bernstein, J., Disappearing Polymorphs. *Acc. Chem. Res.* **1995**, *28*, 193-200.
62. Horvath, I. T.; Rabai, J., Facile catalyst separation without water: fluorous biphasic hydroformylation of olefins. *Science* **1994**, *266*, 72-75.
63. Gladysz, J. A.; Curran, D. P.; Horvath, I. T., *Handbook of Fluorous Chemistry*. Wiley-VCH: Weinheim, **2004**.
64. Wasserman, S. R.; Tao, Y. T.; Whitesides, G. M., Structure and reactivity of alkylsiloxane monolayers formed by reaction of alkyltrichlorosilanes on silicon substrates. *Langmuir* **1989**, *5*, 1074-1087.
65. Kulinich, S. A.; Farzaneh, M., Hydrophobic properties of surfaces coated with fluoroalkylsiloxane and alkylsiloxane monolayers. *Surf. Science* **2004**, *573*, 379-390.
66. Cox, J. R.; Ferris, L. A.; Thalladi, V. R., Selective growth of a stable drug polymorph by suppressing the nucleation of corresponding metastable polymorphs. *Angew. Chem. Int. Ed.* **2007**, *46*, 4333-4336.
67. Pienaar, E. W.; Caira, M. R.; Lotter, A. P., Polymorphs of nitrofurantoin. 2. Preparation and x-ray crystal structures of two anhydrous forms of nitrofurantoin. *J. Crystallogr. Spectrosc. Res.* **1993**, *23*, 785-790.
68. Nitrofurantoin can also be crystallized as two different monohydrates and at least two solvates of this drug are known. See: Pienaar, E. W.; Caira, M. R.; Lotter, A. P., Polymorphs of nitrofurantoin. I. Preparation and x-ray crystal structures of two monohydrated forms of nitrofurantoin. *J. Crystallogr. Spectrosc. Res.* **1993**, *23*, 739-744.
69. Caira, M. R.; Pienaar, E. W.; Loetter, A. P., Polymorphism and pseudopolymorphism of the antibacterial nitrofurantoin. *Mol. Cryst. Liq. Cryst. Sci. Technol., Sect. A* **1996**, *279*, 241-264.
70. We collected the IR spectra at room temperature. To be consistent, we give the distances and angles from the room temperature crystal structures reported by others, and not from the low temperature data collected by us (Section 3.22). Though the

absolute values of distances and angles change slightly between room and low temperature datasets, the trends remain the same.

71. The data were measured using  $\varphi$  and  $\omega$  scans of  $0.5^\circ$  per frame; each frame was exposed to X-rays for 10-20 seconds depending on the scattering power of the crystal. Unit cell parameters were determined using three mutually perpendicular  $\varphi$  scans with 12 frames per scan. Using the orientation matrix obtained from the unit cell, a hemisphere was searched with the program COSMO to determine the number of runs and frames needed for  $0.75 \text{ \AA}$  resolution, 100 % completeness, and at least two fold redundancy when the crystal system is set to triclinic. Cell parameters were refined over all the equivalent reflections in the hemisphere during the data integration. Data integration was performed using the program SAINT and absorption corrections were applied using SADABS multiscan technique. The structures were solved by the direct methods and refined by the least squares methods on  $F^2$  using the program SHELXL-97 incorporated in SHELXTL-PC. Typically, all the non-H-atoms were refined anisotropically and all H-atoms other than those attached to N or O atoms were calculated by geometrical methods and refined using a riding model. Structural analysis was performed by a combination of programs that include XP, XSHELL, Platon, and Mercury. Structural diagrams shown in this thesis were prepared using the program Mercury.
72. Spek, A. L., Single-crystal structure validation with the program PLATON. *J. Appl. Crystallogr.* **2003**, *36*, 7-13.
73. Values in this section are taken from our low temperature structures. For room temperature data see Section 3.21.
74. Murray-Rust, P.; Glusker, J. P., Directional hydrogen bonding to  $sp^2$ - and  $sp^3$ -hybridized oxygen atoms and its relevance to ligand-macromolecule interactions. *J. Am. Chem. Soc.* **1984**, *106*, 1018-1025.
75. Thalladi, V. R.; Nuesse, M.; Boese, R., The Melting Point Alternation in  $\alpha,\omega$ -Alkanedicarboxylic Acids. *J. Am. Chem. Soc.* **2000**, *122*, 9227-9236.

THIS PAGE LEFT INTENTIONALLY BLANK

# 4 FLUOROUS PHARMACEUTICALS – INHIBITION OF NUCLEATION AT HYDROPHILIC SURFACES



THIS PAGE LEFT INTENTIONALLY BLANK

#### 4.1 PHARMACEUTICALS WITH FLUOROUS FRAGMENTS

Fluorinated pharmaceuticals, though unknown until a few decades ago, constitute 20% of the marketed drugs today.<sup>1-3</sup> Much of the interest in fluorinated pharmaceuticals emerges from the small size and high electronegativity of fluorine atom and also the xenophobic nature of fluorous fragments.<sup>4</sup> The van der Waals radius of fluorine (1.47 Å) lies between those of hydrogen (1.2 Å) and oxygen atoms (1.52 Å).<sup>5</sup> For this reason, research in drug discovery often involves replacement of H-atoms or –OH groups by F-atoms. Fluorinated pharmaceuticals, drugs that contain either aromatic F-atoms or fluorous fragments, can enhance the binding between drug and the receptor species through electronic properties, assist the diffusion of the drug across the lipid membranes through lipophilic interactions, and induce conformational or other changes by causing or relieving steric strain.<sup>6</sup>

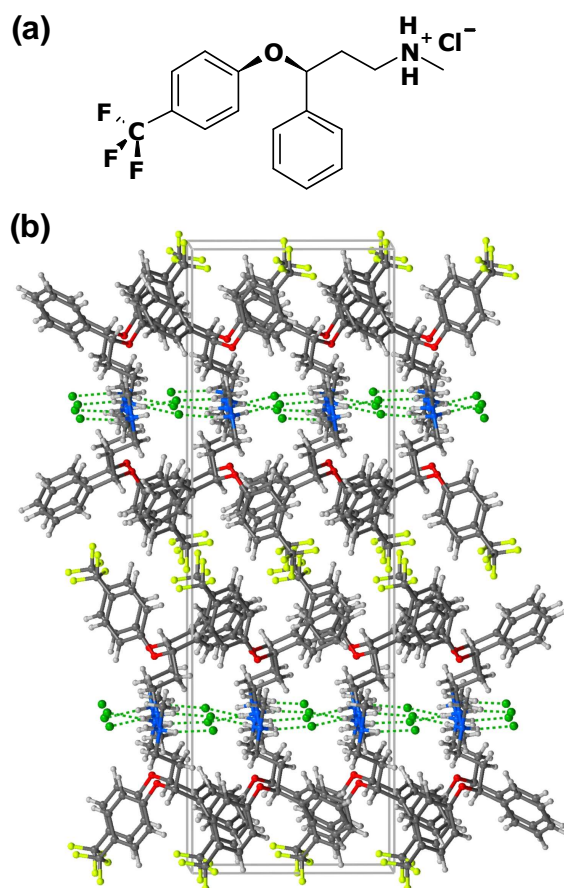


**Figure 4.1** (a) Molecular structure of fluoxetine hydrochloride, a fluorous pharmaceutical marketed as Prozac.<sup>7</sup> (b) Crystal structure of Prozac showing the hydrogen bonded layers that expose fluorous groups at the potential growth faces.<sup>8</sup>

We are interested in those drugs that contain fluororous fragments such as  $-\text{CF}_3$  groups.<sup>9</sup> We expect that in the solid state, these fluororous fragments, due to their xenophobic nature, aggregate into pockets, columns or sheaths that are isolated from hydrogen bonding functional groups. Fluoxetine hydrochloride, the top selling fluorinated drug, serves as a good example (Figure 4.1).<sup>7</sup> Crystal structure of this drug shows distinct lamellar domains of hydrogen bonds, aromatic-aromatic interactions and fluororous-fluororous interactions.<sup>8</sup> We anticipate that many pharmaceuticals with  $-\text{CF}_3$  or other  $-\text{C}_m\text{F}_n$  fragments adopt similar isolated fluororous domains and lend themselves well for the crystal growth studies in hydroxylated and fluororous vials. In such circumstances, drug crystals with xenophobic surfaces are expected to show the *inverse* trend. Stable polymorphs are expected to grow on glass or hydroxylated surfaces and metastable polymorphs on fluororous surfaces. To test this hypothesis, we have selected flufenamic acid, an anti-inflammatory drug,<sup>10</sup> as a model pharmaceutical.<sup>11-13</sup> Flufenamic acid exhibits temperature induced transitions between polymorphs;<sup>14-15</sup> below we discuss the two types of solid state phase transitions that can occur in a given system and their thermodynamic relations.

#### 4.2 ENANTIOTROPIC AND MONOTROPIC PHASE TRANSITIONS

Polymorphs of a compound have different crystal structures and hence different lattice free energies.<sup>16</sup> A higher energy, less stable, polymorph can transform to a lower energy, more stable, polymorph either spontaneously or by external induction such as pressure, temperature or some other factor.<sup>17-19</sup> Transformation of polymorphs at constant pressure is determined by the difference in their free energies ( $\Delta G = \Delta H - T\Delta S$ ). The difference in enthalpy  $\Delta H$  refers to the difference in lattice structure and energy, and the difference in entropy  $\Delta S$  refers to lattice vibrations and disorder. Under specific conditions, a spontaneous transformation involves decrease in free energy ( $\Delta G$  is negative), and a transformation is not spontaneous if there is an increase in free energy ( $\Delta G$  is positive). The thermodynamic conditions and possible directions of the transformations between two polymorphs and liquid for a single component system are shown in Figure 4.2.<sup>20-21</sup>

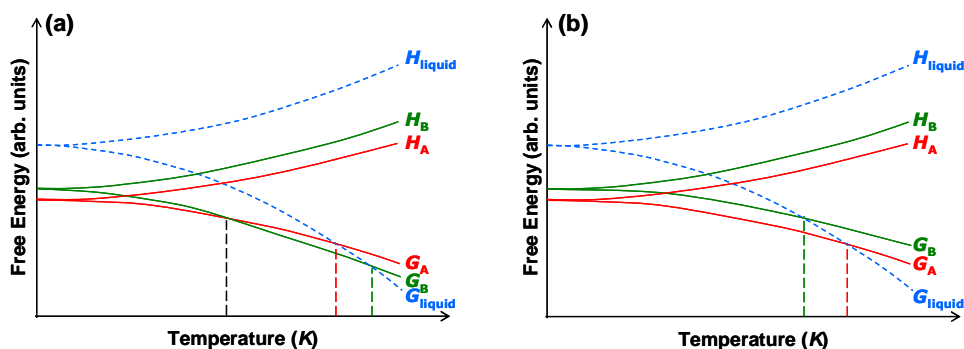


**Figure 4.2** Thermodynamic relationships between polymorphs that are (a) enantiotropic and (b) monotropic. Free energy and enthalpy curves for two polymorphs and liquid are drawn. Note the crossing of free energy curves in the enantiotropic system.

In an enantiotropic system (Figure 4.2a), the two polymorphs can interconvert, as a function of temperature, prior to melting. The temperature at which one form transforms to the other is called the phase transition temperature. Examination of free energy curves indicates that prior to transition temperature, form A is more stable; form B is more stable after the transition point. At the transition temperature, both polymorphs are in equilibrium with each other.

In a monotropic system (Figure 4.2b), one of the two polymorphs is always stable prior to melting. Polymorph B can transform to polymorph A but reverse transition does not take place. This is the difference between enantiotropic and monotropic systems: in the former the phase transition is reversible and in the latter it is irreversible. A closer look at the enthalpy curves in Figure 4.2 is instructive. In a monotropic system, the B→A conversion involves a net reduction in enthalpy; that is the process is exothermic. In an enantiotropic system, an exothermic event refers to B→A transition and an endothermic event indicates A→B transition. Based on the type of transition, exo- or endothermic, we can tell whether a particular polymorph is stable or metastable at a given temperature. The knowledge of polymorphic behavior (monotropic or enantiotropic) of a compound is important in the pharmaceutical industry. Unexpected transformation of one polymorph to another can pose problems in the drug development. Relative thermodynamic stabilities of polymorphs strongly depend on pressure and temperature and phase transitions can be induced by changes in temperature or pressure that often occur in the formulation processes such as tableting, grinding, and drying.

### 4.3 FLUFENAMIC ACID

Flufenamic acid, an analgesic with a fluorine fragment, is multimorphic and up to eight polymorphs (I – VIII) have been reported.<sup>14-15</sup> Five of these polymorphs (IV – VIII) are observed on a hot stage during heating; they are fleeting and their characterization is difficult. The literature contains limited or no physical data on these five forms.<sup>22</sup> Of the remaining three polymorphs, forms I and III can be grown from solutions and form II can be obtained by sublimation or fusion. The thermodynamic relationships between different polymorphs are shown in Figure 4.3. In this work we are primarily interested in polymorphs I and III; they can readily be obtained at room temperature and they are previously characterized by thermal, diffraction and spectroscopic methods. Figure 4.3 shows that forms I and III are enantiotropically related. Below 42 °C, form III is the thermodynamically stable polymorph, and form I is the metastable polymorph. Above 42 °C polymorph I becomes stable and form III metastable. Form II is monotropic with respect to form I, and enantiotropic with respect to form III. Above 104 °C, form II becomes more stable than form III. The relationships between other polymorphs are not fully established; they are plotted in Figure 4.3 to give a complete picture of reported data.

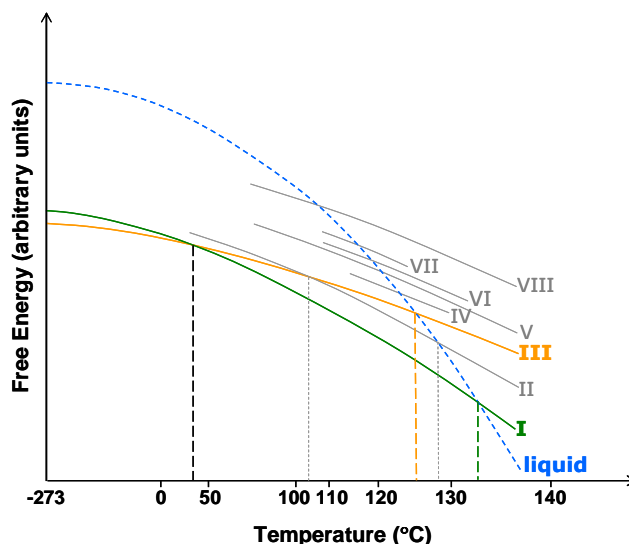


**Figure 4.3** Relative free energies of various polymorphs of flufenamic acid plotted as a function of temperature. Adopted from references 14 and 15.

It is reported that crystallization of flufenamic acid from different solutions yield polymorph **III** from solvents with lower boiling points ( $< 80$  °C), polymorph **I** from solvents with higher boiling points ( $> 130$  °C), and a mixture of both polymorphs from solvents with intermediate boiling points.<sup>23</sup> In these experiments, saturated solutions are made near the boiling points of solvents and crystal growth is induced near those temperatures. This study indicates that the type of polymorph crystallized from a given solvent depends on the temperature of crystal growth; these results are in accordance with the transition temperature between forms **I** and **III**. These results are also relevant to our temperature dependent crystallization studies discussed in Section 4.10. The IR, DSC and X-ray data available for polymorphs **I** and **III** will be useful in this work for comparison and confirmation of results. Additionally, forms **I** and **III** exhibit distinct colors, white and pale-yellow, and morphologies, plates and needles. Most importantly, forms **I** and **III** possess layered crystal structures with sheaths of  $-CF_3$  groups and potentially they can exhibit crystal faces that are fluorophilic and xenophobic. We explored the crystal growth of these two polymorphs in hydroxylated and fluorophilic vials to influence crystal nucleation and to control polymorphism.

#### 4.4 CRYSTAL GROWTH IN HYDROXYLATED AND FLUOROPHILIC VIALS

We prepared the hydrophilic and fluorophilic substrates using the methods described in Chapter 3.<sup>24-26</sup> For each series of crystallization experiments, we prepared 78 mM solution of flufenamic acid in ethanol by stirring the solution at 60°C for 20 minutes. We transferred this freshly prepared solution into ten hydroxylated and ten fluorophilic 1 dram vials until each vial is filled to a third of its height (~1.8 mL). We covered the vials with screw-caps containing holes and allowed ethanol to evaporate slowly. After almost

complete evaporation of solvent (~6 days), crystals of form **I** grew selectively in fluoruous vials while crystals of form **III** grew in hydroxylated vials. In sharp contrast to crystallizations of nitrofurantoin (Chapter 3) or other drugs that did not contain fluoruous groups, crystals of flufenamic acid did not nucleate or grow on the vial walls of either hydroxylated or fluoruous vials (Figure 4.4a). Crystals grown in the fluoruous vials are white with plate-like morphology while needle shaped pale-yellow crystals are grown in hydroxylated vials (Figures 4.4b-c). We repeated these crystallization experiments at least five times and obtained reproducible results.

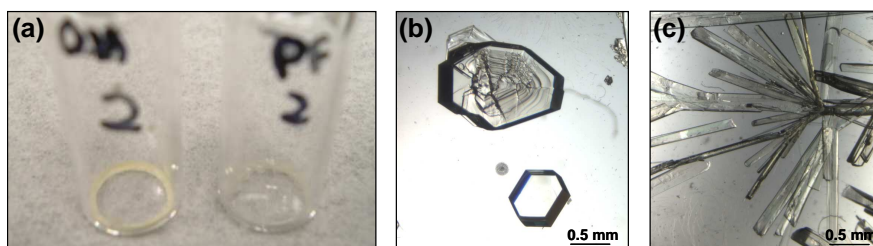


**Figure 4.4** (a) Crystal growth of flufenamic acid from the same bulk solution in hydroxylated (left) and fluoruous (right) vials. Notice the yellow color of the form **III** crystals in the left vial and white color of form **I** crystals in the right vial. Microscopic images of (b) form **I** crystals grown in a fluoruous vial and (c) form **III** crystals grown in a hydroxylated vial.

We characterized the crystalline products by optical microscopy, IR spectroscopy, single crystal and powder X-ray diffraction methods. These methods showed that the white plates formed in fluoruous vials belong to polymorph **I** and the yellow needles crystallized in hydroxylated vials belong to polymorph **III**. In both types of surfaces nuclei did not stick to the walls of the vials and crystals are formed at the end of the evaporation process (Figure 4.4a). These results suggest that there is no specific interaction between xenophobic nuclei of flufenamic acid and the hydroxylated and fluoruous surfaces of vials.

#### 4.5 VISUAL OBSERVATIONS

Figure 4.5 shows stepwise crystallization process in hydroxylated and fluoruous vials. The image on the top shows the beginning of the crystallization. The two types of surfaces exhibit different wetting properties with hydroxylated vials having higher affinity for ethanol than fluoruous vials. The concave menisci in the former vials are more deeper than those in the latter. The bottom image shows the crystallization process after four days. Flufenamic acid does not crystallize on the walls of hydroxylated and fluoruous vials during solvent evaporation. This observation suggests that crystal nuclei do not attach to the hydroxylated surfaces even though ethanol wets these surfaces. In addition, no visible crystallization occurs on the walls of fluoruous vials implying that the attraction between two fluoruous surfaces is not strong enough to promote the adhesion of crystal nuclei. It is possible that a fluoruous solvent with better wetting properties will promote the crystal nucleation on the walls of the fluoruous vials. We did not perform these experiments in this work. As mentioned above, crystals appeared at the end of the evaporation with yellow needles in the hydroxylated vials and white plates in the fluoruous vials.

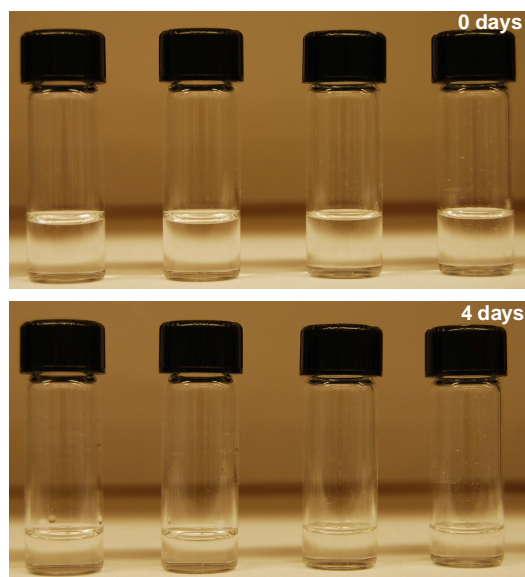


**Figure 4.5** Monitoring of crystal growth of flufenamic acid in hydroxylated (left two) and fluoruous (right two) vials. Notice the differences in the menisci. Notice the lack of crystallization on the walls of fluoruous *and* hydroxylated vials.

#### 4.6 IR SPECTROSCOPIC CHARACTERIZATION OF SOLID FORMS

Forms **I** and **III** show several gross similarities and some important differences in their IR spectra (Figure 4.6). Both forms show broad absorptions of O–H stretching vibrations in the region  $3500\text{--}2250\text{ cm}^{-1}$  characteristic for carboxylic acid. Intramolecular N–H $\cdots$ O bonds between imine and carbonyl groups and intermolecular O–H $\cdots$ O bonds between carboxylic acid groups are responsible for these broad absorptions. The C=O stretching absorption occurs at  $1651\text{ cm}^{-1}$  in form **I** and at  $1655\text{ cm}^{-1}$  in form **III**. These values are significantly lower than expected for an aromatic carboxylic acid; the reduction in stretching frequency of C=O is caused by intramolecular hydrogen bonding with imine group, in addition to the conjugation with the phenyl ring. Between the two polymorphs, the slightly lower C=O absorption frequency for form **I** is a result of slightly elongated C=O bond that is involved in stronger N–H $\cdots$ O=C hydrogen bonds with imine group. The C=O distances for polymorphs **I** and **III** are  $1.234\text{ \AA}$  and  $1.230\text{ \AA}$  respectively.<sup>27,28</sup> The imine N–H stretching vibrations absorb at  $3320\text{ cm}^{-1}$  for form **I** and at  $3314\text{ cm}^{-1}$  for form **III**. These values appear to contradict the previous statement (stronger N–H $\cdots$ O=C hydrogen bonds in form **I**). The apparent contradiction arises from the different conformations of flufenamic acid molecules in forms **I** and **III** (Figure 4.7). Significant differences between the two polymorphs can be also be observed in the fingerprint region (Figure 4.6c) The bond distances given above are taken from previously reported crystal structures determined at room temperature. Molecular structures in Figure 4.7 are plotted from low temperature X-ray crystal structures determined by us.

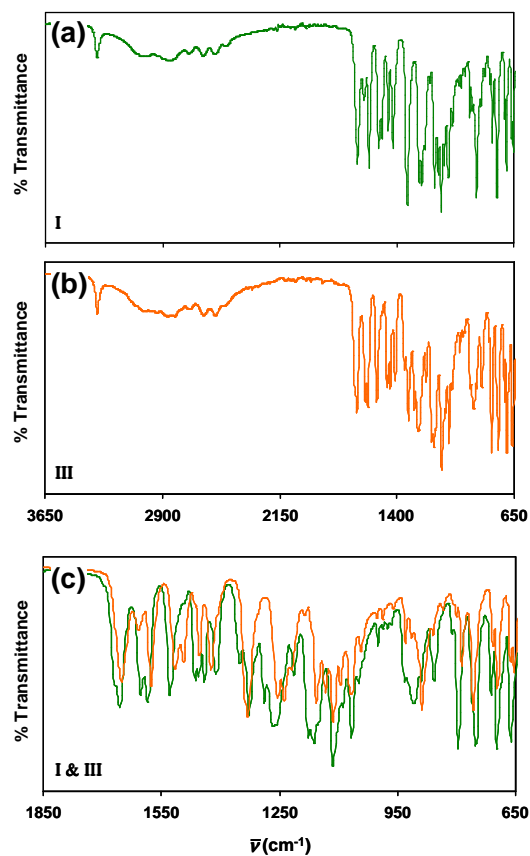


**Figure 4.6** IR Spectra of (a) polymorph I and (b) polymorph III grown in fluorous and hydroxylated vials. These two images show the IR spectra of flufenamic acid in the range 3650-650  $\text{cm}^{-1}$ . (c) Overlaid IR spectra of forms I (green) and III (orange) given in the range 1850-650  $\text{cm}^{-1}$ .

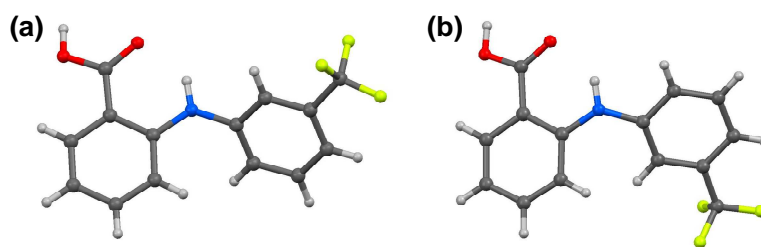


**Figure 4.7** Molecular conformations of flufenamic acid in (a) polymorph I and (b) polymorph III. Notice the opposing orientations of -COOH and -CF<sub>3</sub> groups in form III.

**Table 4.1** Crystallographic data for polymorphs **I** and **III** of flufenamic acid. The temperature of data collection is given as  $T$ . Packing coefficient,  $C_k^*$ , is calculated using the program PLATON.<sup>29</sup>

	<b>I</b>	<b>III</b>
Emp. formula	C <sub>14</sub> H <sub>10</sub> F <sub>3</sub> NO <sub>2</sub>	C <sub>14</sub> H <sub>10</sub> F <sub>3</sub> NO <sub>2</sub>
Formula wt.	281.23	281.23
Crystal system	triclinic	monoclinic
Space group	$P2_1/c$	$C2/c$
$a$ (Å)	12.413(7)	39.6466(11)
$b$ (Å)	7.753(5)	5.04810(10)
$c$ (Å)	12.677(7)	11.9577(4)
$\alpha$ (°)	90	90
$\beta$ (°)	94.739(12)	91.907(2)
$\gamma$ (°)	90	90
$V$ (Å <sup>3</sup> )	1215.8(12)	2391.89(11)
$Z$	4	8
$D_{\text{calc}}$ (Mg/m <sup>3</sup> )	1.536	1.562
$F$ (000)	576	1152
$\mu$	0.134	0.136
$R_1$	0.0369	0.0332
$wR_2$	0.0984	0.0926
GoF	1.038	1.040
$N$ -total	15125	13315
$N$ -independent	3028	3028
$N$ -observed	2626	2592
$N$ -parameters	189	189
$T$ (K)	100	100
$\theta$ range	1.65 - 28.28	2.06 - 28.50°
Index ranges	$-16 \leq h \leq 16$	$-52 \leq h \leq 52$
	$-9 \leq k \leq 10$	$-6 \leq k \leq 6$
	$-16 \leq l \leq 16$	$-15 \leq l \leq 15$
Crystal size (mm <sup>3</sup> )	0.24×0.22×0.20	0.32×0.30×0.07
Crystal shape	plate	needle
Crystal color	white	pale-yellow
Solvent	ethanol	ethanol
$C_k^*$	0.710	0.720

#### 4.7 CRYSTAL STRUCTURES OF FORMS **I** AND **III**

In order to assess the identity of two polymorphs, we determined their three-dimensional structures by single crystal X-ray diffraction methods. Full details of the data collection methodology and crystal structure solution, refinement and analysis are given in Chapter 3. Table 4.1 lists the key crystallographic data for polymorphs **I** and **III** of flufenamic acid. In both forms, carboxylic acid groups form O–H···O hydrogen bonded dimers, with the O···O distances of 2.642 Å in **I** and 2.629 Å in **III**. The carbonyl and imine groups in both polymorphs form intramolecular N–H···O hydrogen bonds, with the N···O distances

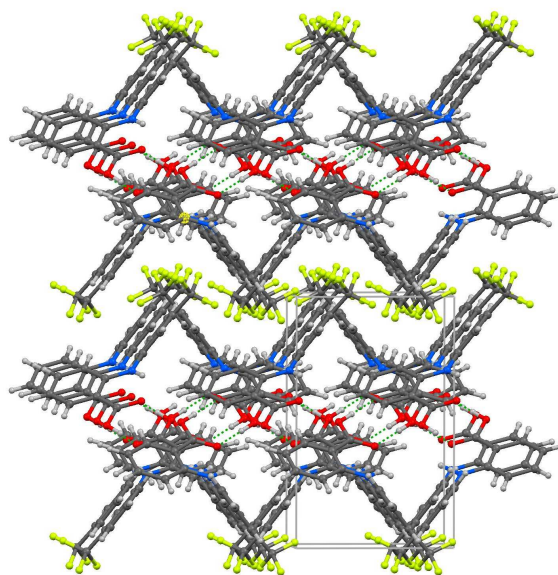


**Figure 4.8** Crystal structure of polymorph **I** showing hydrogen bonded layers. Notice the interdigitation of adjacent layers and sheaths of  $-\text{CF}_3$  groups.

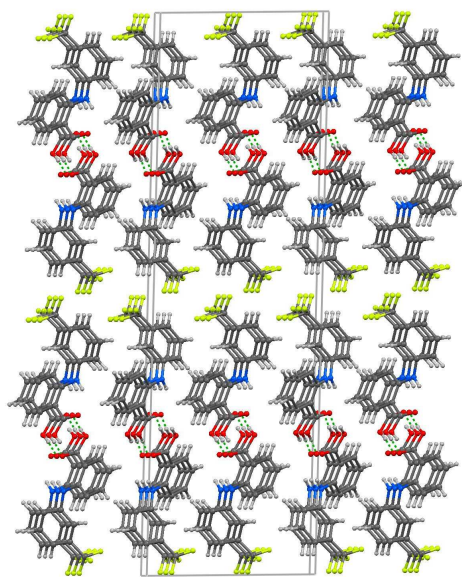


**Figure 4.9** Crystal structure of polymorph **III**. Notice the hydrogen bonded layers and fluorine sheaths between the layers. Contrast Figures 4.8 and 4.9 to notice the absence of corrugation and interdigitation in form **III**.

of 2.649 Å in form **I** and 2.677 Å in form **III**. The phenyl rings are twisted with respect to each other (interplanar angles are 51.2° in form **I** and 41.8° in form **III**) to alleviate the repulsions between the H-atoms on different rings. In both polymorphs, the carboxylic acid groups are nearly coplanar with the attached rings (angle between the planes of acid dimers and phenyl rings are 4.3° in form **I** and 6.3° in form **III**).

The major difference between the two forms at a molecular level occurs in the relative orientation of the -COOH and -CF<sub>3</sub> groups (Figure 4.7). In form **I**, both groups point roughly in the same direction; in form **III** they point in the opposite direction (caused by the rotation of phenyl ring bearing -CF<sub>3</sub> group around the C-N bond). Thus forms **I** and **III** can be considered as conformational and orientational (or packing) polymorphs. The most important feature of the structures is that both polymorphs contain hydrogen bonded layers that are separated by fluororous sheaths of -CF<sub>3</sub> groups (Figures 4.8 and 4.9). One of the important reasons in our selection of flufenamic acid as a model pharmaceutical is that the two solution grown polymorphs have two-dimensional fluororous sheaths. Based on the understanding that hydrogen bonds are stronger and -CF<sub>3</sub>...F<sub>3</sub>C- interactions are weaker, we hypothesized that larger or largest crystal faces of the two polymorphs will expose the fluororous surfaces. The rate of crystal growth in a direction is proportional to the rate of attachment of molecules in that direction.<sup>30</sup> It is safe to assume that rate of growth along the hydrogen bonding is much faster than along the direction of fluororous interaction. Thus, we surmised that the larger or largest crystal faces of form **I** and **III** will be fluororous.

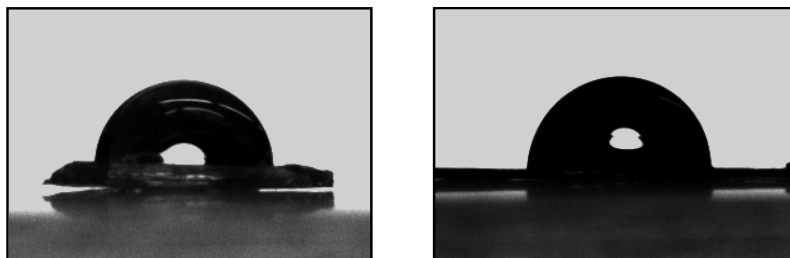


**Figure 4.10** Beading of water droplets on the largest of faces of flufenamic acid polymorphs **I** (left) and **III** (right).

To examine the nature of these faces, we conducted contact angle measurements with water droplets on these crystals. Spreading of water should occur if the largest surfaces are hydrophilic (-COOH groups at the interface); beading of water should occur if the surfaces are hydrophobic (-CF<sub>3</sub> groups at interface). Figure 4.10 shows the images of water droplets on the largest faces of polymorphs **I** and **III**. The measured contact angles are in the range 100-102° and the crystal faces are highly hydrophobic, proving our hypothesis that these faces expose fluororous groups. We assume further in our rationalization of the results that crystal nuclei of these polymorphs also expose similar fluororous surfaces.

#### 4.8 POWDER X-RAY DIFFRACTION ANALYSIS

We pulverized the crystalline products obtained from the experiments with mortar and pestle and exposed the ground materials to X-rays on a Bruker D8 Focus powder diffractometer. We collected the data in the  $2\theta$  range 3–45° at an increment of 0.04° and a scan rate of 4° per minute. Figure 4.11 shows experimental powder patterns of both polymorphs of flufenamic acid along with the patterns calculated from their single crystal structures. The experimental PXRD patterns confirm that while crystals grown in the fluoruous vials correspond to polymorph **I**, those grown in hydroxylated vials belong to polymorph **III**. Unlike the polymorphs of nitrofurantoin, flufenamic acid polymorphs show distinct PXRD patterns. We use PXRD analysis as a tool to confirm that crystals in the bulk sample had the same structures as the ones described in previous section.

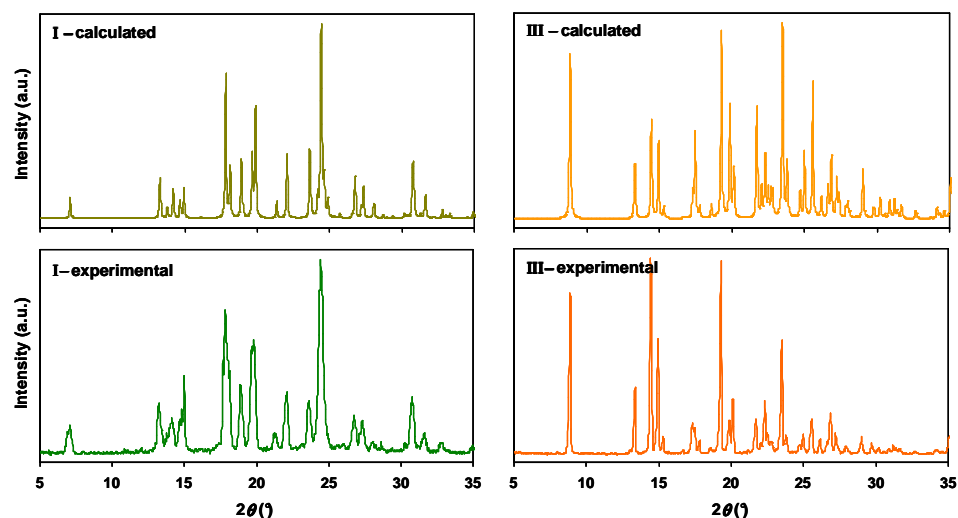


**Figure 4.11** Calculated (top) and experimental (bottom) PXRD patterns of polymorphs **I** (left) and **III** (right) of flufenamic acid. Notice the correspondence between the calculated and experimental patterns for a given polymorph and the contrast between the different polymorphs.

#### 4.9 THERMAL ANALYSIS OF PHASE TRANSITIONS

We collected the differential scanning calorimetry (DSC) data in hermetically sealed and crimped aluminum pans. We heated the samples in the range of 25–350°C at 10 and 2 °C per minute. The DSC traces of polymorphs **I** and **III** are shown in Figure 4.12. Both polymorphs show a single endotherm corresponding to the melting when heated at the rate of 10 °C per minute (133 °C for **I** and 126 °C for **III**). These melting points agree with the reported values.

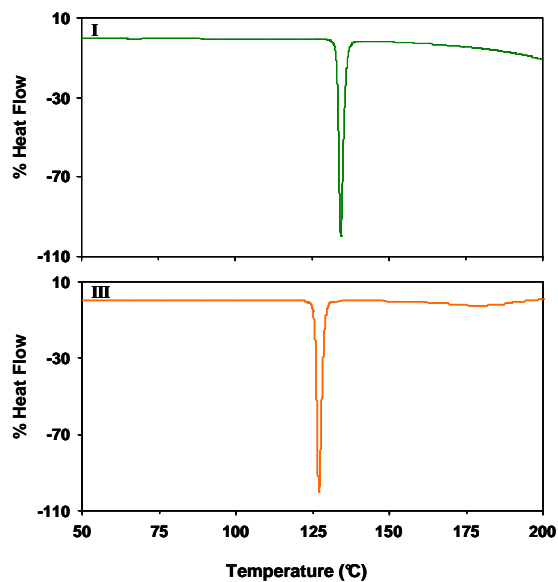


**Figure 4.12** DSC Thermograms of polymorphs **I** (top) and **III** (bottom) showing melting endotherms. The thermograms are recorded at a rate of 10 °C per minute.

We tested the enantiotropic relationship between forms **I** and **III** in the calorimeter using different rates of heating. It is known that form **III** is more stable than form **I** below 42 °C.<sup>14</sup> If the polymorphs are heated at the rate of 10 °C per minute they do not show any other phase transitions other than melting endotherms. If the polymorphs are heated at the slower rate of 2 °C per minute, polymorph **III** shows a small *endotherm* at 120 °C just below the melting point (Figure 4.13).<sup>15</sup> Forms **I** and **III** are enantiotropic; that form **III** absorbs heat when transformed to form **I**, indicates that form **III** is the more stable polymorph at room temperature (below the transition point).

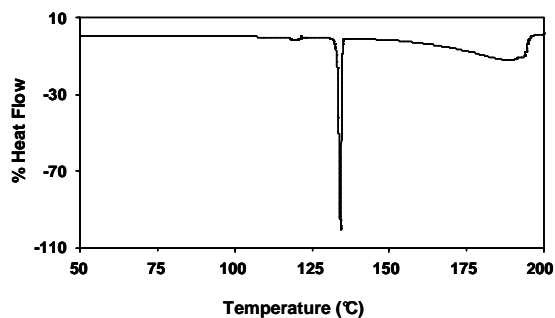


**Figure 4.13** DSC Thermogram of polymorph **III** showing a small endotherm at 120 °C corresponding to **III**→**I** transition and a large melting endotherm at 133 °C. The thermogram is recorded at a rate of 2 °C per minute.

#### 4.10 CRYSTAL GROWTH ABOVE THE PHASE TRANSITION TEMPERATURE

Flufenamic acid provided us with a unique system to test whether the surface effects would be reversed if the crystallization were carried out at a higher temperature. We hypothesized that if the crystal growth is allowed to occur above the phase transition temperature, form **I** (now stable) should appear in hydroxylated vials and form **III** (now metastable) should appear in fluoruous vials. We tested a series of experiments with ethanol at temperatures in the range of 50-70 °C, but the rapid evaporation of ethanol in these conditions yielded mostly form **III** regardless of the surface used. We carried out further experiments in toluene solutions due to its ability to dissolve flufenamic acid and its relatively slower rate of evaporation in the region 70-90 °C compared to other solvents tested.

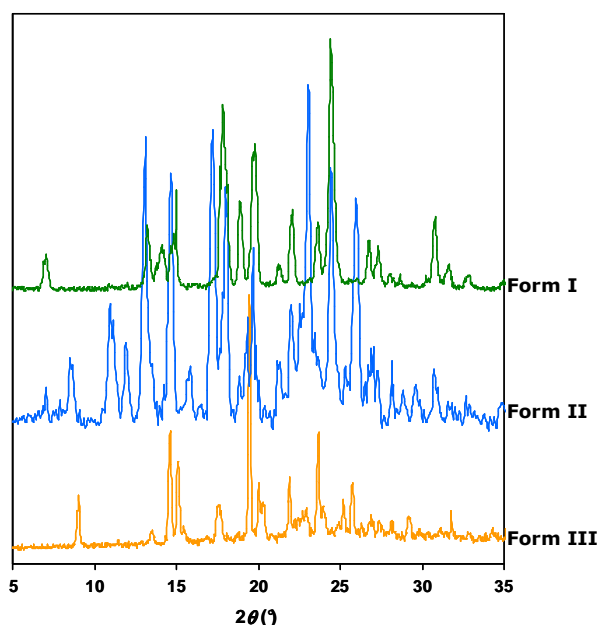


**Figure 4.14** PXRD Patterns of forms **I**, **II** and **III**. Form **II** is grown from toluene solutions in fluoruous vials at 80 °C.

We prepared 42 mM solutions of flufenamic acid in toluene by heating at 60 °C for about 20 minutes and used them for crystallizations immediately. A set of hydroxylated and fluoruous vials containing these solutions are kept at 80 °C in an oven. In the hydroxylated vials, white crystals are formed at the bottom and in the fluoruous vials off-white colored crystals appeared. We characterized the crystals in hydroxylated vials using PXRD and confirmed that they belong to polymorph **I**. Our hypothesis seemed to have worked in that at higher temperatures the stable polymorph **I** crystallized in vials with repelling surfaces. What formed in the fluoruous vials is yet to be determined with confidence, but the PXRD analysis gave us a pattern that did not match polymorph **I** or **III**, but had

several peaks that matched polymorph **II** (Figure 4.14). Interestingly, the off-white crystals formed in fluorous vials turned white in color within 24 hours, and PXRD analysis revealed that these crystals belong to polymorph **I**. It is known that form **II** is metastable and exhibits a monotropic relationship with form **I** at all temperatures. The transition of form **II** to form **I** is therefore not surprising; once the **II**→**I** transition occurs, it is an irreversible process and the crystals remain as form **I** at room temperature.

#### 4.11 SUMMARY AND CONCLUSION

We explored two contrasting surfaces for the crystal growth of polymorphs of flufenamic acid at temperatures below and above the phase transition temperature. We showed that both hydroxylated and fluorous surfaces influence the growth of polymorphs in these two temperature ranges. The hydroxylated surfaces are highly hydrophilic and the fluorous surfaces are highly hydrophobic. When the drug is crystallized from ethanol solution at ~ 25 °C, crystals of metastable polymorph **I** grow exclusively in fluorous vials. Under the same conditions, from the same stock solution, only crystals of stable polymorph **III** grow in the hydroxylated vials. On both types of vials crystals appeared at the end of the solvent evaporation and nothing crystallized on the walls of hydroxylated and fluorous surfaces. These results are in contrast with our previous studies using indomethacin, nitrofurantoin, carbamazepine and other drugs, for which crystals always nucleated on the walls of the hydroxylated vials along the solvent front.

The change in the nature of hydroxylated surfaces from being sticky to nonstick can be understood by noting that flufenamic acid is the only drug we screened that contains fluorous fragments ( $-\text{CF}_3$ ) in the molecular structure. As stated in Section 4.7 we surmise (based on the water contact angles of largest crystal faces) that fluorous nuclei of this drug are highly hydrophobic and do not attach to the hydroxylated surfaces. Thus, nucleation of metastable form is suppressed on the walls allowing for the stable form to nucleate and grow into crystals. In our previous studies we used xenophobic vial surfaces to promote the growth of thermodynamic form by suppressing the nucleation of kinetic form. In this study, we showed the reverse inhibition, clusters of kinetic polymorph exhibit fluorous surfaces and do not nucleate on hydrophilic surfaces. In fluorous vials, the growth of kinetic form may be promoted by favorable interactions between fluorous nuclei and fluorous surfaces of the vial. The observation that crystals did not nucleate on the walls of the fluorous vials can be attributed to poor wetting properties of the ethanol and the weaker fluorous···fluorous interactions between the nuclei and vial walls. It is possible that microscopic nuclei are attached to the surface and allow the growth of metastable form in the fluorous vials. Further studies using fluorinated solvents for crystallization can resolve some of these issues.

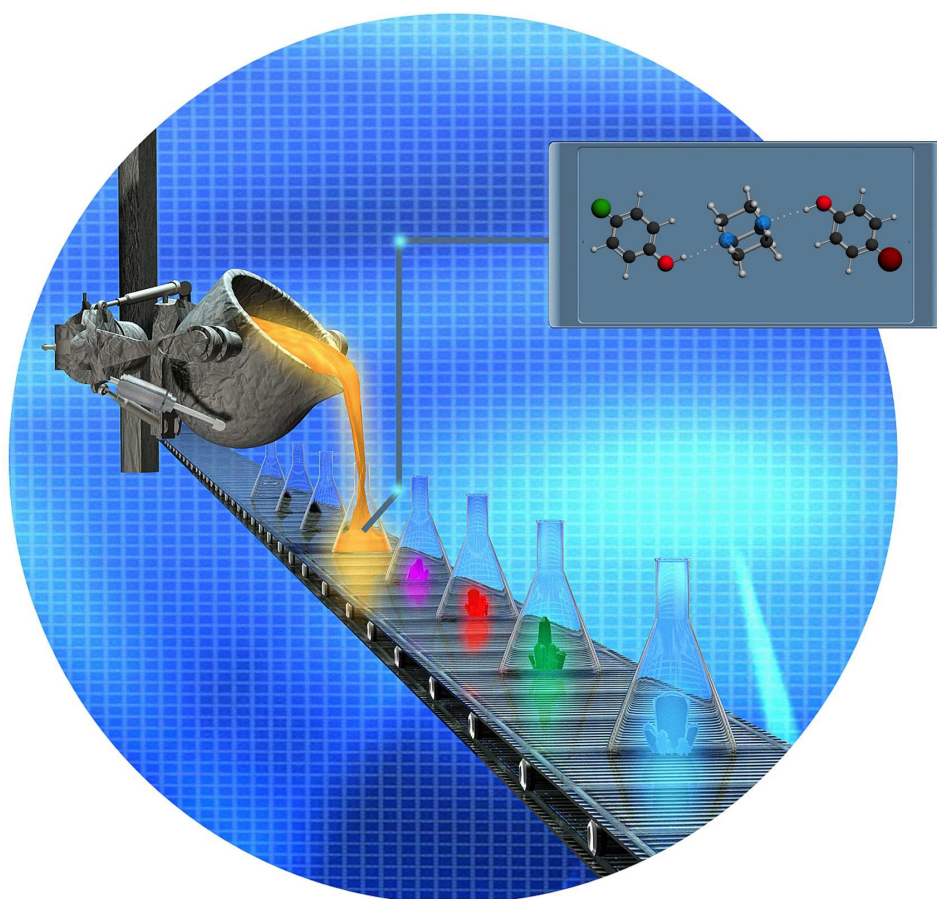
**4.12 REFERENCES**

1. Begue, J.-P.; Bonnet-Delpon, D., Recent advances (1995-2005) in fluorinated pharmaceuticals based on natural products. *J. Fluor. Chem.* **2006**, *127*, 992-1012.
2. Isanbor, C.; O'Hagan, D., Fluorine in medicinal chemistry: A review of anticancer agents. *J. Fluor. Chem.* **2006**, *127*, 303-319.
3. Kirk, K. L., Fluorine in medicinal chemistry: Recent therapeutic applications of fluorinated small molecules. *J. Fluor. Chem.* **2006**, *127*, 1013-1029.
4. Mueller, K.; Faeh, C.; Diederich, F., Fluorine in Pharmaceuticals: Looking Beyond Intuition. *Science* **2007**, *317*, 1881-1886.
5. Bondi, A., van der Waals volumes and radii. *J. Phys. Chem.* **1964**, *68*, 441-451.
6. Ismail, F. M. D., Important fluorinated drugs in experimental and clinical use. *J. Fluor. Chem.* **2002**, *118*, 27-33.
7. Robertson, D. W.; Jones, N. D.; Swartzendruber, J. K.; Yang, K. S.; Wong, D. T., Molecular structure of fluoxetine hydrochloride, a highly selective serotonin-uptake inhibitor. *J. Med. Chem.* **1988**, *31*, 185-189.
8. Wong, D. T.; Bymaster, F. P.; Engleman, E. A., Prozac (fluoxetine, Lilly 110140), the first selective serotonin uptake inhibitor and an antidepressant drug: twenty years since its first publication. *Life Sci.* **1995**, *57*, 411-441.
9. Gladysz, J. A.; Curran, D. P.; Horvath, I. T., *Handbook of Fluorous Chemistry*. Wiley-VCH: Weinheim, **2004**.
10. Winder, C. V.; Wax, J.; Querubin, B. S.; Jones, E. M.; McPhee, M. L., Antiinflammatory and antipyretic properties of N-(a,a,a-trifluoro-m-tolyl)anthranilic acid (CI-440; flufenamic acid). *Arthritis Rheumat.* **1963**, *6*, 36-47.
11. Gilpin, R. K.; Zhou, W., Infrared studies of the polymorphic states of the fenamates. *J. Pharm. Biomed. Anal.* **2005**, *37*, 509-515.
12. Hu, Y.; Liang, J. K.; Myerson, A. S.; Taylor, L. S., Crystallization Monitoring by Raman Spectroscopy: Simultaneous Measurement of Desupersaturation Profile and Polymorphic Form in Flufenamic Acid Systems. *Ind. Eng. Chem. Res.* **2005**, *44*, 1233-1240.
13. Lee, E. H.; Boerrigter, S. X. M.; Rumondor, A. C. F.; Chamarthy, S. P.; Byrn, S. R., Formation and Solid-State Characterization of a Salt-Induced Metastable Polymorph of Flufenamic Acid. *Cryst. Growth Des.* **2008**, *8*, 91-97.
14. Krc, J., Jr., Crystallographic properties of flufenamic acid. *Microscope* **1977**, *25*, 31-45.
15. Burger, A.; Ramberger, R., Thermodynamic relationships between polymorphic modifications: flufenamic acid and mefenamic acid. *Microchim. Acta* **1980**, *1*, 17-28.
16. Bernstein, J., *Polymorphism in Molecular Crystals*. Clarendon Press: Oxford, **2002**.
17. Brittain, H. G., *Polymorphism in Pharmaceutical Solids*. Marcel Dekker: New York, **1999**.
18. Byrn, S. R.; Pfeiffer, R. R.; Stowell, J. G., *Solid-State Chemistry of Drugs*. 2nd ed.; SSCI: West Lafayette, **1999**.
19. Hilfiker, R., *Polymorphism in the Pharmaceutical Industry*. Wiley-VCH: Weinheim, **2006**.

20. Burger, A.; Ramberger, R., On the polymorphism of pharmaceuticals and other molecular crystals. II. Applicability of thermodynamic rules. *Microchim. Acta* **1979**, *2*, 273-316.
21. Yu, L., Inferring Thermodynamic Stability Relationship of Polymorphs from Melting Data. *J. Pharm. Sci.* **1995**, *84*, 966-974.
22. Kuhnert-Brandstaetter, M.; Borcka, L.; Friedrich-Sander, G., Polymorphism of drugs Flufenamic acid and BL 191. *Arch. Pharm.* **1974**, *307*, 845-853.
23. Galdecki, Z.; Glowka, M. L.; Gorkiewicz, Z., Polymorphism of 2-(3-trifluoromethylphenylamino)benzoic acid. *Acta Pol. Pharm.* **1978**, *35*, 77-79.
24. Kulinich, S. A.; Farzaneh, M., Hydrophobic properties of surfaces coated with fluoroalkylsiloxane and alkylsiloxane monolayers. *Surf. Science* **2004**, *573*, 379-390.
25. Ulman, A., Formation and Structure of Self-Assembled Monolayers. *Chem. Rev.* **1996**, *96*, 1533-1554.
26. Wasserman, S. R.; Tao, Y. T.; Whitesides, G. M., Structure and reactivity of alkylsiloxane monolayers formed by reaction of alkyltrichlorosilanes on silicon substrates. *Langmuir* **1989**, *5*, 1074-1087.
27. McConnell, J. F., 3'-Trifluoromethyldiphenylamine-2-carboxylic acid, C<sub>14</sub>H<sub>10</sub>F<sub>3</sub>NO<sub>2</sub> flufenamic acid. *Cryst. Struct. Commun.* **1973**, *2*, 459-461.
28. Murthy, H. M. K.; Bhat, T. N.; Vijayan, M., Structural studies of analgesics and their interactions. IX. Structure of a new crystal form of 2-[[3-(trifluoromethyl)phenyl]amino]benzoic acid (flufenamic acid). *Acta Crystallogr.* **1982**, *B38*, 315-317.
29. Spek, A. L., Single-crystal structure validation with the program PLATON. *J. Appl. Crystallogr.* **2003**, *36*, 7-13.
30. Mullin, J. W., *Crystallization*. 4th ed.; Butterworth-Heinemann: New York, **2001**.

# 5

## SUPRAMOLECULAR SOLID SOLUTIONS – A NEW APPROACH TO MULTICOMPONENT ORGANIC ALLOYS



THIS PAGE LEFT INTENTIONALLY BLANK

## 5.1 BACKGROUND

Multicomponent solids, be they cocrystals or solid solutions, may be viewed as materials that can exhibit functions superior or unavailable to the individual components.<sup>1</sup> Though molecular complexes have been studied for a long time,<sup>2,7</sup> the design of cocrystals containing more than two different components remains a challenging task.<sup>8</sup> Except for a few notable contributions,<sup>9-15</sup> most studies on organic cocrystals led only to the formation of binary organic solids.<sup>1</sup> In contrast, metals and inorganic compounds readily form multicomponent solids in the form of solid solutions.<sup>16,5</sup> Creating multicomponent solid solutions of organic molecules, however, is challenging because these molecules possess intricate shapes and participate in directional intermolecular interactions.<sup>5</sup> Consequently, most of the molecule based solid solutions contain only two components.<sup>17</sup> Here we describe a *supramolecular* approach for the preparation of solid solutions that contain three or more organic molecules. The principal advantage of solid solutions is that their properties can be modulated by gradual modification of the relative ratio of the components.<sup>18</sup>

## 5.2 MOLECULAR CRYSTALS

This work involves crystalline solids that contain single and multiple components and in this context it is useful to define the terms molecular crystal, cocrystal and solid solution. A molecular crystal is a periodic single component solid in which the component molecules are arranged on a three-dimensional lattice (Figure 5.1a). The rationalization and design of crystal structures are the central goals of crystal engineering both to prepare functional solids and to advance our understanding of crystal growth, polymorphism, and structure-property relationships.<sup>2</sup> Polymorphs, crystals of the same compound with different structures, have attracted much recent interest because of their importance in pharmaceutical processing.<sup>19-22</sup> Early work in crystal engineering laid the foundations for

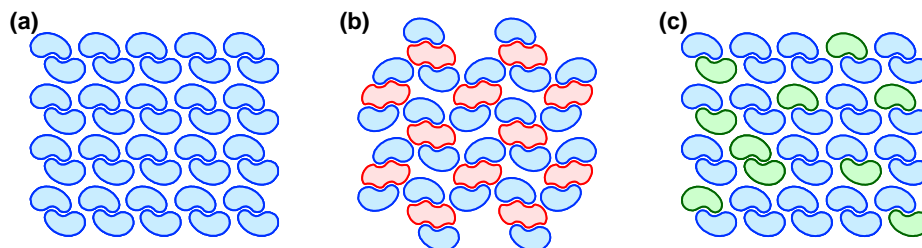


**Figure 5.1** Schematic representations of (a) a crystal, (b) a cocrystal and (c) a solid solution. (a) A single-component crystal is a solid with periodic arrangement of one type of molecule. (b) The cocrystal shown here is made from *two* different molecules; its repeat unit, however, contains *three* molecules. This is an example of a *binary* cocrystal with a *trimolecular* repeat unit. (c) The molecular solid solution shown here is made from two different molecules that have similar sizes and shapes. The components are arranged on a periodic lattice but distributed randomly throughout the crystal. In a cocrystal the components are in a stoichiometric ratio; in a solid solution, they are not. All three solids have periodic structures; all are *crystalline* materials.

the design of two-component solids and the concepts and tools of crystal engineering are now being applied in the preparation of multicomponent pharmaceutical solids.<sup>23</sup> In the past, multicomponent solids are prepared as either cocrystals or solid solutions (Figures 5.1b and 5.1c).

### 5.3 COCRYSTALS

Cocrystals are periodic crystalline solids that contain two or more components in a stoichiometric ratio (Figure 5.1b).<sup>3</sup> Cocrystals have different properties than the crystals of individual components; they are now being considered as new forms of medicines to alter the solubility, dissolution rate, bioavailability, or other properties of pharmaceutical drugs.<sup>24-26</sup> Cocrystals can be made from two molecules of any shape or size that have complementary hydrogen bond functionalities. The crystal structures of cocrystals are different from the pure components and cocrystals often exhibit different sets of hydrogen bonding patterns and supramolecular synthons.<sup>27</sup> We are exploring the design of cocrystals due to their applications in pharmaceutical formulations and also because we use them as starting points to create supramolecular solid solutions.<sup>28</sup>

### 5.4 MOLECULAR SOLID SOLUTIONS

Solid solutions and cocrystals are similar in that they are crystalline and have the overall three-dimensional periodicity, but they differ from each other in several ways. The components within the solid solutions are in nonstoichiometric ratios, they are distributed randomly throughout the crystal, and they must be of similar size and shape in order to form an *organic alloy* (Figure 5.1c).<sup>5</sup> Thermodynamically, solid solutions can be easier to form due to entropic gain achieved from the freedom of nonstoichiometric ratios and random distribution of components. They are akin to metallic alloys in that the different components can be added in diverse ratios to achieve different properties. The major limitation of molecular solid solutions is that different components must be of similar size and shape, and given the complicated three-dimensional structures of most organic and pharmaceutical molecules it is difficult to identify and synthesize the analogues of target molecules.

### 5.5 SUPRAMOLECULAR SOLID SOLUTIONS

Molecular solid solutions are made of two or more molecules that are of the same shape and size. Supramolecular solid solutions are made of two or more supermolecules or molecular assemblies that have the same shape and size. Figure 5.2 shows our strategy for forming supramolecular solid solutions. We begin with a trimolecular motif wherein a central target molecule (A) is connected to two peripheral molecules (B or C) through similar intermolecular interactions. If the two peripheral molecules are identical, binary cocrystals AB<sub>2</sub> or AC<sub>2</sub> are formed. If they are different, a ternary cocrystal BAC or ternary solid solutions A(B<sub>n</sub>C<sub>1-n</sub>)<sub>2</sub> (0 < n < 1) can be formed depending on the size and shape similarities of these peripheral molecules. Adding another isosteric component (D)

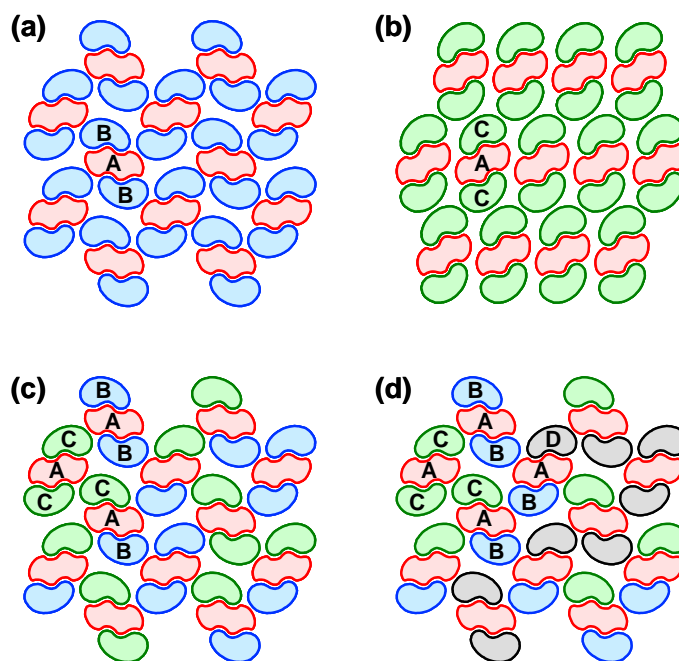


**Figure 5.2** (a and b) Binary cocrystals  $AB_2$  and  $AC_2$ . Note that B and C have similar shapes and sizes. In these diagrams,  $AB_2$  and  $AC_2$  adopt different crystal structures. (c) Ternary solid solution made of A, B and C. In this diagram, the solid solution adopts the structure of  $AB_2$ ; it can as well adopt  $AC_2$  or some other structure. The trimolecular assemblies in (c) may have BAB, CAC or BAC configurations. The overall composition of the ternary solid solution is  $A_n(B+C)_{2n}$ . (d) Quaternary solid solution made of A, B, C and D, with an overall composition  $A_n(B+C+D)_{2n}$ .

leads to a quaternary solid solution. We have used a trimolecular motif to illustrate the concept; a bimolecular motif or any higher order motif can be used with the same effectiveness to prepare alloys.

Because this strategy does not require the analogues of target molecule, it allows the preparation of solid solutions of any potential target molecule by adding complementary molecules of same size and shape. These complementary molecules can be selected depending on the function one is after. This supramolecular strategy makes it easy to prepare truly multi-component solid solutions that contain multiple (>3) different components. In this chapter, we will show the generality of our approach using four different target molecules and two different supramolecular synthons.

## 5.6 SUPRAMOLECULAR SYNTHONS

When designing cocrystals or solid solutions it is important to consider all possible intermolecular interactions such as hydrogen bonds,  $\pi\cdots\pi$  stacking,  $C-H\cdots X$  ( $X = N, O, F$

or  $\pi$ ) interactions and halogen bonds. Hydrogen bonds between N and O atoms are easier to incorporate into a multicomponent solid owing to the preponderance of functional groups containing these heteroatom and differences in acidities and basicities of donor and acceptor molecules. Hydrogen bonds can exist as single point, two-point or multi-point recognition motifs. In this context supramolecular synthons are defined as “structural units within supermolecules which can be formed and/or assembled by known or conceivable synthetic operations involving intermolecular interactions”.<sup>27</sup> Figure 5.3 shows some selected hydrogen bonded supramolecular synthons that we have used in our group in the preparation of multicomponent solids.

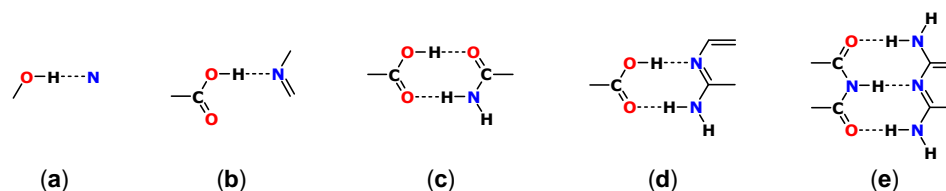


**Figure 5.3** Some supramolecular synthons studied in this work. All the synthons are based on interactions between unlike functional groups; these are also termed heterosynthons. (a) Hydroxy-aza synthon. (b) Acid-pyridyl synthon; usually associated with a corollary C-H...O interaction. (c) Acid-amide synthon. (d) Acid-aminopyridyl synthon. (e) A three point synthon based on N-H...N and N-H...O hydrogen bonds.

### 5.7 DABCO AND 4-*X*-PHENOLS

We use the trimolecular template in Figure 5.2 and begin with the preparation of binary cocrystals and ternary, quaternary and quinary solid solutions formed by [2,2,2]-diazabicyclooctane (DABCO) and 4-*X*-phenols (*X* = Cl, CH<sub>3</sub>, Br, I). We use DABCO as the central molecule and 4-*X*-phenols as the peripheral molecules (Figure 5.4). Each phenol molecule donates one hydrogen bond and a DABCO molecule accepts two hydrogen bonds. Together they form a stoichiometric *binary* cocrystal (two *different* components) with a repeat unit that contains three components and sustained by two O-H...N hydrogen bonds.

The chloro, methyl, bromo and iodo substituents of 4-*X*-phenols have similar shapes, comparable sizes (20, 24, 28, 32 Å<sup>3</sup>)<sup>29</sup> and do not interfere with the O-H...N hydrogen bonding required for the trimolecular assembly. We surmised that the size, shape, and chemical similarity of these 4-*X*-phenols will enable the formation of solid solutions when DABCO is crystallized with two, three or four different phenols. We call these crystalline materials *supramolecular solid solutions* because their repeat unit is a trimolecular assembly.

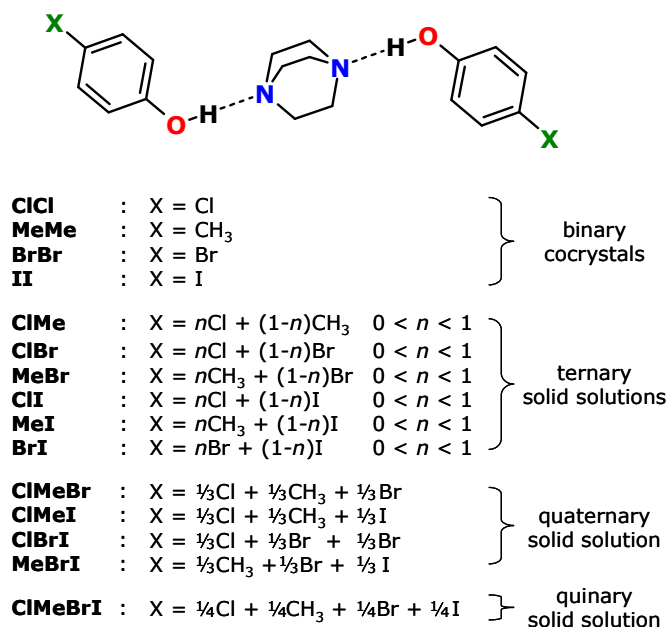


**Figure 5.4** Molecular structures and nomenclature of cocrystals and solid solutions based on DABCO and 4-X-phenols.

## 5.8 CRYSTAL STRUCTURES OF BINARY COCRYSTALS

Single crystals of binary cocrystals and ternary, quaternary and quinary solid solutions (having appropriate quantities of phenols and DABCO) suitable for X-ray diffraction were grown from benzene solutions (Table 5.1, Figure 5.5). Our initial work focused only on the 4-chloro-, 4-methyl- and 4-bromophenols because of their size similarity and the knowledge that chloro-methyl and chloro-bromo exchanges have been attempted before.<sup>2</sup> After successfully preparing the multicomponent solids based on these phenols, we extended our work to the 4-iodophenol. Table 5.1 gives the unit cell data for a total of fifteen multicomponent solids, four cocrystals and eleven solid solutions, made from all possible binary, ternary, quaternary and quinary combinations of DABCO and 4-X-phenols.

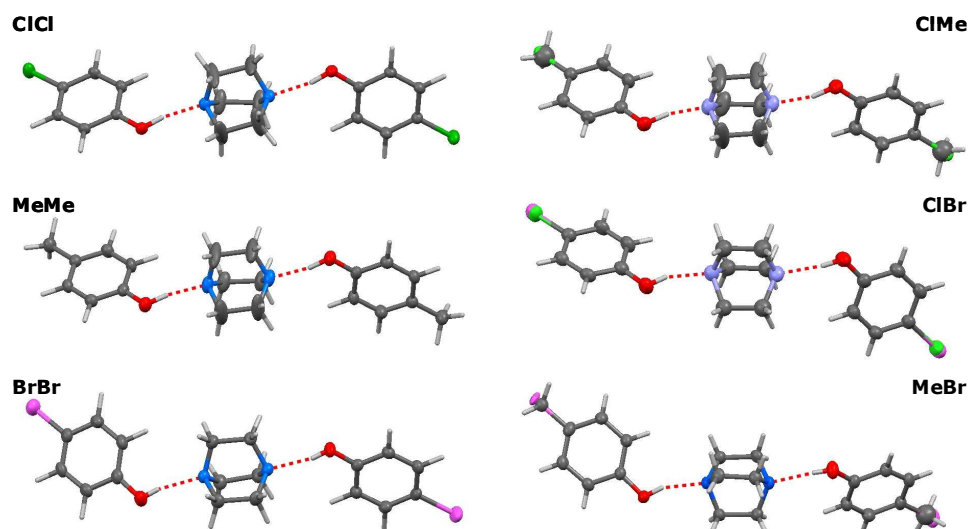


**Figure 5.5** Hydrogen bonded trimolecular assemblies in binary cocrystals (left) and ternary solid solutions (right).

**Table 5.1** Unit cell data for binary cocrystals and ternary, quaternary and quinary solid solutions. Space groups are given in the column *spgr*. Full crystal structures are determined for all the binary and ternary cocrystals; for higher order solid solutions only unit cells are determined.

Name	<i>spgr</i>	<i>a</i> (Å)	<i>b</i> (Å)	<i>c</i> (Å)	$\beta$ (°)	<i>V</i> (Å <sup>3</sup> )
<b>CICI</b>	<i>C2/c</i>	17.987	9.256	11.241	101.85	1831.7
<b>MeMe</b>	<i>C2/c</i>	18.351	9.179	11.254	102.73	1849.0
<b>BrBr</b>	<i>P2<sub>1</sub>/n</i>	6.456	18.577	15.914	91.05	1908.2
<b>II</b>	<i>P2<sub>1</sub>/n</i>	6.518	19.139	16.229	91.04	2024.3
<b>ClMe</b>	<i>C2/c</i>	18.178	9.202	11.260	102.36	1839.9
<b>ClBr</b>	<i>P2<sub>1</sub>/c</i>	18.231	9.165	11.354	94.88	1890.2
<b>MeBr</b>	<i>P2<sub>1</sub>/n</i>	6.443	18.559	15.884	91.36	1898.7
<b>ClI</b>	<i>P2<sub>1</sub>/n</i>	6.484	18.694	15.953	91.15	1933.2
<b>MeI</b>	<i>P2<sub>1</sub>/n</i>	6.459	18.882	16.017	90.86	1953.1
<b>BrI</b>	<i>P2<sub>1</sub>/n</i>	6.485	18.868	16.031	90.06	1961.5
<b>ClMeBr</b>	<i>P2<sub>1</sub>/n</i>	6.443	18.442	15.778	91.59	1874.0
<b>ClMeI</b>	<i>P2<sub>1</sub>/n</i>	6.463	18.605	15.819	91.56	1901.4
<b>ClBrI</b>	<i>P2<sub>1</sub>/n</i>	6.479	18.640	15.941	90.94	1924.2
<b>MeBrI</b>	<i>P2<sub>1</sub>/n</i>	6.466	18.749	15.976	90.91	1936.6
<b>ClMeBrI</b>	<i>P2<sub>1</sub>/n</i>	6.467	18.567	15.869	91.34	1904.7

The binary cocrystals **CICI** and **MeMe** are isostructural; Figures 5.6a and 5.6b show the structures of **CICI** and **MeMe**. The unit cell of **MeMe** is larger than **CICI** in accordance with the larger size of the methyl groups (Table 5.1). As expected, DABCO binds to two

phenol molecules through O–H···N hydrogen bonds (Figure 5.5). This trimolecular assembly is situated on a two-fold axis; that is, the two phenols are symmetry related. The packing of these assemblies in three-dimensions is governed by C–H···O, C–H··· $\pi$  and van der Waals (vdW) interactions.

In the crystal structure of **BrBr** (Figure 5.6c) the hydrogen bonded trimolecular assembly is located on a general position; that is, the two phenols are not related by symmetry. Within the crystal, these assemblies are extended into interconnected chains through type-I and type-II Br···Br interactions.<sup>30</sup> It is likely that **BrBr** crystallizes in a structure different than **ClCl** and **MeMe** in order to accommodate these interactions. Despite the marked differences in their structures, the trimolecular assemblies in all the cocrystals adopt similar conformations (Figure 5.7). Noting this similarity and the similarities in the molecular structures of phenols, we attempted the preparation of ternary solid solutions of **ClMe**, **ClBr** and **MeBr** (Figure 5.4).

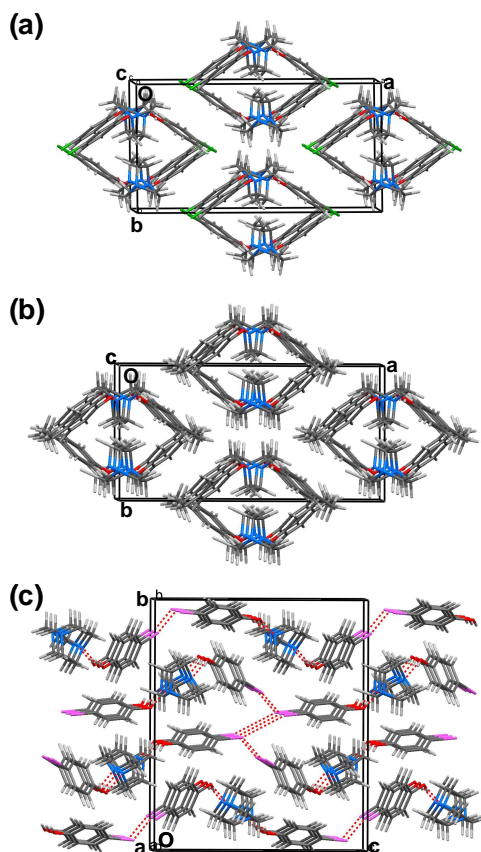


**Figure 5.6** Crystal structures of (a) **ClCl** and (b) **MeMe** (c) **BrBr**. In (c) dashed lines show the O–H···N hydrogen bonds and Br···Br contacts. Note that the overall structures of the **ClCl/MeMe** and **BrBr** cocrystals are different.

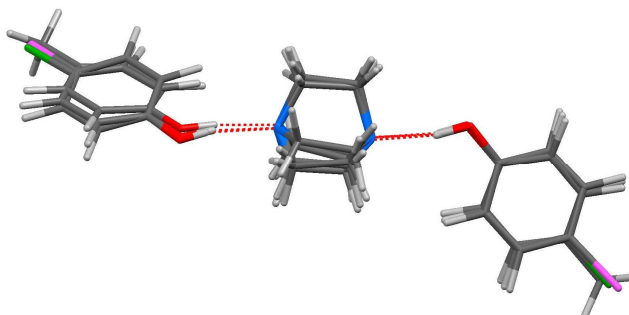


**Figure 5.7** Overlay of trimolecular assemblies in binary cocrystals.

### 5.9 CONTINUOUS SERIES OF TERNARY SOLID SOLUTIONS

We crystallized **CiMe**, **ClBr** and **MeBr** series of solid solutions with varying proportions of corresponding phenols and characterized them using powder X-ray diffraction analysis (Figure 5.8)<sup>31</sup> and IR and <sup>1</sup>H-NMR spectroscopy. We also determined the crystal structures of the ternary solid solutions containing DABCO and the respective phenols in 1:1:1 proportion (Table 5.1, 50X-50Y in Figure 5.8). In these structures, the exchangeable groups (Cl, CH<sub>3</sub>, Br) show ~50% occupancy on both phenols (Figure 5.5).

The 50Cl-50Me ternary solid solution is isostructural to **ClCl** and **MeMe** (Figure 5.9); the volume of its unit cell lies between the volumes of unit cells of **ClCl** and **MeMe** (Table 5.1). Powder X-ray analysis of the **CiMe** series (from 90Cl-10Me to 10Cl-90Me) shows a gradual change of the structure from **ClCl** to **MeMe**. The 50Cl-50Br solid solution adopts the crystal structure of **ClCl**, albeit with decreased symmetry (*C2/c* → *P2<sub>1</sub>/c*; Table 5.1; Figure 5.9). Yet the volume of its unit cell is close to that of **BrBr** indicating the presence of bromine in the crystal. The **ClBr** series of solid solutions adopt the **ClCl** structure up to 40Cl-60Br; from 30Cl-70Br to 10Cl-90Br they adopt the **BrBr** structure (Figure 5.8). In contrast to **ClBr**, the 50Me-50Br solid solution adopts the structure of **BrBr**. **MeBr** solid solutions adopt **MeMe** structure only upto 90Me-10Br. From 80Me-20Br to 10Me-90Br they adopt the structure of **BrBr**.

The Br-atom is larger than Cl-atom and CH<sub>3</sub> group; it also participates in polarization induced attractive Br...Br interactions. Given these two facts, one would expect that **ClBr** and **MeBr** would adopt the structure of **BrBr** to accommodate the larger Br atoms and attractive Br...Br interactions. It is therefore surprising that **ClBr** adopts the structure of **ClCl** and not **BrBr**. The Cl-atom in **ClCl** forms 5 contacts to non H-atoms at vdW+0.2 Å separation, and 7 contacts at vdW+0.3 Å separation. If **ClBr** were to adopt the **BrBr** structure, the Cl-atom would form no contacts even at the separation of vdW+0.3 Å. In contrast, the vdW contacts made by the CH<sub>3</sub> group do not change significantly between **MeMe** or **MeBr** structure. It is possible that **ClBr** adopts the **ClCl** structure because in this structure the Cl-atoms are involved in intermolecular contacts that are of stabilizing nature.

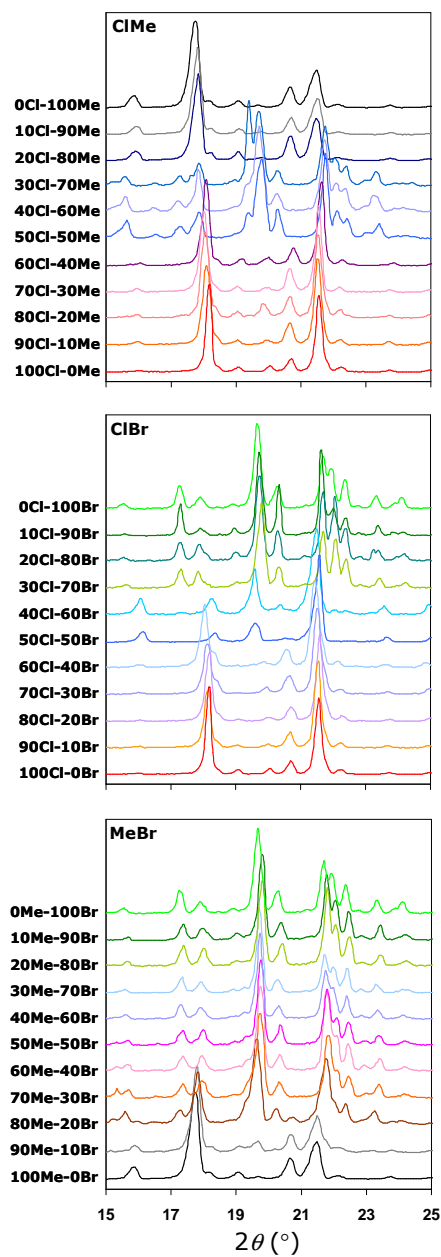


**Figure 5.8** PXRD Patterns of series of **CIME**, **CIBr** and **MeBr** solid solutions. We labeled these solid solutions such that the total phenol content in them is 100%. Thus, 60Cl-40Br indicates that the ternary solid solution consists of 60% chlorophenol and 40% bromophenol. The corresponding binary cocrystals, e.g. 0Me-100Br and 100Me-0Br, border each series at the top and bottom.

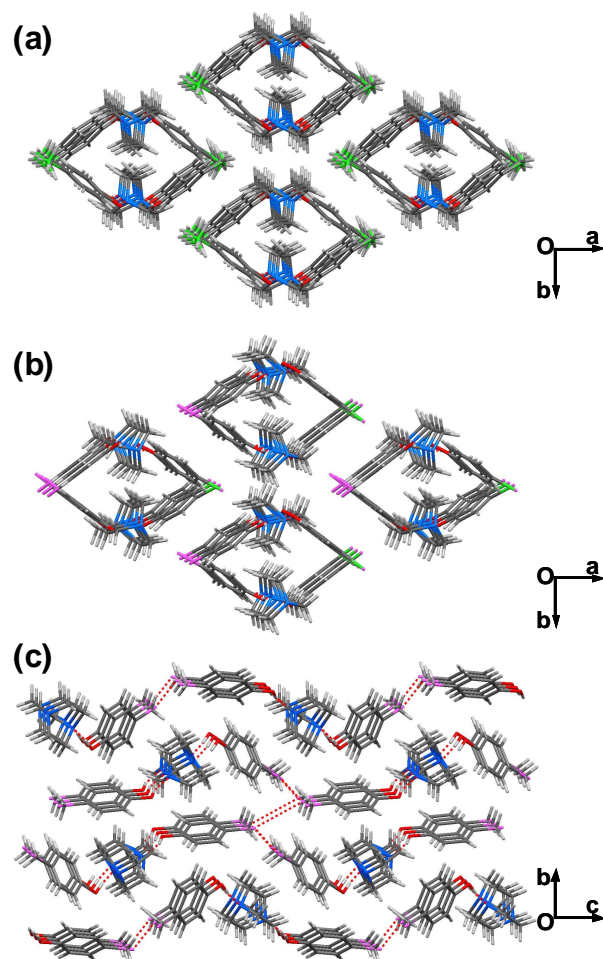


**Figure 5.9** Crystal structures of ternary solid solutions. Note that **CIME** (a) and **ClBr** (b) adopt the structure of **ClCl/MeMe** whereas **MeBr** (c) adopts the structure of **BrBr**.

The X-ray diffraction methods provide useful, yet limited, structural information of solid solutions. Single crystal X-ray analysis affords the structure of the repeat unit as an average of millions of such units. Consequently, we cannot distinguish which of the following compositions the ternary solid solutions adopt: (i) binary motifs  $AB_2$  and  $AC_2$  randomly mixed throughout the crystal; (ii) random mixture of  $AB_2$ ,  $AC_2$ , and  $BAC$ , or (iii) ternary motifs  $BAC$  statistically disordered over two positions such that  $B$  and  $C$  are superposed in the average structure. We can, however, ascertain from these X-ray studies that the repeat unit is indeed a trimolecular assembly and that the solid solution as a whole contains three different components.

### 5.10 SPECTROSCOPIC CHARACTERIZATION OF TERNARY SOLID SOLUTIONS

The IR spectra were recorded in ATR mode on a Perkin Elmer Spectrum One spectrometer. For each measurement only one crystal was taken, which was washed with benzene and dried in air with filter papers immediately prior to the experiment. The broad double hump seen in the region of 1600-2800  $\text{cm}^{-1}$  is characteristic of O–H stretching absorption and overtone from O–H bending respectively (Figure 5.10). An important feature of these spectra is that the broad peak at 3000-3600  $\text{cm}^{-1}$  (corresponding to O–H $\cdots$ O hydrogen bonding in pure phenols) is absent in all of them. These spectra conclusively show that binary cocrystals as well as ternary solid solutions contain only heteromolecular assemblies. We have also collected the  $^1\text{H-NMR}$  spectra of binary cocrystals and all the ternary solid solutions. These spectra showed that the relative contents of DABCO and phenols within a crystal selected for NMR analysis are in agreement with the expected result.

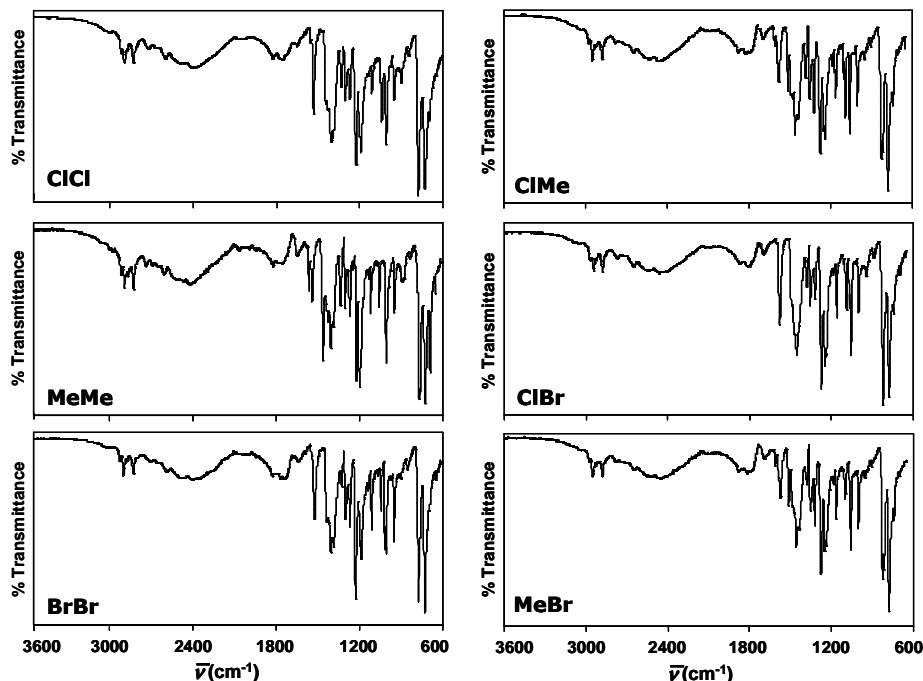


**Figure 5.10** IR spectra of binary cocrystals and ternary solid solutions. Note that **CIME** and **CIBr** adopt the structure of **CICI/MeMe** whereas **MeBr** adopts the structure of **BrBr**.

### 5.11 TRENDS IN THE MELTING POINTS OF SOLID SOLUTIONS

Figure 5.11 shows the differential scanning calorimetry (DSC) results from **CIBr**, **CIME** and **MeBr** series of ternary solid solutions. The melting points of **CIBr** solid solutions gradually decrease from **CICI** to 40Cl-60Br, and then increase to **BrBr**. Figure 5.11

illustrates that solid solutions offer the unique ability to modulate the physical properties of materials in an almost continuous fashion.

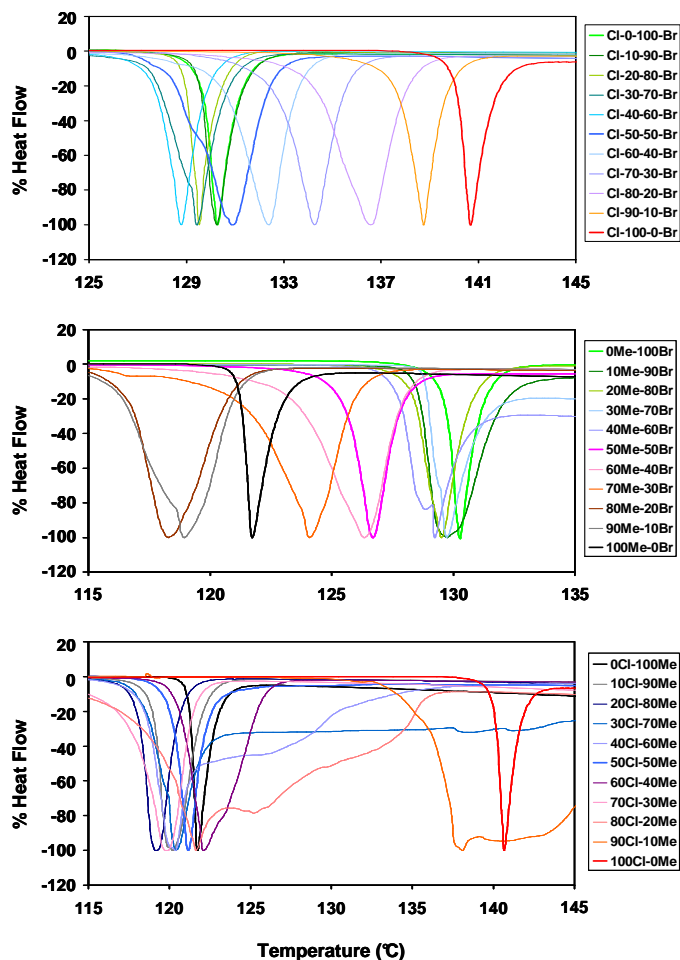


**Figure 5.11** DSC traces of **ClBr**, **MeBr** and **ClMe** solid solutions. In some instances, melting is immediately followed by the decomposition of DABCO. In most cases, the decomposition of DABCO takes place around 170 °C.

## 5.12 QUATERNARY AND QUINARY SOLID SOLUTIONS

The utility of the supramolecular approach to the solid solutions is exemplified by our synthesis of the four quaternary (four-component) solid solutions and a quinary (five-component) solid solution from DABCO and four different phenols. (Table 5.1). For example, the **ClMeBr** solid solution is made from equimolar quantities of the corresponding phenols and the volume of its unit cell ( $1874 \text{ \AA}^3$ ) is close to the average of unit cell volumes of **ClCl**, **MeMe** and **BrBr** ( $1863 \text{ \AA}^3$ ). From the unit cell dimensions

(Table 5.1) and powder X-ray diffraction patterns (Figure 5.17 below), it can be seen that **CIMeBr** adopts the structure of **BrBr**.

The following figures show the characterization of **CIMeBr** by various methods (DSC, IR, NMR and PXRD). The unit cell parameters of **CIMeBr** reported in Table 5.1 are determined by single crystal X-ray diffraction. The IR spectrum (Figure 5.12) shows that a single crystal of **CIMeBr** has only heteromolecular assemblies and the  $^1\text{H}$  NMR spectrum (Figure 5.13) shows that DABCO and three phenols are in 1.5:1:1:1 ratio. The DSC thermogram shows that **CIMeBr** has a distinct melting point that is different from the corresponding binary cocrystals or ternary solid solutions (Figure 5.14).

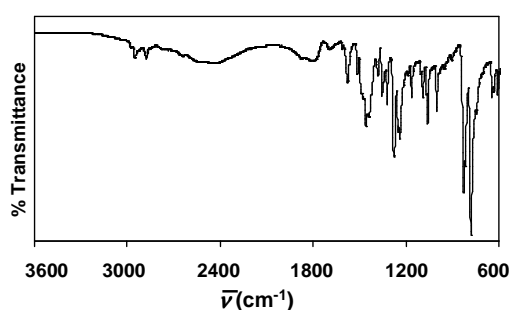


**Figure 5.12** IR spectrum of **CIMeBr** showing the double hump (in the region 1600-2800  $\text{cm}^{-1}$ ) characteristic of hydrogen bonding between DABCO and phenols.

As with IR, for  $^1\text{H}$  NMR spectroscopy only one crystal (washed and dried) was used in each experiment to avoid contamination from any physisorbed materials. The peaks corresponding to different phenols and DABCO are assigned using colored circles and polygons in Figure 5.13. In binary cocrystals there are eight phenolic protons (two distinct sets; each consisting of four protons) and twelve DABCO protons. In order to aid in the analysis of ternary solid solutions, the total proton content (eight) of the phenols is integrated to be  $\sim 200$  units. The twelve protons on DABCO then integrate to  $\sim 300$  units.

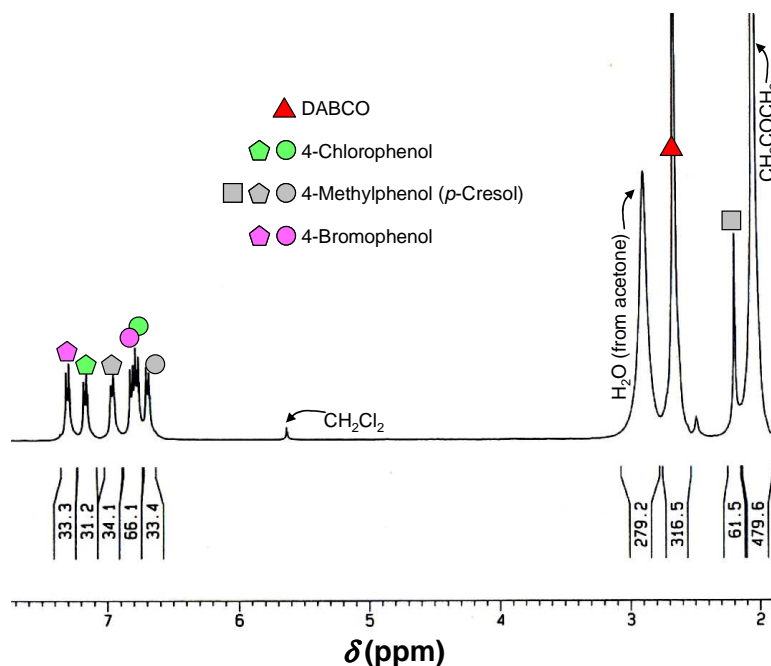


**Figure 5.13.**  $^1\text{H}$  NMR spectrum of **CIMEBr** solid solution collected on a 400Mz NMR spectrometer in acetone- $\text{d}_6$  solvent. The peak at 5.63 ppm belongs to  $\text{CH}_2\text{Cl}_2$  that contaminated acetone- $\text{d}_6$ .

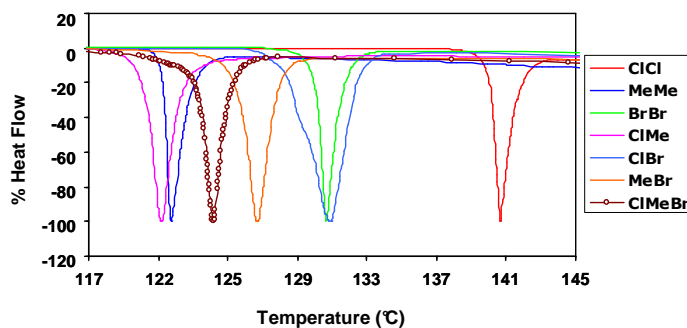


**Figure 5.14.** DSC Trace of **CIMEBr** solid solution (open circles) showing the melting endotherm. DSC Traces of binary cocrystals and 50X-50Y-ternary solid solutions are shown for comparison.

We have characterized the other three quaternary solid solutions and the quinary solid solution **CIMEBrI** in a similar manner. Figure 5.15 shows the  $^1\text{H}$ -NMR spectrum of **CIMEBrI**, taken from a single crystal. The quinary solid solution and the four quaternary solid solutions have melting points that are distinct from the corresponding binary cocrystals and ternary solid solutions (Figures 5.14 and 5.16). It is important to recognize

that **CIMeBr**, **CIMeI**, **ClBrI**, and **MeBrI** are *four*-component solid solutions and **CIMeBrI** is a *five*-component solid solution prepared on the basis of a *three*-component supramolecular assembly. These results show that our approach to the solid solutions is an effective method to create truly multicomponent organic alloys. Unit cell data (Table 5.1) and powder diffraction patterns (Figure 5.17) indicate that **CIMeBr** (and other four component) and **CIMeBrI** solid solutions adopt the structure of **BrBr**.

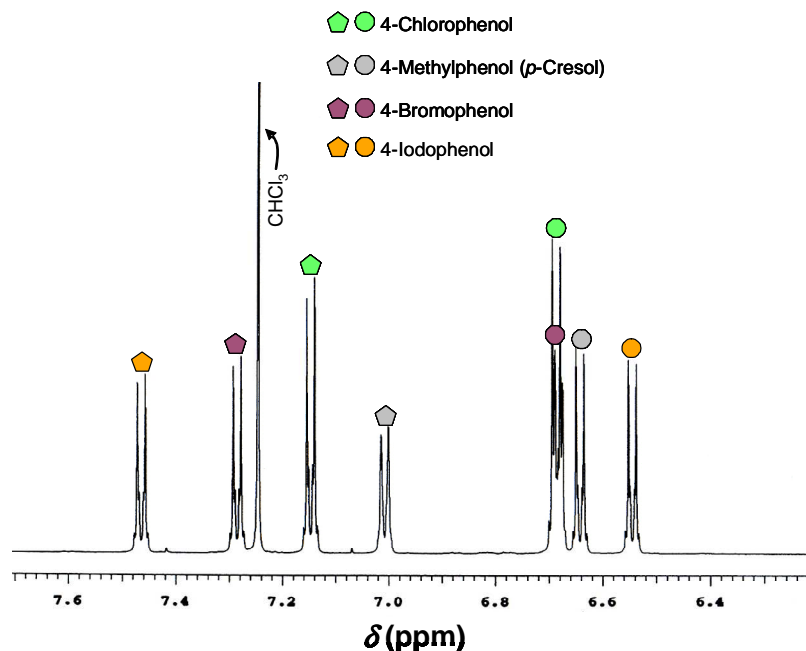


**Figure 5.15** <sup>1</sup>H NMR spectrum of **CIMeBrI** solid solution collected on a 600Mz NMR spectrometer in chloroform-d solvent.

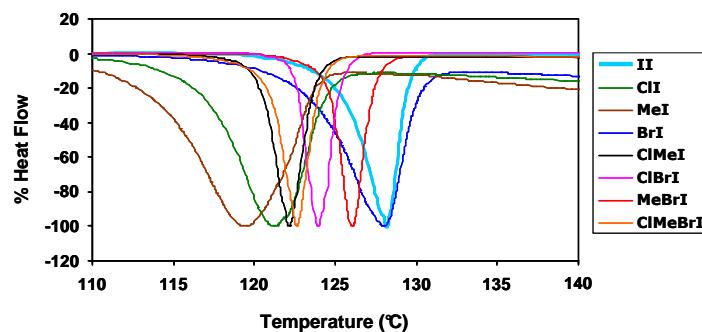


**Figure 5.16** DSC Traces showing the comparison of the melting endotherms of the binary cocrystal and ternary, quaternary and quinary solid solutions containing 4-iodophenol.

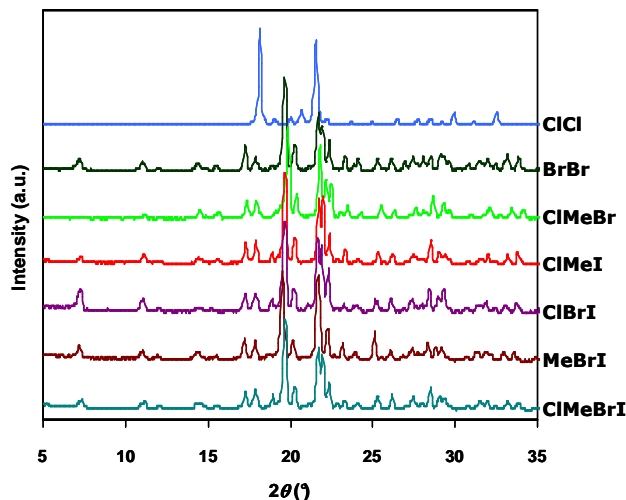


**Figure 5.17** PXRD Patterns of **CIMEBrI** (bottom trace) four quaternary solid solutions. PXRD Patterns of **BrBr** and **ClCl** are shown for comparison. Note that all the four- and five-component solid solutions adopt the structure of **BrBr**.

### 5.13 PREPARATION OF COCRYSTALS AND SOLID SOLUTIONS BY GRINDING

All the cocrystals and solid solutions described above were grown by solution crystallization through the slow evaporation of solvent. The advantage of this method is that it can yield pure crystalline materials suitable for single crystal X-ray analysis; it allows determination of crystal structures and gives access to the three-dimensional coordinacies of atoms in the molecule. There are, however, certain limitations associated with the preparation of multicomponent materials through solution crystallization. The solvent or mixture of solvents should be adjusted based on solubility of the individual components. In addition, an undesired solvate of the target cocrystal can be crystallized instead of the unsolvated product. An alternative approach to make multicomponent materials is to use the solid-state grinding method.<sup>32-34</sup> The main advantage of this method is that it minimizes the solubility problems of disparate components. At its best, this method does not use solvents; in the case of liquid assisted grinding it uses only small volumes of solvent. For this reason, the grinding method offers a green and environment-friendly approach to the preparation of cocrystals. A notable disadvantage of this technique is the inability to prepare diffraction quality crystalline products; that is, crystal structures of the products obtained are usually not determined. The mechanism of how solid state grinding affects cocrystallization is not yet clearly understood.<sup>35</sup> It is suggested that molecular complexes may be formed through vapor diffusion mechanism.<sup>36</sup> We wished to test the neat grinding method in the preparation of our cocrystals and solid solutions from DABCO and appropriate phenols. Molecular complexes of all possible combinations of the components are formed after 20 minutes of solvent free grinding. The products were characterized by IR, DSC and PXRD methods. Figure 5.18 shows the PXRD patterns of quaternary and quinary solid solutions which

match well with the PXRD patterns of the corresponding products crystallized from solution.

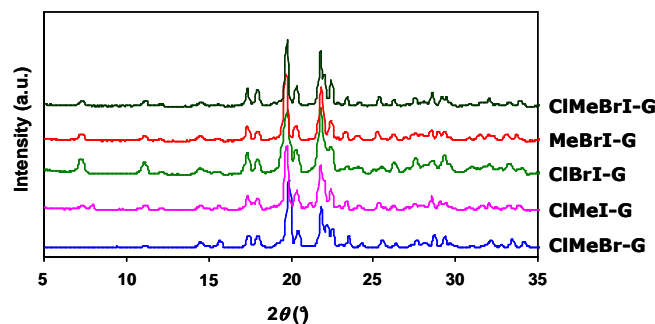


**Figure 5.18** PXRD Patterns of solid solutions prepared by solvent-free grinding. Note the continuous shift of the peaks along  $2\theta$  due to the differences in unit cell volumes.

Materials that have multiple components can exhibit properties that are different from the individual components and often they provide access to phenomena and properties unavailable to single component materials. The advantage of the supramolecular approach shown in Figure 5.2 is that any target molecule capable of forming hydrogen bonds can in principle be complexed with a set of molecules (with exchangeable groups) to form solid solutions. The physical properties of these solid solutions can be finely tuned by changing the nature and relative ratio of the different components. This approach should be useful to all the situations in which binary systems are currently used, but it may find distinctive use in pharmaceutical form selection.<sup>37, 38</sup>

#### 5.14 MULTICOMPONENT SOLIDS WITH DABCO AND 3-X-PHENOLS

We wished to test the generality of our supramolecular approach (Figure 5.2) described above and applied it to other systems. At the beginning, we proceeded with a small change at the molecular level; we replaced the 4-*X*-phenols with 3-*X*-phenols and kept DABCO as the central molecule. It should be noted that very rarely do *meta*- and *para*-substituted compounds show similarity in their structures; though the change we have made appears small, at a supramolecular level this change can be significant.

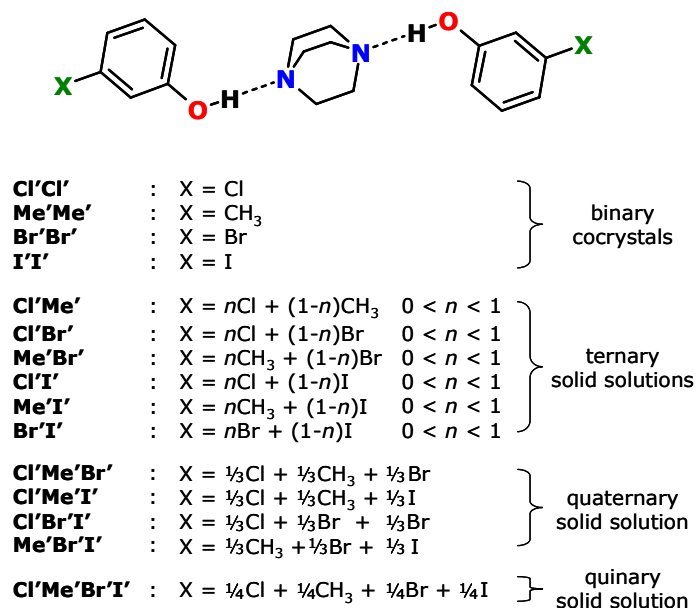


**Figure 5.19** Molecular structures and nomenclature of cocrystals and solid solutions based on DABCO and 3-*X*-phenols.

We have made all the fifteen possible multicomponent solids, four binary cocrystals and eleven three- to five-component solid solutions, using DABCO and 3-*X*-phenols (Figure 5.19). We label these materials in the format **Cl'Cl'** (with a prime next to the exchangeable group) to distinguish them from multicomponent solids made from DABCO and 4-*X*-phenols. We determined the crystal structures of all the cocrystals and most of the solid solutions (Table 5.2). Unlike in the DABCO:4-*X*-phenols, the four cocrystals made from DABCO and 3-*X*-phenols adopt four different crystal structures as suggested by their unit cell parameters given in Table 5.2. Nevertheless, all the cocrystals contain the expected trimolecular assembly in which DABCO and phenol molecules are joined by O–H···N hydrogen bonds. While the trimolecular assembly sits on a two-fold axis in **Cl'Cl'**, in **Me'Me'**, **Br'Br'**, and **I'I'** the trimolecular repeat units are situated in general positions. In addition, one of the two independent phenol molecules in **Me'Me'** is disordered over two positions. Crystal structures of these four cocrystals are given in Figures 5.20 to 5.23.

**Table 5.2** Unit cell data for binary cocrystals and ternary, and quaternary solid solutions made from DABCO and 3-*X*-phenols. Space groups are given in the column *spgr*.

<i>Name</i>	<i>spgr</i>	<i>a</i> (Å)	<i>b</i> (Å)	<i>c</i> (Å)	$\alpha$ (°)	$\beta$ (°)	$\gamma$ (°)	<i>V</i> (Å <sup>3</sup> )
<b>Cl'Cl'</b>	<i>C2/c</i>	17.470	9.357	11.133	90	104.50	90	1761.84
<b>Me'Me'</b>	<i>P-1</i>	6.543	12.518	12.652	115.39	103.20	91.30	902.86
<b>Br'Br'</b>	<i>P2<sub>1</sub>/c</i>	13.679	9.410	15.722	90	112.62	90	1867.97
<b>I'I'</b>	<i>Pbcn</i>	21.637	9.658	18.655	90	90.00	90	3898.16
<b>Cl'Me'</b>	<i>P2<sub>1</sub>/c</i>	13.180	9.397	15.914	90	111.85	90	1829.45
<b>Cl'Br'</b>	<i>P2<sub>1</sub>/c</i>	15.662	9.332	13.414	90	112.21	90	1815.04
<b>Me'Br'</b>	<i>P2<sub>1</sub>/c</i>	15.857	9.364	13.560	90	112.19	90	1864.17
<b>Cl'I'</b>	<i>P2<sub>1</sub>/c</i>	15.798	9.364	13.594	90	111.87	90	1866.28
<b>Br'I'</b>	<i>P2<sub>1</sub>/c</i>	14.030	9.522	15.943	90	112.56	90	1966.97
<b>Cl'Me'Br'</b>	<i>P2<sub>1</sub>/c</i>	13.496	9.407	15.775	90	112.09	90	1855.60
<b>Cl'Me'I'</b>	<i>P2<sub>1</sub>/c</i>	13.691	9.420	15.872	90	111.94	90	1898.84
<b>Cl'Br'I'</b>	<i>P2<sub>1</sub>/c</i>	13.690	9.443	15.787	90	112.15	90	1890.21
<b>Me'Br'I'</b>	<i>P2<sub>1</sub>/c</i>	13.806	9.410	15.825	90	111.97	90	1906.72

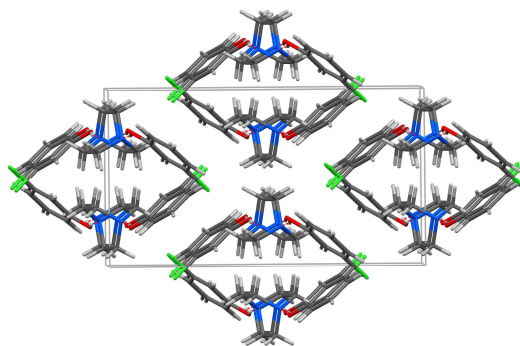


**Figure 5.20** Crystal structure of **Cl'Cl'**. Notice the similarity between this structure and the structures of **ClCl** and **MeMe** belonging to 4-*X*-phenols (Figure 5.6).

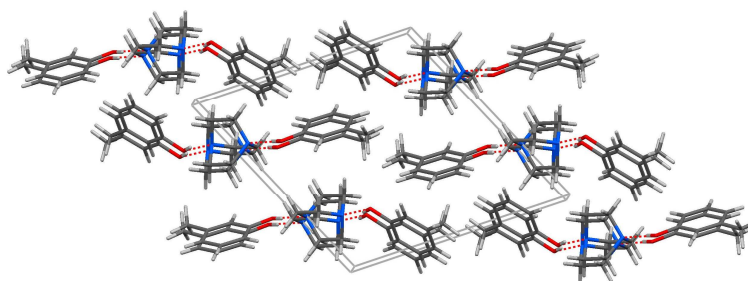


**Figure 5.21** Crystal structure of **Me'Me'**. One of the two *m*-cresol molecules are disordered over two positions; only one position is shown here. Contrast this structure with that of **Cl'Cl'** (Figure 5.20).

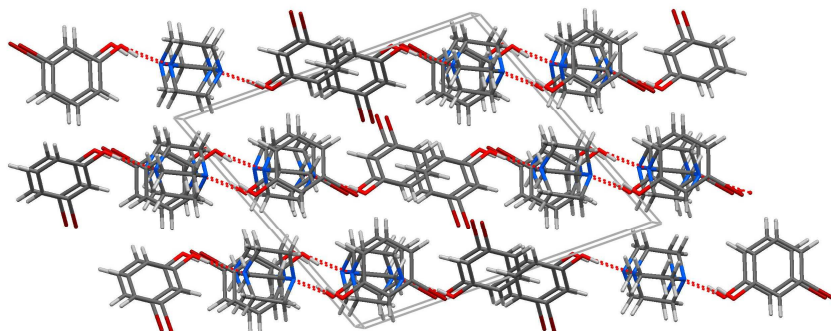


**Figure 5.22** Crystal structure of **Br'Br'**. Contrast this structure with those of **Cl'Cl'** (Figure 5.20) and **Me'Me'** (Figure 5.21).

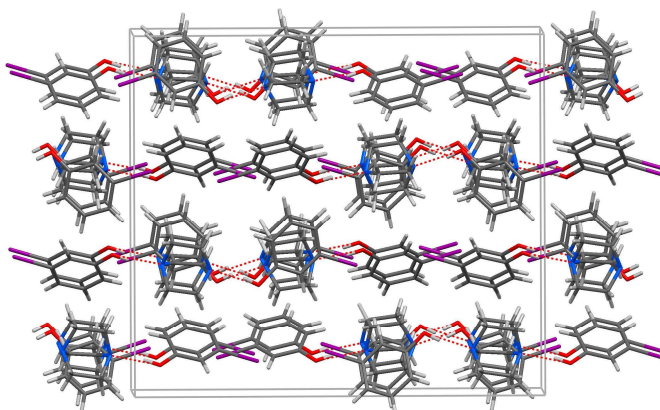


**Figure 5.23** Crystal structure of **IT'**. Contrast this structure with the structures of other three congeners (Figures 5.20-5.22).

The crystal structure of **Cl'Cl'**, the smallest of the four **X'X'** cocrystals, is isostructural to those of **ClCl** and **MeMe**. The other three cocrystals adopt different structures to accommodate intermolecular interactions specific to the corresponding exchangeable group. In **Me'Me'** the disordered phenol rings are situated atop the DABCO molecule such that short  $C-H\cdots\pi$  contacts can be formed with the phenol acting as the  $C-H\cdots\pi$  acceptor and DABCO acting as the donor. Short  $Br\cdots\pi$  interactions are found in **Br'Br'**; one of the two symmetry independent 3-bromophenol molecules is connected to another symmetry related molecule through short contact between the Br-atom and center-point of a  $C=C$  in the ring ( $d_{Br\cdots\pi}$ : 3.35 Å and  $\theta_{C-Br\cdots\pi}$ : 174.2°). Charge transfer interactions between halogen atom and aromatic ring are well-known; the larger the halogen atom, the greater the polarizability, and greater is the stability of the interaction. The second symmetry independent phenol molecule in **Br'Br'** forms a  $C-H\cdots O$  hydrogen bonded

dimer with an inversion related molecule ( $d_{C\cdots O}$ : 3.34Å,  $d_{H\cdots O}$ : 2.47Å, and  $\theta_{C-H\cdots O}$ : 149.2°). In **II'** the I-atom of one phenol molecule is connected to the I-atom on another phenol molecule (that is not related by symmetry) at a separation of 3.69Å.

While the overall crystal structures are a result of delicate interplay between various intermolecular interactions in the solid state and conditions under which the crystals are grown, the differences between these four cocrystals seem to originate from the different steric (*size*) and chemical (*noncovalent bonding*) requirements of the groups Cl, Me, Br and I. These findings are of concern because our goal in this work is to prepare to supramolecular solid solutions that contain various combinations of these phenols. One of the three requirements for forming molecular solid solutions, postulated by Kitaigorodskii, is that two components should have similar crystal structures. The other two requirements are the similarity in size and similarity in shape of the components. Our concern is alleviated to some extent by the observation that the trimolecular assemblies in four cocrystals exhibit similar conformations (Figure 5.24).

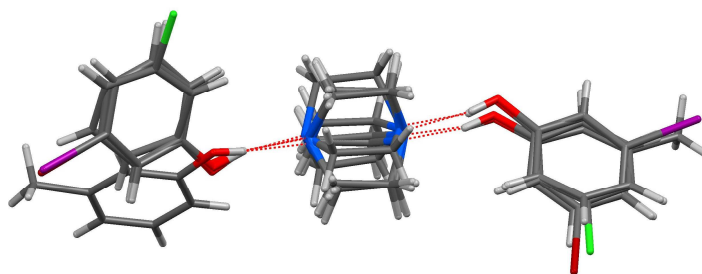


**Figure 5.24** Overlay of trimolecular assemblies in **X'X'** binary cocrystals.

It is instructive to ask the question, why do **X'X'** crystals show so much structural diversity compared to **XX** crystals? The answer has two important interrelated components. The conformational freedom of the trimolecular assembly coupled with the placement of X group at the *meta* position can lead to different starting geometries in solution. These different geometries can be seen in the overlay diagram shown in Figure 5.24. When the X groups are at the *para* position, the rotation of phenols around the O–H $\cdots$ N hydrogen bonds does not lead to *cis-trans* type of geometries. In other words, the hydrogen bonded assemblies in **XX** complexes have fewer starting geometries than in **X'X'** systems. These observations suggest that crystal design with conformationally flexible molecules or *supermolecules* has lower predictability than their rigid counterparts. In the case of supermolecules, one way to minimize this problem is to use multi-point hydrogen bonding synthons between the components. In the present design, we use a single point synthon, O–H $\cdots$ N hydrogen bond, as a design element. We show in Chapter 6 that use of a two-point synthon gives greater predictability over local geometry and minimizes complications in the outcomes of crystal design.

The high overlay coefficient between hydrogen bonded assemblies of different **X'X'** cocrystals encouraged us to attempt the preparation of solid solutions using these

materials. Indeed, mixing of DABCO and different 3-*X*-phenols in appropriate ratios in solution followed by evaporation yielded single crystals of the respective multicomponent solid solutions. We determined the crystal structures of most of the ternary solid solutions and unit cell parameters for quaternary and quinary solid solutions (Table 5.2). Figure 5.25 shows the trimolecular repeat units in **Cl'Cl'** and **Br'Br'** cocrystals and the 50:50 ternary solid solution **Cl'Br'**. This representative example shows that it is indeed possible to make solid solutions of **X'X'** cocrystals even though individually they adopt very different structures. One of the implicit advantages of the supramolecular solid solutions is that the repeat unit is a supermolecule that is *larger* than the molecules. Thus, within these supermolecules the change we make (e.g., replacing Cl with Br) is relatively smaller and the overall similarity coefficient between the repeat units is higher, which allows them to form solid solutions.

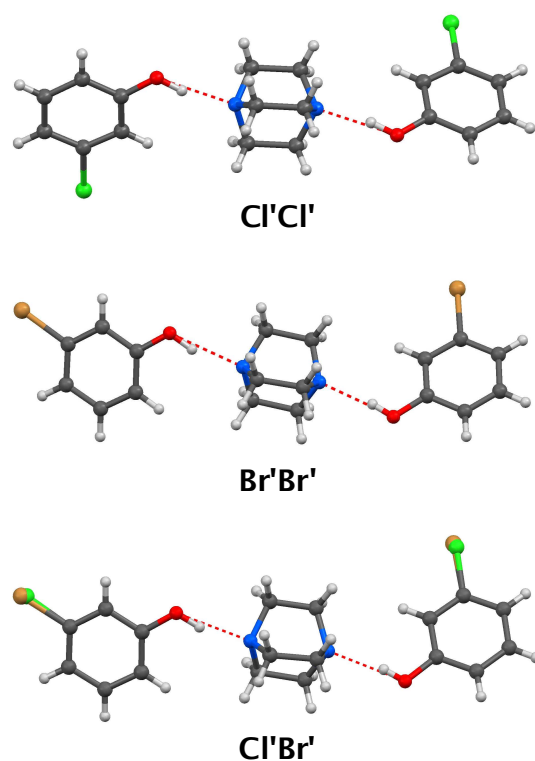


**Figure 5.25** Trimolecular assemblies in **Cl'Cl'** and **Br'Br'** cocrystals and **Cl'Br'** solid solution. Note that two chlorophenol molecules in **Cl'Cl'** are related by a two-fold axis; in **Br'Br'** the phenol molecules are symmetry independent. The **Cl'Br'** solid solution adopts the structure of **Br'Br'** cocrystal.

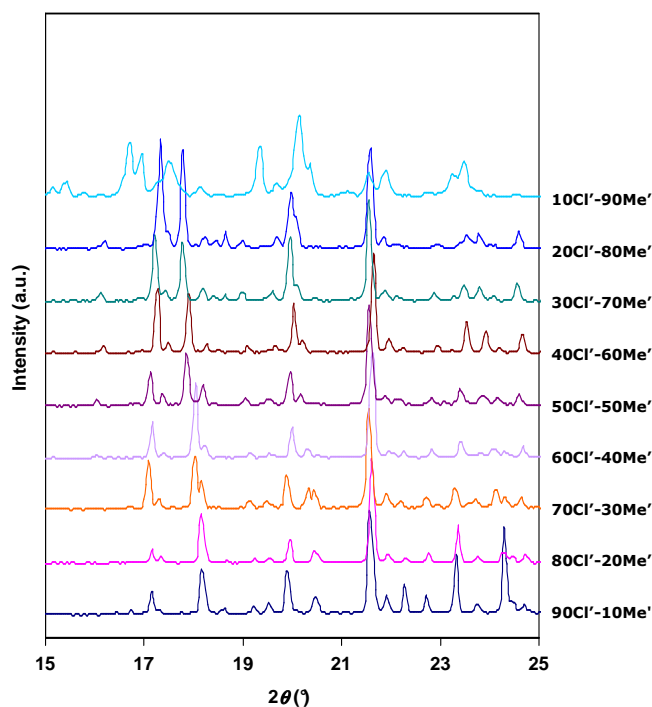


**Figure 5.26** PXRD Patterns of **Cl'Me'** series of solid solutions. We labeled these solid solutions such that the total phenol content in them is 100%. Thus, 60Cl'-40Me' indicates that the ternary solid solution consists of 60% 3-chlorophenol and 40% *m*-cresol.

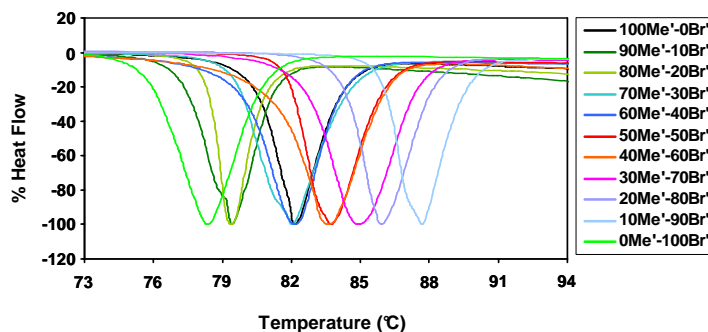


**Figure 5.27** DSC traces of **Cl'Me'** series of solid solutions. Notice the gradual change in the melting points.

Following our success in the preparation of ternary solid solutions and the other higher order solutions containing equimolar quantities of 3-*X*-phenols, we prepared the continuous series **Cl'Me'**, **Cl'Br'** and **Me'Br'** solid solutions. In each series, we prepared a total of nine solid solutions and characterized them with IR and NMR spectroscopy and PXRD analysis. Figure 5.26 shows the diffraction patterns of **Cl'Me'** series as a

representative example. Again, the structures smoothly transition from one cocrystal (**Cl'Cl'**) to another (**Me'Me'**). As with the **XY** series, the **X'Y'** series of solid solutions also showed a continuous change in their physical properties. The melting endotherms determined by DSC showed gradual transition in the melting points of different solid solutions. Figure 5.27 shows the DSC thermograms of **Me'Br'** series as a representative example.

### 5.15 MULTICOMPONENT SOLIDS WITH 4,4'-BIPYRIDYL AND 4- AND 3-X-PHENOLS

To further examine the efficacy of our approach, we began the preparation of solid solutions that contained a new target central molecule while preserving the peripheral phenol molecules. The central molecule we chose for this purpose is 4,4'-bipyridyl (**BP**), an aromatic diaza compound that is, like DABCO, capable of forming two hydrogen bonds with phenolic donors. The N-atoms are less basic in **BP** than they are in DABCO and the backbone is aromatic. While the lower basicity can decrease the potency of cocrystallization, the aromatic rings in **BP** can lead to well-developed and more ordered crystals. Our work in these systems is in early stages and in this chapter we limit our discussion to some binary cocrystals and ternary solid solutions. We expect that this system will also yield higher order solid solutions just the way DABCO complexes did. Table 5.3 shows the unit cell data on some of the multicomponent solids we have crystallized so far. This data shows that **BP-X** series **BP-X'** series of cocrystals adopt different structures; within each series however different cocrystals adopt similar structures. We have shown the repeat units of some of the crystal structures in Figure 5.28.

**Table 5.3** Unit cell data for binary cocrystals and ternary solid solutions made from BP and 3-X- and 4-X-phenols. Space groups are given in the column *spgr*.

<i>Name</i>	<i>spgr</i>	<i>a</i> (Å)	<i>b</i> (Å)	<i>c</i> (Å)	$\beta$ (°)	<i>V</i> (Å <sup>3</sup> )
<b>BP-BrBr</b>	<i>P2<sub>1</sub>/c</i>	11.710	9.959	18.703	107.25	2083.0
<b>BP-II</b>	<i>P2<sub>1</sub>/c</i>	19.369	9.612	19.327	110.78	3364.4
<b>BP-BrI</b>	<i>P2<sub>1</sub>/c</i>	19.091	9.567	19.411	112.00	3287.0
<b>BP-Cl'Cl'</b>	<i>P2<sub>1</sub>/c</i>	7.379	17.749	7.709	99.52	995.8
<b>BP-Br'Br'</b>	<i>P2<sub>1</sub>/c</i>	7.550	17.502	7.811	100.51	1014.8
<b>BP-I'I'</b>	<i>P2<sub>1</sub>/c</i>	8.061	16.140	8.585	104.42	1081.8
<b>BP-Cl'Br'</b>	<i>P2<sub>1</sub>/c</i>	7.466	17.639	7.755	99.99	1005.7
<b>BP-Me'Br'</b>	<i>P2<sub>1</sub>/c</i>	7.577	17.436	7.868	100.62	1021.7
<b>BP-Cl'I'</b>	<i>P2<sub>1</sub>/c</i>	7.748	17.050	8.094	101.89	1046.3
<b>BP-Br'I'</b>	<i>P2<sub>1</sub>/c</i>	7.834	16.826	8.204	102.50	1055.8

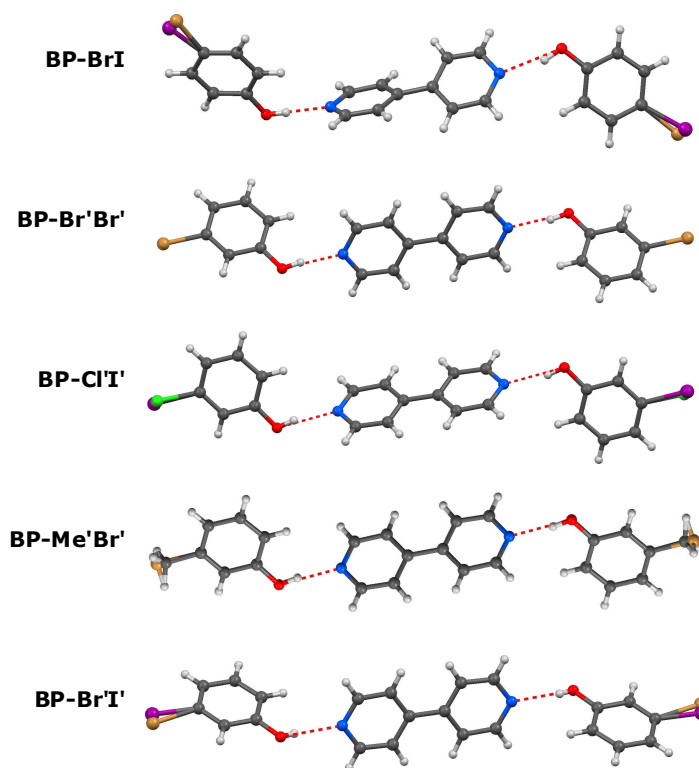


**Figure 5.28** Trimolecular assemblies in some of the cocrystals and solid solutions formed by BP and 3-*X*- and 4-*X*-phenols.

### 5.16 MULTICOMPONENT SOLIDS WITH HYDROXY...AMINO RECOGNITION

The organic alloys we described so far have used a single point hydrogen bond between hydroxy and aza groups. Once the hydrogen bonds are formed between a central diaza molecule and two peripheral phenol molecules, the assembly becomes ‘saturated’ and does not form further hydrogen bonds. In other words, the supramolecular repeat unit in these complexes is a *discrete* trimolecular assembly. We wished to further test the generality of our approach by applying it to compounds that can form extended hydrogen bonded arrays upon cocrystallization.

Hydroxy and amine groups are common functional groups in organic chemistry and for the most part they have been used in crystal engineering as hydrogen bond *donors* with *other* acceptors such as pyridyl N-atom or carbonyl O-atom. In the early 1990s it has been explicitly recognized that (a) the hydroxy group has two lone pairs and one H-atom and amine group has two H-atoms and one lone pair (Figure 5.29a) and (b) these two groups are complementary in terms of their hydrogen bonding capabilities.<sup>39-42</sup> If the two groups are present in 1:1 stoichiometry in a crystal, each group would form a total of four

bonds, one covalent and three noncovalent. The hydroxy group donates one hydrogen bond and accepts two, and the amine group donates two and accepts one hydrogen bond. Each heteroatom then adopts a tetrahedral geometry which allows us to deduce possible supramolecular structures.<sup>39</sup> Hydroxy...amino recognition refers to the noncovalent bonding of these two groups such that each group is *saturated* with respect to hydrogen bonding and adopts a tetrahedral geometry.<sup>43</sup> It is possible that other factors can influence the bonding between hydroxy and amine groups and prevent them from forming hydroxy...amino recognition.<sup>44</sup>

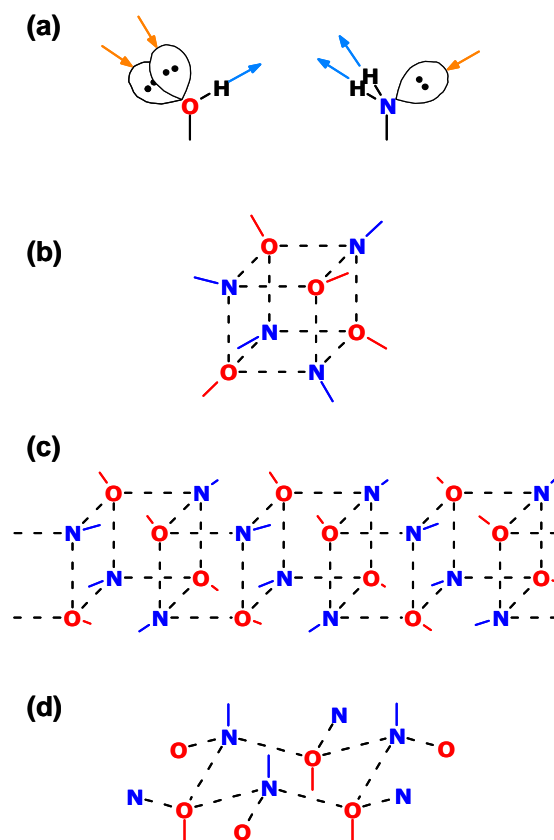


**Figure 5.29** (a) Hydrogen bond complementarity of hydroxy and amine groups showing the lone pairs and H-atoms. (b-d) Some superstructures resulting from hydroxy...amino recognition. See text for details.

Figure 5.29 shows some of the possible superstructures that can be built from hydroxy...amino recognition. These structures range from discrete clusters such as the cubic arrangement (Figure 5.29b), one-dimensional tapes such as adjoined squares across opposite edges (Figure 5.29c) or two-dimensional sheets such as adjoined hexagons (Figure 5.29d) across all edges (honeycomb structure if the hexagon is planar and

wurtzite structure if the hexagon adopts a chair conformation).<sup>39</sup> There are other possible superstructures that can result from hydroxy...amino recognition.

In order to apply the hydroxy...amino recognition to our approach of supramolecular solid solutions, we have selected hydroquinone (HQ) as central molecule and *para*-substituted anilines (4-*X*-anilines) as the peripheral molecules. A distinct advantage with this system is that we can choose 1,4-diaminobenzene (phenylenediamine, PD) as the central molecule and *para*-substituted phenols (4-*X*-phenols) as the peripheral molecules. When taken together, the HQ:4-*X*-aniline complexes and PD:4-*X*-phenol complexes can be isostructural and provide us with yet another way of incorporating multiple molecules into a single crystalline solid solution. To date, we have been able to crystallize all the four possible cocrystals and ternary solid solutions of HQ:4-*X*-aniline complexes and two cocrystals of the PD: 4-*X*-phenol complexes (Table 5.4)

**Table 5.4** Unit cell data for binary cocrystals and ternary solid solutions made from HQ and 4-*X*-anilines and binary cocrystals made from PD and 4-*X*-phenols. Space groups are given in the column *spgr*.

<i>Name</i>	<i>spgr</i>	<i>a</i> (Å)	<i>b</i> (Å)	<i>c</i> (Å)	$\alpha$ (°)	$\beta$ (°)	$\gamma$ (°)	<i>V</i> (Å <sup>3</sup> )
<b>HQ-ClCl</b>	<i>P2<sub>1</sub>/c</i>	10.674	6.152	13.405	90	97.57	90	872.60
<b>HQ-MeMe</b>	<i>P-1</i>	6.013	8.527	17.815	86.40	84.87	89.88	908.00
<b>HQ-BrBr</b>	<i>P2<sub>1</sub>/n</i>	4.522	9.063	22.172	90	93.49	90	907.03
<b>HQ-II</b>	<i>P2<sub>1</sub>/c</i>	10.873	4.930	18.108	90	93.24	90	969.21
<b>HQ-ClBr</b>	<i>P2<sub>1</sub>/n</i>	4.569	9.003	21.791	90	92.94	90	895.27
<b>HQ-CII</b>	<i>P2<sub>1</sub>/c</i>	10.661	4.868	17.958	90	94.21	90	929.47
<b>PD-BrBr</b>	<i>P2<sub>1</sub>/c</i>	10.637	4.829	18.159	90	95.60	90	928.19
<b>PD-II</b>	<i>P2<sub>1</sub>/c</i>	10.616	5.376	16.479	90	92.19	90	939.67

We crystallized the multicomponent solids in Table 5.4 using combinations of solutions that included ethanol, methanol, ether and benzene. The anilines tended to decompose in solutions due to exposure to light and air and frequently posed problems in preparing good quality crystals. Crystallizations in dark and under relatively dry environments gave purer crystalline products. We characterized the cocrystals and solid solutions by IR and NMR spectroscopy, PXRD and DSC as well as single crystal diffraction analysis.

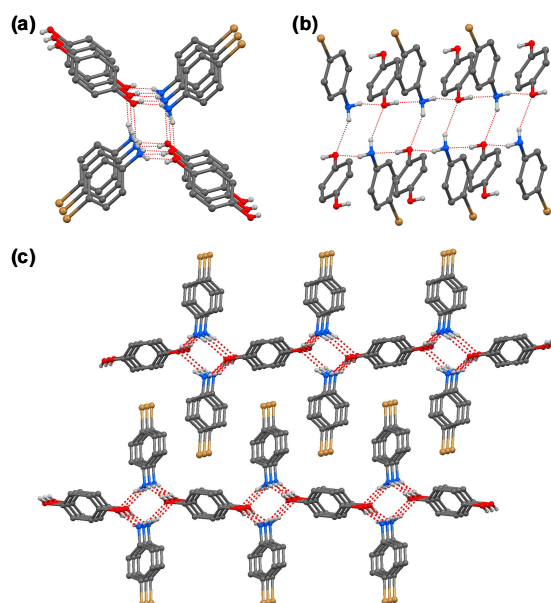


**Figure 5.30** Crystal structure of **HQ-BrBr** showing (a-b) hydroxy···amino recognition in Figure 5.29c and (c) interlayer packing.

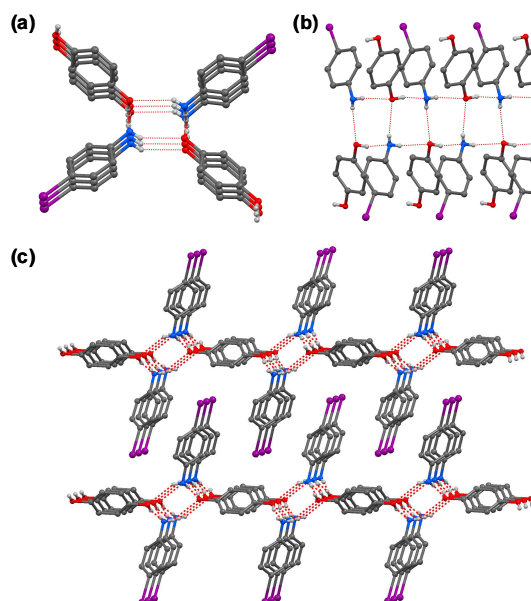


**Figure 5.31** Crystal structure of **HQ-II** showing (a-b) hydroxy···amino recognition in Figure 5.29c and (c) interlayer packing. Notice the difference in molecular orientations compared to **HQ-BrBr**.

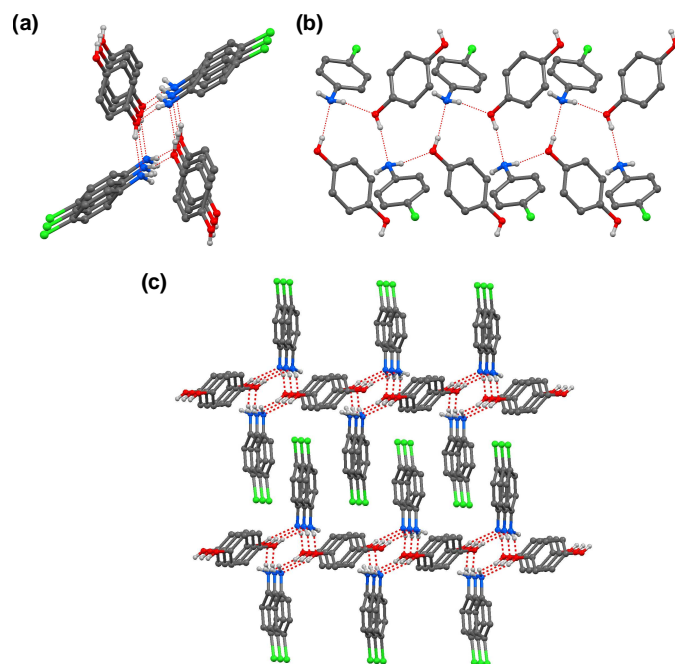


**Figure 5.32** Crystal structure of **HQ-CICI** showing (a-b) hydroxy...amino recognition in Figure 5.29c that is disrupted at one N-H group and (c) interlayer packing.

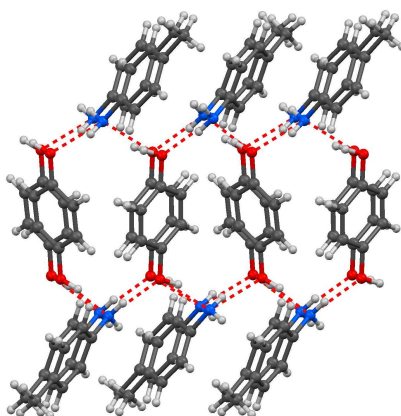


**Figure 5.33** Crystal structure of **HQ-MeMe** showing a disrupted hydroxy...amino recognition pattern. Note that one of the two N-H groups and a C-H from methyl group form N-H... $\pi$  and C-H... $\pi$  interactions (not drawn on image) with adjacent toluidine rings.

Figures 5.30a and 5.30b show the hydrogen bonding around hydroxy and amine groups in **HQ-BrBr**. Each of the heteroatom is involved in three hydrogen bonds and adopts tetrahedral geometry. The overall superstructure is that of adjoined squares, a one-

dimensional pattern, shown in Figure 5.29c. Each HQ molecule is involved in such superstructure at both hydroxy groups leading a two-dimensional layer structure (Figure 5.30c). Bromoaniline molecules project outward from this layer at each corner of the square and lead to an interdigitated packing of successive layers. Crystals of **HQ-II** adopt a very similar structure (Figure 5.31) with hydroxy...amino recognition in Figure 5.29c and an interdigitated layered packing.

Though **HQ-CICl** adopts a similar overall structure (Figure 5.32c), it does not exhibit full hydroxy...amino recognition (Figures 5.32a and 5.32b). In this structure, one of the N-H groups does not form N-H...O hydrogen bond; instead it forms an N-H... $\pi$  bond with the neighboring HQ molecule. The **HQ-MeMe** cocrystal adopts a completely different structure (Figure 5.33) with broken hydroxy...amino recognition. In this structure also, one of the two N-H groups is involved in N-H... $\pi$  bond; this time, however, the bond is donated to the aromatic ring of a neighboring aniline molecule.

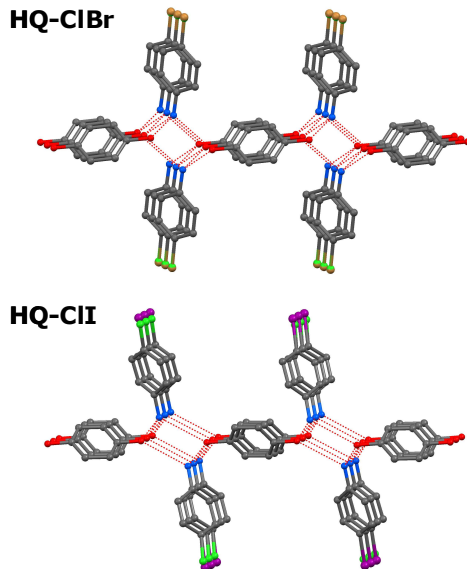


**Figure 5.34** Crystal structures of **HQ-CIBr** and **HQ-CII** showing portions of a single layer. Note that **HQ-CIBr** is isostructural to **HQ-BrBr** (Figure 5.30) and **HQ-CII** is isostructural to **HQ-II** (Figure 5.31).

Despite the differences in these structures, different *binary* cocrystals can be combined together to form *ternary* solid solutions. To date, we have been able to obtain diffraction quality crystals of two ternary solid solutions. Crystals of **HQ-CIBr** are isostructural to **HQ-BrBr** and crystals of **HQ-CII** are isostructural to **HQ-II** (Figure 5.34). Further characterization with DSC showed that the solid solutions have distinct melting endotherms compared to the individual cocrystals or physical mixtures of corresponding cocrystals.

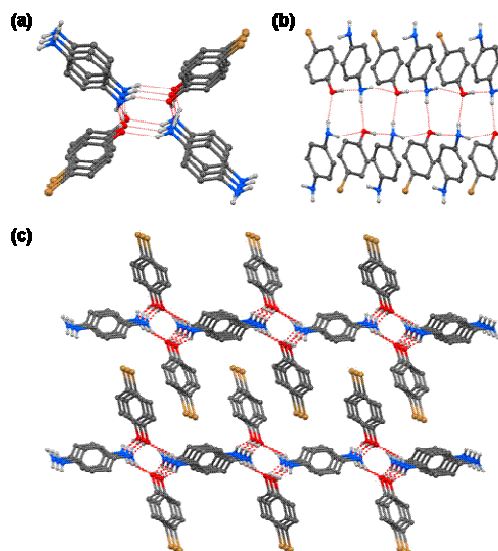


**Figure 5.35** Crystal structure of **PD-BrBr** showing (a-b) hydroxy...amino recognition in Figure 5.29c and (c) interlayer packing. Note that this structure is similar to **HQ-II**.

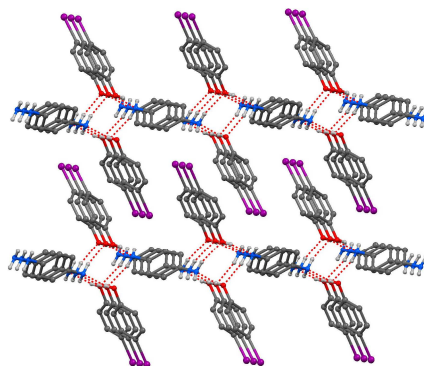


**Figure 5.36** Crystal structure of **PD-II** showing the interlayer packing.

After successfully preparing the HQ based cocrystals, we wished to test if PD based cocrystals can be formed with 4-*X*-phenols, and if such cocrystals exhibited any relationship with the corresponding HQ cocrystals. Table 5.4 shows that the two cocrystals **PD-BrBr** and **PD-II** indeed show similarities to **HQ-II** at the unit cell level. Full structural determination showed that **PD-BrBr** is isostructural with **HQ-II** (Figure 5.35) and **PD-II** has the same overall structure (Figure 5.36) as **HQ-II** but with some variations in the parameters of hydroxy...amino recognition. These structures show some of the diversity seen in compounds containing stoichiometric amounts of hydroxy and amine groups. They also illustrate the power of supramolecular solid solutions to create multicomponent solids using different types of supramolecular synthons and target materials.

### 5.17 SUMMARY AND CONCLUSION

We have developed a supramolecular approach for the preparation of multicomponent organic alloys.<sup>28</sup> This approach involves the (a) preparation of molecular assemblies in solution from a target molecule and a set of other molecules that have the same size and shape and (b) crystallization of all the components into a single crystalline solid. We call the obtained products supramolecular solid solutions because the repeat unit in these alloys is a molecular assembly (Figure 5.2).

We have successfully prepared six different series of multicomponent solids; they included four different target molecules and two different supramolecular synthons. We showed that solid solutions can be made from cocrystals that adopt different structures independently. Often in a continuous series of solid solutions the structure changes from one cocrystal type to the other.

The approach we developed for multicomponent solids is generic; it is applicable to any target molecule capable of forming hydrogen bonding or other specific intermolecular interactions. Cocrystals are extensively used in the preparation of photographic, magnetic, optical, liquid crystalline and pharmaceutical materials.<sup>1</sup> We believe extension of our concept to these research areas will lead to new and unforeseen discoveries and materials with improved properties. In the pharmaceutical realm, for example, the ability to continuously tune physical properties is rarely explored. In addition, we believe that supramolecular solid solutions offer a way to prepare cocrystals that are otherwise unyielding by methods such as seeding or additives. We envisage several applications of our approach that include pharmaceutical alloys with fine-tunable properties, crystals with reduced symmetry (for nonlinear optics), organic semiconductors and templates for solid state photochemistry.

**5.18 REFERENCES**

1. Herbststein, F. H., *Crystalline Molecular Complexes and Compounds: Structure and Principles*. Oxford University Press: New York, **2006**.
2. Desiraju, G. R., *Crystal Engineering: The Design of Organic Solids*. Elsevier: Amsterdam, **1989**.
3. Etter, M. C., Hydrogen bonds as design elements in organic chemistry. *J. Phys. Chem.* **1991**, *95*, 4601-4610.
4. Foster, R., *Organic Charge-Transfer Complexes*. Academic Press: New York, **1969**.
5. Kitaigorodsky, A. I., *Mixed Crystals*. Springer-Verlag: New York, **1984**.
6. Lehn, J. M., *Supramolecular Chemistry: Concepts and Perspectives*. John-Wiley: New York, **1995**.
7. MacDonald, J. C.; Whitesides, G. M., Solid-State Structures of Hydrogen-Bonded Tapes Based on Cyclic Secondary Diamides. *Chem. Rev.* **1994**, *94*, 2383-2420.
8. We do not consider solvates in which the component selection is largely circumstantial than design. .
9. Aakeroy, C. B.; Desper, J.; Urbina, J. F., Supramolecular reagents: versatile tools for non-covalent synthesis. *Chem. Commun.* **2005**, 2820-2822.
10. Aakeroy, C. B.; Beatty, A. M.; Helfrich, B. A., "Total synthesis" supramolecular style: design and hydrogen-bond-directed assembly of ternary supermolecules. *Angew. Chem. Int. Ed.* **2001**, *40*, 3240-3242.
11. Bhogala, B. R.; Basavoju, S.; Nangia, A., Three-Component Carboxylic Acid-Bipyridine Lattice Inclusion Host. Supramolecular Synthesis of Ternary Cocrystals. *Cryst. Growth. Des.* **2005**, *5*, 1683-1686.
12. Cheung, E. Y.; Kitchin, S. J.; Harris, K. D. M.; Imai, Y.; Tajima, N.; Kuroda, R., Direct Structure Determination of a Multicomponent Molecular Crystal Prepared by a Solid-State Grinding Procedure. *J. Am. Chem. Soc.* **2003**, *125*, 14658-14659.
13. Friscic, T.; Trask, A. V.; Jones, W.; Motherwell, W. D. S., Screening of Inclusion Compounds and Systematic Construction of Three-Component solids by Liquid-Assisted Grinding. *Angew. Chem. Int. Ed.* **2006**, *45*, 7546-7550.
14. Lynch, D. E.; Smith, G.; Byriel, K. A.; Kennard, C. H. L., The unique occurrence of an organic tri-heteromolecular adduct: the crystal structure of the (3:1:1) 4-aminobenzoic acid-2,4,6-trinitrobenzoic acid-1,3,5-trinitrobenzene cocrystal. *J. Chem. Soc., Chem. Commun.* **1992**, 300-301.
15. Smolka, T.; Boese, R.; Sustmann, R., Design of a three component crystal based on the cocrystal of phenazine and 2,2'-dihydroxybiphenyl. *Struct. Chem.* **1999**, *10*, 429-431.
16. Solid solutions of metals, or alloys, are easy to form because of the spherical shape of the components and the isotropic nature of their inter-component interactions.
17. For an exception, see: Sada, K.; Inoue, K.; Tanaka, T.; Epergyes, A.; Tanaka, A.; Tohnai, N.; Matsumoto, A.; Miyata, M., Multicomponent organic alloys based on organic layered crystals. *Angew. Chem. Int. Ed.* **2005**, *44*, 7059-7062. Note, however, that the multicomponent solid solutions in this work are based on ionic components.
18. For example, solid solutions of insulin and a lipophilically modified insulin show superior *in vivo* therapeutic properties. See: Brader, M. L.; Sukumar, M.; Pekar, A. H.; McClellan, D. S.; Chance, R. E.; Flora, D. B.; Cox, A. L.; Irwin, L.; Myers, S. R.,

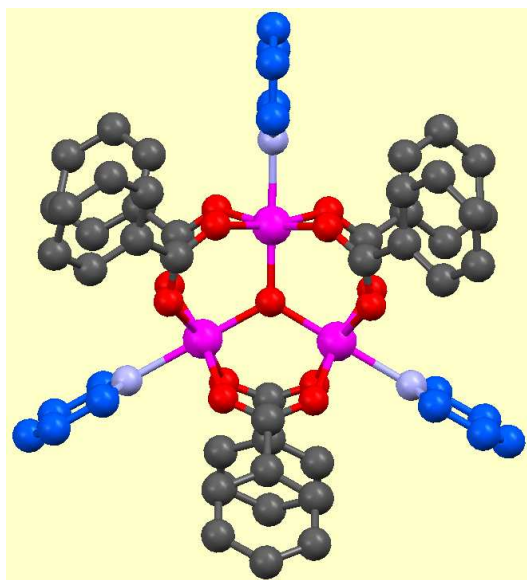
- Hybrid insulin cocrystals for controlled release delivery. *Nature Biotech.* **2002**, *20*, 800-804. In this paper, homogeneous mixtures of insulin and its derivative are described as cocrystals. We note that these mixtures, though crystalline, are in fact solid solutions.
19. Bernstein, J., *Polymorphism in Molecular Crystals*. Clarendon Press: Oxford, **2002**.
  20. Brittain, H. G., *Polymorphism in Pharmaceutical Solids*. Marcel Dekker: New York, **1999**.
  21. Byrn, S. R.; Pfeiffer, R. R.; Stowell, J. G., *Solid-State Chemistry of Drugs*. 2nd ed.; SSCI: West Lafayette, **1999**.
  22. Hilfiker, R., *Polymorphism in the Pharmaceutical Industry*. Wiley-VCH: Weinheim, **2006**.
  23. Etter, M. C., Encoding and decoding hydrogen-bond patterns of organic compounds. *Acc. Chem. Res.* **1990**, *23*, 120-126.
  24. Stahly, G. P., Diversity in Single- and Multiple-Component Crystals. The Search for and Prevalence of Polymorphs and Cocrystals. *Cryst. Growth. Des.* **2007**, *7*, 1007-1026.
  25. Trask, A. V.; Motherwell, W. D. S.; Jones, W., Pharmaceutical Cocrystallization: Engineering a Remedy for Caffeine Hydration. *Cryst. Growth. Des.* **2005**, *5*, 1013-1021.
  26. Vishweshwar, P.; McMahon, J. A.; Bis, J. A.; Zaworotko, M. J., Pharmaceutical cocrystals. *J. Pharm. Sci.* **2006**, *95*, 499-516.
  27. Desiraju, G. R., Supramolecular synthons in crystal engineering - a new organic synthesis. *Angew. Chem. Int. Ed.* **1995**, *34*, 2311-2327.
  28. Dabros, M.; Emery, P. R.; Thalladi, V. R., A supramolecular approach to organic alloys: cocrystals and three- and four-component solid solutions of 1,4-diazabicyclo[2.2.2]octane and 4-X-phenols (X = Cl, CH<sub>3</sub>, Br). *Angew. Chem. Int. Ed.* **2007**, *46*, 4132-4135.
  29. Kitaigorodsky, A. I., *Molecular Crystals and Molecules*. Academic Press: New York, **1973**.
  30. Pedireddi, V. R.; Reddy, D. S.; Goud, B. S.; Craig, D. C.; Rae, A. D.; Desiraju, G. R., The nature of halogen...halogen interactions and the crystal structure of 1,3,5,7-tetraiodadamantane. *J. Chem. Soc., Perkin Trans. 2* **1994**, 2353-2360.
  31. The powder X-ray data were collected on a Rigaku Geigerflex D-MAX/A diffractometer or Bruker D8 Focus diffractometer using Cu-K $\alpha$  radiation. The instruments were equipped with vertical goniometers, scintillation counters as detectors, and applied Bragg-Brentano geometry for data collection. Samples were finely ground using a mortar and pestle and transferred to a glass sample holder that had loading dimensions 1.6 cm x 2 cm. The data were collected in the  $2\theta$  range 5-50° (step size = 0.05°) and at a scan rate of 2° per minute.
  32. Braga, D.; Grepioni, F., Making crystals from crystals: a green route to crystal engineering and polymorphism. *Chem. Commun.* **2005**, 3635-3645.
  33. Patil, A. O.; Curtin, D. Y.; Paul, I. C., Solid-state formation of quinhydrone from their components. Use of solid-solid reactions to prepare compounds not accessible from solution. *J. Am. Chem. Soc.* **1984**, *106*, 348-353.
  34. Trask, A. V.; Motherwell, W. D. S.; Jones, W., Solvent-drop grinding: green polymorph control of cocrystallisation. *Chem. Commun.* **2004**, 890-891.

35. Chadwick, K.; Davey, R.; Cross, W., How does grinding produce co-crystals? Insights from the case of benzophenone and diphenylamine. **2007**, *9*, 732-734.
36. Rastogi, R. P.; Bassi, P. S.; Chadha, S. L., Kinetics of reaction between naphthalene and picric acid in the solid state. *J. Phys. Chem.* **1962**, *66*, 2707-2708.
37. Almarsson, O.; Zaworotko, M. J., Crystal engineering of the composition of pharmaceutical phases. Do pharmaceutical co-crystals represent a new path to improved medicines? *Chem. Commun.* **2004**, 1889-1896.
38. Trask, A. V.; Motherwell, W. D. S.; Jones, W., Pharmaceutical Cocrystallization: Engineering a Remedy for Caffeine Hydration. *Cryst. Growth Des.* **2005**, *5*, 1013-1021.
39. Ermer, O.; Eling, A., Molecular recognition among alcohols and amines: super-tetrahedral crystal architectures of linear diphenol-diamine complexes and aminophenols. *J. Chem. Soc., Perkin Trans. 2* **1994**, 925-944.
40. Hanessian, S.; Gomtsyan, A.; Simard, M.; Roelens, S., Molecular Recognition and Self-Assembly by Weak Hydrogen Bonding: Unprecedented Supramolecular Helicate Structures from Diamine/Diol Motifs. *J. Am. Chem. Soc.* **1994**, *116*, 4495-4496.
41. Hanessian, S.; Simard, M.; Roelens, S., Molecular Recognition and Self-Assembly by Non-amidic Hydrogen Bonding. An Exceptional Assembler of Neutral and Charged Supramolecular Structures. *J. Am. Chem. Soc.* **1995**, *117*, 7630-7645.
42. Loehlin, J. H.; Etter, M. C.; Gendreau, C.; Cervasio, E., Hydrogen-Bond Patterns in Several 2:1 Amine-Phenol Cocrystals. *Chem. Mater.* **1994**, *6*, 1218-1221.
43. Dey, A.; Kirchner, M. T.; Vangala, V. R.; Desiraju, G. R.; Mondal, R.; Howard, J. A. K., Crystal Structure Prediction of Aminols: Advantages of a Supramolecular Synthon Approach with Experimental Structures. *J. Am. Chem. Soc.* **2005**, *127*, 10545-10559.
44. Allen, F. H.; Hoy, V. J.; Howard, J. A. K.; Thalladi, V. R.; Desiraju, G. R.; Wilson, C. C.; McIntyre, G. J., Crystal Engineering and Correspondence between Molecular and Crystal Structures. Are 2- and 3-Aminophenols Anomalous? *J. Am. Chem. Soc.* **1997**, *119*, 3477-3480.

THIS PAGE LEFT INTENTIONALLY BLANK

# 6

## SYNTHESIS AND STRUCTURES OF TRIGONAL MANGANESE CARBOXYLATES – TOWARD OCTUPOLAR NONLINEAR OPTICAL MATERIALS



THIS PAGE LEFT INTENTIONALLY BLANK

## 6.1 INTRODUCTION

**6.1.1 Background.** The scope of this thesis chapter is distinct from previous chapters. The work described here has multilevel goals. The initial goal of this work is to make octupolar nonlinear optical (NLO) materials based on trigonal metal-carboxylate (TMC) clusters. Because we use manganese as the metal species in these TMCs and because extended frameworks based on the TMCs can potentially have defined cavities within the crystals, this project has other attendant goals in the creation of magnetic and porous materials. Materials with NLO characteristics are the basis for the modulation and routing functions of current optoelectronic and future all-optical devices.<sup>1</sup> These devices are used in a range of industries, but most notably in telecommunications and optical data processing. Currently, widely used NLO materials are inorganic solids, such as  $\text{LiNbO}_3$  (lithium niobate),  $\text{LiB}_3\text{O}_5$  (lithium borate) and  $\text{KH}_2\text{PO}_4$  (potassium dihydrogenphosphate). Purely inorganic solids such as these, though robust and efficient, are difficult to modify and not amenable to create improved optical materials.

**6.1.2 Dipolar Organic Materials.** Studies in the past three decades have shown that organic molecules with “donor–conjugated-bridge–acceptor” (D– $\pi$ –A) geometry possess attractive NLO properties.<sup>2</sup> Nonlinear optical materials based on these *dipolar* molecules display ultrafast response time and better processability compared to traditional inorganic solids. Organic dipolar molecules can be modified to improve NLO properties by increasing the length of the  $\pi$ -electron bridge and the strength of the donor and acceptor groups. Despite this control, D– $\pi$ –A structures have some defects. One of these defects is that dipole-dipole interactions result in anti-parallel (centrosymmetric) molecular arrangement, which causes cancellation of NLO activity in the solid state. To overcome the dipolar intermolecular interactions various approaches have been explored. In one approach, the poled polymer technique, a polymer with covalently attached dipoles is heated close to its glass-transition temperature and then cooled to room temperature while a strong electric field is applied.<sup>1</sup> Under the influence of the field, the dipolar molecules are forced to arrange in acentric fashion. The drawback of this method is that molecules relax, with time, back into anti-parallel orientations.

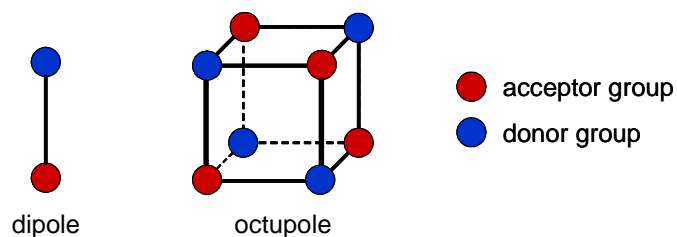


**Figure 6.1** Schematic representation of dipole and octupole.

**6.1.3 Octupolar Symmetries.** To overcome the intrinsic limitations of dipolar species, a new non-dipolar model has been proposed for the creation of NLO materials (Figure 6.1).<sup>3</sup> This model introduced species that have come to be known as *octupolar* molecules.

Octupolar symmetry has several advantages. It removes the ground state dipole moment in the molecules, which can promote assemblies other than anti-parallel centrosymmetric packing. Another major advantage of octupoles is that they are three-dimensional, that is, their hyperpolarizabilities ( $\beta$ s), can be much larger than the one-dimensional dipolar species. In addition, the  $\beta$  of octupoles can be continuously increased with increasing conjugation while that of dipolar structures increases to a maximum value and then decreases with extended conjugation. Yet another advantage of octupoles is that they can be expressed in different symmetries (Figure 6.2), that is, a number of routes can be explored for making new and improved NLO materials.<sup>4</sup>

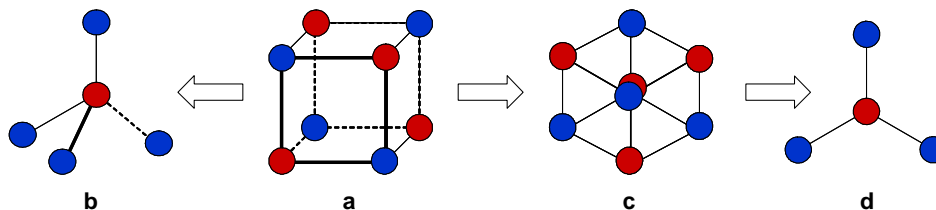


**Figure 6.2** Various symmetries of octupolar systems. (a) Cube octupole with eight alternated charges at the corners. (b) Tetrahedral octupoles generated by projection of the charges into center of the cube. (c) and (d) Trigonal octupoles generated by projection onto the plane of the cube.

**6.1.4 Octupolar Molecular Materials.** First discovered octupolar molecule that showed NLO activity was 1,3,5-triamino-2,4,6-trinitrobenzene.<sup>5</sup> Most of the known trigonal octupolar systems are based on organic molecules. The trigonal (Figures 6.2c and 6.2d) and tetrahedral (Figure 6.2b) octupolar symmetries are relatively easy to design based on the well established trigonal and tetrahedral geometries in organic molecules. For example, the functionalization at 1,3, and 5 positions of aromatic systems (phenyl,<sup>6-8</sup> triazine,<sup>9-12</sup> or boroxane<sup>13</sup>) produces the 2D molecules with trigonal ( $C_3$ ,  $C_{3v}$ ,  $D_3$  or  $D_{3h}$ ) symmetry (Figures 6.2c and 6.3a). Trigonal symmetry shown in Figure 6.2d can be achieved, for example, based on  $C^+$  template (crystal violet, Figure 6.3c). Other molecular octupoles in which 3D symmetries are used include tetrahedral ( $T_d$ ) tin derivative<sup>14</sup> or bis(bipyridyl) zinc(II) complex (Figures 6.2b and 6.3d)<sup>15</sup> and the cubic paracyclophane derivative (Figures 6.2a and 6.3b).<sup>16</sup> Recently, chemists have been using coordination chemistry as a powerful tool to synthesize octupolar molecules. The first transition-metal complex ( $[\text{Ru}(2,2'\text{-bpy})_3]^{2+}[\text{PF}_6]_2^-$ ) with large  $\beta$  values was reported by Zyss.<sup>17</sup> After this work many octupolar NLO materials based on metal complexes have been investigated.<sup>18-20</sup>

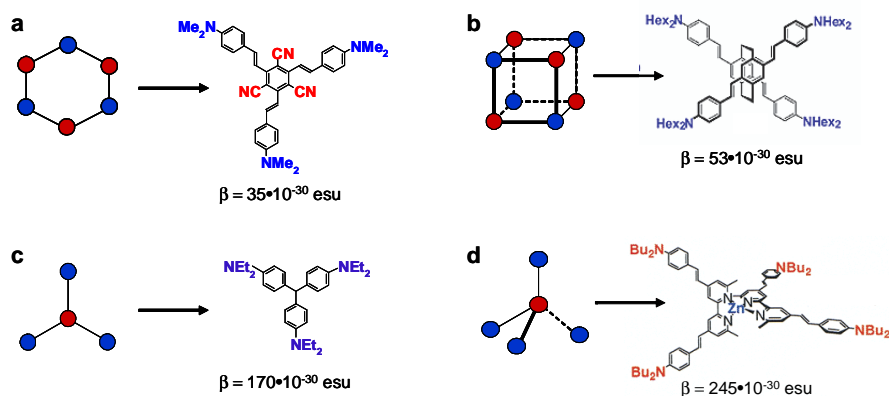


**Figure 6.3** Examples of 2D and 3D octupolar molecules with trigonal, tetrahedral and cubic symmetries.

**6.1.5 Octupolar 2D Supramolecular Materials.** To date, the design of octupolar NLO materials has focused mostly on molecular systems. Assembly of octupolar molecules into acentric *networks*, however, has not been fully explored. Figure 6.4 shows three network arrangements that we will encounter in this study. Two of them  $6^3$  and  $3^6$  nets possess nodes with trigonal symmetry and they are good candidates for supramolecular octupolar assemblies. Two reports from the literature explored the 2D trigonal  $3^6$  networks based on organic and metal complex chromophores (Figure 6.5).<sup>21, 22, 12</sup> We note here that both these designs offer synthons (herringbone interactions and coordinate bonds) that direct the molecular arrangement in two dimensions. The assembly in the third dimension, however, is not controlled by predetermined functional groups. In other words, these materials adopt 3D noncentrosymmetry by chance; the design was limited only to two dimensions. The absence of such *supramolecular* octupolar materials indicates the difficulty in the design of systems that have octupolar symmetry and that can assemble into acentric solid state structures.

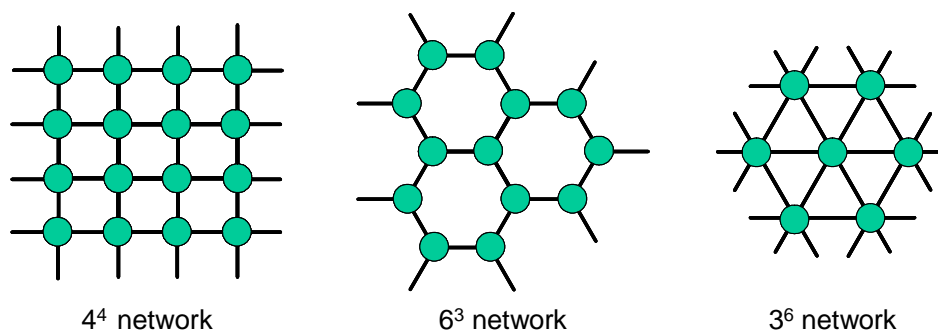


**Figure 6.4** Representation of 2D network arrangements. The  $X^Y$  terminology used here has its origin in defining nets as a collection of nodes connected by linkers. In  $6^3$  net, for example, each node is connected to 3 other nodes, and the smallest cycle contains 6 nodes.

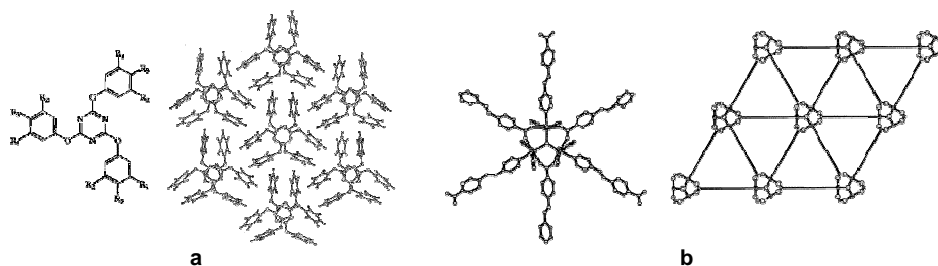


**Figure 6.5** Schematic representation of 2D octupolar materials. **(a)** 2,4,6-Triaryloxy-1,3,5-triazines. **(b)** Trigonal network made from  $[\text{Cd}_3(\mu_3\text{-OH})(\text{L})_3(\text{py})_3]^{2+}$ ,  $\text{L} = 4\text{-}[2\text{-}(4\text{-pyridyl})\text{ethenyl}]\text{benzoate}$ .

**6.1.6 Critical Need for 3D Octupolar Supramolecular Materials.** The purpose of this work is to develop a strategy for the synthesis of 3D octupolar materials that can show high NLO activity at molecular and crystalline state. As NLO molecules we propose trigonal metal-organic clusters (Figure 6.6); these clusters offer synthetic design analogous to organic compounds and possess robustness of inorganic systems. Special advantages of metal-organic framework structures include: strong bonding that provides network robustness, bridging ligands that can be modified by organic synthesis, and the ability to create desired geometrical assembly. The clusters can first be created and studied at molecular level (that is, 0D systems); these clusters can then be assembled into 2D or 3D frameworks through metal-ligand bonding. By selecting proper organic ligands we can tailor physical properties and through a combination of metal species, carboxy and aza ligands, it may be possible to design materials for applications in catalysis, magnetism, sorption, and non-linear optics.

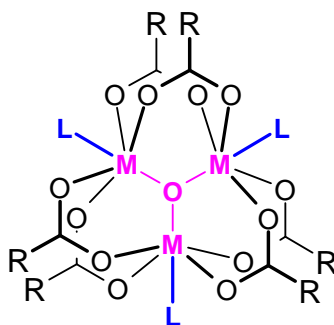


**Figure 6.6** Molecular structure of TMC. This cluster consists of trigonal planar  $M_3O$  group in which central oxygen functions as bridging ion. All the metals display octahedral coordination.

**6.1.7 Functionalized Materials based on Metal Carboxylate Clusters.** Some examples from recent literature illustrate the utility of metal-organic frameworks in the above mentioned applications. Kim and coworkers reported chiral metal-organic framework for the catalysis of enantioselective trans-esterification reactions (Figure 6.7a).<sup>23</sup> Of special interest is also the design of stable nano- or micro porous networks. Porous materials are mainly used for size selective sorption, molecular recognition, or gas storage. Yaghi and coworkers demonstrated crystalline extra-large porous frameworks made of octahedral  $Zn_4O$  nodes with pore sizes up to  $28.8\text{\AA}$  (Figure 6.7b).<sup>24, 25</sup> These materials can sorb 240 mL/g of methane at 36 atm. Metal-organic frameworks can also show interesting magnetic properties. Antiferromagnetism, ferrimagnetism and ferromagnetism are common phenomena of the magnetic spins in solid state. The nanoscale metal-organic Kagome lattice built by Zawarotko and colleagues has interesting (spin frustrated) magnetic properties at room temperature.<sup>26</sup> This Kagome lattice is formed from dicopper paddle-wheel cluster with isophthalate bridges (Figure 6.7c).

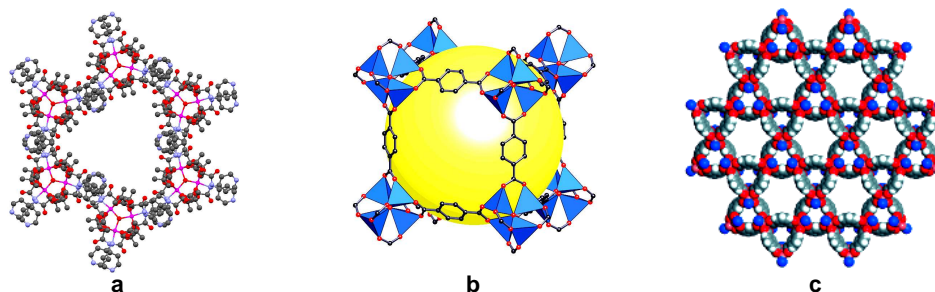


**Figure 6.7** Examples of frameworks built from metal-carboxylate clusters (a) Chiral hexagonal framework made from  $[Zn_3O(OOCR)_6(H_2O)_3]^{2-}$ . (b) Porous solids constructed by octahedral  $Zn_4O(OOCR)_6$  units, and (c) Kagome network based on  $Cu_2(OOCR)_4$  units.

## 6.2 DESIGN, SYNTHESIS, AND IR ANALYSIS OF TMCs

Our work so far has been primarily synthetic in nature. We have just begun to characterize the crystal structures obtained from various TMC derivatives synthesized in this work. We will describe two categories of TMC related structures and two other clusters with higher nuclearity ( $Mn_6$  and  $Mn_{13}$ ), and their potential use as nodes in generating new types of porous frameworks. We are currently in the process of obtaining NLO characterizations of these compounds through collaboration. We begin with our original design strategy that we hoped will generate 3D acentric structures.

**6.2.1 Design strategy for 3D Octupolar Materials.** Our strategy for making 2D trigonal octupolar assemblies and their possible arrangement in three dimensions is shown in Figure 6.8. This design starts with the molecular trigonal units shown in Figure 6.8a. When these two octupolar units are connected at their corners, they can form an acentric hexagonal 2D network (Figure 6.8b). Stacking of the 2D networks can lead to either 3D noncentrosymmetric (Figure 6.8c) or 3D centrosymmetric structure (Figure 6.8d). We should note here that the  $6^3$  net in Figure 6.8b is based on two different nodes (centers of red and blue triangles). If one were to consider the topology of this net based on any one node (red or blue) this net will then become a  $3^6$  net, that is, it is acentric in two dimensions.

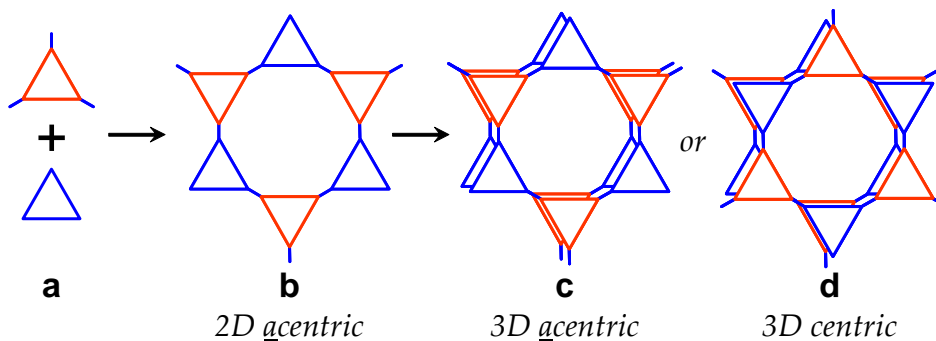


**Figure 6.8** Strategy for the synthesis of 3D noncentrosymmetric crystals.

We have designed trigonal metal clusters to achieve 3D acentric structures exclusively. The geometry of the TMC enables the binding of three in-plane monodentate ligands projected trigonally, and six out-of-plane bridging bidentate ligands projected perpendicular to the  $Mn_3O$  core. We use pyridine derivatives for the first set of ligands, and benzoic acid derivatives for the second set of ligands; we refer to them, in the following sections, as pyridyl and acid ligands. Use of TMCs allows 3D design (Figure 6.9). These TMCs are also modular in their design, that is, one can make multiple derivatives through changes in metal ions and two sets of ligands.

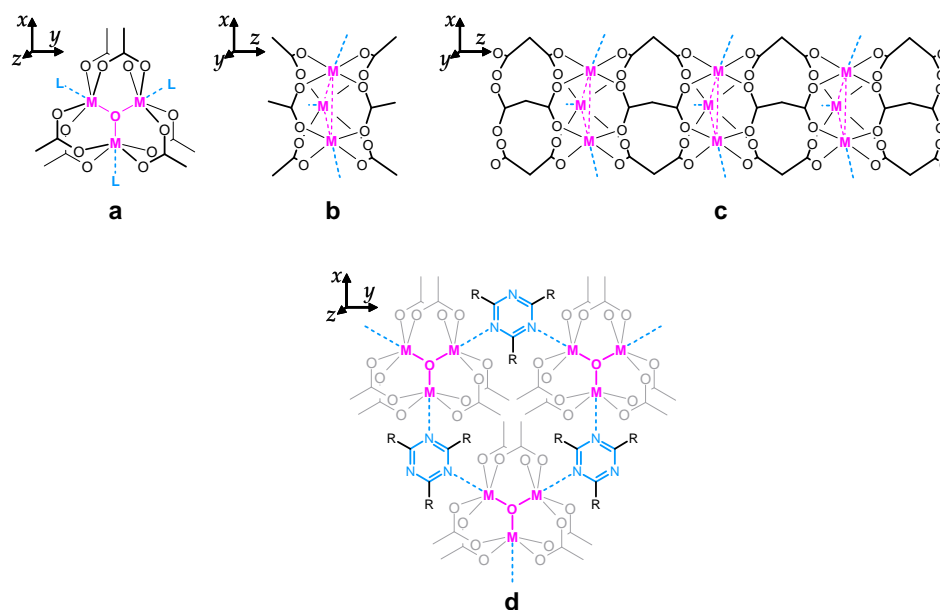


**Figure 6.9** Expected 3D arrangement of trigonal metal organic frameworks. (a) TMC viewed down  $z$ -axis. (b) Side view of TMC (down  $y$ -axis). (c) Acentric assembly of TMC along the  $z$ -axis by an appropriately shaped diacid. (d) 2D noncentrosymmetric arrangement of TMCs and triazines in  $xy$ -plane.

**6.2.2 Synthetic Approach.** The strategy shown in Figure 6.9 involves combining three different entities (metal ions, pyridyl ligands, and acid ligands) in one pot to create network solids. To synthesize 3D acentric materials directly is ambitious and turned out to be challenging. Our initial attempts to create such 3D material through one pot synthesis led to insoluble powders (that may well be the desired materials) that are difficult to characterize. We quickly realized the need to learn synthetic as well as structural chemistry of TMCs and decided to explore the synthesis and structures of *discrete* TMCs. We argued that due to their trigonal symmetry these TMCs should act as useful candidates to explore  $3^6$  nets. Also, we hoped to explore metal-to-ligand and ligand-to-metal charge transfer within these TMCs to modulate  $\beta$ . The question that we faced at this point was – where to start? We needed to decide on the types of metal, the in-plane ligands and the bridging ligands. Thus, we approached the Cambridge Structural Database (CSD) to determine the known structural chemistry of TMCs.

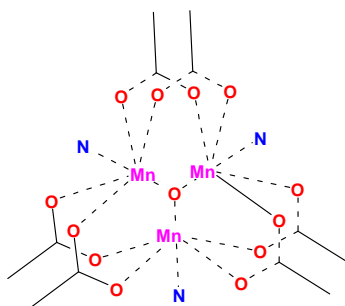


**Figure 6.10** Quest fragment used in the CSD query. All the bonds attached to Mn are defined as ‘any’ bonds. Only aza and carboxylate ligands are searched.

**6.2.3 Known Structural Chemistry of TMCs – CSD Analysis.** Figure 6.10 shows the CSD search fragment we used to retrieve the known TMC structures. We chose to restrict the search to in-plane ligands with aza donors and carboxylates as bridging ligands. This search showed 104 hits with TMC units, of which 71 are unique. That is, the other 33 hits belong to duplicate structure determinations. The following features appeared from an analysis of these structures. Of the 71 structures, 54 TMCs are based on homo-metallic cores (that is all the three metal ions are same), and 17 TMCs are based on hetero-metallic cores. A gratifying finding is that these TMCs are not restricted to any specific metal species. Currently TMCs with Fe, Cr, V, Mn, Zn, Ru, and Ga metal ions are known. Another way of classifying the 71 hits is based on the space group symmetry: 41 of these TMCs crystallize in centrosymmetric space groups, and 30 belong to acentric space groups. A large number (50) of these TMCs include non-aromatic acid ligands. Of the 21 TMCs that contain aromatic pyridyl and acid ligands, most of them are based on benzoic acid and pyridine.

We are interested in exploring all-aromatic TMCs because they are expected to show high  $\beta$  values (systems with closely spaced multiple aromatic units can show large  $\beta$  values even in the absence of conjugation; see for example NLO activities of calixarenes<sup>27</sup>). Most of the reported studies are centered on synthesis, characterization, magnetism, and intermetallic charge transfer of TMCs. Little or no attention is placed on the NLO effects and supramolecular structural control of TMCs. We anticipated that creating a number of TMCs with different acid and pyridyl ligands will lead to the discovery of new network topologies and new chemistry with a rich variety of compounds.

A key feature of TMC systems, like other metal containing systems, is that they display structural portability. That is, TMCs containing different metal species, but similar structure have similar structure. This feature is especially useful in the current study because electronic character of the core can be modulated to control the nonlinear properties of the clusters<sup>19</sup>. A relevant example that illustrates the structural portability involves:  $[M_3O(\text{AcO})_6\text{Py}_3]^+[\text{X}]^-$ . A variety of homo- and hetero-metallic TMCs based on this core are isostructural. We expect that our studies based on one metal species (that is, Mn) can be extended to other metals without the loss of designed structural features.

**6.2.4 Synthesis of Discrete TMCs.** As shown above a number of metal ions can be used to prepare TMCs. We chose Mn as the metal species in this work because Mn based TMCs are stable and they can be created under aerobic conditions (Figure 6.11). An advantage with Mn TMCs is that they can be synthesized using a predictable comproportionation reaction.<sup>28</sup> In addition, Mn TMCs can be prepared in two flavors; we call them charged TMCs and neutral TMCs (Equations 1 and 2; see below). Charged TMCs contain three Mn<sup>3+</sup> ions as part of the Mn<sub>3</sub>O core; that is when a full cluster is formed the cluster will have one unit of positive charge ([Mn<sub>3</sub>O(RCOO)<sub>6</sub>L<sub>3</sub>]<sup>+</sup>). On the other hand, the neutral TMCs have the general formula Mn<sub>3</sub>O(RCOO)<sub>6</sub>L<sub>3</sub>; that is the overall charge of the cluster is zero. Our initial interest and focus is on the charged TMCs, because we hoped that these TMCs can have full trigonal symmetry at the molecular level, at least in solution. In neutral TMCs, the molecules may or may not maintain trigonal symmetry because the charge can be localized or delocalized on the metal ions (that is the arrangement can be: Mn<sup>2+</sup>Mn<sup>3+</sup>Mn<sup>3+</sup> or [Mn<sup>2.66+</sup>]<sub>3</sub>). One final note on the choice of the anion: we used perchlorate (ClO<sub>4</sub><sup>-</sup>) anion in this study largely because of synthetic ease. We expect that these anions can be replaced by safer anions such as BF<sub>4</sub><sup>-</sup> if these TMCs were ever to be synthesized in large scale.

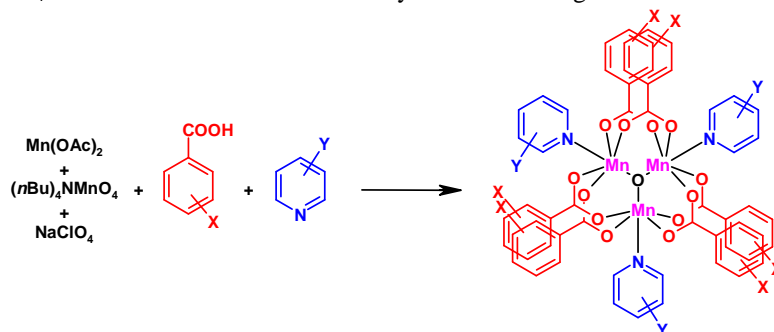
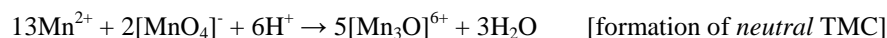
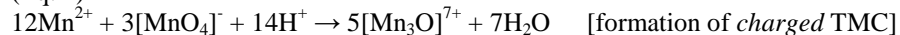


**Figure 6.11** Scheme for the synthesis of TMC.

The following two equations show the comproportionation reactions for the synthesis of neutral and charged TMCs.



(Eq. 1)



(Eq. 2)

We found that these reactions are highly reliable and can be achieved selectively by manipulating the experimental conditions. Oxidation can be carried out with KMnO<sub>4</sub> or <sup>n</sup>Bu<sub>4</sub>NMnO<sub>4</sub>; again we found that the latter reagent is more reliable and broadly applicable for the synthesis of a range of TMCs. One particularly attractive experimental feature of these neutral and charged TMCs is their markedly different color: charged TMCs are brown in color and the neutral clusters are dark green. For the following

syntheses, all chemicals and solvents were purchased from commercial sources and used without further purification. All manipulations were performed under aerobic conditions.

**6.2.4.1 Synthesis of  ${}^n\text{Bu}_4\text{NMnO}_4$ .** This compound was synthesized by a slight modification of a literature report.<sup>29</sup> Aqueous solutions of  $\text{KMnO}_4$  (2.50g, 15.8 mmol, dissolved in 60 mL of water) and  ${}^n\text{Bu}_4\text{NBr}$  (6.00g, 18.6 mmol, dissolved in 40 mL of water) were mixed together with vigorous stirring. After 20 minutes a purple precipitate was filtered, washed with deionized water (500mL) and a small amount (25-50 mL) of diethyl ether, and dried in vacuo. The typical yield of this reaction was >80%. After drying, the product was placed in an Erlenmeyer flask and the flask was quickly sealed under  $\text{N}_2$  gas using parafilm. This sealed flask was then kept in a refrigerator and the permanganate was used in the synthesis of TMC within one week.

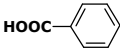
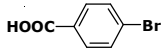
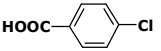
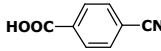
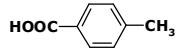
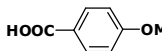
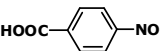
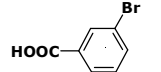
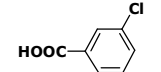
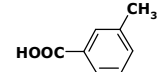
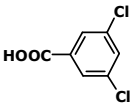
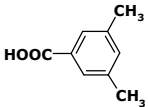
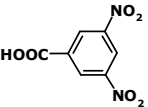
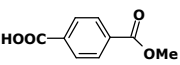
**6.2.4.2 Synthesis of Charged TMCs ( $[\text{Mn}_3\text{O}(\text{OOCR})_6\text{L}_3]\text{ClO}_4$ ).** The complexes were prepared following the modified method described by Vincent.<sup>30</sup>  $\text{Mn}(\text{O}_2\text{CMe})_2 \cdot 4\text{H}_2\text{O}$  (2.00g, 8.15 mmol) and acid (61.4 mmol) and pyridine (30.7 mmol) derivatives were dissolved in 25-50 mL of absolute EtOH in an Erlenmeyer flask. To this mixture was added  ${}^n\text{Bu}_4\text{NMnO}_4$  (1.14g, 3.15 mmol) in small portions under continuous stirring. Immediately after adding the permanganate,  $\text{NaClO}_4$  (0.69g, 5.65mmol) was added in portions, and 15 minutes after this latter addition a brown solid product appeared in the flask. This brown precipitate was collected by filtration and dried in vacuo. Recrystallization was carried out in dichloromethane, acetonitrile, or benzene; after several days small gold colored microcrystals of the desired products were obtained. The morphology of these crystals depended on the TMC and hinted at the possibility of different types of underlying structures. Typical yields in these reactions were in the range of 70 – 85%.

**6.2.4.3 Synthesis of Neutral TMCs ( $\text{Mn}_3\text{O}(\text{OOCR})_6\text{L}_3$ ).** To obtain neutral complexes the procedure described above was modified, that is the amount of  ${}^n\text{Bu}_4\text{NMnO}_4$  was reduced according to the stoichiometric ratio given in Equation 1 above. Only 1.25 mmol of  ${}^n\text{Bu}_4\text{NMnO}_4$  was required to react with 8.15 mmol of  $\text{Mn}(\text{O}_2\text{CMe})_2 \cdot 4\text{H}_2\text{O}$ . After the addition of  ${}^n\text{Bu}_4\text{NMnO}_4$  the homogenous solution was turned to a dark green color. The mixture was stirred for 1h and the product was left undisturbed overnight in the refrigerator. The resultant precipitate was collected by filtration (yield: >80%). Recrystallization from dichloromethane, acetonitrile, or EtOH yielded brown crystals with TMC dependent morphologies.

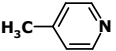
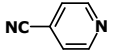
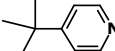
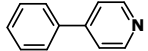
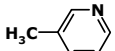
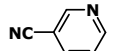
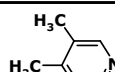
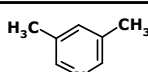
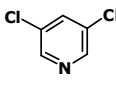
**6.2.5 Selection of Ligands (Acids and Pyridines).** The major criterion we applied in selecting these ligands is that they must be aromatic and conjugated. We chose functional groups that do not interfere with the formation of TMC. Also, we chose relatively simple groups so that we can understand structural chemistry of a molecule with complicated shape. The deliberate choice of electron donating and withdrawing groups on acids as well as pyridyl ligands is to test the effects on  $\beta$  with these variations. Tables 6.1 and 6.2 show the acid and pyridyl ligands used in the TMC synthesis. Frequently we refer to TMCs with the acid and pyridyl acronyms shown in these Tables. For example, ‘BA-4P’ refers to a TMC made from six benzoic acid and three 4-picoline ligands. One more note

on the acronyms used: we refer to charged clusters as TMCs; neutral clusters are always referred as neutral TMCs. Table 6.3 lists current status of various TMCs we are working with.

**Table 6.1** Molecular structures and acronyms of acid ligands used in the synthesis of TMCs.

				
<b>BA</b>	<b>4BrBA</b>	<b>4ClBA</b>	<b>4CNBA</b>	<b>pTA</b>
				
<b>AA</b>	<b>4NO<sub>2</sub>BA</b>	<b>3BrBA</b>	<b>3ClBA</b>	<b>mTA</b>
				
<b>35ClBA</b>	<b>35MeBA</b>	<b>35NO<sub>2</sub>BA</b>	<b>AE</b>	

**Table 6.2** Molecular structures and acronyms of pyridyl ligands used in the synthesis of TMCs.

				
<b>Py</b>	<b>4P</b>	<b>4CNPy</b>	<b>4'BuPy</b>	<b>4PhPy</b>
				
<b>3P</b>	<b>3BrPy</b>	<b>3CNPy</b>	<b>34Lu</b>	<b>35Lu</b>
				
<b>35ClPy</b>	<b>Imd</b>			

**Table 6.3** Current status of TMCs synthesized in this work.

	Py	4P	4CNPY	4 <sup>t</sup> BuPy	4PhPy	3P	3BrPy	3CNPY	34Lu	35Lu	35ClPy	Imd
BA	S	S C C		S C	S	S C			S	S	S	
	S	S	S			S		S	S	S	S	
4BrBA		S	S			S		S	S	S		
4ClBA		S	S			S		S	S	S		
		S	S			S		S	S	S		
4CNBA		S			S	S		S				
<i>p</i> TA	S C	S C	S	S		S C		S	S C	S C	S	S
	S	S	S			S		S	S	S	S	
4OMe BA		S	S			S		S	S	S		
4NO <sub>2</sub> BA		S	S	S		S		S	S	S	S	
3BrBA		S	S			S		S	S	S		
		S	S			S		S	S	S		
3ClBA		S	S			S		S	S	S	S	
	S	S	S			S		S	S	S	S	
<i>m</i> TA	S C	S C	S			S		S	S C			
	S	S	S			S		S	S	S	S	
34ClBA		S	S			S		S	S			
34MeBA		S	S			S		S	S	S		
35NO <sub>2</sub> BA	S	S	S			S		S	S	S		
		S	S			S		S	S	S		
AE						S						
	S	S				S						

**S** - Synthesized charged TMCs.

**S** - Synthesized neutral TMCs.

**C** - TMCs for which crystallographic data were collected.

**6.2.6 Spectroscopic Characterization of TMCs.** Though Mn TMCs made in this work are thoroughly soluble in organic solvents, especially CHCl<sub>3</sub>, it is not easy to collect <sup>1</sup>H NMR (or <sup>13</sup>C NMR) spectra of these compounds due to the influence of the paramagnetic Mn ions.<sup>31</sup> This influence results in broadened and highly separated peaks (chemical shifts range from -150 to +100 ppm in <sup>1</sup>H NMR). The analysis of these spectra is not trivial; in fact, this analysis itself is part of major research in organic-inorganic spectroscopy. We have thus resorted to IR spectroscopy as a quick tool to verify the formation of TMCs in our reactions. Our IR analysis showed two interesting features: (i) it is easy to distinguish between neutral and charged TMCs; and (ii) acid ligands have distinguishable, characteristic bands but pyridyl ligands do not have such bands, at least in the typical 600 – 4000 cm<sup>-1</sup> region.

**6.2.6.1 Distinguishing Charged and Neutral TMCs through IR Spectroscopy.** Figure 6.12 shows the IR spectra of some representative charged and neutral TMCs. The region between 1700 and 600 cm<sup>-1</sup> is dominated by absorptions due to the symmetric and asymmetric stretching of the bridging carboxylate groups ( $\nu$ -COO). These are strong bands appearing at about 1380 cm<sup>-1</sup> and 1600 cm<sup>-1</sup> respectively. The medium strong

bands due to the absorption by the perchlorate anion ( $\nu\text{-Cl-O}$ ) are found near  $1100\text{ cm}^{-1}$  for all charged TMCs. Several IR bands below  $800\text{ cm}^{-1}$  may be assigned to other acid and pyridine absorptions. One of these bands at about  $620\text{ cm}^{-1}$ , however, arises from an asymmetric stretch of the central  $\text{Mn}_3\text{O}$  unit. The main difference between charged and neutral TMCs is the absence of perchlorate stretching near  $1100\text{ cm}^{-1}$  (contrast Figures 6.12a and b). We use this region to diagnose the TMC products obtained in our synthesis.

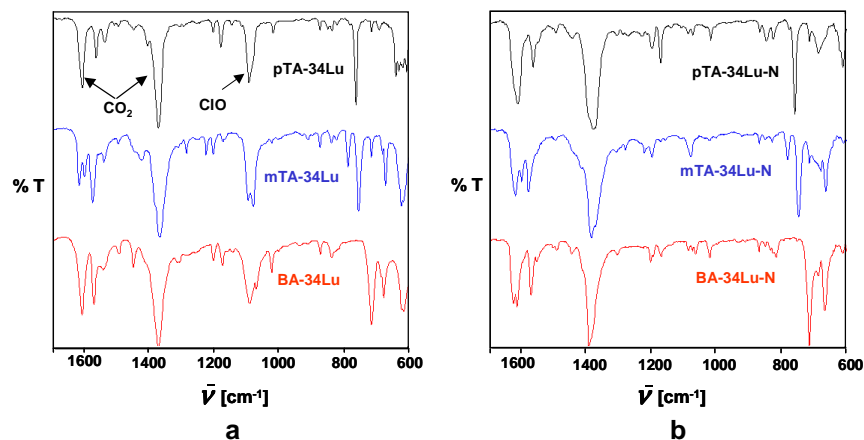


**Figure 6.12** Comparison of IR spectra of the charged (a) and neutral (b) TMCs.

**6.2.6.2 Finger Prints of Acid and Pyridyl Ligands in IR Spectra.** As noted above, acid groups can be differentiated and identified from IR spectra. The main differences in a series of TMCs that differ only in acid groups lie in the asymmetric stretching zone ( $\nu_{as}\text{-COO}$ ) of the carboxylate groups. In Figure 6.13a we analyze IR spectra of three TMCs with same pyridyl ligand but different acid ligands. The fine structure in the  $\nu_{as}\text{-COO}$  region shows that for *p*TA-34Lu and *m*TA-34Lu there is only one strong band ( $\sim 1600$  and  $\sim 1574\text{ cm}^{-1}$ ); however for the BA-34Lu this band is split into two bands (at  $\sim 1604$  and  $\sim 1568\text{ cm}^{-1}$ ). The symmetric stretching ( $\nu_s\text{-COO}$ ) always appears at  $\sim 1380\text{ cm}^{-1}$  as a single band (Figures 6.13a and 6.13b). A similar analysis for pyridyl ligands (Figure 6.13b; same acid ligand but different pyridyl ligands) shows that there are no characteristic peaks that can tell one pyridyl ligand from another. The three spectra shown in Figure 6.13b do not differ noticeably.

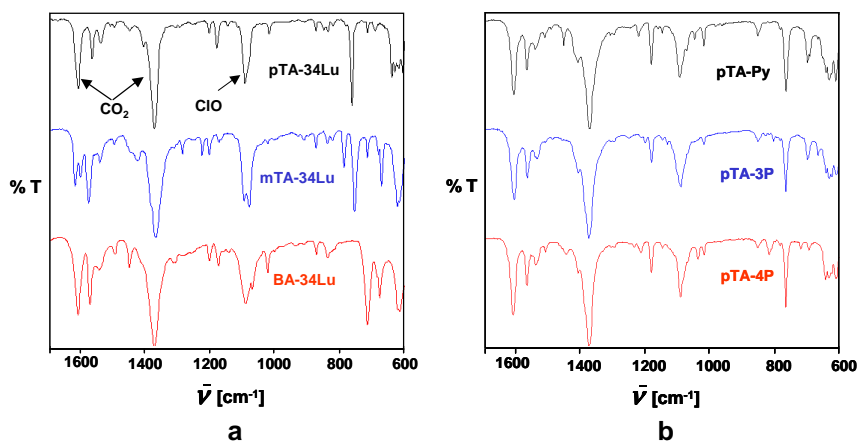


**Figure 6.13** IR spectra of TMCs with (a) different acid ligands and (b) different pyridyl ligands.

### 6.3 CRYSTAL STRUCTURAL ANALYSIS OF TMCs

**6.3.1 General Considerations in Structural Analysis.** As noted earlier much of my effort in this work was focused on the synthesis of TMCs (both charged and neutral). Our structural analysis is still at an early stage; therefore *we will limit our discussion only to the structures of charged TMCs*. Of the 65 charged TMCs synthesized, about 30 compounds showed good crystallinity, but only 17 were good enough for single crystal X-ray data analysis. These compounds typically adopt layered structures in the solid state, and displayed some of the known crystal growth and structure analysis problems with layered structures. We frequently encountered layer misalignment or twinning; typically we had to mount 3-4 crystals on the diffractometer before a single crystal was found that can give reasonable unit cell data. Also, even after the data collection these systems routinely gave problems during structure solution and refinement. For these reasons, most of the structures in this study are only partially solved and/or refined. In future work I will spend more time towards the complete refinement of these structures and their detailed analysis. We classified the 10 TMC structures (to be discussed in the following sections) into two categories; structures of these two categories along with those of hexa- and tridecanuclear Mn-carboxylate clusters are presented below. Table 6.4 shows the salient crystallographic parameters for the structures reported here. Figure 6.14 shows the numbering scheme used in this study; consistency in this numbering simplifies comparison across a series of derivatives (see, for example, Table 6.6).

**Table 6.4** Space group and unit-cell data for the structures reported in this work.

TMC	Space Group	<i>a</i>	<i>b</i>	<i>c</i>	$\alpha$	$\beta$	$\gamma$	Solvate
BA-Py	<i>P</i> 6 <sub>3</sub> / <i>m</i>	13.482	13.482	19.032	90	90	120	C <sub>5</sub> H <sub>5</sub> N
BA-4P	<i>P</i> 6 <sub>3</sub> / <i>m</i>	13.955	13.955	18.227	90	90	120	C <sub>6</sub> H <sub>6</sub>
BA-4P	<i>P</i> 6 <sub>3</sub> / <i>m</i>	13.966	13.966	18.233	90	90	120	CH <sub>2</sub> Cl <sub>2</sub>
BA-3P	<i>P</i> 6 <sub>3</sub> / <i>m</i>	13.151	13.151	21.277	90	90	120	C <sub>6</sub> H <sub>6</sub>
<i>p</i> TA-Py	<i>Pccn</i>	14.128	17.328	25.754	90	90	90	
<i>m</i> TA-Py	<i>P</i> 2 <sub>1</sub> 2 <sub>1</sub> 2	14.365	16.887	12.828	90	90	90	
<i>p</i> TA-4P	<i>P</i> 2 <sub>1</sub> 2 <sub>1</sub> 2 <sub>1</sub>	15.702	16.185	27.016	90	90	90	CH <sub>2</sub> Cl <sub>2</sub>
<i>p</i> TA-3P	<i>P</i> 2 <sub>1</sub> 2 <sub>1</sub> 2 <sub>1</sub>	15.678	17.074	25.362	90	90	90	C <sub>6</sub> H <sub>6</sub>
<i>m</i> TA-4P	<i>P</i> 4̄2 <sub>1</sub> <i>m</i>	15.891	15.891	13.659	90	90	90	C <sub>6</sub> H <sub>6</sub> (?)
3CIBA-4P	<i>P</i> 4̄2 <sub>1</sub> <i>m</i>	15.795	15.795	13.799	90	90	90	C <sub>6</sub> H <sub>6</sub> (?)
<i>m</i> TA-34Lu	<i>P</i> 2 <sub>1</sub> 2 <sub>1</sub> 2	16.589	16.593	13.731	90	90	90	C <sub>6</sub> H <sub>6</sub>
<i>m</i> TASC	<i>P</i> 1̄	15.677	15.820	16.117	92.194	94.923	110.756	
<i>p</i> TAMn <sub>6</sub>	<i>Ccca</i>	18.362	25.413	18.514	90	90	90	

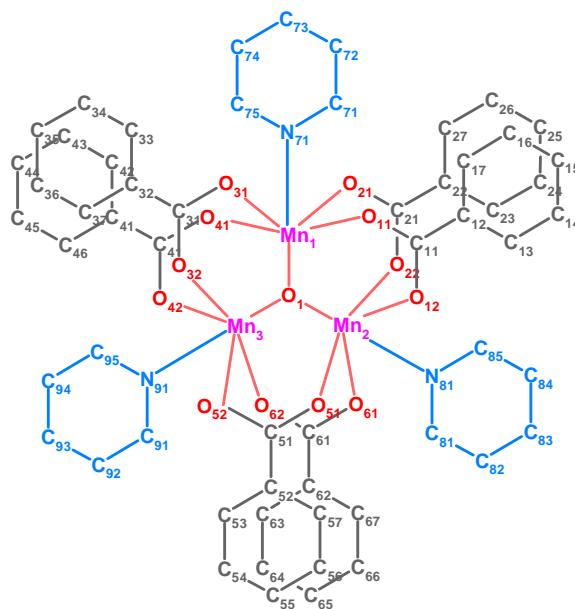


**Figure 6.14** Atom numbering scheme used in this study. Acid rings are labeled C<sub>12</sub>-C<sub>17</sub>, C<sub>22</sub>-C<sub>27</sub>, C<sub>32</sub>-C<sub>37</sub>, C<sub>42</sub>-C<sub>47</sub>, C<sub>52</sub>-C<sub>57</sub>, and C<sub>62</sub>-C<sub>67</sub>, and pyridine rings are labeled N<sub>71</sub>C<sub>71</sub>-C<sub>75</sub>, N<sub>81</sub>C<sub>81</sub>-C<sub>85</sub>, N<sub>91</sub>C<sub>91</sub>-C<sub>95</sub>. Rings numbered from C<sub>12</sub>-C<sub>17</sub> to C<sub>42</sub>-C<sub>47</sub> correspond to Type-I acid ligands; rings C<sub>52</sub>-C<sub>57</sub> and C<sub>62</sub>-C<sub>67</sub> correspond to Type-II acid ligands (see Section 6.3.6). Similarly, Type-A pyridyl ligand is numbered N<sub>71</sub>C<sub>71</sub>-C<sub>75</sub> and, Type-B pyridyl ligands are numbered N<sub>81</sub>C<sub>81</sub>-C<sub>85</sub> and N<sub>91</sub>C<sub>91</sub>-C<sub>95</sub>.

**6.3.2 Structures Adopting Idealized Acentric  $6^3$  Networks.** We began our analysis with BA-Py, a TMC with no substituents on either acid or aza-aromatic ligands. We expected that this will be a good starting point for exploring and designing new types of structures within the family of all-aromatic TMCs. Our CSD analysis showed that there are several analogues of BA-Py reported in the literature; Table 6.5 provides some details of metal ions, counter anions, and solvated guest species included in the crystals. Each structure in this Table is identified with a REFCODE, a unique name assigned to each entry in the CSD.

All these structures (except VOVBAJ) have similar crystal structures; they follow the general trend that metal ions can be exchanged without the loss of structural similarity. These entries also display the crystallographic problems we referred to above, and these problems are responsible for: (i) incorrect space group assignment; (ii) lack of coordinate data on solvated molecules; and (iii) incompletely refined anions. This incomplete data on anions and solvates again refer to the major focus of the previous studies: that is, they are concerned with the *molecular* structure of TMC but not with the *supramolecular* structure. Two key points (in addition to those listed in footnotes <sup>§</sup> and <sup>\*\*</sup> on next page) can be concluded from an analysis of the structures in Table 6.5: (i) They contain both homo and hetero-metallic TMCs; (ii) They contain significantly different anions. But, all the anions adopt pseudo-octahedral geometry in the crystal.

**Table 6.5** Molecular and crystal structural analogues of  $[\text{Mn}_3\text{O}(\text{BA})_6\text{Py}_3]^+[\text{ClO}_4]^- \cdot \text{C}_6\text{H}_6$

REFCODE	TMC	Anion	Guest
GOMWUA	$[\text{Cr}_3\text{-O-(BA)}_6\text{-Py}_3]^-$	$\text{ClO}_4^-$	Pyridine
NUXBAJ01/02	$[\text{MnCr}_2\text{-O-(BA)}_6\text{-Py}_3]^+$	$\text{ClCrO}_3^-$	Pyridine
PAMCOV01	$[\text{Ru}_3\text{-O-(BA)}_6\text{-Py}_3]^+$	$\text{PF}_6^-$	not refined
PAZZAR	$[\text{Fe}_3\text{-O-(BA)}_6\text{-Py}_3]^+$	$\text{NO}_3^-$	$\text{CH}_2\text{Cl}_2$
QOPLUC	$[\text{Fe}_3\text{-O-(BA)}_6\text{-Py}_3]^+$	$\text{ClO}_4^-$	Pyridine
ZAVJOV	$[\text{Cr}_3\text{-O-(BA)}_6\text{-Py}_3]^+$	$\text{ClO}_4^-$	not refined
ZASTOC <sup>§</sup>	$[\text{Cr}_3\text{-O-(BA)}_6\text{-(Piperidine)}_3]^+$	$\text{ClO}_4^-$	not refined
VOVBAJ <sup>**</sup>	$[\text{Ga}_3\text{-O-(BA)}_6\text{-(4-Picoline)}_3]^+$	$\text{GaCl}_4^-$	4-Picoline

We have synthesized charged Mn-TMC with BA and Py ligands, and grown single crystals of its benzene solvate, that is ( $[\text{Mn}_3\text{O}(\text{BA})_6\text{Py}_3]^+[\text{ClO}_4]^- \cdot \text{C}_6\text{H}_6$ ). So far the single crystals obtained from this compound are small and not suitable for single crystal X-ray studies. The hexagonal prism morphology of the crystals, however, points to a structure similar to the analogues listed in Table 6.5. IR analysis showed stretchings for carboxylate and perchlorate species; that is, we have a charged TMC. Powder X-ray diffraction analysis of the sample matches with those of BA-Py analogues shown in Table 6.5. Based on these results, we attribute the structure of BA-Py to structures in Table 6.5, and in the following discuss its structure based on the Cr (GOMWUA).

### 6.3.3 Crystal Structure of $[\text{Mn}_3\text{O}(\text{BA})_6\text{Py}_3]^+[\text{ClO}_4]^- \cdot \text{C}_6\text{H}_6$ (based on GOMWUA).

This compound crystallizes in the trigonal space group  $P6_3/m$ . The discussion of its structure is divided into a description of molecular structure and the assembly of TMC units into  $3^6$  networks through C–H...O hydrogen bonds. Guest inclusion and an analysis toward structural mimicry and structural variation are discussed at the end of this section.

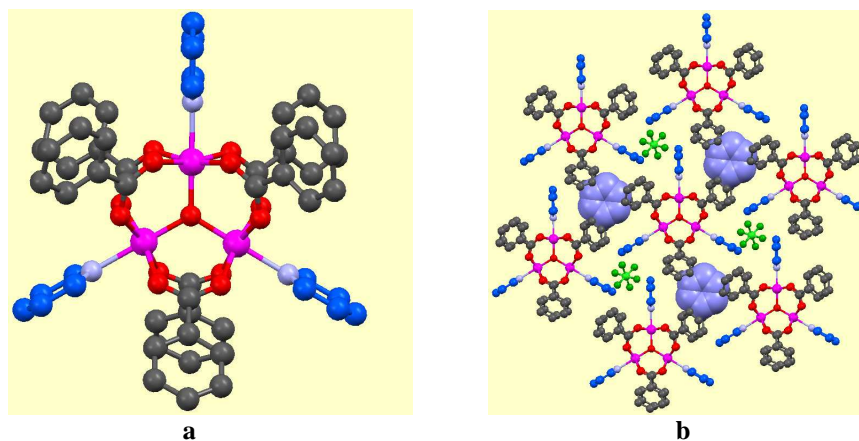


**Figure 6.15** (a) Molecular structure of BA-Py complex, (b) Assembly of trigonal units into 36 network. TMCs and perchlorate anions (green color) are shown in ball-and-stick model and benzene molecules are shown in space-filling model. Hydrogen atoms are omitted for clarity.

**6.3.3.1 Molecular Structural Features.** The TMC unit is located on a  $\bar{6}$  ( $3/m$ ) axis in the crystal, that is, it maintains molecular symmetry in the crystal (Figure 6.15a). This means that the TMC is noncentrosymmetric at molecular level, and all acid ligands are symmetry related as are the pyridyl ligands. In terms of atom labeling (see Figure 6.14) all acid rings are now numbered  $C_{12}$ - $C_{17}$  and all pyridyl rings are labeled  $N_{71}C_{71}$ - $C_{57}$ . The guest molecule (benzene in this structure; disordered pyridine in GOMWUA) is also located on  $\bar{6}$  ( $3/m$ ) axis. The counter ion (that is,  $ClO_4^-$ ), is also located on a  $6_3/m$  axis. Perchlorate ion should be tetrahedral; but, by the imposition of  $6_3/m$  symmetry, it is disordered and adopts pseudo-octahedral geometry in which four O atoms occupy six positions at the apices of a pseudo-octahedron. We note that all O atoms of the perchlorate ion are symmetry equivalent. All the Mn ions adopt octahedral coordination as expected. All the pyridyl ligands lie perpendicular to the plane of central  $Mn_3O$  unit.

**6.3.3.2 C–H...O Hydrogen Bonding between and  $ClO_4^-$  and TMC.** Major intermolecular interactions in this structure exist between the positively charged TMC and negatively charged perchlorate ion. The interactions, however, are not of ionic character (the + charge on the TMC is largely confined the central  $Mn_3O$  core, whereas perchlorate interacts with peripheral phenyl rings). Each of the six O atoms in perchlorate anion is connected to six distinct TMC units through short C–H...O hydrogen bonds (Table 6.6). One of the *meta* C–H groups from each benzoate contributes to this hydrogen bonding; each TMC is therefore connected to six  $ClO_4^-$  ions and vice versa. Three of these six TMCs are in one layer; three others are in an adjacent layer; these layers are parallel to (001), that is, *ab*-plane. Benzoate C–H groups are more acidic and easily accessible (less hindered) compared to the pyridyl C–H groups; therefore, it seems logical that they are involved in these short C–H...O hydrogen bonds.

**6.3.3.3 Guest Inclusion in TMC Layers – Acentric  $3^6$  Networks.** As mentioned above, this is a layered structure in which TMC units along with solvated benzene molecules are packed into one layer and perchlorate anions are sandwiched between adjacent TMC layers. In each layer, TMCs are arranged into a  $3^6$  network, that is, if lines were to be drawn between central O atoms of nearest TMCs (within the layer) they would result in a trigonal  $3^6$  network with O atoms acting as nodes. TMCs are held into this trigonal network through short C–H...O hydrogen bonds they form with perchlorate anions. The trigonal arrangement of TMCs (enforced by C–H...O bonds between TMCs and perchlorate anions), however, results in the juxtaposition of benzoate rings as shown in Figure 6.15b. Due to the 3D shape of the TMC molecule, this juxtaposition creates a cavity within the layers, and solvated benzene molecule occupies this cavity. It is important to note that reasonably short C–H...C contacts (C...C 3.7–3.8 Å) are seen between the benzoate rings forming this cavity, but this type of phenyl...phenyl arrangement is distinctly different from the traditional herringbone and stacking interactions usually adopted by aromatic rings.

**Table 6.6** Geometrical parameters for C–H...O Interactions\*.

TMC	CHO	C...O (Å)	H...O (Å)	C-H...O (°)	CH Type	Location
<b>BA-Py·C<sub>6</sub>H<sub>6</sub></b>	C16-H16...O1A	3.37	2.30	173	N/A	within 3 <sup>6</sup> nets
<b>BA-4P·C<sub>6</sub>H<sub>6</sub></b>	C16-H16...O1A	3.51	2.44	171	N/A	within 3 <sup>6</sup> nets
<b>BA-4P·CH<sub>2</sub>Cl<sub>2</sub></b>	C16-H16...O1A	3.54	2.47	170	N/A	within 3 <sup>6</sup> nets
<b>BA-3P·C<sub>6</sub>H<sub>6</sub></b>	Coordinate Data Not Available					
<b>pTA-Py</b>	C17-H17...O2A	3.32	2.43	139	Type-I	within 4 <sup>4</sup> nets
	C26-H26...O1A	3.27	2.32	146	Type-I	within 4 <sup>4</sup> nets
	C82-H82...O2A	3.61	2.57	161	Type-B	within 4 <sup>4</sup> nets
	C82-H82...O3A	3.45	2.61	134	Type-B	within 4 <sup>4</sup> nets
<b>mTA-Py</b>	C17-H17...O2A	3.27	2.41	135	Type-I	within 4 <sup>4</sup> nets
	C24-H24...O1A	3.30	2.35	146	Type-I	within 4 <sup>4</sup> nets
	C82-H82...O3A	3.19	2.32	136	Type-B	within 4 <sup>4</sup> nets
	C85-H85...O2A	3.52	2.65	137	Type-B	within 4 <sup>4</sup> nets
<b>pTA-4P·CH<sub>2</sub>Cl<sub>2</sub></b>	C17-H17...O1A	3.39	2.64	126	Type-I	within 4 <sup>4</sup> nets
	C26-H26...O2A	3.47	2.42	163	Type-I	within 4 <sup>4</sup> nets
	C34-H34...O4A	3.71	2.71	153	Type-I	within 4 <sup>4</sup> nets
	C44-H44...O1A	3.45	2.40	162	Type-I	within 4 <sup>4</sup> nets
	C44-H44...O3A	3.54	2.70	134	Type-I	within 4 <sup>4</sup> nets
<b>pTA-3P·C<sub>6</sub>H<sub>6</sub></b>	C16-H16...O1A	3.50	2.63	137	Type-I	within 4 <sup>4</sup> nets
	C16-H16...O4A	3.54	2.62	144	Type-I	within 4 <sup>4</sup> nets
	C26-H26...O2A	3.27	2.32	146	Type-I	within 4 <sup>4</sup> nets
	C34-H34...O3A	3.52	2.53	152	Type-I	within 4 <sup>4</sup> nets
	C44-H44...O1A	3.39	2.48	142	Type-I	within 4 <sup>4</sup> nets
<b>mTA-4P</b>	C13-H13...O1A	3.13	2.43	122	Type-I	within 4 <sup>4</sup> nets
	C14-H14...O1A	3.17	2.51	118	Type-I	within 4 <sup>4</sup> nets
<b>3CIBA-4P</b>	Coordinate Data Not Available					
<b>mTA-34Lu·C<sub>6</sub>H<sub>6</sub></b>	ClO <sub>4</sub> : Coordinate Data Not Available					

\* C–H bond lengths are normalized to 1.08 Å. N/A = Not applicable.

**Table 6.7** Geometrical parameters for the interactions between aromatic rings.

TMC	X...X	$\alpha^*$	Ring-1	Ring-2	Location
BA-Py•C <sub>6</sub> H <sub>6</sub>	3.87	0	Acid	Acid	between 3 <sup>6</sup> nets
BA-4P•C <sub>6</sub> H <sub>6</sub>	4.06	0	Acid	Acid	between 3 <sup>6</sup> nets
BA-4P•CH <sub>2</sub> Cl <sub>2</sub>	4.04	0	Acid	Acid	between 3 <sup>6</sup> nets
BA-3P•C <sub>6</sub> H <sub>6</sub>	Coordinate Data Not Available				
<i>p</i> TA-Py	3.87	17.37	Type II	Type B	within 4 <sup>4</sup> nets
	4.20	15.14	Type I	Type I	within 4 <sup>4</sup> nets
<i>m</i> TA-Py	3.56	6.15	Type II	Type B	within 4 <sup>4</sup> nets
	4.22	5.64	Type I	Type I	within 4 <sup>4</sup> nets
<i>p</i> TA-4P•CH <sub>2</sub> Cl <sub>2</sub>	3.61	7.05	Type II	Type B	within 4 <sup>4</sup> nets
	3.73	12.49	Type II	Type B	within 4 <sup>4</sup> nets
<i>p</i> TA-3P•C <sub>6</sub> H <sub>6</sub>	3.82	13.28	Type II	Type B	within 4 <sup>4</sup> nets
	3.82	10.2	Type II	Type B	within 4 <sup>4</sup> nets
	4.12	26.42	Bz-Solvate	Type A	within 4 <sup>4</sup> nets
<i>m</i> TA-4P	3.50	1.11	Type II	Type B	within 4 <sup>4</sup> nets
3CIBA-4P	Coordinate Data Not Available				
<i>m</i> TA-34Lu•C <sub>6</sub> H <sub>6</sub>	3.68	1.4	Type II	Type B	within 4 <sup>4</sup> nets
	3.62	2.91	Bz-Solvate	Type A	within 4 <sup>4</sup> nets

\* Angle between the planes of interacting aromatic rings.

**6.3.3.4 Structural Analysis for Further Design.** The trigonal layer structure shown in Figure 6.15b is acentric, but the adjacent layers are inversion related. This inversion is favored by stacking interactions between acid rings between layers (Table 6.7). We analyzed this structure in terms of short intermolecular contacts to identify portions of TMC that are critical for the formation of the trigonal network, and portions that are not. We expected that changing the non-critical portions will allow us to reproduce this trigonal structure, and that changing the critical portion will result in different types of networks. It is obvious that we can introduce new groups on either the benzoate or the pyridyl (or both) groups. All the CH groups on the benzoate phenyl rings are involved in short contacts with the nearest O or C atoms. That is, replacing these CH groups will most likely influence the trigonal structure. The CH groups on the pyridyl molecules, however, are not involved in any short contacts. The nearest contact atoms (along the CH bond vectors) are about 4.2-4.5 Å away from the carbon atoms of the pyridyl ring. Therefore, we argued that substituting H-atoms on pyridyl rings (with simple groups such as CH<sub>3</sub>) should retain the current trigonal structure.

In the following, we discuss structures that resulted from substituting the pyridyl CH groups. An analysis of the intermolecular contacts around trapped benzene molecule is also interesting. Benzene makes van der Waals contacts with benzoate rings above and below its molecular plane. Along the CH bond vector, however, the nearest contacts are 4-7 Å away (from the C atoms). We also argued that replacing the benzene with guest molecules such as mesitylene and trichlorobenzene should retain the current structure, but, so far our efforts have not been successful in producing crystals containing these guest species.

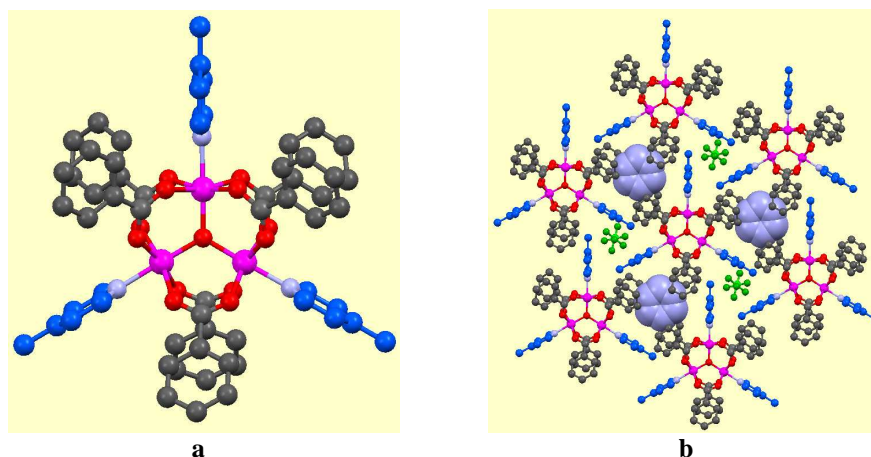


**Figure 6.16** (a) Molecular structure of **BA-4P** complex. (b) Assembly of trigonal units into 2D acentric ( $3^6$ ) network (benzene solvate). Hydrogen atoms are omitted for clarity.

**6.3.4 Crystal Structure of  $[\text{Mn}_3\text{O}(\text{BA})_6(4\text{-Picoline})_3]^+[\text{ClO}_4]^- \cdot \text{C}_6\text{H}_6$ .** Changing the pyridine ligand to 4-picoline does not change the supramolecular structure as predicted by the analysis given above. In fact, this compound is isostructural to the pyridine derivative described in the previous section. The TMC units retain their acentric trigonal symmetry in the crystal. They are held into acentric 2D trigonal ( $3^6$ ) networks through short C-H...O hydrogen bonds with  $\text{ClO}_4^-$  ions (Table 6.6). Again, the  $\text{ClO}_4^-$  ions adopt pseudo-octahedral geometry in which four O atoms share six apices of a pseudo-octahedron. All the six O atoms are symmetry equivalent. The juxtaposition of benzoate rings again results in cavities similar to those seen in the previous structure; benzene molecules are trapped into these cavities with similar intermolecular contacts described in previous section. Figures 6.16a and b show details of BA-4P benzene solvate structure at the molecular and crystal level. As explained above, we tried to grow crystals of BA-4P containing guests that are laterally expanded. These trials, however, produced crystals in which dichloromethane (solvent used for the crystallization) is included within the cavities.

**6.3.5 Crystal Structure of  $[\text{Mn}_3\text{O}(\text{BA})_6(4\text{-Picoline})_3]^+[\text{ClO}_4]^- \cdot \text{CH}_2\text{Cl}_2$ .** The  $\text{CH}_2\text{Cl}_2$  solvate of BA-4P is isostructural to the benzene solvate described above. The only difference is that the solvent molecule is disordered (it does not possess three-fold symmetry) such that two Cl atoms occupy the three apices of an equilateral triangle, and the C atom occupies two positions situated above and below the triangle formed by the three Cl atoms. Figures 6.17a and b show details of BA-4P $\cdot\text{CH}_2\text{Cl}_2$  solvate structure at the molecular and crystal level. The ability to change the guest species without changing the overall structure again indicates that the guest molecules play the role of ‘space-fillers’ and that they are not involved in structure directing intermolecular interactions.

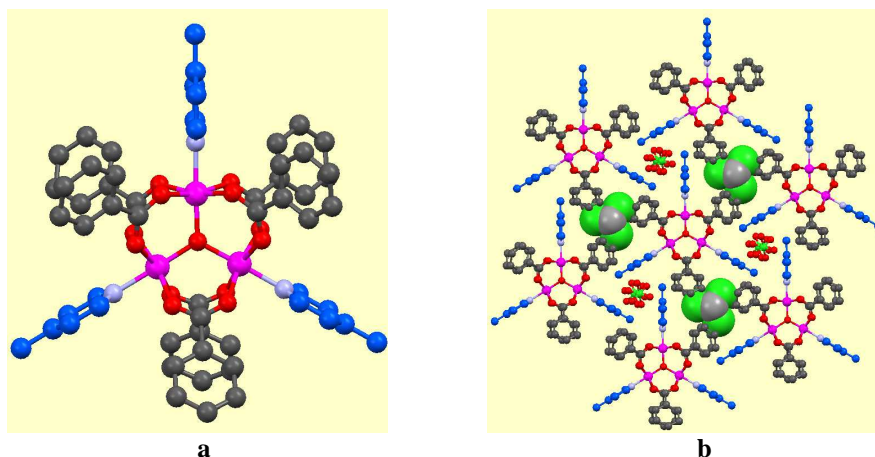


**Figure 6.17** (a) Molecular structure of BA-4P complex. (b) Assembly of trigonal units into 2D acentric ( $3^6$ ) network (dichloromethane solvate). Hydrogen atoms are omitted for clarity.

**6.3.6 Crystal Structure of  $[\text{Mn}_3\text{O}(\text{BA})_6(3\text{-Picoline})_3]^+[\text{ClO}_4]^- \cdot \text{C}_6\text{H}_6$ .** We have been able to grow crystals (with hexagonal morphology) of BA-3P in benzene. These crystals, however, diffracted poorly and X-ray data was not good enough for full structure determination. To date, we have been able to determine the space group and locate the  $\text{ClO}_4^-$  anions and the central  $\text{Mn}_3\text{O}-(\text{OOC})_6$  units from the available data. Further refinement of this structure is not possible because of poor quality of the X-ray data (obtained from crystals that are either twinned or display layer misalignment). A comparison of the unit cell parameters in Table 6.4 (and location of  $\text{ClO}_4^-$  anions and  $\text{Mn}_3\text{O}$  units within the unit cell) with previous structures indicates that the BA-3P is isostructural to BA-Py and BA-4P. These results show that acentric  $3^6$  networks can be reliably generated within the family of BA-Py TMC structures by incorporating small substituents on the pyridyl ligands. The overall structure, however, remains centrosymmetric; thus, we focused our attention on changing the benzoate ligands to explore new types of structures.

**6.3.7 Crystal Structure of  $[\text{Mn}_3\text{O}(\text{pTA})_6(\text{Py})_3]^+[\text{ClO}_4]^-$ : Acentric  $4^4$  and  $\bar{C}$  Centric  $3^6$  Networks.** Changing the benzoic acid ligands to *p*-toluic acid changes the structure type as expected from the analysis given in Section 6.3.3. In the following we describe two sets of structures, one belonging to centrosymmetric space groups (e.g., *pTA*-Py, this section), and the others belonging to noncentrosymmetric space groups (e.g., *mTA*-Py, next section). The similarities and differences between these networks and design considerations are given below.

**6.3.7.1 Reduction of Molecular Symmetry.** This TMC perchlorate crystallizes in the centrosymmetric space group *Pccn* ( $P\cdot 2_1/c\cdot 2_1/c\cdot 2/n$ ). The TMC unit is located on the 2-fold axis (as opposed to be on the  $\bar{6}$  axis as in the case of BA-Py, BA-4P, and BA-3P series of structures described above). That is, the TMC unit does not retain its three-fold molecular symmetry in the crystal. It follows then that the six acid ligands are not equivalent in the crystal; similarly the three pyridyl ligands are also not equivalent (see Figure 6.18). We can see that changing the acid ligand from BA to *pTA* *does* change the structure type as expected.

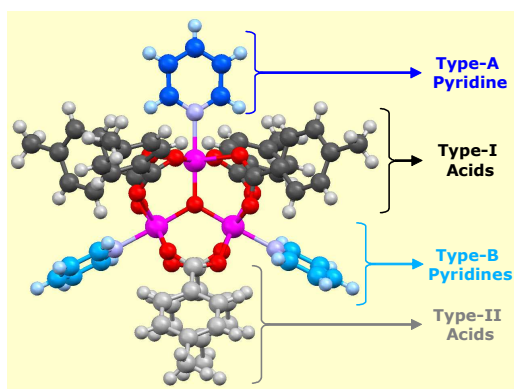


**Figure 6.18** Molecular structure of *pTA*-Py complex. Two types of acid rings (Type I and Type II) and two types of pyridine rings (Type A and Type B) are indicated by different colors.

**6.3.7.2 Classification of Ligands into Groups.** The molecular symmetry of TMC is reduced in the crystal because different acid and pyridyl ligands have different packing preferences. Based on the analysis of this structure and a number of other TMC structures to be discussed below, we classified acid and pyridyl ligands into two groups each. One group of acids, which we call Type-I acids, contain four acid ligands; the second group, Type-II acids, contains the other two acid ligands. Similarly, in the case of pyridyl ligands ‘Type-A’ consists of one pyridyl group (that is projected along [001]), and ‘Type-B’ consists of other two pyridyl groups. Figure 6.18 shows coloring scheme used for identifying different acid and pyridyl ligands in the TMC and their relative geometrical arrangement.

**6.3.7.3 Acentric  $4^4$  Networks Parallel to (001).** The crystal structure of *p*TA-Py can be sectioned into  $4^4$  nets (Figure 6.19) that lie parallel to (001). In these nets, each TMC has four neighbors, and if we consider each TMC to be a node, the smallest cycle connecting nearest nodes has four nodes in it. This is the reason we call the arrangement shown in Figure 6.19 as  $4^4$  net. Two types of intermolecular interactions ( $\pi \cdots \pi$  stacking and C–H $\cdots$ O hydrogen bonds) are responsible for holding the TMC units together within this  $4^4$  net. Stacking ( $\pi \cdots \pi$ ) interactions between the aromatic rings of Type-II acids and Type-B pyridyl ligands act as the node connectors in the net (Table 6.7). In addition, the  $\text{ClO}_4^-$  ions are situated in the square-cavities formed within the  $4^4$  net; the O atoms of  $\text{ClO}_4^-$  ions are involved in the formation of C–H $\cdots$ O interactions with the CH groups of Type-I acids and Type-B pyridyl units (Table 6.6). We should note here that unlike in BA-Py, BA-4P, BA-3P series of structures, both acid and pyridyl CH groups form the CHO bonds in this structure. This may be partly due to the reduced CH acidity of *p*TA ligands (caused by the incorporation of methyl groups). An important aspect of this  $4^4$  arrangement of TMC units is that it is noncentrosymmetric in two dimensions. Any acentric arrangement of octupolar units (be it octupolar at the supramolecular level or not) is an important step forward in the design of materials that display second order NLO effects. We have fully explored this 2D acentric arrangement in the design of solid state NLO materials that are noncentrosymmetric in three dimensions (Sections 6.3.8–6.3.14).

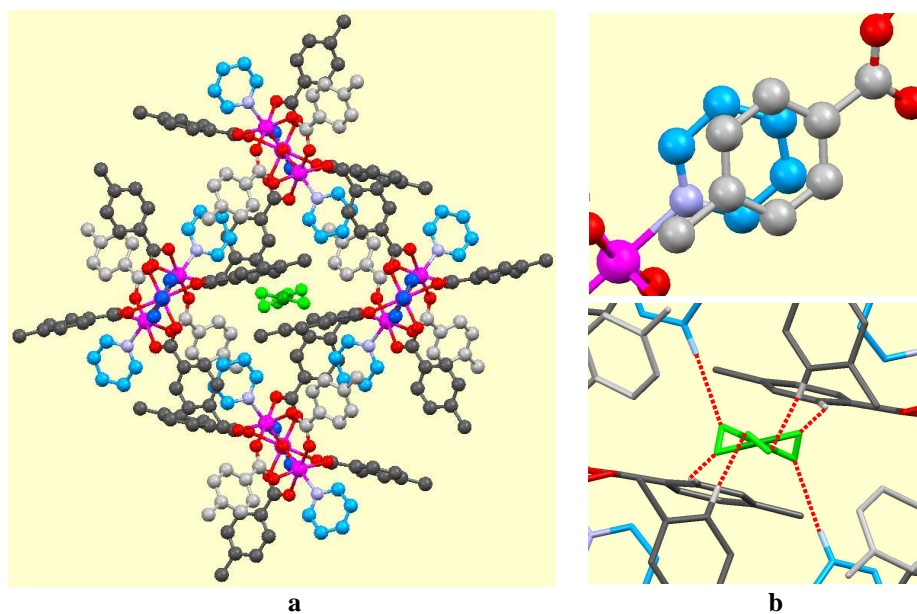


**Figure 6.19** (a) Acentric arrangement of *p*TA-Py molecules into  $4^4$  networks perpendicular to the *c*-axis. (b) Two types of intermolecular interactions:  $\pi \cdots \pi$  stacking of Type-B pyridyl and Type-II acid rings (top) and C–H $\cdots$ O hydrogen bonds between the  $\text{ClO}_4^-$  anion and the C–H groups of Type-I acid and Type B pyridyl rings (bottom).

**6.3.7.4 Stacking of  $4^4$  Networks – Acentric TMC Chains along [001] and Centric Pseudo-Trigonal Layers Parallel to (220) and  $(1\bar{1}0)$ .** Stacking of  $4^4$  nets along [001] completes the description of crystal structure of *pTA-Py*. Given that *Pccn* is a centrosymmetric space group, and that the  $4^4$  nets themselves are acentric, it is obvious that adjacent  $4^4$  nets are related by an inversion center. This is, in a broad sense, correct. It is, however, instructive to analyze the stacking of individual TMC units along [001] (as opposed to the stacking of  $4^4$  nets as a whole). TMCs stacked along [001] form a chain structure (mediated by C–H $\cdots\pi$  interactions between Type-A pyridyl ring and Type-II acid rings; see Figure 6.20) in which adjacent TMCs are  $2_1$ -axis related. That is, these TMC chains along [001] are acentric. Thus, we can pin-point the location of inversion center in terms of TMC packing: adjacent TMC chains are inversion related. An analysis of intermolecular interactions between TMC units that are related by inversion center showed that there are hardly any interactions; the only possible interactions are between the *para*-CH<sub>3</sub> groups of two of the Type-I acids and the aromatic ring of Type-A pyridyl ligand. The parameters for this interaction are: C $\cdots\pi$  = 3.67 Å and C–H $\cdots\pi$  = 110°. (In general, inversion center is expected to maximize close-packing. In this structure, however, this statement does not hold true. The lack of maximization of close-packing due to inversion suggested to us that we may be able to remove the inversion center by suitably substituting the acid ligands.) We therefore expected that moving the CH<sub>3</sub> group to the *meta* position would alter interchain packing; this change might as well remove the unwanted center of symmetry.

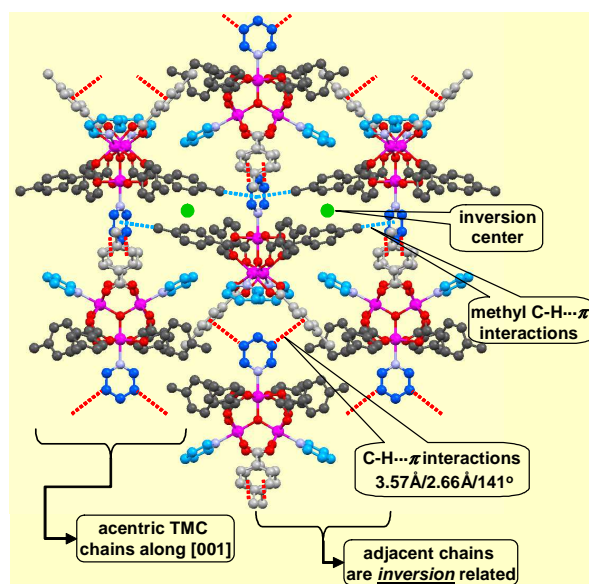


**Figure 6.20** Trigonal centrosymmetric networks parallel to (220). The C–H $\cdots\pi$  interactions between Type-A pyridyl and Type-II acid rings lead to the formation of acentric TMC chains along [001].

**6.3.8 Structures Adopting Acentric  $4^4$  and  $\underline{A}$ centric  $3^6$  Networks.** In the following sections we will describe structures that are designed to adopt 3D noncentrosymmetric packing of molecules. This design is based on the 2D acentric  $4^4$  network discussed above. All the structures to be discussed are crystallized in noncentrosymmetric space groups. We begin with the structure of *mTA*-Py where the  $\text{CH}_3$  group on the acid ligands is relocated to the *meta* position. We should note here that from the analysis given above, we need to relocate  $\text{CH}_3$  groups on only two of the acid ligands. Such an exercise, however, would remove the octupolar symmetry from the TMC unit, and is also synthetically demanding.

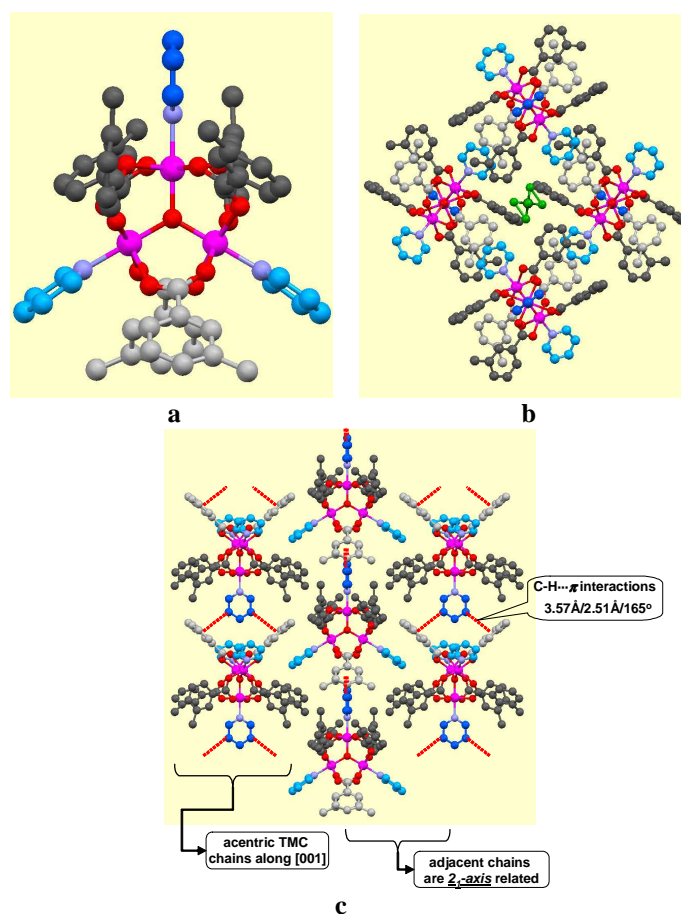


**Figure 6.21** (a) Molecular structure of *mTA*-Py complex. Acid rings are colored dark gray (Type I) and light gray (Type II), and pyridines rings are colored blue (Type A) and light blue (Type B). (b) and (c) Assembly of TMCs in the crystal into acentric  $4^4$  [parallel to (001)] and  $3^6$  networks [parallel to (220)] respectively.

**6.3.9 Crystal Structure of  $[\text{Mn}_3\text{O}(\text{mTA})_6(\text{Py})_3]^+[\text{ClO}_4]^-$ .** This TMC crystallizes in the noncentrosymmetric space group  $P2_12_12_1$ . As in  $p\text{TA-Py}$ , the TMC units are located on the 2-fold axis along  $c$ -axis. Thus, the TMC does not retain its 3-fold molecular symmetry in the crystal. Reduction of symmetry means that all acid and pyridyl ligands are not equivalent in their packing patterns. As in the previous case, we classified the acid and pyridyl groups into Types I and II and Types A and B based on their packing characteristics (Figure 6.21a). Again, as in  $p\text{TA-Py}$ , TMC units are assembled into acentric  $4^4$  nets based on stacking interactions between Type-II acid rings and Type-B pyridyl rings, and C–H $\cdots$ O interactions between perchlorate O atoms and benzoate and pyridyl CH groups (Figure 6.21b, Tables 6.6 and 6.7). Until the formation of  $4^4$  nets, the crystal structural features are similar to those in  $p\text{TA-Py}$ , though there are significant differences in the molecular conformations.

The difference between the  $p\text{TA-Py}$  and  $m\text{TA-Py}$  structures (in terms of centricity) is that adjacent  $4^4$  nets in the latter are translation related, as opposed to be inversion (as in the case of former). That is structure of  $m\text{TA-Py}$  is *acentric* in three dimensions. The stacking of  $4^4$  nets along [001] can be best visualized by looking at layers of molecules along (110) or  $(1\bar{1}0)$ . Figure 6.21c shows that the molecules are arranged into acentric trigonal ( $3^6$ ) nets within these 220 layers. Again, TMCs stacked along [001] form an acentric chain structure (mediated by C–H $\cdots\pi$  interactions between Type-I pyridyl ring and Type-II acid rings; see Figure 6.21c) in which adjacent TMCs are translation related. Adjacent TMC chains are related by a  $2_1$ -axis (recall that in  $p\text{TA-Py}$  adjacent chains are inversion related); this is the difference that lies at the origin of 3D noncentrosymmetry in  $m\text{TA-Py}$ .

It appears that moving the methyl group from *para* to *meta* positions on the acid ligands does remove the centrosymmetry as suggested in the previous section. In the following sections we will describe five other structures that are similar to  $m\text{TA-Py}$  in design and packing features. That is all the five structures to be discussed below are noncentrosymmetric, and all these are based on the acentric  $4^4$  net observed in  $p\text{TA-Py}$  and acentric stacking of these nets to complete the 3D structure.

**6.3.10 Crystal Structure of  $[\text{Mn}_3\text{O}(\text{pTA})_6(\text{4-Picoline})_3]^+[\text{ClO}_4]^- \cdot \text{CH}_2\text{Cl}_2$ .** This TMC crystallizes in the noncentrosymmetric space group  $P2_12_12_1$ . The asymmetric unit contains a full TMC molecule; though six acid ligands and three pyridyl ligands are symmetry independent, they can be again classified into Types I-II and Types A-B sets based on their packing patterns (Figure 6.22a). Figures 6.22a and b show the  $4^4$  and  $3^6$  nets observed in this structure. Stacking and C–H $\cdots$ O interactions (Tables 6.6 and 6.7) govern the formation  $4^4$  net (only acid groups, but not pyridyl ligands, contribute to C–H $\cdots$ O bonds). Replacing pyridine with 4-picoline elongates the stacking axis ( $c$ -axis) because it is in this direction that the Type-A pyridyl ligand is projected into the groove formed by Type-II acid and Type-B pyridyl ligands in the two structures discussed in Sections 6.3.7 and 6.3.8 (see Figure 6.21c). In  $p\text{TA-Py}$  and  $m\text{TA-Py}$  structures the Type-I pyridyl ligand is tightly held into this groove by short C–H $\cdots\pi$  interactions; in the current  $p\text{TA-4P}$  structure, the methyl group Type-A 4-picoline ligand is projected into this groove, and creates some void space. Solvated  $\text{CH}_2\text{Cl}_2$  guest molecules occupy this

space. The TMC units along [001] are now held together by a combination of interactions between Type-A and Type-B pyridyl ligands, and Type-II acid groups, and the guest molecules. The overall structure again is acentric that is built upon acentric  $4^4$  and  $3^6$  nets (Figures 6.22b and c).

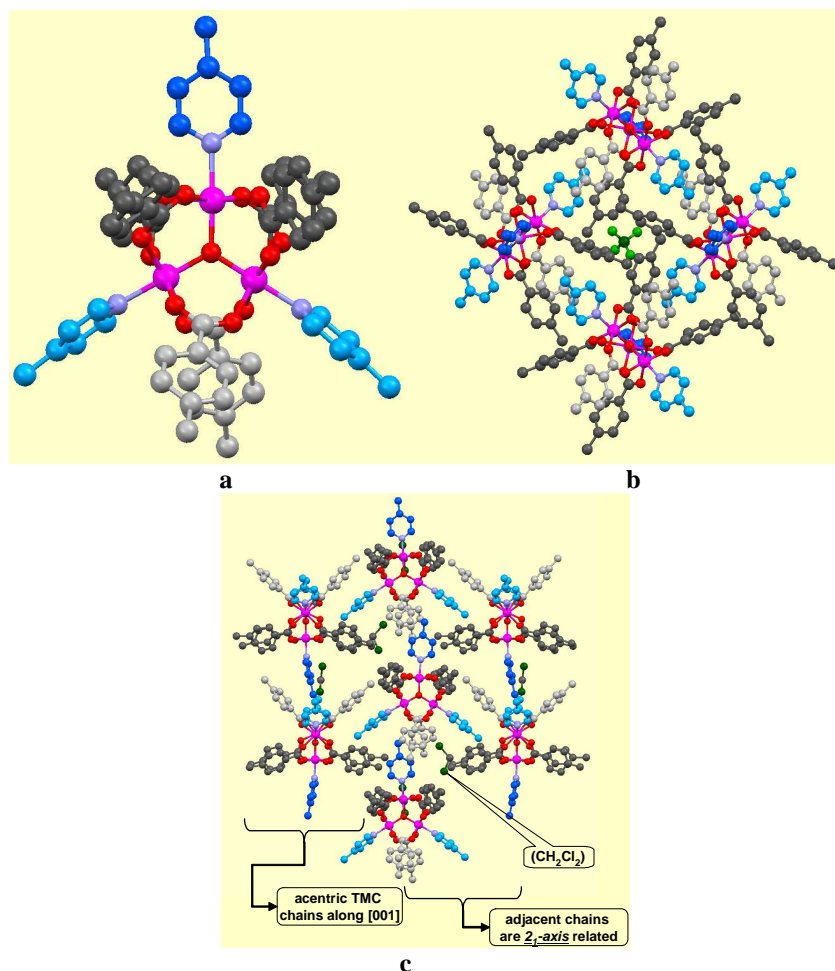


**Figure 6.22** (a) Crystal structure of *pTA-4P* complex. (b) Arrangement of TMCs into  $4^4$  networks parallel to (001). (c) Assembly of acentric TMC chains into noncentrosymmetric ( $3^6$ ) networks parallel to (220).

**6.3.11 Crystal Structure of  $[\text{Mn}_3\text{O}(\text{pTA})_6(\text{3-Picoline})_3]^+[\text{ClO}_4]^- \cdot \text{C}_6\text{H}_6$ .** This TMC crystallizes in the noncentrosymmetric space group  $P2_12_12_1$  and has a structure that is very similar to *pTA-4P* described above. As in *pTA-4P* the asymmetric unit contains a full TMC molecule; again the acid and pyridyl groups are symmetry independent but can be grouped into two sets each (Figure 6.23a). Figures 6.23b and c show  $4^4$  and  $3^6$  nets in this structure. Tables 6.6 and 6.7 show the C–H $\cdots$ O and stacking parameters involved in

the formation of these nets. As in *pTA-4P* insertion of methyl group onto pyridyl ring creates void space along stacking axis (*c*-axis) and this time solvated benzene molecules fill this space.

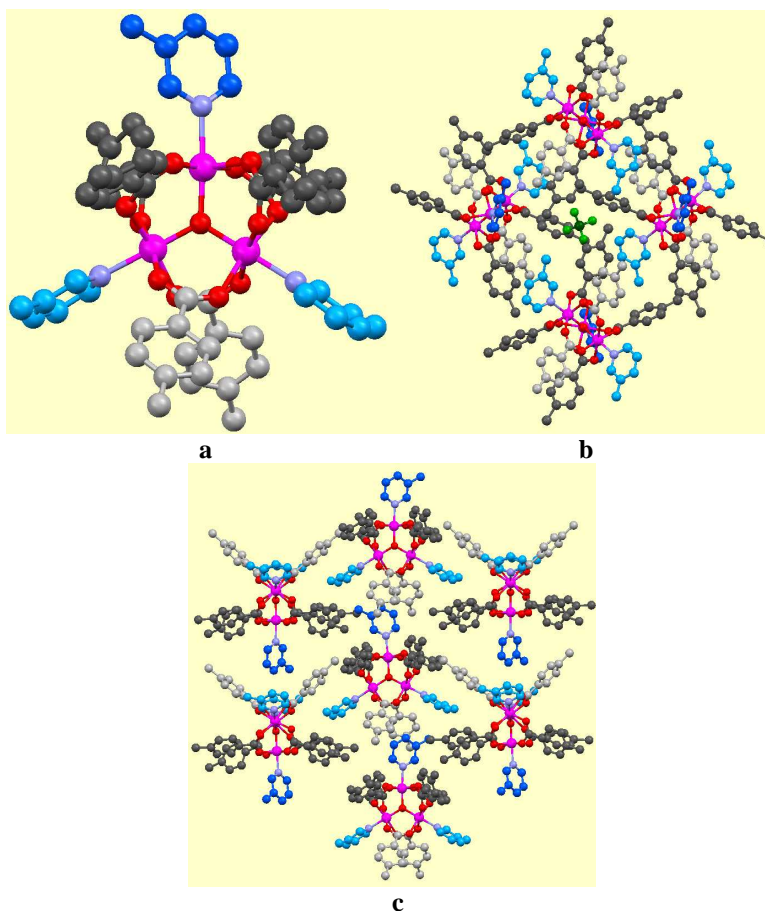


**Figure 6.23** (a) Molecular structure of *pTA-3P* complex. (b) and (c) Acentric  $4^4$  and  $3^6$  networks of TMCs.

**6.3.12 Crystal Structure of  $[\text{Mn}_3\text{O}(\text{mTA})_6(4\text{-Picoline})_3]^+[\text{ClO}_4]^-$ .** This TMC crystallizes in the noncentrosymmetric *tetragonal* space group  $P\bar{4}2_1m$ . The molecule is located on a 2-fold axis; acid and pyridyl ligands are grouped into two sets each as before (Figure 6.24a). This is the first structure in which the four-fold symmetry of the  $4^4$  nets is fully realized. In all the structures discussed above (Sections 6.3.7-6.3.10) although the structures contained  $4^4$  nets, they all adopt low symmetry orthorhombic space groups. As far as the packing patterns are concerned this structure is similar to the acentric structures above: it has acentric  $4^4$  nets (parallel to *ab*-plane) that are stacked (along *c*-axis) on each other by translation leading to the formation of acentric  $3^6$  nets (Figures 6.24b and c).

This is not a fully refined structure; in two of the acid groups (Type II) the methyl groups are disordered. There appears to be a disordered benzene ring close to these disordered methyl groups; the final details of this structure are yet to be determined.

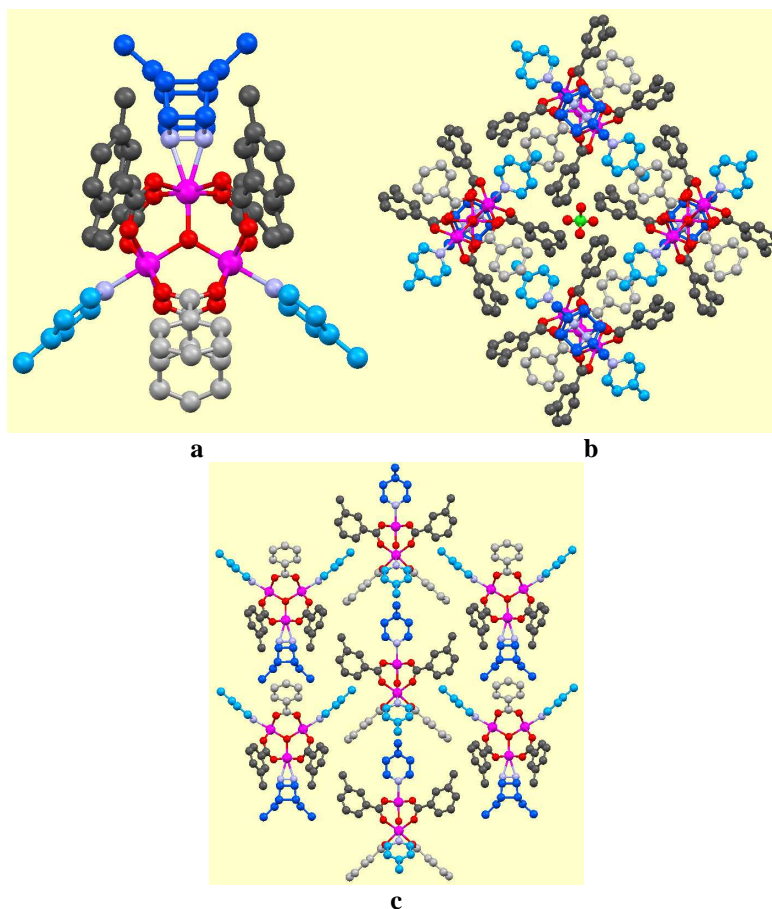


**Figure 6.24** (a) Molecular structure of *mTA-4P* complex with disordered Type-A pyridyl ligands. (b) and (c) Assembly of TMCs into high symmetry  $4^4$  and  $3^6$  networks.

**6.3.13 Crystal Structure of  $[\text{Mn}_3\text{O}(\text{3CIBA})_6(\text{4-Picoline})_3]^+[\text{ClO}_4]^-$ .** We have been able to grow thin (square-shaped) plate-like crystals of this compound and collect X-ray data on them. The quality of the data, however, is poor; so far we have been able to determine the unit cell and space group but not the full structure. This TMC, like *mTA-4P*, crystallizes in the noncentrosymmetric tetragonal space group  $P\bar{4}2_1m$ . Based on the similarity in cell dimensions of this structure and *mTA-4P* (Table 6.4), and based on the chloro-methyl exchange rule in crystal engineering,<sup>32</sup> we expect that this TMC has a structure similar to *mTA-4P*; that is it is 3D acentric built upon acentric  $4^4$  and  $3^6$  nets.

**6.3.14 Crystal Structure of  $[\text{Mn}_3\text{O}(m\text{TA})_6(3,4\text{-Lutidine})_3]^+[\text{ClO}_4]^-$ .** This TMC crystallizes in the noncentrosymmetric space group  $P2_12_12$ . This structure is also not fully refined at this stage, but the positions of non-H atoms that were refined so far clearly indicate the overall structural details. The TMC units are located on the 2-fold axis along  $c$ -axis. As before, acid and pyridyl ligands can be grouped into two sets each (Figure 6.25a). All the pyridyl ligands (Types A and B) are disordered such that 3,4-Lutidine rings appear as though they are 3,4,5-collidine rings; two of the acid ligands (Type II) are disordered such that they appear as 3,5-dimethylbenzoate rings. The structure is similar to the acentric structures above; it is built up on acentric  $4^4$  and  $3^6$  nets, again through stacking and C–H...O interactions. As expected the methyl groups on the pyridyl rings create void space and solvated benzene molecules occupy this space.

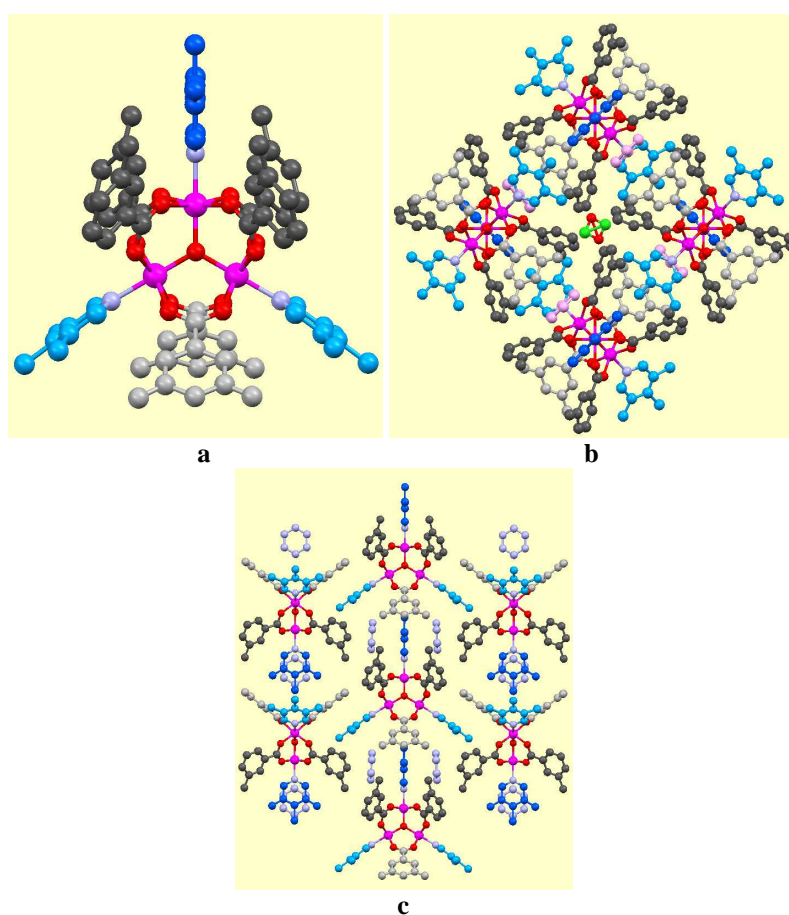


**Figure 6.25** (a) Disordered molecular structure of  $m\text{TA-34Lu}$  complex. (b) and (c) Assembly of TMCs into  $4^4$  and  $3^6$  networks.

The results presented in Sections 6.3.7 to 6.3.13 clearly show that 3D noncentrosymmetric structures can be designed with confidence within a subset of

charged TMC systems. All these structures contain, consistently, acentric  $4^4$  and  $3^6$  networks. The ability to design such a large number of acentric solids within a family of octupolar molecules has not been achieved so far. One additional feature to note in these systems is that the TMCs have complex 3D shape and adopted a range of molecular conformations within these acentric solids. Despite this complexity, the TMCs fit well for the design of predictable solid state structures. We conclude our discussion of TMCs here and in the following sections we will discuss two other clusters with increased nuclearity.

#### 6.4 CLUSTERS OF HIGHER NUCLEARITY

During the course of TMC synthesis, we have discovered two clusters of higher nuclearity. These clusters were formed, unexpectedly, when we used di or triaza ligands. We have not yet optimized these syntheses. In the following section these clusters are presented along with their synthesis.

**6.4.1 Synthesis and Structure of  $\text{Mn}_6(\text{OOCR})_{10}(\text{CH}_3\text{CN})_4$ .** A mixture of  $\text{Mn}(\text{O}_2\text{CMe})_2 \cdot 4\text{H}_2\text{O}$  (2.0g, 8.15 mmol), *p*-toluic acid (10.1g, 74.18 mmol) and triazine (1.0g, 12.36 mmol) were dissolved in 25 mL of absolute EtOH. To this solution was added  ${}^n\text{Bu}_4\text{NMnO}_4$  (1.14g, 3.15 mmol) in small portions. Immediately after adding the permanganate,  $\text{NaClO}_4$  (0.69g, 5.65mmol) was added in portions and the mixture was stirred for 1h. The product was collected by filtration and dried in vacuo. Recrystallization was carried out in acetonitrile and thin needle shaped crystals were collected after two days. The structure of this cluster is shown below. We will explore the geometry of this cluster to see if any extended networks can be built from it.

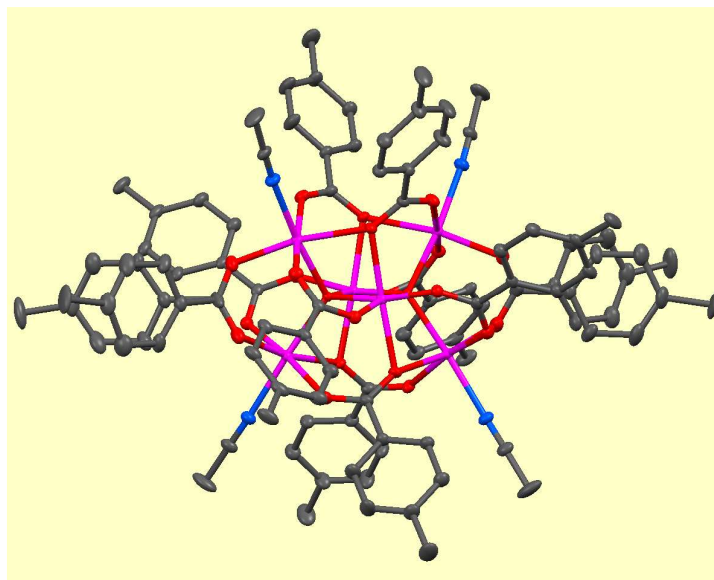


**Figure 6.26.** Molecular structure of  $\text{Mn}_6(\text{OOCR})_{10}(\text{CH}_3\text{CN})_4$  complex (ellipsoid mode). Hydrogen atoms are omitted for clarity.

**6.4.2 Synthesis, Structure, and Magnetic Properties of  $\text{Mn}_{13}\text{-}\mu^3\text{O}_2\text{-}\mu^5\text{O}_6(\text{OOCR})_{12}(\text{C}_2\text{H}_5\text{O})_6$ .** A mixture of  $\text{Mn}(\text{O}_2\text{CMe})_2\cdot 4\text{H}_2\text{O}$  (0.20g, 0.81 mmol), *m*-toluic acid (0.836g, 6.14 mmol) and pyrimidine (1mL, 12.6 mmol) were dissolved in 25 mL of absolute EtOH. To this solution was added  ${}^n\text{Bu}_4\text{NMnO}_4$  (0.05g, 0.12 mmol) in small portions. The mixture was stirred for 1h and the product was left undisturbed overnight in the refrigerator. The gray product was collected by filtration and dried in vacuo. Recrystallization was carried out in EtOH. After ~2 weeks gold microcrystals with needle shapes of the desired product were obtained.

Structural analysis showed that the cluster contains 13 Mn ions in three oxidation states and two environments. Figure 6.27a shows the core of the cluster which is made of 13 Mn ions (one  $\text{Mn}^{4+}$ , six  $\text{Mn}^{3+}$ , and six  $\text{Mn}^{2+}$ ) 12 benzoate ligands, 8 oxide ligands (two in  $\mu^3$  and six in  $\mu^5$  coordination), and six ethoxide ligands. From Figure 6.27a we can see that the core of the cluster has cubic geometry; we call this core ‘super cube’ cluster.

The most interesting aspect of this cluster is that the 12 benzoate ligands are projected away from the cube in an octahedral fashion. We hope to develop this cluster as an octahedral node from which to generate porous network with simple cubic geometry, much in the same way as Yaghi uses  $\text{Zn}_4\text{O}$  octahedral nodes to build porous solids (see Figure 6.7b).<sup>25</sup>

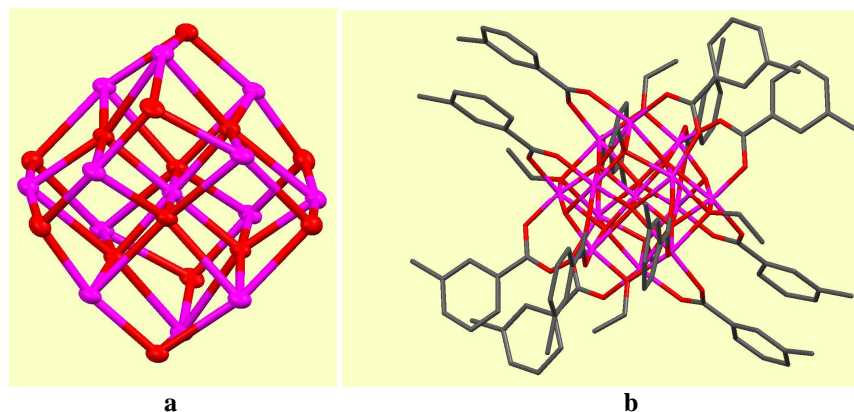


**Figure 6.27** Molecular structure of  $\text{Mn}_{13}\text{-}\mu^3\text{O}_2\text{-}\mu^5\text{O}_6(\text{OOCR})_{12}(\text{C}_2\text{H}_5\text{O})_6$  cluster. (a) Core of the cluster (without benzoate and ethyl groups) showing the ‘super cube’. (b) Full structure of the cluster showing the octahedral disposition of the twelve benzoate rings. Hydrogen atoms are omitted for clarity.

## 6.5 SUMMARY AND CONCLUSION

Crystallographic data presented above show that we are able to synthesize octupolar molecular materials containing Mn-carboxylate clusters. By changing the acid and pyridine derivatives we can design 3D noncentrosymmetric arrangements of charged TMCs in solid state. To date we have collected X-ray data, refined and analyzed structures only of charged TMCs. Future work should be focused on crystal growth, X-ray data collection, structure refinement and analysis of remaining charged and neutral trigonal clusters, to explore similarities and differences among these neutral and charged clusters. In this work, to make the TMCs we were using Mn metal, which has octahedral geometry. It would be also interesting to study NLO effects of TMCs made of other metals. Other metals that could be explored for the synthesis of the new TMCs in this work are: Fe, Cr, Zn, Ru, Ir, Rh and V, with those acid and pyridine derivatives that produced successful noncentrosymmetric materials.

**6.6 REFERENCES**

1. Nalwa, H. S.; Miyata, S.; Editors, *Nonlinear Optics of Organic Molecules and Polymers*. **1997**.
2. Kanis, D. R.; Ratner, M. A.; Marks, T. J., Design and construction of molecular assemblies with large second-order optical nonlinearities. Quantum chemical aspects. *Chem. Rev.* **1994**, *94*, 195-242.
3. Zyss, J.; Ledoux, I., Nonlinear optics in multipolar media: theory and experiments. *Chem. Rev.* **1994**, *94*, 77-105.
4. Ledoux, I.; Zyss, J., Multipolar engineering of molecules and materials for quadratic nonlinear optics. *Compt. Rend. Phys.* **2002**, *3*, 407-427.
5. Bredas, J. L.; Meyers, F.; Pierce, B. M.; Zyss, J., On the second-order polarizability of conjugated p-electron molecules with octupolar symmetry: the case of triaminotrinitrobenzene. *J. Am. Chem. Soc.* **1992**, *114*, 4928-4929.
6. Cho, B. R.; Park, S. B.; Lee, S. J.; Son, K. H.; Lee, S. H.; Lee, M.-J.; Yoo, J.; Lee, Y. K.; Lee, G. J.; Kang, T. I.; Cho, M.; Jeon, S.-J., 1,3,5-Tricyano-2,4,6-tris(vinyl)benzene Derivatives with Large Second-Order Nonlinear Optical Properties. *J. Am. Chem. Soc.* **2001**, *123*, 6421-6422.
7. Omenat, A.; Barbera, J.; Serrano, J. L.; Houbrechts, S.; Persoons, A., Columnar liquid crystals with highly polar groups. Evaluation of the nonlinear optical properties. *Adv. Mater.* **1999**, *11*, 1292-1295.
8. McDonagh, A. M.; Humphrey, M. G.; Samoc, M.; Luther-Davies, B.; Houbrechts, S.; Wada, T.; Sasabe, H.; Persoons, A., Organometallic Complexes for Nonlinear Optics. 16. Second and Third Order Optical Nonlinearities of Octopolar Alkynylruthenium Complexes. *J. Am. Chem. Soc.* **1999**, *121*, 1405-1406.
9. Brasselet, S.; Cherioux, F.; Audebert, P.; Zyss, J., New Octupolar Star-Shaped Structures for Quadratic Nonlinear Optics. *Chem. Mater.* **1999**, *11*, 1915-1920.
10. Cherioux, F.; Audebert, P.; Maillotte, H.; Zyss, J., Synthesis and characterization of an octupolar polymer and new molecular octupoles with off-resonant third order optical nonlinearities. *Chem. Commun.* **1999**, 2083-2084.
11. Thalladi, V. R.; Brasselet, S.; Blaser, D.; Boese, R.; Zyss, J.; Nangia, A.; Desiraju, G. R., Engineering of an octupolar nonlinear optical crystal: tribenzyl isocyanurate. *Chem. Commun.* **1997**, 1841-1842.
12. Thalladi, V. R.; Brasselet, S.; Weiss, H.-C.; Blaser, D.; Katz, A. K.; Carrell, H. L.; Boese, R.; Zyss, J.; Nangia, A.; Desiraju, G. R., Crystal Engineering of Some 2,4,6-Triaryloxy-1,3,5-triazines: Octupolar Nonlinear Materials. *J. Am. Chem. Soc.* **1998**, *120*, 2563-2577.
13. Alcaraz, G.; Euzenat, L.; Mongin, O.; Katan, C.; Ledoux, I.; Zyss, J.; Blanchard-Desce, M.; Vaultier, M., Improved transparency-nonlinearity trade-off with boroxine-based octupolar molecules. *Chem. Commun.* **2003**, 2766-2767.
14. Lequan, M.; Branger, C.; Simon, J.; Thami, T.; Chauchard, E.; Persoons, A., Hyperpolarizability of tetraorganotin compounds determined by the hyper-Rayleigh scattering technique. *Chem. Phys. Lett.* **1994**, *229*, 101-104.
15. Maury, O.; Viau, L.; Senechal, K.; Corre, B.; Guegan, J.-P.; Renouard, T.; Ledoux, I.; Zyss, J.; le Bozec, H., Synthesis, linear, and quadratic-nonlinear optical properties of

- octupolar D3 and D2d bipyridyl metal complexes. *Chem. Eur. J.* **2004**, *10*, 4454-4466.
16. Bartholomew, G. P.; Ledoux, I.; Mukamel, S.; Bazan, G. C.; Zyss, J., Three-Dimensional Nonlinear Optical Chromophores Based on Through-Space Delocalization. *J. Am. Chem. Soc.* **2002**, *124*, 13480-13485.
  17. Dhenaut, C.; Ledoux, I.; Samuel, I. D. W.; Zyss, J.; Bourgault, M.; Le Bozec, H., Chiral metal complexes with large octupolar optical nonlinearities. *Nature* **1995**, *374*, 339-342.
  18. Evans, O. R.; Lin, W., Crystal Engineering of NLO Materials Based on Metal-Organic Coordination Networks. *Acc. Chem. Res.* **2002**, *35*, 511-522.
  19. Coe, B. J.; Harris, J. A.; Brunschwig, B. S.; Asselberghs, I.; Clays, K.; Garin, J.; Orduna, J., Three-Dimensional Nonlinear Optical Chromophores Based on Metal-to-Ligand Charge-Transfer from Ruthenium(II) or Iron(II) Centers. *J. Am. Chem. Soc.* **2005**, *127*, 13399-13410.
  20. Maury, O.; Le Bozec, H., Molecular Engineering of Octupolar NLO Molecules and Materials Based on Bipyridyl Metal Complexes. *Acc. Chem. Res.* **2005**, *38*, 691-704.
  21. Lin, W.; Wang, Z.; Ma, L., A Novel Octupolar Metal-Organic NLO Material Based on a Chiral 2D Coordination Network. *J. Am. Chem. Soc.* **1999**, *121*, 11249-11250.
  22. Thalladi, V. R.; Boese, R.; Bresselet, S.; Ledoux, I.; Zyss, J.; Jetti, R. K. R.; Desiraju, G. R., Steering non-centrosymmetry into the third dimension: crystal engineering of an octupolar nonlinear optical crystal. *Chem. Commun.* **1999**, 1639-1640.
  23. Seo, J. S.; Whang, D.; Lee, H.; Jun, S. I.; Oh, J.; Jeon, Y. J.; Kim, K., A homochiral metal-organic porous material for enantioselective separation and catalysis. *Nature* **2000**, *404*, 982-986.
  24. Eddaoudi, M.; Moler, D. B.; Li, H.; Chen, B.; Reineke, T. M.; O'Keeffe, M.; Yaghi, O. M., Modular Chemistry: Secondary Building Units as a Basis for the Design of Highly Porous and Robust Metal-Organic Carboxylate Frameworks. *Acc. Chem. Res.* **2001**, *34*, 319-330.
  25. Rowsell Jesse, L. C.; Millward Andrew, R.; Park Kyo, S.; Yaghi Omar, M., Hydrogen sorption in functionalized metal-organic frameworks. *Journal of the American Chemical Society* **2004**, *126*, 5666-5667.
  26. Moulton, B.; Lu, J.; Hajndl, R.; Hariharan, S.; Zaworotko, M. J., Crystal engineering of a nanoscale Kagome lattice. *Angew. Chem. Int. Ed.* **2002**, *41*, 2821-2824.
  27. Hennrich, G.; Murillo, M. T.; Prados, P.; Song, K.; Asselberghs, I.; Clays, K.; Persoons, A.; Benet-Buchholz, J.; de Mendoza, J., Tetraalkynyl calix[4]arenes with advanced NLO properties. *Chemical Communications (Cambridge, United Kingdom)* **2005**, 2747-2749.
  28. Lippard, S. J.; Editor, *Progress in Inorganic Chemistry, Vol. 36.* **1988**.
  29. Sala, T.; Sargent, M. V., Tetrabutylammonium permanganate; an efficient oxidant for organic substrates. *J. Chem. Soc., Chem. Commun.* **1978**, 253-254.
  30. Vincent, J. B.; Chang, H. R.; Folting, K.; Huffman, J. C.; Christou, G.; Hendrickson, D. N., Preparation and physical properties of trinuclear oxo-centered manganese complexes of general formulation  $[\text{Mn}_3\text{O}(\text{O}_2\text{CR})_6\text{L}_3]^{0,+}$  (R = methyl or phenyl; L = a neutral donor group) and the crystal structures of  $[\text{Mn}_3\text{O}(\text{O}_2\text{CMe})_6(\text{pyr})_3](\text{pyr})$  and  $[\text{Mn}_3\text{O}(\text{O}_2\text{CPh})_6(\text{pyr})_2(\text{H}_2\text{O})] \cdot 0.5\text{MeCN}$ . *J. Am. Chem. Soc.* **1987**, *109*, 5703-5711.

31. Canada-Vilalta, C.; Streib, W. E.; Huffman, J. C.; O'Brien, T. A.; Davidson, E. R.; Christou, G., Polynuclear Manganese Complexes with the Dicarboxylate Ligand m-Phenylenedipropionate: A Hexanuclear Mixed-Valence (3MnIII,3MnIV) Complex. *Inorg. Chem.* **2004**, *43*, 101-115.
32. Desiraju, G. R., *Crystal Engineering: The Design of Organic Solids*. Elsevier: New York, **1989**.